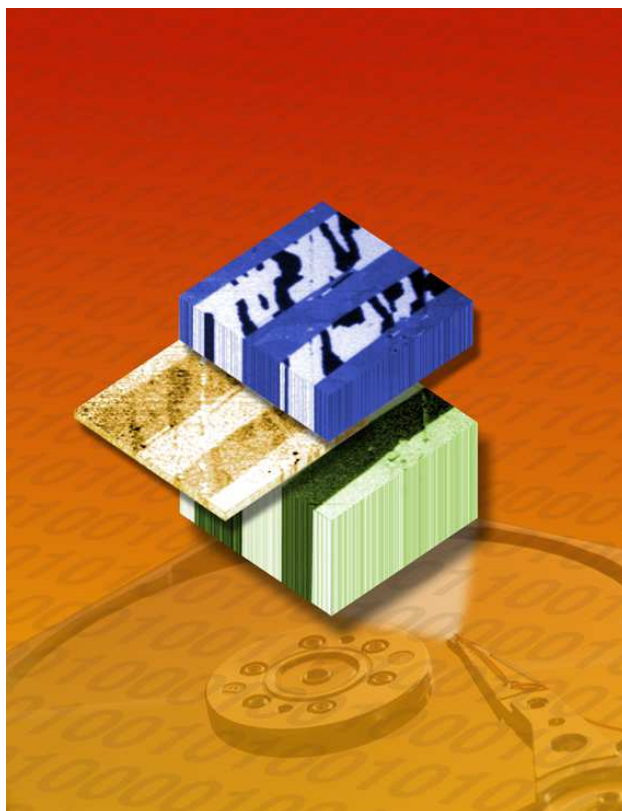


Exchange Coupling of Co and Fe on Antiferromagnetic NiO  
Investigated By Dichroism X-Ray Absorption  
Spectromicroscopy



INAUGURAL - DISSERTATION

zur Erlangung des Doktorgrades  
der Mathematisch-Naturwissenschaftlichen Fakultät  
der Heinrich-Heine-Universität Düsseldorf

vorgelegt von Hendrik Ohldag  
aus Düsseldorf

Universitäts und Landbibliothek Düsseldorf  
2003



Referent: Prof. Dr. E. Kisker

Korreferent: Prof. Dr. K. Schierbaum

Tag der mündlichen Prüfung: 31. Oktober 2002

Gedruckt mit der Genehmigung der Mathematisch-Naturwissenschaftlichen Fakultät der  
Heinrich-Heine-Universität Düsseldorf



# Kurzfassung

In der vorliegenden Arbeit wird die magnetische Kopplung zwischen einer dünnen Schicht eines metallischen Ferromagneten und der antiferromagnetisch geordneten NiO(001) Oberfläche mit Hilfe polarisationsabhängiger Röntgenabsorptions Spektromikroskopie untersucht.

Derartig gekoppelte magnetische Systeme weisen typische Veränderungen in ihren anisotropen magnetischen Eigenschaften auf. Dabei handelt es sich um eine kollineare Ausrichtung von *uniaxialer* und *unidirektionaler* Anisotropie. Die Magnetisierung des Ferromagneten ist preferentiell parallel zu einer bestimmten Achse oder sogar einer bestimmten Richtung orientiert. Die Orientierung der Achse ist bestimmt durch die Wechselwirkung mit dem Antiferromagneten. Obwohl beide Effekte bereits vor über 40 Jahren entdeckt wurden sind sie bis heute unverstanden, da experimentelle Daten über die magnetischen Eigenschaften der Grenzfläche nicht zur Verfügung standen. Die hier angewendete Technik erlaubt nun erstmals eine gleichzeitige Charakterisierung der chemischen und magnetischen Eigenschaften jedes Elementes in einer magnetischen Multilagenstruktur, sei es ein Ferro- oder Antiferromagnet. Somit ist Röntgenabsorptions Spektromikroskopie optimal geeignet zur Erforschung moderner magnetischer Multilagen Dünnschichtsysteme.

Die folgenden Ergebnisse werden im Rahmen der Arbeit präsentiert:

Die Orientierung der magnetischen Momente an der gesputterten (001) Oberfläche von NiO weicht von der im Festkörper ab, bedingt durch die mit dem Sputterprozess verbundenen Gitterverzerrungen. Im Falle der in einer Sauerstoffatmosphäre getemperten Oberfläche von NiO entspricht die magnetische Orientierung der im Festkörper, wohingegen die beobachteten Domänenwände an der Oberfläche signifikant von denen im Festkörper abweichen, um der Symmetriebrechung an der Oberfläche Rechnung zu tragen. Eine Reorientierung der antiferromagnetischen Momente parallel zur Grenzfläche wird beobachtet wenn eine dünne Schicht ferromagnetischen Kobalts oder Eisen deponiert wird. Dies führt zur Ausbildung einer antiferromagnetischen Domänenwand parallel zur Grenzfläche.

Der ferromagnetische Film weist eine uniaxiale Anisotropie parallel zur antiferromagnetischen Achse auf. Sauerstoffdiffusion an der Grenzfläche zwischen ferromagnetischem Metall und antiferromagnetischem Metalloxid führt zur Bildung eines ferrimagnetischen Mischoxides an der Grenzfläche, welches die parallele Kopplung bestimmt.

Für Kobaltfilme auf polychristallinem NiO wurde gefunden, dass ein geringer Anteil der Grenzfläche *nicht* einem äusserem magnetischen Feld folgt. Dieser Anteil sogenannter *gepinnter* Momente wird als Ursache der unidirektionalen Anisotropie identifiziert.

Die in dieser Arbeit gewonnenen experimentellen Ergebnisse erlauben eine umfassende Charakterisierung der magnetischen sowie chemischen Eigenschaften der NiO(001) Oberfläche, sowie der Co/NiO(001) und der Fe/NiO(001) Grenzfläche und dienen als Grundlage für zukünftige theoretische Modelle.



# Contents

<b>Introduction</b>	<b>1</b>
<b>I Motivation and Background</b>	<b>3</b>
<b>1 Exchange Anisotropy</b>	<b>5</b>
1.1 Magnetic Anisotropy . . . . .	5
1.2 Exchange Bias . . . . .	8
1.2.1 History . . . . .	8
1.2.2 Phenomenology . . . . .	9
1.2.3 Unsolved Issues . . . . .	11
1.3 Technical Applications . . . . .	13
1.4 Theoretical Approaches . . . . .	16
1.4.1 The Meiklejohn Approach - Rigid AFM - Weak Coupling . . . . .	16
1.4.2 Néel Approach - Weak AFM . . . . .	18
1.4.3 Partial Domain Wall Approach - Strong Coupling . . . . .	19
1.4.4 Random Interface Model . . . . .	20
1.4.5 Spin-Flop Coupling . . . . .	20
1.4.6 Polycrystalline Antiferromagnets . . . . .	21
1.5 Experimental Approaches . . . . .	23
1.5.1 Uncompensated Moments . . . . .	23
1.5.2 Antiferromagnetic Surfaces - The Missing Experiment . . . . .	23
<b>2 Dichroism X-Ray Absorption Spectromicroscopy</b>	<b>27</b>
2.1 Polarized X-Rays . . . . .	28
2.1.1 Linear and Circular Polarized X-rays . . . . .	28
2.1.2 Mixed Polarization . . . . .	30
2.2 Experimental Techniques . . . . .	31
2.2.1 Total Electron Yield Spectroscopy . . . . .	31
2.2.2 Depth Sensitivity . . . . .	33
2.2.3 Photoemission Electron Microscope . . . . .	34
2.3 X-Ray Absorption Line Shape . . . . .	37
2.3.1 Overview . . . . .	37

2.3.2	Energy Dependence - Chemical Specificity . . . . .	38
2.3.3	Dichroism - Magnetic Sensitivity . . . . .	42
2.3.4	X-Ray Magnetic Circular Dichroism - XMCD . . . . .	43
2.3.5	X-ray Magnetic Linear Dichroism - XMLD . . . . .	47
<b>3</b>	<b>Antiferromagnetic Structure of NiO</b>	<b>53</b>
3.1	Introduction . . . . .	53
3.1.1	NiO as a Model Antiferromagnet . . . . .	53
3.1.2	AFM Domain Formation . . . . .	54
3.2	Spin Symmetry in NiO . . . . .	54
3.2.1	T(win)-Domains . . . . .	54
3.2.2	T-Domain Walls . . . . .	56
3.3	Easy Spin Axes in NiO . . . . .	58
3.3.1	S(pin)-Domains . . . . .	58
3.3.2	AFM Domains and Lattice Distortions . . . . .	60
3.3.3	Summary . . . . .	61
<b>II</b>	<b>Experiments and Results</b>	<b>63</b>
<b>4</b>	<b>Preparation of NiO</b>	<b>65</b>
4.1	NiO(001) Single Crystal Surfaces . . . . .	65
4.1.1	Surface Structure . . . . .	65
4.1.2	Surface Chemistry . . . . .	66
4.2	Thin Films . . . . .	68
4.2.1	Sputter Deposited Exchange Biased Co/NiO . . . . .	68
4.2.2	Electron Beam Deposited Metal Films . . . . .	69
<b>5</b>	<b>Antiferromagnetic Domain Pattern on NiO(001)</b>	<b>71</b>
5.1	Sputtered Surfaces . . . . .	72
5.1.1	Domain Topology on Sputtered Surfaces . . . . .	72
5.1.2	AFM Axes on Sputtered Surfaces . . . . .	73
5.1.3	Summary on Sputtered Surfaces . . . . .	77
5.2	Annealed Surfaces . . . . .	77
5.2.1	In-Plane Versus Out-Of-Plane Axes . . . . .	78
5.2.2	AFM Axes on Cleaved Surfaces . . . . .	79
5.2.3	Surface Domain Wall versus Bulk Domain Wall . . . . .	88
5.2.4	Summary for Annealed Surfaces. . . . .	90
<b>6</b>	<b>Parallel Exchange Anisotropy in Co(Fe)/NiO(001)</b>	<b>93</b>
6.1	General Domain Pattern on Co/NiO and Fe/NiO . . . . .	93
6.2	Observations on Co/NiO(001) . . . . .	95
6.2.1	Azimuthal Dependence of XMLD and XMCD Images . . . . .	95

6.2.2	Local XMCD and XMLD Spectra . . . . .	98
6.3	AFM Reorientation . . . . .	100
6.3.1	AFM Reorientation upon Deposition of a FM . . . . .	100
6.3.2	Possible Reasons for the AFM Reorientation . . . . .	101
6.3.3	Reorientation and Lattice Distortion . . . . .	101
6.3.4	Interfacial Exchange Anisotropy . . . . .	103
6.4	Summary on Parallel Exchange Anisotropy . . . . .	104
<b>7</b>	<b>Blocking Temperature and AFM Domain Structure</b>	<b>105</b>
7.1	Antiferromagnetic Domains Pattern near $T_N$ . . . . .	106
7.2	Temperature Dependence of the Coupled Domain Pattern . . . . .	108
7.3	Summary on AFM/FM Domain Structure Close to $T_N$ . . . . .	110
<b>8</b>	<b>Interfacial Spins in Co/NiO and Exchange Anisotropy</b>	<b>111</b>
8.1	Chemical Reaction at the Metal/NiO Interface . . . . .	112
8.1.1	Introduction . . . . .	112
8.1.2	Results on Co/NiO . . . . .	113
8.2	Free Interfacial Spins and Uniaxial Exchange Anisotropy . . . . .	115
8.2.1	Ni XMCD of a Buried Co/NiO Interfaces . . . . .	116
8.2.2	CoO XMLD of the Co/NiO Interface . . . . .	117
8.2.3	Temperature Dependence of the Interfacial Spin Polarization . . . . .	119
8.2.4	Magnetic Properties . . . . .	122
8.2.5	Discussion: Interfacial Uniaxial Exchange Anisotropy . . . . .	124
8.2.6	Summary: Origin of Coercivity Increase . . . . .	124
8.3	Interfacial Spins and Unidirectional Exchange Anisotropy . . . . .	125
8.3.1	Pinned Interfacial Spins and Exchange Bias . . . . .	126
8.3.2	Hysteresis Loops using XMCD . . . . .	127
8.3.3	Diluted Pinned Interfacial Spins . . . . .	131
8.3.4	Discussion: Interfacial Unidirectional Exchange Anisotropy . . . . .	133
8.3.5	Summary: Origin of Exchange Bias . . . . .	134
<b>9</b>	<b>Summary</b>	<b>137</b>
	<b>Bibliography</b>	<b>148</b>
	<b>Appendix</b>	<b>151</b>



# List of Tables

1.1	Capabilities of Different Methods Sensitive to Antiferromagnetic Order . . . .	24
2.1	Binding Energies and Spin-Orbit Coupling of 3d-Metals . . . . .	40
3.1	Possible Spin Symmetries in NiO . . . . .	56
3.2	Possible Walls Between T-domains . . . . .	58
5.1	AFM Axes Determined from XMLD Signal and Comparison to Bulk Structure	83
8.1	Thermodynamic Properties of Selected 3d-metals and their Oxides . . . . .	113



# List of Figures

1.1	Exchange Anisotropy . . . . .	9
1.2	Exchange Bias in a Magnetic Storage Device . . . . .	15
1.3	Exchange Bias Models . . . . .	17
1.4	Ideal and Non-Ideal Interfaces . . . . .	22
2.1	Synchrotron Radiation and Polarization . . . . .	28
2.2	Experimental Geometry . . . . .	30
2.3	Resonant X-ray Absorption Process and Electron Yield . . . . .	32
2.4	Electron Path within X-PEEM . . . . .	35
2.5	Chemical and Elemental Sensitivity of X-ray Absorption . . . . .	39
2.6	Origins of Dichroism . . . . .	45
2.7	Imaging of Ferromagnetic Domains Using XMCD . . . . .	47
2.8	Imaging of Antiferromagnetic Domains Using XMLD . . . . .	50
3.1	The Crystal Structure of NiO . . . . .	55
3.2	Possible Walls between T-domains. . . . .	57
3.3	Possible Spin Directions in a T-domain. . . . .	59
4.1	LEED of NiO(001) Surface. . . . .	66
4.2	XAS of Sputtered and Cleaved NiO(001) Surfaces. . . . .	67
5.1	Domain Topology of NiO(001) . . . . .	72
5.2	Domain Topology of Sputtered NiO(001) . . . . .	74
5.3	Angular Dependence of Contrast on Sputtered NiO(001) . . . . .	75
5.4	Polarization Dependence of AFM Domain Pattern . . . . .	78
5.5	In-Plane Domain Pattern on NiO . . . . .	80
5.6	Out-Of-Plane Domain Pattern on NiO . . . . .	82
5.7	Solving the Ambiguity in an XMLD Image . . . . .	84
5.8	Antiferromagnetic Domains Observed at Annealed NiO(001) Surface . . . . .	86
5.9	Domain Walls on the NiO(001) Surface . . . . .	87
5.10	Surface and Bulk Domain Walls . . . . .	89
6.1	FM and AFM Domain Topology on Coupled Systems . . . . .	94
6.2	Azimuthal Dependence of FM and AFM Contrast on Co/NiO(001) . . . . .	96

6.3	Local Spectra of Co and NiO domains . . . . .	99
6.4	In-Plane Reorientation of AFM NiO upon Co Deposition . . . . .	100
6.5	Visualization of the In-Plane Reorientation . . . . .	102
7.1	Temperature Dependence of AFM Surface Domain Pattern . . . . .	107
7.2	Temperature Dependence of AFM/FM Exchange Coupled Domain Pattern . . . . .	109
8.1	Absorption Spectra of Co/NiO . . . . .	114
8.2	Interfacial Ni Moment in Co/NiO with AFM Contrast . . . . .	115
8.3	Pure Interfacial Ni Moment in Co/NiO without AFM Contrast . . . . .	116
8.4	XMLD Images of 2ML of CoO Prepared on NiO at RT. . . . .	118
8.5	XMCD Spectra of Co and Interfacial Ni in $\text{CoNiO}_x$ . . . . .	120
8.6	Interfacial Spin Polarization and Annealing . . . . .	121
8.7	Relation between Interfacial Thickness and Coercivity. . . . .	122
8.8	The 'Third' Layer in AFM/FM Pairs. . . . .	123
8.9	Vertical versus Horizontal Loop Shift in Interfacial Hysteresis . . . . .	126
8.10	How External Magnetic Fields Influence the Electron Yield . . . . .	128
8.11	How To Measure Element Specific Hysteresis Loops Using XMCD . . . . .	129
8.12	XMCD Spectra of Co and NiO in Polycrystalline Co/NiO . . . . .	132
9.1	The Summary Image . . . . .	138

# Introduction

For the purpose of this thesis the magnetic exchange coupling between a ferromagnetic metal and the antiferromagnetic NiO(001) surface has been investigated. The coupling between magnetic layers with different magnetic properties is of special interest for modern magnetic data storage applications. The storage media itself as well as the data readout sensors consist of several magnetic layers coupled to each other via their interface. For example an antiferromagnetic/ferromagnetic interface is utilized in a hard disk read head to introduce a so-called *unidirectional anisotropy* or *exchange bias*. The directional anisotropy in the magnetic sensor, that is the existence of a preferred magnetic direction, makes it possible to distinguish between up and down bits on the hard disk material. Although the effect is already used in today's devices its origin is not understood. The reason for this is that very little data exists, which provides detailed information about the antiferromagnetic/ferromagnetic interface. Conventional methods to characterize magnetic systems are either not suitable for thin film systems or are not sensitive to antiferromagnetic order. The technique used in this thesis, *polarization dependent x-ray absorption spectromicroscopy*, provides exactly the sensitivity needed. The approach combines chemical, surface and magnetic sensitivity and allows most strikingly one to address *both* ferromagnetic as well as antiferromagnetic order at the same time.

To address the problem of exchange coupling and biasing a suitable antiferromagnetic substrate had to be chosen. Ideally its bulk properties should be well known and recipes to prepare high quality surfaces should be established. Thus the magnetic ordering found at the surface or interface can be compared to the known bulk structure. This work was been started at the Institute of Applied Physics where the oxidic antiferromagnetic materials NiO, CoO and MnO are extensively studied (see for example [26, 27]) and NiO was chosen as the antiferromagnetic substrate because of its convenient ordering temperature at 525K. Furthermore the polarization dependence of the NiO x-ray absorption spectra had already been established in detail [1].

For the first experiment a photoemission electron microscope was used to image the spatial distribution of the antiferromagnetic vector at the NiO(001) surface. The experiment was carried out in collaboration with Dr. N.B. Weber using the commercial STAIB PEEM at the elliptical undulator beamline at the BESSY2 synchrotron in Berlin (Germany). Images of the antiferromagnetic surface domain structure were obtained and qualitative information about the antiferromagnetic axis in each domain were derived. For a subsequent experiment

the PEEM2 instrument, located at the Advanced Light Source (ALS) in Berkeley (USA), was used. The direction of the spin axis in each antiferromagnetic domain could now be unambiguously identified and for the very first time antiferromagnetic domain walls were directly observed.

In the following Dr. Weber continued to study the antiferromagnetic structure of the bare NiO surface in more detail using the STAIB instrument [105] at the BESSY2 synchrotron. The experiments described in this thesis on the other hand, focus more on the interface between NiO and an adjacent ferromagnet deposited onto the antiferromagnet and were carried out at the ALS using the PEEM2 microscope. The question is why a ferromagnet shows a distinct anisotropic behavior if in contact to an antiferromagnet and what in addition happens to the magnetic structure of the antiferromagnet if a ferromagnet is deposited on top. The experimental findings reported in this thesis are listed:

1. NiO(001) surfaces have been prepared by annealing in an oxygen atmosphere. The antiferromagnetic spin axis which is observed at the surface is the same as it has been reported in the bulk [108]. However at the surface antiferromagnetic domain walls are observed that are not present in the bulk of the material. These are related to the symmetry breaking at the surface.
2. The surface specific domain walls are not observed on surfaces prepared by sputtering due to the lattice distortion caused by the ion bombardment [32].
3. Upon deposition of a ferromagnetic material the surface specific domain walls disappear and the antiferromagnetic spin axis undergoes a reorientation into the surface plane. An antiferromagnetic domain wall parallel to the surface is formed [62].
4. The ferromagnet exhibits a distinct easy axis of magnetization parallel to the antiferromagnetic spin axis underneath. Clearly parallel coupling between the two different magnetic systems is observed.
5. Oxygen diffusion at the interface leads to formation of a ferrimagnetic mixed oxide layer [61].
6. Finally, thin Cobalt films grown on polycrystalline NiO have been investigated. A small fraction of moments within the mixed oxide layer are shown not to rotate together with an external field and do serve as an internal field causing the unidirectional anisotropy of the system [63].

The study presented here is the first report of a complete chemical and magnetic characterization of an antiferromagnetic/ferromagnetic interface. The quantitative characterization of antiferromagnetic surfaces has been particularly difficult in preceding experimental approaches and is the main reason for the lack of theoretical models to describe the observed uniaxial and unidirectional anisotropy quantitatively.

## Part I

# Motivation and Background



# Chapter 1

## Exchange Anisotropy

In this first chapter exchange anisotropy is reviewed with respect to the experimental results reported in this thesis. After Meiklejohn and Bean discovered exchange anisotropy on CoO/Co nanometer sized particles in 1956 [52], they presented a first model based on their data [53, 51] and the results obtained from permalloy films grown on antiferromagnetic FeMn and NiMn by Kouvel et al [43, 42]. Although the Meiklejohn model is rather intuitive it represents a powerful approach to the phenomenology of exchange anisotropy and is discussed in detail in sections 1.2 and 1.4.1.

Over the last 15 years exchange anisotropy has attracted enormous interest within the magnetic storage industry because of its role in modern disk drive read heads and future permanent magnetic storage devices. The structure of these devices and the particular role of exchange anisotropy is described in section (1.3). Many different systems exhibiting exchange anisotropy have been studied in the last decade and the experimental as well as the theoretical effort to understand exchange anisotropy has been dramatically increased. Modern reviews including theoretical limitations and experimental difficulties can be found in [59, 8, 83]. A summary of the most prominent theoretical approaches is given in section (1.4), followed by a brief analysis of the experimental difficulties to corroborate the models in section (1.5).

### 1.1 Magnetic Anisotropy

#### The Isotropic Ferromagnet

The phenomena of magnetic anisotropy and methods to determine it quantitatively from macroscopic is introduced in the following. The magnetic free energy  $F$  of a simple isotropic ferromagnet, that is a ferromagnet in which the magnetization is homogenously distributed over the entire volume (*single domain*) but can point in any direction in space, consists of only the so-called *Zeeman energy*.

$$F = -HM \cos(\varphi_{\text{FM}} - \varphi_{\text{H}}) \quad (1.1)$$

If the external field  $H$ , which is pointing along the direction  $\varphi_{\text{H}}$  is changed the ferromagnet responds by changing the direction  $\varphi_{\text{FM}}$  of its magnetization  $M$ . All angles in this case are

relative to a laboratory system and correspond to distinct directions. The Zeeman energy favors a parallel alignment of the magnetization in the ferromagnet with the external field. If the external field is positive the magnetization will point into the positive direction as well. Immediately upon reversal of the external field into the negative direction the magnetization will then point into the negative direction.

### The Anisotropic Ferromagnet

The above situation is hardly ever realized exactly. More often it will be necessary to increase the field further into the opposite direction before the majority of the magnetization will be parallel to the external field again. Furthermore it is then observed that the reversal process and the field which is necessary to reverse the magnetization depends on the angle between the external field and a particular crystal axis. The magnetic properties in such a system are not isotropic anymore, thus this behavior is referred to as *magnetic uniaxial anisotropy*. In the presence of an uniaxial anisotropy the free magnetic energy will be lowered by the anisotropy energy  $K_a$  if the magnetization is aligned parallel to a certain axis (*easy axis*). The perpendicular axis is energetically unfavorable (*hard axis*). A direct consequence is that the magnetic system experiences a torque  $T$  caused by the change in magnetic energy if the magnetization is dragged away from the anisotropy axes. If the easy axis includes an angle  $\varphi_a$  with the external field the free energy and the torque can be written,

$$F = -HM \cos(\varphi_{FM} - \varphi_H) + K_a \cos^2(\varphi_{FM} - \varphi_a) \quad (1.2)$$

$$T = \frac{dF}{d\varphi_{FM}} = +HM \sin(\varphi_{FM} - \varphi_H) - 2K_a \sin(2(\varphi_{FM} - \varphi_a)) \quad (1.3)$$

### Origin of anisotropy

The microscopic origin of the magnetic anisotropy is the spin-orbit coupling which couples the spin of each atom to its orbital moment. While the spin can in principle point in every direction the much smaller orbital moment is tightly locked to the electronic properties of the crystal and the symmetry of the lattice. Consequently the magnetic energy is lowered if the orbital moment is aligned parallel to a particular crystal axis. Due to the fact that the spin-orbit coupling is only a small perturbation to the Hamiltonian the anisotropy energy is typically much smaller than the Zeeman energy. Therefore it is still possible to drag the spins away from the easy axis if the field is just large enough and the Zeeman energy compensates the anisotropy energy. Typical values of  $K_a$  are (1 – 50  $\mu\text{eV}$ ) per atom and this corresponds to external fields of 10-500 mTesla.

In equation 1.2 or 1.3 the anisotropy constant  $K_a$  is denoted as an energy but in practice anisotropy constants are often given as energy densities  $k_a$ . This is useful with respect to the classification of anisotropy energies into bulk and surface or interface specific properties. The bulk anisotropy energy  $k^V$  is typically given in units of  $\text{J}/\text{m}^3$  or  $\text{erg}/\text{cm}^3$ , while surface or interface anisotropy energies  $k^S$  are given in  $\text{J}/\text{m}^2$  or  $\text{erg}/\text{cm}^2$ . The total anisotropy energy  $K$  originating from all contributing volumes  $V_i$  and surfaces or interfaces  $A_i$  can then be

calculated in the following way.

$$K_{\text{tot}} = k_i^V V_i + k_j^A A_j \quad (1.4)$$

### Experimental Determination of Anisotropy Energies

Two different techniques are generally used to characterize the magnetic anisotropy of a sample. The first method is  $(M, H)$  hysteresis loops in which the magnetization of the sample along a certain axis is measured while the applied field is reversed. The second method is  $(T, \phi)$  torque measurements. A large magnetic field (1-2 Tesla) is applied to the sample and can be rotated around its azimuth. The torque that the sample experience is measured by a spring or similar device. Both techniques lead to quantitative information about the anisotropy energy.

In a  $(M, H)$  hysteresis loop the anisotropy constant  $K_a$  can be calculated from the field which is necessary to reverse the magnetization along the easy axis (*coercive field*  $H_c$ ). For this purpose the external field has to be applied parallel to the easy axis. The Zeeman energy exactly matches the anisotropy energy if the external field  $H$  balances the coercive field  $H_c$ .

$$K = \frac{M}{2} H_c \quad (1.5)$$

A typical hysteresis loop measured under these conditions is shown in the bottom left panel of figure 1.1 as an example. The shape of the loop is roughly square. The ferromagnet retains its magnetization even if no external field is applied (*remanence magnetization*  $M_r$ ) and the absolute value of the coercive field  $H_c$  is the same for the positive and the negative direction of the applied external field, the loop is symmetric with respect to zero applied field.

The torque curve obtained from such a sample is shown in the upper left panel of figure 1.1. At  $\phi = 0^\circ$  and  $\phi = 180^\circ$  the external field is applied along the easy axis and no torque is present, because these are energetically stable configurations. At  $\phi = 90^\circ$  and  $\phi = 270^\circ$  meta stable configurations are found when the magnetization is dragged parallel to the hard axis. The torque vanishes for these angles. Altogether the torque curve follows a  $\sin(2(\varphi_{\text{FM}} - \varphi_a))$  dependence. The  $\sin(\varphi_{\text{FM}} - \varphi_H)$  component denoted in equation (1.3) is not observed. It is suppressed by the strong external field which always aligns the magnetization parallel so that  $\varphi_{\text{FM}} = \varphi_H$  and the Zeeman term and its related torque vanishes. The anisotropy energy can be directly extracted from the torque curve.

$$K_u = \frac{1}{2} T_{45^\circ} \quad (1.6)$$

### Coherent Rotation Model

The expression for the free energy  $F$  can be evaluated numerically to model the magnetic behavior of anisotropic magnetic systems and corroborate the experimentally found values for the anisotropy energies. For a given system the magnetization reversal is simulated by sweeping the external field step by step pseudo-adiabatically and calculating the next minima for the free energy depending on the direction of the sample magnetization. This approach

is called the *coherent rotation model*, because it assumes a single domain behavior of the magnetic systems, and thus all the magnetic moments in the sample rotate coherently. It is a rather crucial simplification so in general the exact shape of a  $(M, H)$  loop will not be reproduced. Nevertheless the qualitative azimuthal dependence of the the magnetic properties as well as their key features like coercive field and remanence magnetization are typically in good agreement with the experimental data if appropriate values for the anisotropy energies are assumed.

The model can easily be extended to describe more complicated systems consisting of different magnetic layers. In this case the contribution of the volume anisotropy of each layer as well as the coupling between the different layers through their interface is considered. The coupling is usually described by an interface anisotropy which favors a certain relative alignment of adjacent layers, for example parallel, antiparallel or perpendicular.

## 1.2 Exchange Bias

An overview about the history of exchange bias and the relevant external parameter has been given for example by Nogués *et al.* [59] and Berkowitz *et al.* [8]. Both reviews include a summary of experimental work and the unsolved issues in exchange anisotropy. The following section is based on these two publications.

### 1.2.1 History

In 1956 W. H. Meiklejohn and C. P. Bean investigated the magnetic properties of small cobalt particles (20nm) that were exposed to air and therefore coated with cobaltous oxide [52, 53]. The authors were in particular interested in= the influence of the antiferromagnetically ordered cobalt oxide on the magnetic properties of the ferromagnetic cobalt. Because the Néel temperature of CoO is 293K they had to perform the magnetic characterization at lower temperatures and cooled their samples with liquid nitrogen to 77K. During the cooling process a magnetic field was applied strong enough to saturate the Co, typically 20kOe. They discovered...

...a new type of magnetic anisotropy (...) which is best described as an exchange anisotropy. This anisotropy is the result of an interaction between an antiferromagnetic material and a ferromagnetic material.

The exchange anisotropy is a unidirectional anisotropy in that it produces one easy direction of magnetization.

In order to best observe the exchange anisotropy of a randomly oriented compact of fine particles, the material is cooled from the paramagnetic state of the oxide to the antiferromagnetic state in a saturating magnetic field [52].

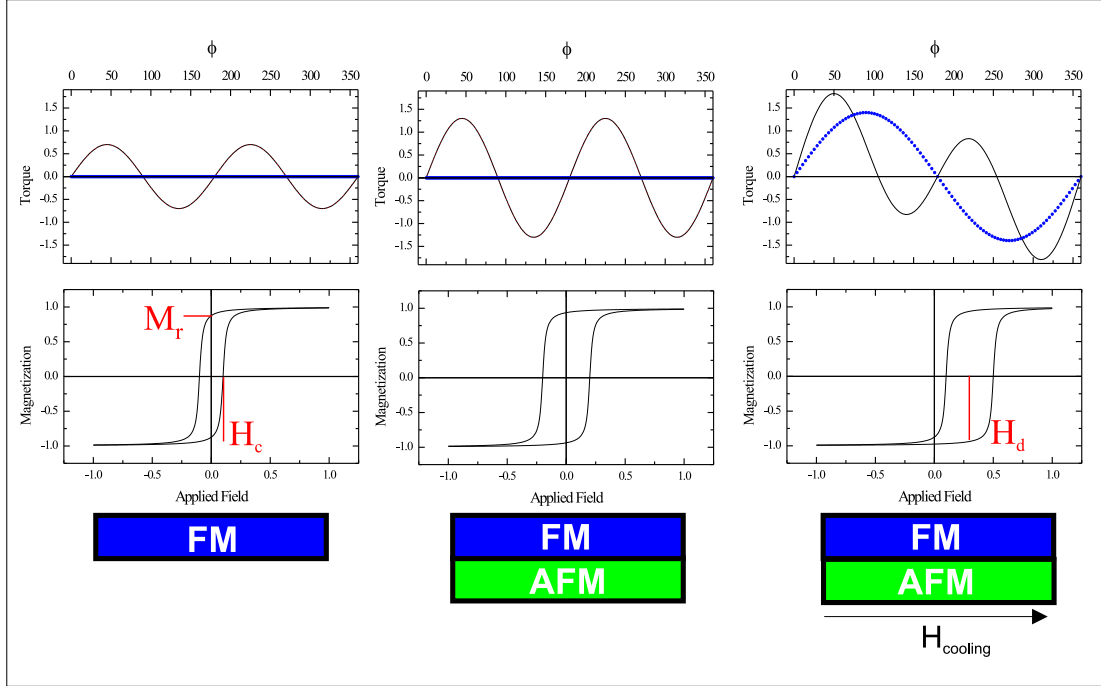


Figure 1.1: Exchange Anisotropy

Macroscopic magnetic properties determined by  $(M, H)$  hysteresis loops and  $(T, \phi)$  torque curves. Depicted are a single ferromagnet (left), a ferromagnet coupled to an antiferromagnet without further treatment (middle) and after cooling through the Néel temperature in an external field (right). The remanent magnetization  $M_r$  appears to be the same in all cases, while changes in the coercive field  $H_c$  and the torque  $T$  are observed. Exchange coupling between the two layers lead to an increase in  $H_c$  and the maximum torque  $T$ . After field cooling a horizontal shift of the hysteresis loop  $H_d$  is observed and the torque curve exhibits an additional  $\sin(\phi)$  component indicated by the blue curve.

### 1.2.2 Phenomenology

Sketches of hysteresis loops and torque curves to illustrate the findings of Meiklejohn and Bean are shown in figure 1.1. The data obtained from a bare ferromagnet (left panel) were discussed in the last section 1.1. The square shaped  $(M, H)$  loop with distinct magnetic remanence and coercive field is an indication of the presence of an uniaxial anisotropy. Another indication is the  $\sin(2\phi)$  behavior of the torque curve. The loop shown in the center panel sketches the properties of exactly the same ferromagnet in contact with an antiferromagnet. The system has been cooled down below the Néel temperature of the antiferromagnet but without external field applied. Qualitatively, the  $(M, H)$  loop and the torque curve look the same, but the coercive field is increased compared to the single ferromagnet. The uniaxial anisotropy  $K_a$  is increased in antiferromagnetic/ferromagnetic coupled systems.

If an external field is applied during the cooling procedure (*field cooling*) the magnetic properties change drastically. The positive and negative coercive fields are different since the loop shows now a horizontal shift  $H_d$ . In the case depicted in the right panel of figure 1.1  $H_d$  is assumed to be large enough so that the coercive field is always positive, which means that at zero field the sample is always magnetized in the negative *direction*, independent of its history. This behavior, the preferential alignment of the magnetization along a particular direction in contrast to a distinct axis is referred to as *unidirectional anisotropy* or *exchange bias* (**EB**) and characterized by an anisotropy energy ( $K_d$ ). Note, that in this example the loop shift towards the positive field direction has been introduced by a field applied into the negative direction during cooling. This is the situation of the so-called *negative exchange bias*. The torque curve of an exchange biased system in figure 1.1 shows the following behavior. In addition to the  $\sin(2\varphi)$  component a  $\sin(\varphi)$  appears in the torque curve. As has been pointed out earlier in section 1.1, the  $\sin(\varphi)$  component is common at smaller external fields when the magnetization is not completely parallel aligned with the external field, but vanishes at higher fields (1-2 Tesla). In contrast the  $\sin(\varphi)$  component in exchange biased samples persists in fields up to 5 Tesla. It appears that the existence of exchange bias is connected to a strong 'inner' field  $H_d$  of the investigated sample.

Finally, the results of Kouvel *et al.* on Permalloy/FeMn and Permalloy/NiMn [43, 42] brought new insight into the nature of the unidirectional anisotropy. In their experiments they changed the thickness  $t_{\text{FM}}$  of the ferromagnetic layer and observed that the loop shift is inversely proportional to  $t_{\text{FM}}$ <sup>1</sup>. Because of this behavior they concluded that the unidirectional anisotropy originates directly from the antiferromagnetic/ferromagnetic interface. The contribution of such an interface anisotropy to the total free energy decreases with increasing ferromagnetic bulk anisotropy and Zeeman energy<sup>2</sup>

Altogether it appears from these observation it appears that exchange bias is caused by an inner field  $H_d$  originating from the antiferromagnetic-ferromagnetic interface pointing in the direction of the cooling field. It is large enough so that it cannot be overcome by an external field of several Tesla. These very general observations are summarized in the following two equations.

$$H_{\text{eff}} = H_{\text{ext}} + H_d \quad (1.7)$$

$$\text{and } H_d = \frac{K_d}{M} = \frac{\sigma_{\text{int}}}{m t_{\text{FM}}} \quad (1.8)$$

The second equation relates the experimentally determined loop shift  $H_d$  with the unidirectional anisotropy energy  $K_d$ . The latter one is often described in terms of the interfacial exchange energy density  $\sigma_{\text{int}}$ , which is a specific quantity and independent of the ferromagnetic thickness and magnetization.

<sup>1</sup>Note, that this is only true above a certain thickness of the ferromagnet. If the ferromagnet is thinner than about 10 monolayers the bias field does not increase with  $\frac{1}{t_{\text{FM}}}$  anymore.

<sup>2</sup>More recently Thomas *et al.* could show that the unidirectional anisotropy decreases with a decay length of 0.2nm to 0.5nm if the two magnetic layers are separated by a non-magnetic spacer layer [97]. This observation demonstrates the interfacial nature of the unidirectional anisotropy further.

Since this early approach was presented many different models have tried to explain the size and the origin of the inner interfacial field leading to the interfacial exchange energy  $\sigma_{\text{int}}$ . Section 1.4 presents an overview of these different models, but first it is important to enumerate the unsolved issues which these models have to explain.

### 1.2.3 Unsolved Issues

#### Size of Exchange Bias

The simplest model based on a completely uncompensated and rigid antiferromagnet presented by Meiklejohn and Bean [51] overestimates the loop shift by orders of magnitude (section 1.4.1). Based on this model the exchange bias field originates from uncompensated magnetic moments located at the antiferromagnetic surface and should vanish on compensated surfaces. Furthermore it should be larger on ordered antiferromagnetic single crystals than on disordered polycrystalline antiferromagnets. Experimental findings on different systems collected in [59] show that none of these expectations are fulfilled. So far there is no conclusive approach which adequately describes the size of the exchange bias field on all types of antiferromagnetic surfaces. In particular the influence of the magnetic anisotropy of the antiferromagnet on the unidirectional anisotropy of the entire system remains an open question and is suspected to play an important role in all of the unsolved issues and experimental findings listed below.

#### Temperature Dependence

Intuitively one would assume that exchange bias disappears together with the long range order of the antiferromagnet above the Néel temperature. In contrast it has been observed for many different antiferromagnets that the unidirectional anisotropy already vanishes at lower temperatures. The temperature where the unidirectional anisotropy vanishes is called the *blocking temperature*  $T_B$ . For example, in exchange biased samples based on NiO with a Néel temperature of 523K the loop shift typically disappears around 475K.

#### Thickness Dependence

Exchange bias is not observed if the thickness of the antiferromagnetic layer  $t_{\text{AFM}}$  is below a critical thickness which depends on the antiferromagnetic material. Above this thickness the bias field increases until it reaches a limit, typically for  $t_{\text{AFM}} = 10 - 20\text{nm}$ . This dependence is complicated to describe in a general theoretical approach, because of the fact that properties like crystallographic grain size or Néel temperature, which is often not known, depend strongly on the film thickness.

#### Training Effect

In many different systems the size of the loop shift decreases and even vanishes after continuously cycling the magnetization and might even vanish. This so-called *training effect* appears

to be more pronounced using antiferromagnets with a low anisotropy or if the operating temperature is close to the Néel temperature. It is supposed that this effect is related to a partial reorientation of the antiferromagnet. A reorientation of the antiferromagnetic microstructure will then cause the interfacial spins which introduce the loop shift to break loose.

### Field Dependence

In general the loop shift depends only very little on the cooling field. An exception has been reported by Nogués *et al.* who found a strong dependence of the bias field for FeF<sub>2</sub>/Fe and MnF<sub>2</sub>/Fe [58]. After field cooling in more than 1 Tesla they even observed *positive bias* which means that the loop shift is observed into the same direction as the cooling field and a magnetization opposite to the cooling field is favored in the zero-field state. So far this behavior has only been reported on fluorine-based antiferromagnets.

### Antiferromagnetic Orientation

From a theoretical point of view it is still unclear whether the magnetic axis of the antiferromagnet and the uniaxial anisotropy of the entire system are coupled parallel or antiparallel in 'real' antiferromagnetic/ferromagnetic systems. Calculations on ideal interfaces suggest perpendicular coupling due to frustration, which is caused by the concurrence between the directional exchange of spins in the ferromagnet and the antiferromagnet and the axial symmetry of the antiferromagnetic spin lattice. The fact that ideal flat interfaces are often not realized may be the crucial factor.

Experimental evidence for perpendicular coupling has been found using neutron scattering, a bulk sensitive technique, on ferrimagnetic/antiferromagnetic Fe<sub>3</sub>O<sub>4</sub>/CoO [33]. Furthermore Moran *et al.* report perpendicular coupling in the system Fe/FeF<sub>2</sub>, by comparing the antiferromagnetic susceptibility and the ferromagnetic hysteresis loop. Both systems are special, considering that Fe<sub>3</sub>O<sub>4</sub> is not a ferromagnet but a ferrimagnet and the unidirectional anisotropy on FeF<sub>2</sub> shows a strong cooling field dependence not observed on other antiferromagnets. The results reported in this thesis for conventional exchange coupling between ferromagnetic/antiferromagnetic Co/NiO and Fe/NiO indicate parallel coupling.

### Coercivity

As described earlier the coercivity of a ferromagnetic film increases if in contact with an antiferromagnet. It appears as that the bulk anisotropy of the antiferromagnet adds to the total anisotropy energy. The coercivity increases further if the unidirectional anisotropy vanishes close to the blocking temperature. The same behavior is observed for decreasing thickness of the antiferromagnet. Altogether this leads to the notion that the coercivity increase is closely related to the rigidness of the antiferromagnet. Thin antiferromagnets exhibit a smaller volume anisotropy and therefore their magnetic microstructure can be changed easier by the external field or the coupling to the ferromagnet. The same is true close to the Néel temperature when the long range antiferromagnetic order becomes weaker. In case of a totally rigid

antiferromagnet no coercivity increase would be observed.

## 1.3 Technical Applications

### Introduction

Magnetism and data storage are closely connected since little permalloy rings placed on a current grid were used to permanently store information instead of mechanically punching holes into stripes made from cardboard. Nevertheless, these 'devices' were still macroscopic. The age of microscopic magnetic data storage begun with the first hard disk (RAMAC), introduced in the late 1950s by IBM. Using hard disks the binary information was stored on a spinning disk of a magnetic material by magnetizing areas in one or the other direction with a small electromagnet and reading it out again with a little coil that sensed the magnetic stray field which arose from these *bits* above the disk. Although the size of a single bit was still of the order of  $10^{-6}\text{m}^2$ , there seemed to be no mechanical limit to further decrease the dimensions. Today, disk materials like granular FeCrCoPtB compounds together with highly miniaturized electromagnets are used which allow the creation of magnetic bits as small as  $10^{-14}\text{m}^2$ . An improvement of 8 orders of magnitude in 40 years! However, the challenge remained to detect the stored information from these tiny magnetic bits with high enough accuracy to allow read out rates of 100 Megabytes per second. While the write heads and the storage media simply have become more sophisticated over the last 40 years, today's read head developments bear little resemblance to the idea of an inductive coil. Instead multilayer structures consisting of many different layers of ferromagnetic and other materials are used which employ the so-called *giant magneto resistance effect* or GMR. Its phenomenology and the relevance of exchange anisotropy in read heads based on the GMR are described below.

### Giant Magneto Resistance

In a stack of Fe/Cr multilayer the magnetization of adjacent ferromagnetic Fe layers can be oriented parallel or antiparallel depending on the thickness of the Cr interlayer (*interlayer exchange coupling*). The size of the interlayer exchange energy is such that even in the case of antiparallel coupling the two ferromagnetic layer can still be aligned parallel with an external field of 15kOe, when the Zeeman energy overcomes the antiferromagnetic exchange energy. In the late 1980s M. N. Baibich and G. Binasch independently found that the electric resistance of such a structure changes dramatically between the remanent (antiparallel orientation) and the saturated (parallel orientation) state [6, 9]. Changes of up to 40% were observed and for this reason the effect was referred to as the *giant magneto resistance effect* (GMR).

In the early 1990s the concept of magneto resistive sensors was already established using the so-called *anisotropic magneto resistance* (AMR), where the resistance changes by 1% if the magnetization is rotated from the easy axis to the hard axis. Since then the storage density was increased by an order of magnitude every 5 years compared to a 10 year schedule before the use of magneto resistive read heads. The discovery of GMR now opened the door

for a new class of magnetic sensors with much improved sensitivity and signal to noise ratio and made it possible to keep the pace set by magneto resistive sensors for another decade.

However to use GMR sensors in magnetic storage two important obstacles had to be overcome. First of all the coercive field of these sensors needed to be decreased from 15kOe to a few Oersted to be feasible as a read head or a storage element for example. Second and even more important read head sensors need to be capable of distinguishing between two different directions of an external field. This is the point where exchange anisotropy came into play, by introducing a preferred direction into a GMR sensor, changing its uniaxial magnetic symmetry into a unidirectional one.

### Read Heads and Magnetic Random Access Memory

A few years after its discovery on Fe/Cr the GMR effect was observed between soft magnetic materials by B. Dieny *et al.* [19]. Based on these findings IBM proposed a possible structure for a magnetic read head [99]. The basic idea behind the sensor is shown in figure 1.2. Two soft ferromagnetic materials are separated by a nonmagnetic material. The materials and thicknesses are chosen such that this structure does indeed show a GMR effect (for example CoFe/Cu/CoFe) but are not antiferromagnetically coupled through the interlayer. Instead the bottom layer is attached to an antiferromagnet and treated such that it shows considerable exchange bias. This can be seen in the hysteresis loop of such a sample shown in the lower left of figure 1.2. The top layer (shown in red) acts as the sensor and can be saturated completely to the left or right by an external field of less than 20 Oersted. The bottom layer (blue) is *pinned* by the antiferromagnet and serves as a reference layer. If the external field remains below 200 Oersted it will maintain its magnetization in one predefined direction. External fields of less than  $\pm 200$  Oersted (the unidirectional anisotropy of the pinning layer) and more than  $\pm 20$  Oersted (the uniaxial anisotropy of the sensor layer, marked by a red bar) will therefore only change the relative orientation of the sensor layer and the reference layer from parallel to antiparallel. At the same time the resistance of the structure will change within the range of the GMR. Structures based on this principle are used in modern read heads and has allowed the increase of hard disk storage density in a reliable manner by an order of magnitude over the last 5 years.

Finally this scheme can be used to build a magnetic memory cell (*Magnetic Random Access Memory MRAM*) in which the information is stored magnetically (permanently) and can be read out electronically (fast). For this purpose the metallic interlayer is replaced by an isolator (*Tunnel Magneto Resistance TMR*) and the current is driven perpendicular to the interfaces. To allow fast switching of the top layer beyond the established Oersted switching new approaches have to be followed for example switching by so-called *spin injection*. For an overview see [67].

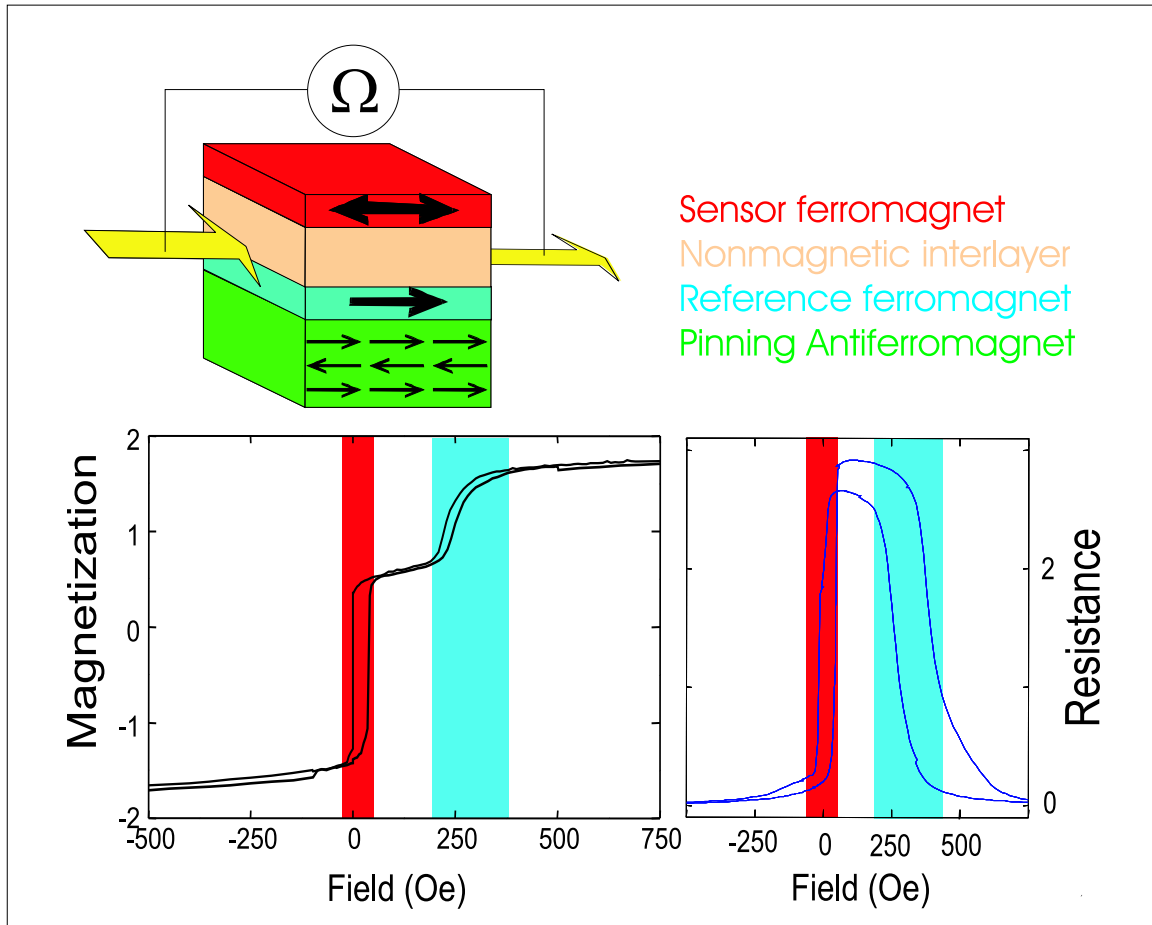


Figure 1.2: Exchange Bias in a Magnetic Storage Device

Top: Magnetic multilayer structure used in a GMR sensor. The electric resistance depends on the relative orientation of the sensor ferromagnet (red) and the reference ferromagnet (blue) separated by a non magnetic material like copper. The magnetization of the reference layer is fixed (*pinned*) into one direction by the exchange interaction with the antiferromagnet (green). Bottom: The hysteresis loop (left) of the reference layer is shifted along the field axis, while the hysteresis loop of the sensor layer remains symmetric around zero field. The resistance of such a structure (right) changes if the signal layer is switched without the reference layer.

## 1.4 Theoretical Approaches

The fact that the technological relevance of exchange anisotropy increased dramatically during the 1990s led to an huge increase in both experimental and theoretical work. Many different systems exhibiting exchange bias were studied experimentally. In parallel theoretical models were developed in order to provide a common approach to describe the observed phenomena and to hopefully help to engineer an exchange biased interface. So far this has not been accomplished.

The different theoretical approaches were first summarized in the review articles by Nogueés and Schuller[59], and Berkowitz and Takano [8]. Recent reviews by Stamps *et al.* [83] and Kiwi *et al.* [39] focussed more strongly on the different theoretical approaches and include description of polycrystalline samples as well. The summary of theoretical approaches in this section is based on the different review articles.

### 1.4.1 The Meiklejohn Approach - Rigid AFM - Weak Coupling

Meiklejohn and Bean presented a phenomenological description of exchange anisotropy [53, 51]. They assumed a coherent rotation for the magnetization  $m$  of the ferromagnet. For the case of collinear alignment of the unidirectional anisotropy  $\sigma_{\text{int}}$ , external field  $H_{\text{ext}}$  and ferromagnetic  $k_{\text{FM}}$  as well as antiferromagnetic  $k_{\text{AFM}}$  anisotropy one finds the following expression for the magnetic free energy per unit area,  $f$ , at the interface depending on the direction of the ferromagnetic magnetization  $\varphi_{\text{FM}}$  and the net magnetization at the antiferromagnetic interface  $\varphi_{\text{AFM}}$ .

$$f = -H_{\text{ext}} m t_{\text{FM}} \cos(\varphi_{\text{FM}}) + k_{\text{FM}} t_{\text{FM}} \cos^2(\varphi_{\text{FM}}) + k_{\text{AFM}} t_{\text{AFM}} \cos^2(\varphi_{\text{AFM}}) - \sigma_{\text{int}} \cos(\varphi_{\text{FM}} - \varphi_{\text{AFM}}) \quad (1.9)$$

In addition to the terms in (1.2) this expression for the the free energy density includes a rotation of the antiferromagnet axis caused by the coupling to the ferromagnet. Furthermore the magnetization  $m$  of the ferromagnet and the thickness of both the antiferromagnet and the ferromagnet are considered. In general the antiferromagnetic bulk anisotropy energy  $k_{\text{AFM}} t_{\text{AFM}}$  is much larger than the ferromagnetic bulk anisotropy  $k_{\text{FM}} t_{\text{FM}}$  and by minimizing the expression with respect to  $\varphi_{\text{FM}}$  and  $\varphi_{\text{AFM}}$  one finds the same equation as predicted intuitively in (1.8) for the unidirectional bias field

$$H_{\text{d}} = \frac{\sigma_{\text{int}}}{m t_{\text{FM}}} \quad \text{if } k_{\text{AFM}} t_{\text{AFM}} \ll \sigma_{\text{int}} \quad (1.10)$$

The condition  $k_{\text{AFM}} t_{\text{AFM}} \ll \sigma_{\text{int}}$  means that the antiferromagnetic structure is assumed to be rigid for the Meiklejohn approach to be valid. The antiferromagnetic axis should not deviate from its easy axis during the magnetization reversal to provide a stable reference for the ferromagnet. In the other extreme case of an antiferromagnet with a small anisotropy the coupling to the ferromagnet will force the antiferromagnetic spins to simply follow the ferromagnetic spins. Any configuration that was originally achieved by field cooling is therefore destroyed by a single reversal process and no exchange bias will be observed. For the

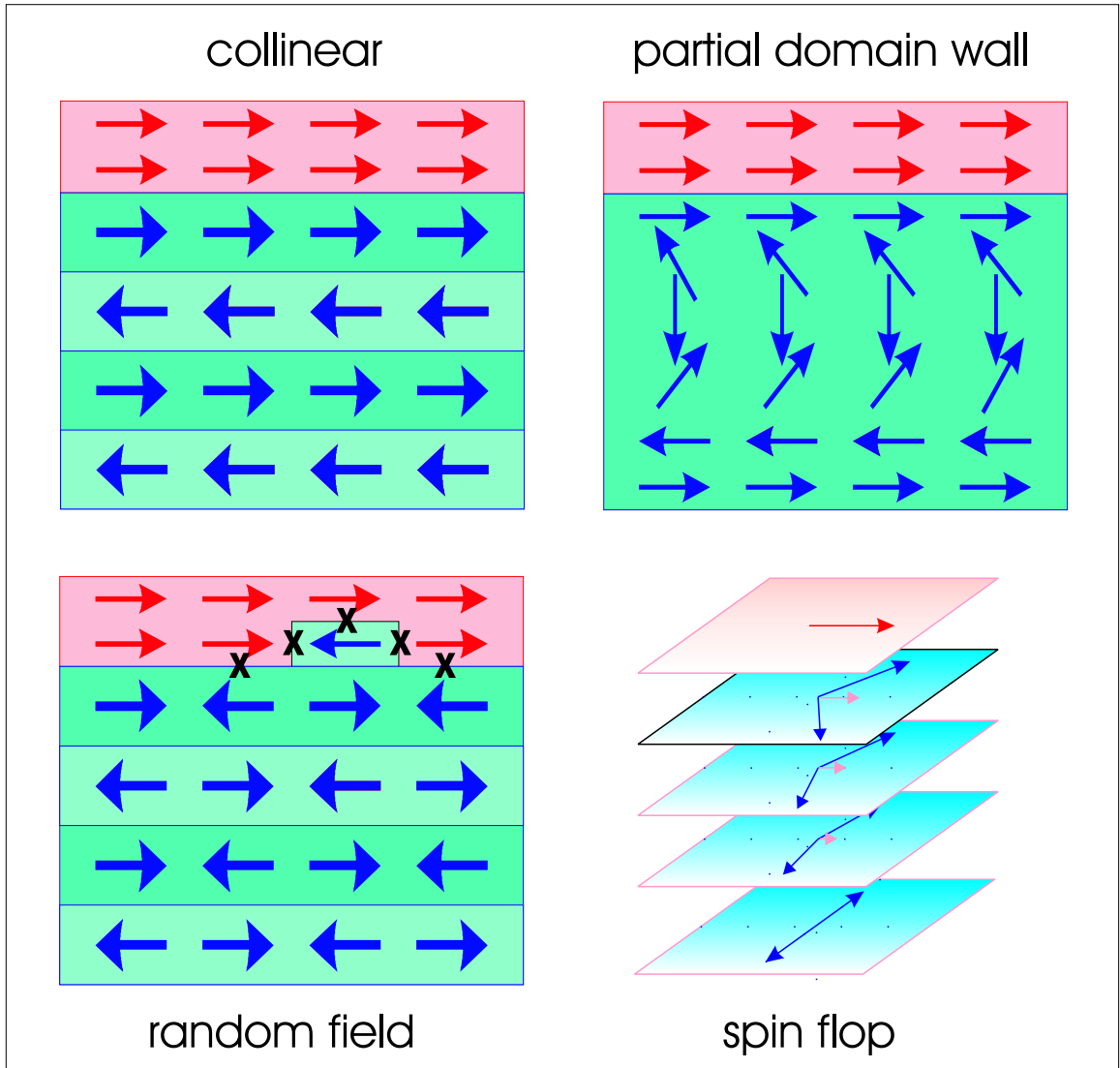


Figure 1.3: Exchange Bias Models

Different magnetic interface configurations considered in the exchange bias models based on single crystal antiferromagnets with ideal or non-ideal interfaces. The collinear model is described in section 1.4.1, the partial domain wall model in section 1.4.2 and section 1.4.3, the random interface model in section 1.4.4 and the spin-flop model in section 1.4.5.

intermediate region of similar interfacial energy and antiferromagnetic anisotropy energy the formation of a domain wall in the antiferromagnet has to be considered. Such models will be discussed in the following sections.

Based on the assumption of a rigid bulk antiferromagnet with a magnetically uncompensated surface as it is shown in the upper left panel of figure 1.3 the interfacial exchange energy  $\sigma$  can be calculated from Heisenberg-like exchange energy between the magnetic spins in the ferromagnet and the antiferromagnet  $J_{F/AF}$ . It results from the energy difference between parallel and antiparallel spin alignment at the interface.

$$\sigma_{\text{int}} = E_{\uparrow\uparrow} - E_{\uparrow\downarrow} = \frac{J_{F/AF}}{2a^2} \quad (1.11)$$

Assuming a typical Heisenberg-like spin-spin exchange energy of  $10^{-21}$  J and a lattice constant  $a$  of  $3.5 \cdot 10^{-10}$  m, values for  $\sigma$  of  $10 \text{mJ}\{\text{m}^2$  can be expected, but the maximal experimentally observed values are 2-3 orders of magnitude smaller. It will be the main result of this thesis to show that this approach is however reasonable if one takes into account that the unidirectional anisotropy originates only from a small portion of the interface and that this portion can be determined experimentally between 1%-5%. Exchange coupling across the remaining fraction of the interface only contributes to the total uniaxial anisotropy of the system.

Another experiment which demonstrates the strength of this approach has been performed by Jiang *et al.* [36]. The authors investigated so-called *artificial antiferromagnets*, consisting of Fe/Cr multilayers, as described in section 1.3. Depending on the Cr thickness the magnetization of adjacent Fe layers is either oriented antiparallel (forming an antiferromagnet) or parallel (forming a ferromagnet). For antiparallel coupling exactly the situation as depicted in the upper left of figure 1.3 is realized considering only the Fe layers. The investigated samples did indeed show exchange bias and the loop shift  $H_d$  followed equation 1.10.

The Meiklejohn-Bean model represents the most intuitive approach to exchange bias by relating the loop shift only to the net magnetization originating from the antiferromagnet located right at the interface. Apart from the size of the predicted bias field, its major deficiency is that it excludes the appearance of bias on compensated antiferromagnetic surfaces. To address this issue Binek *et al.*[10] recently presented a generalized Meiklejohn-Bean approach. The authors include the Zeeman energy of a possible residual moment in the antiferromagnet and its coupling to the ferromagnet as well as the antiferromagnetic structure. The origin of the residual moment can be attributed to rough compensated interfaces for example. This approach extends the Meiklejohn-Bean idea to uncompensated surfaces as well. The authors were able to qualitatively explain the dependence of the exchange bias field on the thickness of the antiferromagnet. This shows that a description in the framework of a coherent rotation models seems to be basically sound.

#### 1.4.2 Néel Approach - Weak AFM

L. Néel addressed the coupling between antiferromagnets and ferromagnets in general [57] without the assumption of a rigid antiferromagnet. He calculated the continuous magnetiza-

tion profile that evolves between a fully uncompensated antiferromagnet and a ferromagnet upon reversal of the ferromagnet. In his model  $\varphi(i)$  is the angle between the magnetization of the ferromagnet or the antiferromagnet and the common easy axis in the  $i$ th layer. The magnetization of each layer is assumed to be homogeneous, which leads to the following differential equation for  $\varphi$

$$J \frac{d^2 \varphi(i)}{di^2} - 4K \sin(\varphi(i)) = 0 \quad (1.12)$$

The model is still restricted to fully uncompensated interfaces and single crystals. For typical values for  $J$  and  $K$  Néel could derive the magnetization profile for rather thick ferromagnets and antiferromagnets (10-100nm). For these thicknesses stable configurations or magnetic domains are established in each layer separated by a domain wall parallel to the interface. The Néel model first predicted that a certain minimum antiferromagnetic thickness is necessary for stable exchange bias<sup>3</sup>. Furthermore it forms the basis for future models assuming the formation of planar walls parallel to the antiferromagnetic-ferromagnetic interface.

### 1.4.3 Partial Domain Wall Approach - Strong Coupling

In their approach Mauri, Siegmann, Bagus and Kay extended the idea of Néel by allowing the ferromagnet to be thin and therefore forming the parallel domain wall mostly in the thick antiferromagnet [50]. However they did not explicitly exclude the formation of a domain wall in the ferromagnet. Their description is restricted to perfectly uncompensated interfaces similar to Meiklejohn and Néel. In contrast to the work by Néel they allowed the formation of a so-called *partial domain wall*. They conclude that in the presence of such a domain wall the exchange energy of an ideal interface is decreased and were able to account for the discrepancy between the observed exchange energy and the one predicted by the Meiklejohn model.

The proposed domain wall configuration which evolves upon reversal of the magnetization into the hard direction is shown in the lower right panel of figure 1.3. Allowing the antiferromagnet to rotate and by considering strong interfacial coupling the system will avoid the frustrated configuration which gives rise to the anisotropy energy in the Meiklejohn approach by maintaining the parallel coupling between ferromagnetic and antiferromagnetic spins at the interface. However the formation of the domain wall consumes energy and the system will flip back into its original configuration if the external field is switched off. In this case the observed exchange bias field can be calculated to be

$$H_d = \frac{2\sqrt{A_{\text{AFM}} K_{\text{AFM}}}}{m_{\text{FM}} t_{\text{FM}}} \quad (1.13)$$

Instead of originating only from the interfacial layer the exchange energy is now distributed into the depth of the antiferromagnet over a domain wall of width  $\pi\sqrt{A_{\text{AFM}} K_{\text{AFM}}}$ , where  $A_{\text{AFM}} \sim J_{\text{AFM}}/a$  is the *exchange stiffness*. The effective interfacial energy is lowered by a

<sup>3</sup>Note, that the reason for the existence of a minimum AFM thickness for the presence of exchange bias might also be the thickness dependence of the antiferromagnetic ordering temperature

factor of 100 compared to the Meiklejohn approach. The so-called *Mauri Model* or *Partial Wall Model* is restricted to perfect uncompensated interfaces. Its basic idea, the fact that the antiferromagnet is in general not static, appears to be reasonable and is therefore considered in many recent approaches to describe exchange anisotropy. It is often adapted to polycrystalline systems as well (see section 1.4.6).

#### 1.4.4 Random Interface Model

Another approach to effectively lower the interfacial exchange energy was proposed by Malozemoff [48, 49]. In his model he also assumes a rigid single crystalline antiferromagnet but he now allows a rough surface. The example in the lower left panel of figure 1.3 shows a compensated interface<sup>4</sup>. The basic idea of the random field approach is that any imperfection due to steps or defects at the interface will cause perturbations in the magnetic order on both compensated as well as uncompensated surfaces. The defect as shown in the sketch causes an imbalance between positive and negative coupling across the interface and therefore a unidirectional anisotropy on an uncompensated interface.

In the random field model the quantity of interest,  $\sigma_{\text{int}}$ , is randomly distributed and its average over a small area will not vanish. For example the positions of frustrated interactions in the magnetic order due to a single defect on an uncompensated surface are marked with an (x) in figure 1.3. The system will try to minimize the increase in magneto static energy caused by the defect by rearranging the magnetization around the defect on a typical length of a domain wall width  $L = \pi\sqrt{AK}$ . Within this relatively small area ( $L^2$ ) formed by the defect, the interfacial energy, is now on average reduced by  $1/\sqrt{N}$  with  $\sqrt{N} = L/a$ .  $N$  is the number of sites within the area and  $a$  is the lattice constant. A detailed analysis yields the exchange energy at the interface with roughness parameter  $z$ , which is again reduced compared to the Meiklejohn model.

$$\sigma_{\text{int}} = \frac{4zJ_{\text{FM/AFM}}}{\pi aL} \quad (1.14)$$

#### 1.4.5 Spin-Flop Coupling

The approach of Koon [40] focusses on compensated antiferromagnet surfaces. He calculates the stable magnetic configuration at the interface and finds that ferromagnetic and antiferromagnetic axes are aligned perpendicular to avoid frustration, because of the definite sign of the exchange energy  $J_{\text{FM/AFM}}$ . The spins right at the interface will now cant a little bit out of their easy axes and give rise to a small magnetization parallel to the ferromagnetic magnetization during the field cooling. Based on the assumption that the antiferromagnet is frozen, as depicted in the upper right panel of figure 1.3 this coupling scheme gives rise to an unidirectional anisotropy into the direction of the cooling field.

A more recent micromagnetic investigation of the Koon model by Schulthess and Butler [77] showed that spin-flop coupling at ideal uncompensated surfaces only leads to increased

---

<sup>4</sup>Note that the model is not only restricted to uncompensated interfaces.

coercivity but not to exchange bias. In order to observe a unidirectional anisotropy as a result of spin-flop coupling the uncompensated moment in the antiferromagnet, indicated by the red arrows in figure 1.3, needs to be 'frozen'. Considering realistic coupling and anisotropy energies the situation in figure 1.3 cannot be achieved following the authors. The canted spins in the antiferromagnet rotate symmetric with respect to the direction of the ferromagnetic anisotropy axis and completely reversible and the resulting moment therefore only causes an increase in uniaxial anisotropy.

Another indication that the situation described by the Koon model might not be realized in real systems are the results on the NiO(001) surface described in this thesis, the very surface used by Koon for his model. In all cases parallel coupling between the ferromagnet and the antiferromagnet are found. Koon himself suggested in unpublished work<sup>5</sup>, that roughness at the interface will lead to a transition to collinear coupling.

#### 1.4.6 Polycrystalline Antiferromagnets

All previously introduced theoretical approaches deal with exchange bias on single crystalline samples. However, real device structures are based on polycrystalline antiferromagnets. In this case the description appears to be even more complicated based on the increased complexity of the systems. Figure 1.4 shows the transition from single crystal to polycrystalline systems. While the single crystal surface is homogeneous the magnetic properties of the polycrystalline system may change from grain to grain. Uncompensated moments may originate from domain walls, grain boundaries or defects. The anisotropy of each grain might be different due to local defects and therefore the thickness of partial domain walls might vary as well. This already points out that a complete description of exchange anisotropy would need to consider all the above approaches and combine them.

#### The Approach by Stiles and McMichael

Extensive theoretical work on polycrystalline samples has been presented by Stiles and McMichael [84, 85, 86], who investigated the temperature dependent behavior and the coercivity increase as well as the exchange bias effect in polycrystalline antiferromagnet/ferromagnet systems. Their model is based on the coupling between the magnetic moment of the ferromagnet and net interface magnetization of each antiferromagnetic grain as well as the formation of a partial domain wall in the antiferromagnet due to the antiferromagnetic bulk anisotropy. The coupling right at the interface is assumed to be parallel and Spin-Flop coupling is found not to be relevant for these polycrystalline samples. Assuming a certain anisotropy energy for the antiferromagnet and crystallite sizes the shape of the hysteresis loops as well as the dependence on the antiferromagnetic thickness and the sample temperature can be qualitatively reproduced.

---

<sup>5</sup>A reference to this can be found in [59] page 565, right column first paragraph.

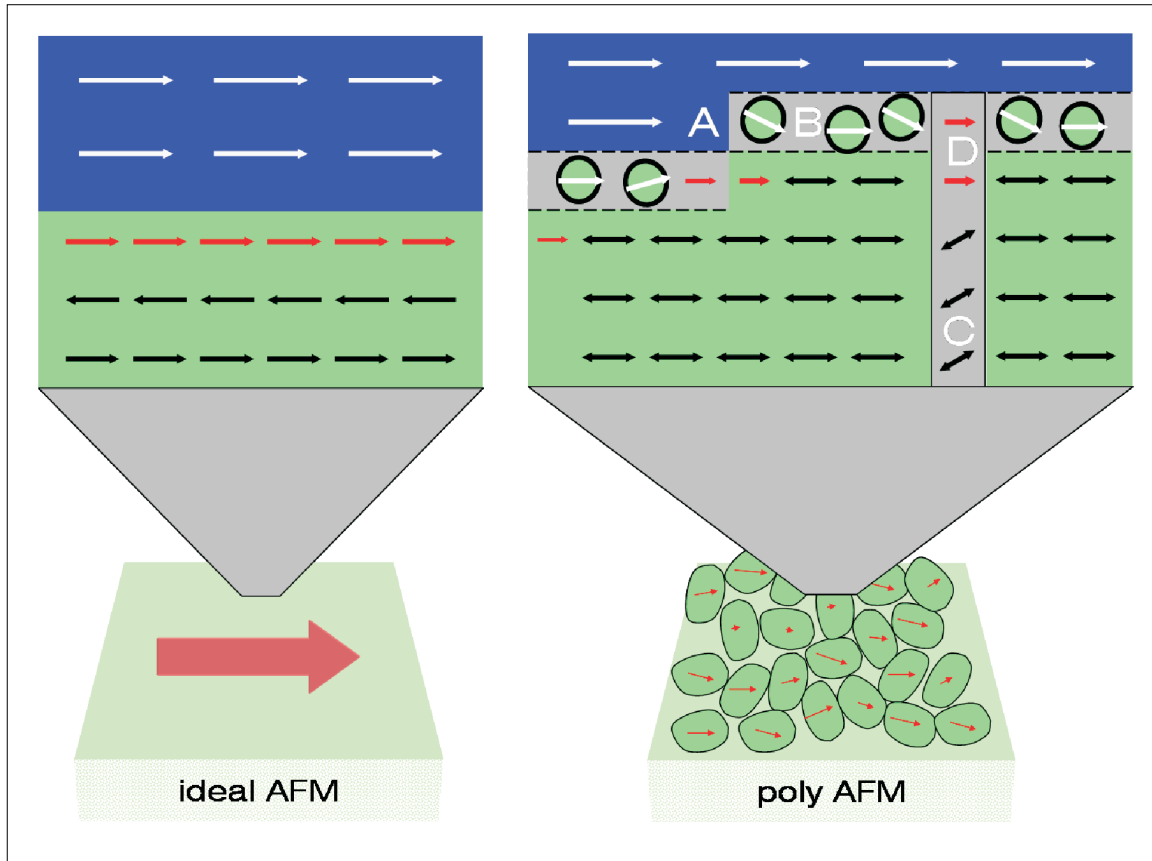


Figure 1.4: Ideal and Non-Ideal Interfaces

The magnetic structure at an ideal single crystalline uncompensated interface compared to the situation at a polycrystalline interface. In contrast to the ideal interface the polycrystalline structure may exhibit steps (A), gradual interfaces (B), grain boundaries (C) and domain walls (D) parallel as well as perpendicular to the interface.

### The Approach by Kim and Stamps

The model proposed by Kim and Stamps includes Spin-Flop coupling as well as partial domain wall formation between antiferromagnet and ferromagnet [37, 38, 83, 82]. It furthermore includes the effect of defects placed within the partial domain wall which lead to a lateral variation of the antiferromagnetic anisotropy energy. The interesting aspect of their approach is that they assumed that the coupling across the interface is a mix out of two coupling mechanisms. While Spin-Flop coupling leads to a coercivity increase the formation of a partial domain wall on some parts of the interface causes a relatively small bias field.

The experimental findings reported in section 6 of this thesis suggest parallel coupling across the entire interface rather than spin-flop coupling as assumed by Kim and Stamps.

Nevertheless the basic assumption that the observed uniaxial and unidirectional anisotropy in antiferromagnetic/ferromagnetic exchange coupled systems originates from different areas of the interface exhibiting a different antiferromagnetic anisotropy is corroborated experimentally.

## 1.5 Experimental Approaches

Today the calculation of the unidirectional anisotropy energy  $K_d$  from first principles for a particular microstructure of the interface has not yet been achieved. Even the origin of  $K_d$  is still not completely established. This is due to the lack of experimental methods to give detailed information about antiferromagnetic as well as ferromagnetic thin film surfaces and interfaces. Furthermore in all recent models the coupling between antiferromagnet and ferromagnet is mediated by a residual magnetization in the antiferromagnet at the interface to the ferromagnet. The origin and quantification of this residual moment has not yet been determined. It will be demonstrated in this thesis that polarization dependent x-ray absorption spectro-microscopy is capable of yielding exactly the desired information.

### 1.5.1 Uncompensated Moments

Takano *et al.* [93] first observed uncompensated spins in the bulk of bare CoO by measuring the remanent magnetization at 77K. Their experiments showed that the amount of uncompensated spins increased with decreasing grain size, leading to the conclusion that uncompensated moments in polycrystalline samples are mainly located at grain boundaries. After depositing a ferromagnet they could furthermore observe that the exchange bias field increases with decreasing grain size of the antiferromagnetic substrate. This work represents the *first clear experimental evidence* that exchange bias is connected to an uncompensated spin structure in the antiferromagnet.

In a more recent study Miltenyi [55] showed that due to imperfections in the chemical order uncompensated moments can be created in the bulk. A certain portion of these moments is supposed to extend to the interface and be responsible for the parallel coupling between antiferromagnet and ferromagnet. The first experimental evidence for interfacial antiferromagnetic uncompensated moments has been reported by Antel *et al.* on Co/FeMn using the same technique as used in the experiments described in this thesis. However FeMn is a disordered alloy and it remains unclear whether the detected moments are exclusively located at the interface or whether they are related to the structural bulk properties of this particular material. The unambiguous identification of uncompensated spins right at the interface between antiferromagnet and ferromagnet has been accomplished only recently [61]

### 1.5.2 Antiferromagnetic Surfaces - The Missing Experiment

To characterize the magnetic order at the antiferromagnetic - ferromagnet interface a technique needs to be capable of addressing three different issues listed below associated with

	Neutrons	STM	SHG	XAS
Surfaces, Thin Films	-	+	+	+
Buried Interfaces	-	-	+	+
Element Specific	-	0	-	+
Quantitative	+	0	0	+
FM and AFM	+	+	-	+
Imaging	-	+	+	+

Table 1.1: Capabilities of Different Methods Sensitive to Antiferromagnetic Order

Different methods which are in principle capable to characterize antiferromagnet order are listed and their abilities are compared. The methods evaluated here are neutron diffraction, scanning transmission microscope (STM), second harmonic generation (SHG) and x-ray absorption spectroscopy (XAS).

antiferromagnets. Table 1.1 summarizes the capabilities of different approaches and techniques.

1. The technique needs to be sensitive to  $\langle M^2 \rangle$ , because of the compensated nature of the antiferromagnetic spin structure.
2. The detected signal should not be influenced by the signal arising from the ferromagnetic layer. It is essential to be able to chose between ferromagnetic and antiferromagnetic sensitivity.
3. The technique has to exhibit an appropriate depth sensitivity so that it can be applied to thin film and multilayered structures of technological and scientific interest.

A classical approach to characterize antiferromagnets is the diffraction of polarized neutrons. By making use of the magnetic moment of the neutron and the fact that its de-Broglie wavelength is of the order of typical lattice constant, the diffraction pattern not only depends on the crystal symmetry but on the spin symmetry as well. Unfortunately this technique is typically only applicable to bulk samples. A way to avoid this problem is to use multilayered structures as done by Borchers *et al.* [11], Ijiri *et al.* [33] and van der Zaag *et al.* [103]. They investigated the particular exchange biased systems  $\text{Fe}_3\text{O}_4/\text{CoO}$  and  $\text{Fe}_3\text{O}_4/\text{NiO}$ .

Scanning tunnelling microscopy is extremely surface sensitive and using tips made out of a magnetic material the spin dependency of the tunnelling current can be used to image the spin order of only the surface layer [106]. In principle the atomic resolution can be used to image the antiferromagnetic spin order directly [30]. The lateral resolution of this technique is extremely high, however it offers no depth resolution and is not able to access the structure of a buried interface.

Another approach capable of addressing antiferromagnetic order is second harmonic generation [25][24]. This technique uses a focussed beam of a very intense pulsed laser source and analyzes the polarization dependence of the reflected beam at twice the frequency of the

incoming light. Due to the high intensity of the incoming beam, higher orders in the optical properties of the crystal become relevant and detectable. The polarization of the incoming beam is modulated by the conventional first order magneto optical kerr effect which is proportional to  $\langle M \rangle$ . The polarization of the frequency doubled intensity is then modulated by  $\langle M^2 \rangle$  and therefore sensitive to antiferromagnetic order. The frequency doubling only appears if the symmetry of the crystal is broken, for example right at the interface. In principle this technique represents a useful approach to characterize antiferromagnetic surfaces and interfaces with laboratory light sources. Nevertheless the quantitative analysis of the data is still difficult.

It becomes obvious why x-ray absorption spectroscopy was chosen as a technique for this project from the last column of table 1.1. XAS appears to be an ideal tool for addressing the magnetism of thin films, surfaces and buried interfaces at a distance of less than 10 nm from the surface. The technique requires tunable x-ray sources, where the energy of the x-rays can be chosen over a certain range (*synchrotron*). One particular advantage of x-ray absorption is that it can be used as a spectroscopic technique as well as to derive contrast in a microscope. Synchrotron sources and the theoretical background of XAS as well as microscopes based on this approach are discussed in the next section.



## Chapter 2

# Dichroism X-Ray Absorption Spectromicroscopy

*X-Ray Absorption Spectroscopy* (XAS) and *X-Ray Absorption Microscopy* are the techniques used throughout this work, in particular the analysis of the line shape of absorption resonances for the so-called *soft x-ray* region (250-1500eV). X-rays of such energy cause excitations of localized 2p core level electrons into empty 3d final states in transition metals like Mn, Fe, Co, Ni, Cu. The intensity of this transition, hence the line shape of the absorption resonance is strongly influenced by the chemical environment and magnetic symmetry of each species.

All experimental approaches and techniques described here in this chapter were performed using synchrotron radiation as the only available source of tuneable and polarized x-rays of such energy. An introduction into the matter of synchrotron radiation is given in the book by D. Attwood [5]. Here only a very brief description of the polarization properties of synchrotron radiation is given at the beginning of this chapter.

The x-ray absorption cross section is measured by either detecting the intensity of the transmitted x-rays using the *Lambert-Beer* law or by collecting the electron yield emitted from the sample. The second approach is referred to as *Total Electron Yield* technique. (TEY).

Microscopy experiments are performed using a Photoemission Electron Microscope. A PEEM magnifies and images the lateral distribution of the electron yield across the sample surface. Review papers focussing on magnetic imaging methods are presented for example by J. Stöhr *et al.* [90], F.U. Hillebrecht [31] and in articles by W. Kuch *et al.* and A. Scholl *et al.* in 'Magnetic nanostructures' edited by H. Hopster [44, 75]. A general overview about PEEM has been given by E. Bauer [7].

The last section of this chapter finally discusses the detailed dependence of the XAS line shape on different chemical and magnetic environments. A detailed overview about soft x-ray absorption spectroscopy can be found in the book of J. Stöhr [87]. More recent reviews have been given by F.M.F. de Groot [17] (chemical XAS) and J. Stöhr [90, 89] (dichroism XAS).

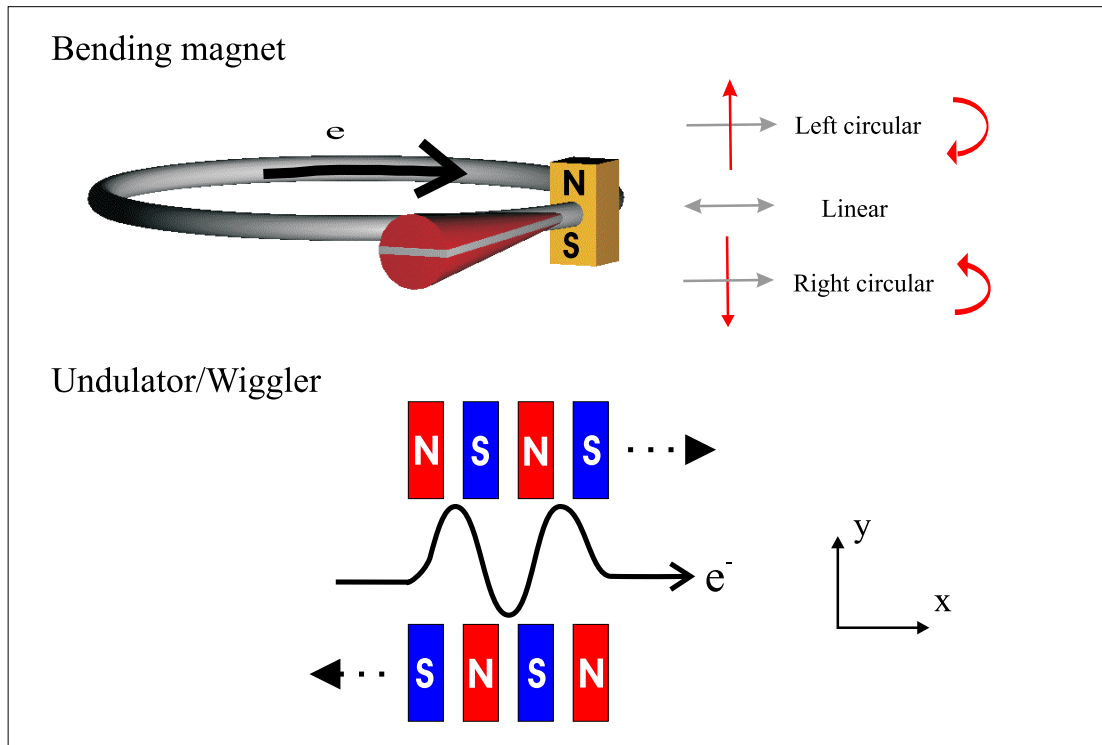


Figure 2.1: Synchrotron Radiation and Polarization

Top: A bending magnet (yellow) generates linear polarized x-rays in the ring plane (grey). Out of the ring plane (red) a vertical polarization exists exhibiting a phase difference of  $\pm\frac{\pi}{2}$  relative to the horizontal component.

Bottom: An undulator or wiggler consists of several dipole magnets with opposite orientation positioned along the path of the electron beam (x-direction). The distance between the magnets in an undulator is chosen such the single intensities add up coherently in contrast to a wiggler where the intensities add up linearly. If the upper and lower poles can change their relative position the polarization (y-direction) or the energy (x-direction) of the emitted x-rays can be changed (*elliptical polarizing undulator*).

## 2.1 Polarized X-Rays

### 2.1.1 Linear and Circular Polarized X-rays

A synchrotron or electron storage ring is a source of polarized x-rays. During operation relativistic electrons are kept on a closed orbit using deflector dipole magnets and focussing quadrupole and sextupole magnets and the 'ring' is in reality a symmetric polygon. A dipole magnet is the source of a continuous spectrum ranging from the infrared into the hard x-rays region. The maximum photon energy originating from a bending magnet is

$E_{max} = 665eVE^2[GeV]B[T]$  (see for example [72, 56]), where  $E$  is the kinetic energy of the electrons in the storage ring in GeV and  $B$  the field strength in the bending magnet in Tesla. A particular x-ray energy is chosen by using a grating monochromator. The x-rays are finally focussed on the sample position by mirrors suitable for the desired x-ray region.

In general, x-rays can be extracted at two positions within the polygon. At every corner dipole magnet (bending magnet) the electrons are accelerated transverse and longitudinally within a certain interaction volume and emit radiation like a Hertz dipole. Due to their relativistic energy the intensity is only emitted in a very narrow cone with an opening angle  $\alpha = 1/2\gamma$  (Lorentz transformation). This is shown in the left panel of figure 2.1. Parallel to the orbit plane only transverse **acceleration** perpendicular to the original propagation direction is observed and the emitted radiation is therefore polarized horizontally. At the same time the electrons experience a longitudinal **deceleration**, parallel to their original propagation direction. The resulting radiation is transformed by the Lorentz transformation into a  $\pm 90^\circ$  phase shifted vertical polarized electromagnetic wave. The sign depends on the angle between transverse and longitudinal acceleration as shown in figure 2.1.

A periodic magnetic structure where the electrons are subsequently deflected in opposite directions but altogether preserve their original propagation direction is implemented in the straight sections of the synchrotron. Such a structure is sketched in the lower panel of figure 2.1. In the simplest case the intensities emitted by each of the  $N$  magnet pairs are added up linearly (*wiggler*) and the total output intensity is increased by a factor of  $N$  compared to a simple bending magnet. If now the distance between the poles in x-direction is chosen adequately wave fronts with a particular frequency emitted from adjacent magnet pairs will add up coherently (*undulator*). Positive interference between the wavefront is observed for a particular frequency  $f$  and multiples of  $f$ , where  $f$  is inverse proportional to the time  $T$  the electrons travel between two magnet pairs. For this reason the frequency or energy of the x-rays emitted from an undulator depend on the distance between the magnets in x and y direction and the magnetic field strength. Since typically permanent magnets with a fixed distance in x-direction are in an undulator, the x-ray energy is chosen by changing the so-called *gap* or distance in y-direction between the poles. If the field between the poles is decreased (by increasing the gap) the time of flight between adjacent dipole magnets is decreased and thus the frequency of the coherently generated x-rays is increased. A larger distance between the magnet pole leads a higher output energy!

The x-rays emitted from a conventional undulator are horizontally polarized. However, if in addition to the distance in y-direction also the relative alignment of the magnet poles along the x-axis, as indicated by the dotted arrows in figure 2.1 is changed, additional polarization components perpendicular to the original horizontal polarization can be produced. Such a structure is referred to as elliptical polarizing undulator (EPU). Linear polarized light of every orientation as well as left and right circular or elliptical polarized with variable degree of circular polarization are obtained from an EPU.

### 2.1.2 Mixed Polarization

For the experiments presented in this thesis variable x-ray polarization was essential, in particular the ability to change the angle between the incident polarization vector and a distinct crystal axis. The geometry that applies to all experiments is shown in Figure 2.2. For experiments involving the commercial STAIB PEEM the angle of incidence ( $\theta$ ) was  $15^\circ$  for the ALS PEEM2 this angle was fixed at  $30^\circ$ . The horizontal polarization component  $E_{\parallel}$  is always parallel to the sample surface. The sample can be rotated around its surface normal such that  $E_{\parallel}$  component includes any angle  $\phi$  with a particular crystallographic in-plane axis, for example [100]. The vertical polarization component  $E_{\perp}$  and the surfaces normal include a fixed angle, that is the angle of incidence  $\theta$ . Note, that the vertical polarization component also shows a small projection onto the surface plane.

Some of the experiments could be performed using an EPU which allows to choose the ratio between  $E_{\perp}$  and  $E_{\parallel}$  continuously between 0 and 1, but most of the experiments used a bending magnet x-ray source. Nevertheless it was desirable to use vertical polarized x-rays in this setup, too. This is achieved for some particular experiments which are not sensitive to the handedness or phase difference between different polarization components by regarding circular polarized x-rays as superposition of pure horizontal and vertical polarized x-rays without phase difference. The detected signals can then as well be regarded as a superposition of the signals which are detected for pure horizontal and vertical polarization. In the following circular polarization will be referred to as *mixed polarized* if used in this

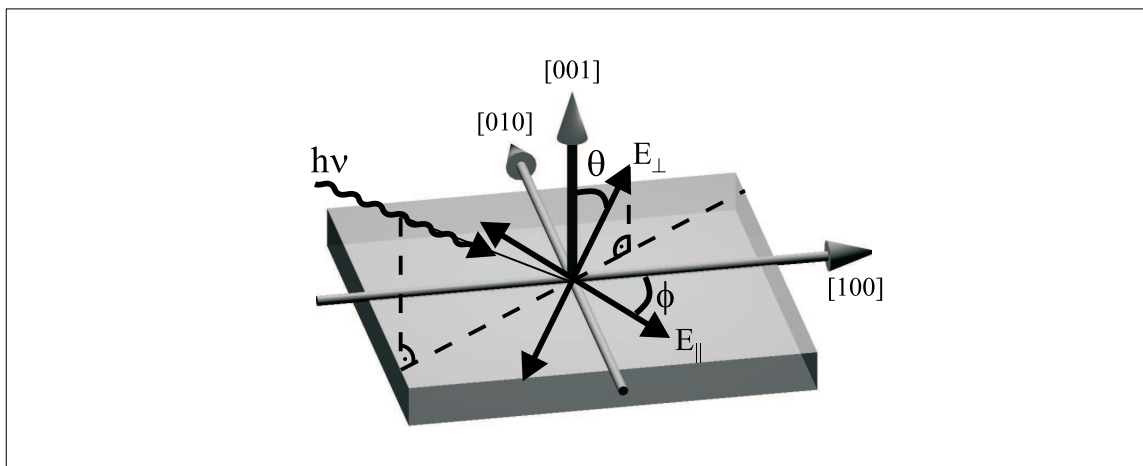


Figure 2.2: Experimental Geometry

X-rays are incident onto the sample under an angle  $\theta$ . The incident polarization can be split in two main polarization components  $E_{\parallel}$  and  $E_{\perp}$ . The angle  $\theta$  determines the angle between  $E_{\perp}$  and the surface normal. The sample can further be rotated around its normal by an angle  $\phi$  which is determined by the angle between  $E_{\parallel}$  and a distinct in-plane sample direction.

context.

To determine the ratio between  $E_{\perp}$  and  $E_{\parallel}$  the relation between degree of circular polarization and the horizontal and vertical components of the electric field is given in the following.

$$P_c = \left( \frac{2E_{\parallel}E_{\perp}}{E_{\perp}^2 + E_{\parallel}^2} \right)^2 \quad (2.1)$$

For a typical value for the circular polarization of  $P_c = 0.75 \pm 0.05$  the ratio between vertical and horizontal polarization is  $\epsilon = E_{\perp}/E_{\parallel} = (0.58 \pm 0.03)$ . The detected signal for mixed polarization  $I_{\text{mix}}$  is a superposition of the signals  $I_{\perp}$  and  $I_{\parallel}$  detected for pure vertical or horizontal polarization, thus the signal arising only from the vertical component can be extracted in the following if  $\epsilon$  is known.

$$I_{\text{mix}} = \frac{I_{\parallel} + \epsilon I_{\perp}}{(1 + \epsilon)} \rightarrow I_{\perp} = \frac{(1 + \epsilon)I_{\text{mix}} - I_{\parallel}}{\epsilon} \quad (2.2)$$

Note, that the signal detected with pure horizontal polarization  $E_{\parallel}$  has to be known for this purpose. But this can be obtained at a bending magnet source by choosing only the x-rays emitted parallel to the ring plane as shown in figure 2.1.

## 2.2 Experimental Techniques

The spectral and polarization dependence of the x-ray absorption cross section has been detected using the electron yield method. The detection method was used in two different ways. First by spatially averaging over the illuminated sample area yielding spectroscopic information (XAS). The other detection method included the use of a Photoemission electron microscope (PEEM) which magnifies and images the lateral distribution of the electron yield can be magnified and imaged. The lateral variation of elements and their chemistry as well as their ferromagnetic and antiferromagnetic order can be resolved using PEEM. For an overview about microscopy and spectroscopy using synchrotron radiation and electron yield see [90, 41, 31]

### 2.2.1 Total Electron Yield Spectroscopy

#### Concept

The absorption of an incident x-ray by a core level electron and the recombination processes which cause the electron yield emitted from the sample is depicted in figure 2.3. The incoming photon produces a photoelectron and the resulting core recombines by emitting an Auger electron. The photo electron and the Auger electron may now either be emitted into the vacuum or due to their limited mean free path lose their energy by inelastic scattering. In this case a larger number of low energy secondary electrons per initial photo electron is generated. Due to their larger mean free path the secondary electrons will eventually be emitted into the vacuum. If the sample is grounded through a current amplifier the electron

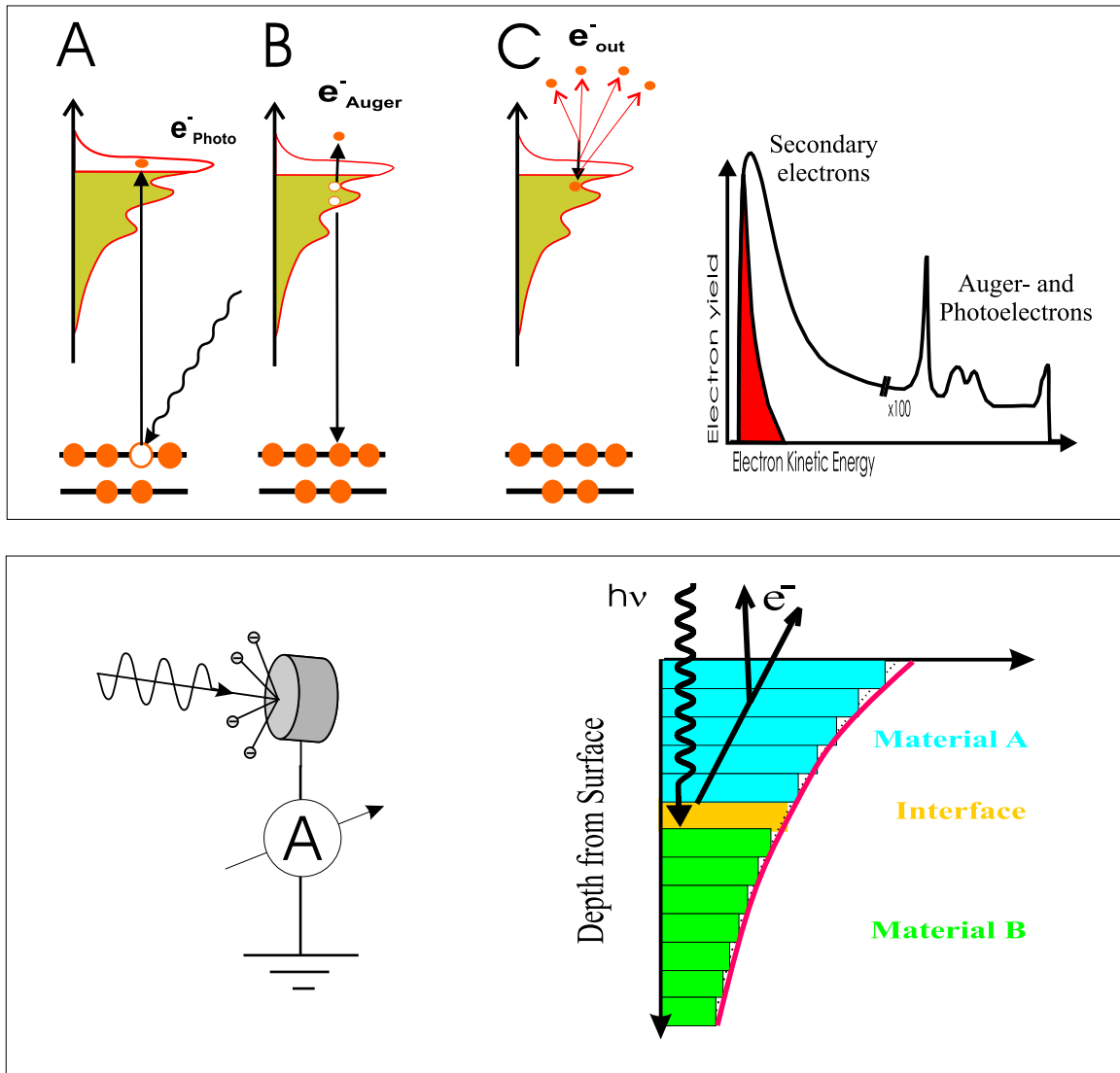


Figure 2.3: Resonant X-ray Absorption Process and Electron Yield

Top: Soft x-rays are absorbed by exciting a core level electron into an empty final state (A). Recombination of the core hole leads to the emission of an Auger electron (B). The Auger- and the photoelectron are either emitted into the vacuum or lose their energy due to inelastic scattering producing numerous low energy secondary electrons (C). The energy spectrum of all electrons escaping the sample is shown on the right, consisting mostly (90%) of electrons with a kinetic energy of less than 5eV.

Bottom left: The current between the sample and ground potential is proportional to the electron yield generated by x-ray absorption process.

Bottom right: The contribution of deeper layers to the TEY signal decays exponentially with distance  $z$  to the surface.

current which is necessary to compensate for the emitted charge can finally be measured (see bottom left of figure 2.3. Typical sample currents obtained using synchrotron radiation are between 0.1-10nA.

The total electron yield is proportional to the absorption coefficient  $\mu(E)$ . At normal x-ray incidence the total electron yield  $dN_e$  from a layer of thickness  $dz$  at depth  $z$  is related to the x-ray absorption  $\mu(E)$  by [56]:

$$dN_e \sim \mu(E) \exp(-z\mu(E)) \exp(-z/\lambda) dz \quad (2.3)$$

The second exponential term denotes the probability of an electron generated at a distance  $z$  from the surface to leave the sample. The electron mean free path  $\lambda$  is a combination of the mean free path of the initial photo and auger electrons (very short  $< 1\text{nm}$ ) as well as the secondary low energy electrons (long  $> 10\text{nm}$ ). Spectroscopic information is only be obtained from layers that contribute to the electron yield. Experimental values for the effective  $\lambda$  vary between 1.5nm to 2.5nm.

The first exponential function describes the decay of the x-ray intensity while penetrating the material. Because the decay length of the x-rays is in general much larger this term is usually neglected and the x-ray intensity is assumed to be constant within the probing depth of the TEY method<sup>1</sup>. Integrating equation 2.3 yields the direct proportionality between TEY and  $\mu(E)$ .

### 2.2.2 Depth Sensitivity

The depth profile of the total electron yield method is shown in figure 2.3. The sketch shows the exponential decay of the contribution of each atomic layer in a stack of two materials to the total electron yield. It is assumed that the interfacial layer consists of both materials and that  $\lambda$  is constant over the entire volume. Deeper layers contribute with a smaller electron yield to the total yield than surface layers. A rough estimate yields that 82% of the electron yield originates from the first 2nm. For this reason the TEY technique is characterized as a surface sensitive technique. If material B is buried deeper than about 10nm from the surface it is usually not detected in a TEY experiment.

The electron yield arising from the buried layer B is suppressed by layer A, but the relative contribution of the top layer of material B to the total signal arising from material B is independent of the thickness of top layer, material A. Again, assuming a typical  $\lambda$  of 2nm and an atomic layer thickness of 0.2nm the contribution of the top layer of material B to the electron yield of material B is always between 8% and 10%. This means that if the chemical properties of the top layer of material B are different of the other bulk layers its contribution can be identified.

In conclusion the total electron yield detection exhibits excellent surface and interface specificity. It is well suited to investigate thin film and multilayer systems with a total thickness of less than 10nm. Each element in such a structure will contribute significantly to the electron yield.

---

<sup>1</sup>This is appropriate even right at the absorption resonance where the decay length might be as short as 10nm.

### 2.2.3 Photoemission Electron Microscope

#### Overview

The idea of cathode lens microscopy had been developed in the first half of the last century. Driven by the increased use of synchrotron radiation in the late 1980s and the success of electron yield based absorption spectroscopy a UHV compatible synchrotron based Photoemission Electron Microscopes (PEEM) had been proposed by Tonner and Harp [98] and a few years later by Engel *et al.* [22]. A recent review about the success of modern cathode lens microscopy has been given by E. Bauer [7].

#### Concept

The concept of PEEM is explained in the following. Figure 2.4 shows a sketch of a two lens PEEM. The radiation of monochromatic x-rays onto the sample surface leads to emission of electrons. If the absorption coefficient  $\mu$  varies laterally so will the electron yield. The excited electrons are accelerated towards the microscope. An electrostatic objective lens<sup>2</sup> and a projective lens will magnify and image the electron yield on a two dimensional electron detector, for example a phosphor screen or a micro channel plate. The visible light image emitted from the detector can then be recorded using a CCD camera. It is a common feature of all cathode lens microscopes that the sample itself, as the cathode, is part of the optical system.

The sketched microscope consists of two triode electrostatic lenses. The outer electrodes are on the same potential as the microscope housing, while the inner electrode is on high negative voltage. The equipotential lines produced by such a arrangement resemble the shape of thick concave optical lens. They are shown within the projection lens.

#### Abberations and Lateral Resolution

Deviations from the cylindrical symmetry (stigmatism) of each lens can be corrected for by a electrostatic sextupole stigmator [4]. If the optical elements are not completely aligned on axis electrostatic deflectors are used [4]. But there are more sources of abberations to consider in an electron microscope. The kinetic energy  $E$  of the excited electrons are spread over a very wide range from 0eV up to the x-ray energy (500-1000eV) (see for example figure 2.3) and electrons with an angular momentum  $p$  parallel as well as perpendicular to the microscope axis are collected by the accelerating field. Since the focal point for each electron  $(E, p)$  is different this leads to *chromatic abberations* and *spherical abberations*. In an optical microscope chromatic abberations can be corrected for by convex lenses, but convex lens cannot be formed with cylinder symmetrical electrostatic lenses [73] and for this reason it is complicated to compensate for these kind of abberations in an electron microscope.

The easiest way to 'correct' for these abberations in a PEEM is to place an aperture in the back focal plane (the one defined for 0eV electrons and normal incidence) and exclude all

---

<sup>2</sup>Sometimes a magnetic objective lens with the advantage of smaller abberations is used. This is not feasible to study magnetic systems because of its residual fields at the sample position

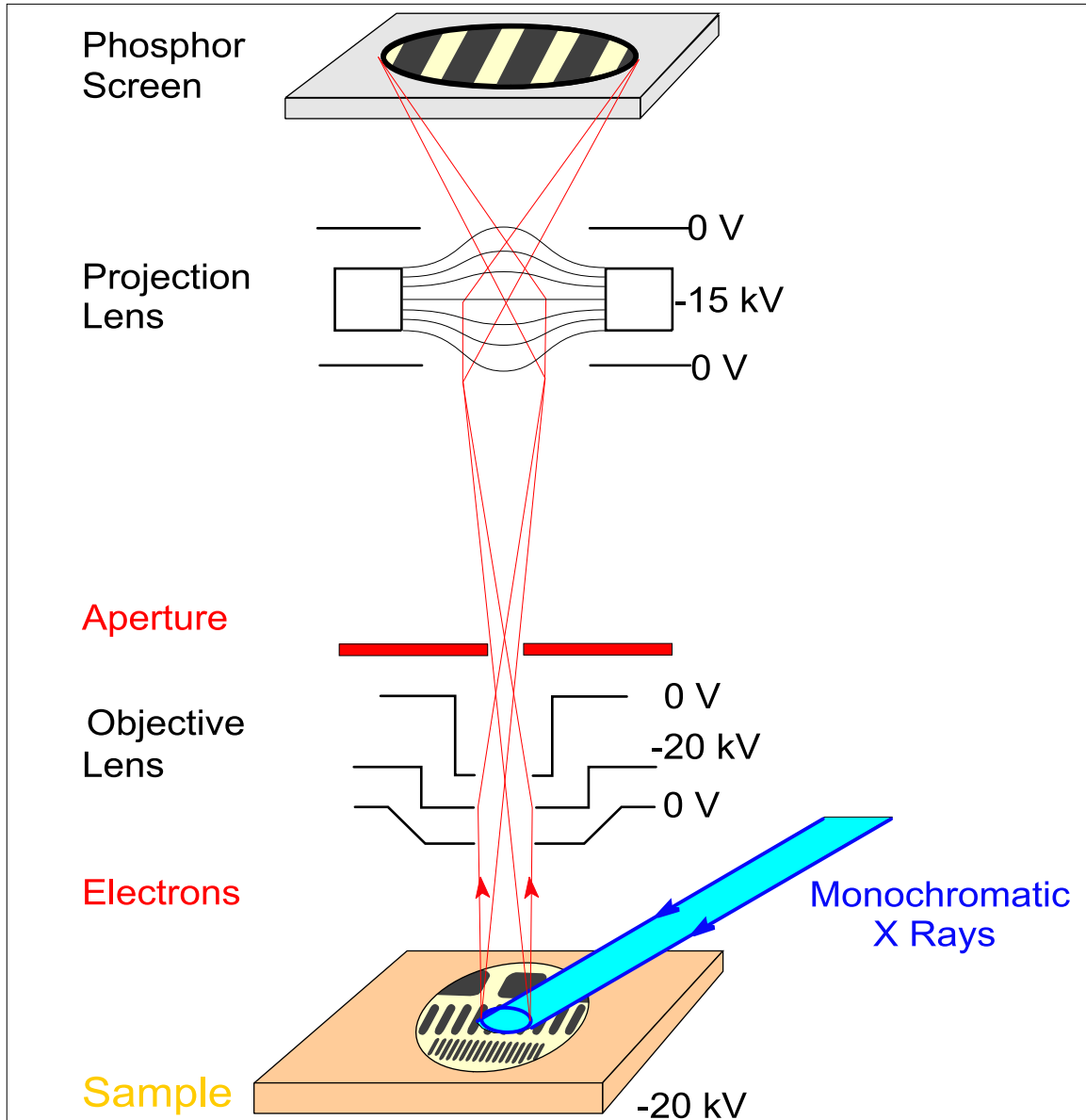


Figure 2.4: Electron Path within X-PEEM

Irradiation of a surface with (monochromatic) x-rays leads to the emission of secondary electrons. The spatial distribution of the electron yield is magnified onto a screen by electrostatic lenses. A voltage of 10 kV per millimeter is applied to the sample (cathode) to accelerate the electrons toward the microscope column. Energy and angular selection of the electrons passing through the microscope column is achieved by an aperture in the back focal plane of the objective lens.

electron from the optical path that do not have the right energy or angular momentum. A disadvantage of this method is that it limits the transmission of the microscope to about 1% in order to reach the desired 20-50nm lateral resolution. A more recent approach<sup>3</sup> [74, 65] includes the use of electrostatic mirrors that do have negative aberrations [70] and can be configured such that they cancel out the positive aberrations caused by the cathode and the objective lens. Such a microscope will allow to achieve a lateral resolution of 20-50nm without limiting the transmission and an ultimate resolution of 1-2nm.

### Microscopes

Two different microscopes were used for the experiments. One microscope was the commercial STAIB-PEEM [34] microscope. The other microscope used was the PEEM2 instrument [4] built at the Advanced Light Source (ALS) in Berkeley (CA), USA. Both microscopes are equipped with a stigmator unit and an aperture and both microscopes use an electrostatic objective lens and two projective lenses. The typical spatial resolution obtained with the STAIB PEEM using synchrotron radiation was 120-150nm and about 50-70nm was obtained using PEEM2. The resolution limit for both microscopes is in principle a factor 2 to 3 better but depends strongly on the flatness of the sample surface as well as the intensity of the incoming x-rays and thus the intensity of the image. To adjust the lens voltages such that the best resolution is achieved a large magnification has to be chosen. But with increasing magnification the total image intensity detected by the camera decreases significantly and the exposure time needed for every image time becomes too long to practically focus the image. For this reason the theoretical resolution limit is often not achieved for practical reasons.

The main difference between the two setups is that PEEM2 is located permanently at beamline 7.3.1.1 at the ALS, while the STAIB PEEM can be moved to different locations. For this reason it was possible to use this microscope in combination with an EPU beamline and full polarization control. The advantage of the PEEM2 is the mechanical stability and the close connection to a particular beamline which allows to optimize the optics as well as the acquisition software very well.

Using the PEEM2 setup XAS spectra from small areas (less than  $1\mu m^2$ ) on the sample (*XAS Spectromicroscopy*) can easily be obtained by synchronizing beamline and microscope control software. While the x-ray energy is moved step by step through an absorption resonance a PEEM image is acquired at each energy. The result is a so-called *image stack*. The dependence of the image intensity or electron yield of a particular spot yields a local x-ray absorption spectra. The XAS spectra are extracted after the actual image acquisition with the help of image processing software. The spectra can then be processed (background subtraction and normalization).

Using the STAIB PEEM only one image stack was acquired "manually". For this purpose the monochromator was moved 'manually' after each image was acquired. The actual electron current in the storage ring and the incoming intensity measured by the electron yield

---

<sup>3</sup>These are the SMART project at BESSY2 (spectromicroscopy for all relevant techniques) and the PEEM3 microscope planned at the ALS

from a gold mesh located upstream was also noted by hand to appropriately normalize the spectra at the end. Unfortunately this method is rather time consuming. Nevertheless the experimental results obtained by this method at BESSY2 could later be reproduced using the more sophisticated approach available at the ALS.

## 2.3 X-Ray Absorption Line Shape

The following overview is taken from textbooks and articles about electrodynamics by J. D. Jackson [35], quantum mechanics by A. Messiah [54], the theory of angular momentum and its coupling rules by D. M. Brink and G. R. Satchler [12] and x-ray absorption spectroscopy by J. Stöhr [87] and F.M.F. de Groot [17].

### 2.3.1 Overview

It is evident from the Maxwell equations that the interaction of light with matter yields important information about the properties and the symmetries of the studied system. The electric field in vacuum  $\vec{E}$  is connected with the dielectric polarization in matter  $\vec{D}$  via the dielectric function  $\epsilon$  [35].

$$\vec{D} = \epsilon_0 \epsilon \vec{E} \quad \text{with} \quad \epsilon = \epsilon_r + i\epsilon_i \quad (2.4)$$

The dielectric function represents the optical properties of the material or the response of the system to an external electromagnetic field. For the energy range which is discussed here, the optical properties are defined by the electronic structure of the material. The real part of  $\epsilon$  describes how strong an external wave can polarize the matter. The imaginary part describes the *dissipation* of energy and for this reason is closely related to the absorption cross section. Both parts are function of the energy and the polarization of the incoming wave, hence  $\epsilon = \epsilon(\omega)$  is a tensor quantity reflecting the symmetry and energy dependence of the electronic structure of the investigated system.

For a detailed calculation of  $\epsilon(\omega)$  a quantum mechanical approach employing time dependent perturbation theory is used, leading to an expression for the absorption cross section known as *Fermis Golden Rule*. The expression describes the probability for an electromagnetic dipole transition  $|e\mathbf{z}|$  from an initial state of the electronic structure  $|i\rangle$  to a final state  $|f\rangle$  to occur.

$$|\langle f | e\mathbf{z} | i \rangle|^2 \delta(E_f - E_i - \hbar\omega) \quad (2.5)$$

For a dipole transition to occur the energy of the incoming photon has to match the energy difference between two possible electronic states (delta function = energy conservation) of the system. Furthermore the intensity of a particular optical transition between two electronic states of the system can be calculated from its Hamiltonian. They can be precisely calculated if the wave functions of initial and final states are known, but an already very general conclusion about possible transitions (non vanishing dipole matrix element) can be drawn from the symmetry of the dipole operator  $e\mathbf{z}$  and its exchange properties (conservation of angular momentum) with the spin operator  $\mathbf{S}$  the angular momentum  $\mathbf{L}$  and the total angular

momentum  $\mathbf{J}$  derived by spin-orbit coupling. For an unpolarized incident electromagnetic wave one finds

$$\Delta\mathbf{S} = 0 \quad (2.6)$$

$$\Delta\mathbf{L} = \pm 1 \quad (2.7)$$

$$\Delta\mathbf{J} = 0, \pm 1 \quad (2.8)$$

Hence, only optical dipole transitions which do not change the spin of the system and increase or decrease the angular momentum by 1 are observed. The necessity of energy conservation and the optical transition rules which in other words represent the conservation of angular momentum limit the number of possible transitions. They represent the origin of the elemental and chemical sensitivity and enable the unambiguous identification of elements and their chemical state in an unknown sample.

So far, unpolarized x-rays were considered, but the conservation of angular momentum leads to another set of transition rules regarding the orientation of the total angular momentum  $m_J$  for polarized x-rays. This is of particular importance here since in magnetic systems electronic states with different orientation of the total angular momentum are not evenly populated and for this reason the following rules give rise to a *dichroism effect* in magnetic systems, that means the optical properties or  $\epsilon$  depends on the polarization of the incoming x-rays

$$\Delta m_J = \begin{cases} 0 & \vec{E} \parallel \vec{M} \\ +1 & \vec{\sigma} \parallel \vec{M} \\ -1 & \vec{\sigma} \perp \vec{M} \end{cases} \quad (2.9)$$

### 2.3.2 Energy Dependence - Chemical Specificity

#### XAS, Spin-orbit Coupling and Atomic States

The lower panel in figure 2.5 shows soft x-ray absorption spectra of Fe, Co, Ni in the metallic as well as in a particular oxidation state. The absorption peaks or so called  $2p - 3d$  white lines of each element appear at characteristic photon energies and consists of 2 pronounced *resonances*. While the bare metals exhibit a simple line shape, the oxides reveal a more rich structure. The origin of the energy position (elemental sensitivity), the peak height (concentration sensitivity) and the fine structure (chemical sensitivity) of an x-ray absorption resonance is explained in the following using the transition of a 2p electron into two different final states as shown in the top panel of figure 2.5.

The first example, on the left side in the upper panel depicts the  $2p^6 3p^9 \rightarrow 2p^5 3p^{10}$  transition of an  $2p$  electron into a 3d shell filled with 9 electrons (1 hole, as for example in Ni). The second example assumes a 3d final state with 8 electrons (2 holes, as for example in Co or NiO) or  $2p^6 3p^8 \rightarrow 2p^5 3p^9$ . The possible ground and excited states are obtained by coupling spin and orbital momentum. The lowest energy states follow Hund's rules. All possible states for the two configurations are illustrated in the figure.

For the single hole configuration only a  ${}^2D \rightarrow {}^2P$  is observed ( $\Delta S = 0$   $\Delta L = +1$ ). The spin orbit coupling of the 2p-core hole splits the final state into  ${}^2P_{3/2}$  and  ${}^2P_{1/2}$ . Both

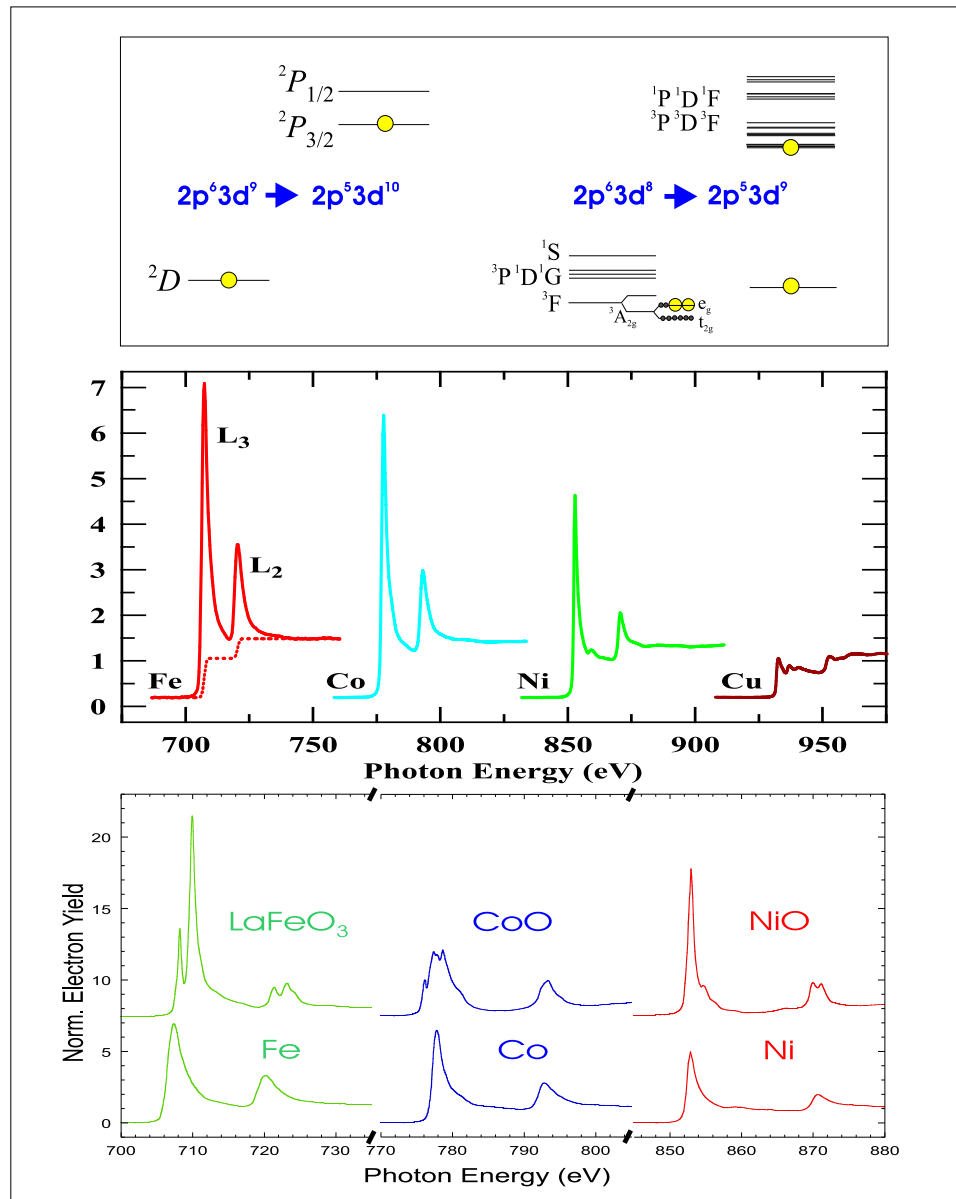


Figure 2.5: Chemical and Elemental Sensitivity of X-ray Absorption

Top: Ground state and excited state for a  $2p^6 3d^9$  and  $2p^6 3d^8$  configuration. For a  $d^9$  configuration the  ${}^2P$  final state is only split by spin orbit interaction. In case of the  $d^8$  configuration also the  ${}^3F$  ground state is split by a cubic crystal field in  $e_g$  and  $t_{2g}$  symmetry.

Center: L-edge XAS of metallic Fe, Co, Ni and Cu. Each resonance shows a  $L_3$  and a  $L_2$  resonance. The contribution of the  $2p - 3s$  resonance is indicated in the Fe spectra.

Bottom: L-edge XAS of Fe, Co, Ni and related oxides [69]. Crystal field and charge transfer multiplet splitting cause the fine structure in the oxide XAS.

Element	$E_{2p_{3/2}}$	$E_{2p_{1/2}}$	$E_{\bar{l}\bar{s}}$
Mn	638.7eV	649.9eV	11.2eV
Fe	706.8eV	719.9eV	13.1eV
Co	778.1eV	793.2eV	15.1eV
Ni	852.7eV	870.0eV	17.3eV
Cu	932.7eV	952.3eV	19.6eV

Table 2.1: Binding Energies and Spin-Orbit Coupling of 3d-Metals

final states although they exhibit a different total angular momentum  $J$  can be accessed by an optical transition from the ground state with respect to equation (2.6). This is because the  $^2D$  ground state is split as well into  $^2D_{5/2}$  and  $^2D_{3/2}$ . The spin orbit splitting in the ground state is typically not directly observed in an x-ray absorption experiment because it is much smaller than the experimental energy resolution (0.05-0.1eV) and the  $^2D_{5/2}$  and  $^2D_{3/2}$  states appear at basically the same energy<sup>4</sup>. The two resulting transitions are referred to as  $L_3$  (lower energy) and  $L_2$  (higher energy) absorption line, the entire spectrum is often called *L-edge* absorption spectra.

The same basic line shape will be observed for the excitation of the  $d^8$  configuration, although the situation is more complicated, because the possible states are now obtained by coupling spin and orbital moment of two electrons. The symmetry of the ground state is  $^3F_4$ . The symmetry of the final state which can be excited by the optical transition is  $^3D$ , Note that this is not the ground state of the  $2p^53p^9$  configuration. The final state is again spin-orbit split into two distinguishable states formed by a  $^3D_2$  and  $^3D_1$ ,  $^3D_3$  configuration (not shown in the figure). All these states can be accessed from the ground state due to the small spin-orbit coupling in the ground state.

### White Line Intensities and Energy Position

The different optical transitions can now be distinguished by scanning the energy of the incoming x-rays and monitoring the x-ray absorption cross section (see section 2.2.1). The electron binding energy as well as the spin-orbit coupling of a  $2p$  electron depends strongly on the charge of the nucleus. For this reason it is possible to distinguish the absorption resonance of Ni from that of Co by the x-ray energy where they appear, although their line shape is very similar. The  $2p$  binding energies of the elements of interest are shown in table 2.1 (taken from [5]). Considering that monochromatic x-rays with a bandwidth better than 0.5eV are available in this energy region different elements in an unknown sample can be identified by the absolute energy position where the  $L_3$  and  $L_2$  absorption resonances appear.

This is now shown in the center panel of figure 2.5. For each of the investigated 3d-transition metals an absorption peak at the energies mentioned in the table appears. Each

<sup>4</sup>The spin-orbit energy is inverse proportional to the distance between the electron and the nucleus. While the spin orbit coupling is of the order of 10-20eV in the 2p core levels it is very small for the 3d final states (0.001-0.01eV)

white line exhibits a certain line width (1-2eV) due to the finite lifetime. An interesting observation is that the white line intensity decreases with increasing atomic number. This is due to the fact that at the same time the number of d-electrons increases and therefore the number of possible final states decreases. The so-called *white line sum rule* states that the integrated intensity of a 2p white line is proportional to the number of holes in the d-shell of the particular element. The white line sum rule can be used to determine the absolute or relative concentration of an element in a sample. For the absolute determination the integrated intensity needs to be compared to a suitable standard sample. For a relative determination a knowledge of the relative number of holes in the d-shell is sufficient.

So far no transition into an s-orbital is considered, although they are optically allowed. Their contribution to the spectrum is indicated with a step like underground in the Fe spectra in figure 2.5. Because of their spherical symmetry they do not play a role in the magnetic studies presented in this thesis. They can be subtracted from the spectrum by using Voigt- or in the simplest case arctan functions [15]

### Multiplet Splitting

The next question that needs to be addressed is why the spectrum of Ni and NiO for example can be distinguished. The charge of the nucleus is the same in both cases, so the absorption lines should appear at the same positions which they do. A general observation is that the white line intensity of the NiO spectrum will be larger following the white line sum rule due to the different oxidation state. Furthermore the step-like underground observed in the metal x-ray absorption will be decreased in the oxide, because of hybridization between the nickel s-orbital and the oxygen p-orbital. Optical transitions into the *sp* hybrid orbital from the metal 2p-orbital are suppressed because of the  $\Delta L = \pm 1$  rule. Altogether the peak intensity to background ratio is increased in the oxide with respect to the metal.

The more pronounced difference is the shape of the absorption resonance itself. In the lower panel of figure 2.5 the spectra of some 3d metals and a particular oxide are shown. In this case the intensities of the oxide XAS are scaled such that the shape of the spectra can be compared. Note that otherwise the white line sum rule could be observed in all cases. All oxide spectra show a rich fine structure, where each of the  $L_3$  and  $L_2$  resonance splits further up into different peaks. The splitting is referred to as *multiplet splitting*. The effect of multiplet splitting is that the  $m_J$  degeneracy (for example  ${}^3F_4$  with  $m_J = -4 \dots +4$ ) of a given atomic state is cancelled and the different  $m_J$  sub levels in ground and final state are now separated by a few hundred meV to a few eV and thus can be identified. The  $m_J$  sub-levels are not shown in figure 2.5 because they appear at basically the same energies in the bare metals. Two possible origins of multiplet splitting especially in oxides are discussed in the following.

### Ligand Field Multiplet

So far only the ground state of a single atom has been considered. However, in the solid state the atom is embedded into a matrix and the influence of its neighbors onto the atomic

Hamiltonian is described in terms of a perturbation introduced by the ligand field. The dominant ligand field in 3d metals and their oxides is the one with cubic symmetry. It splits the ground state into different sub levels and the binding energy of an electron now depends on its  $m_J$  quantum number that is the direction of its momentum. The splitting is typically quantified by a number referred to as  $10D_q$ .

In an octahedral symmetry like in NiO for example the field of the surrounding atoms has cubic symmetry  $O_h$ . The d-orbitals pointing into the direction of the neighbors ( $d_{3z^2-r^2}$ ,  $d_{x^2-y^2}$ ) interact more strongly and are therefore more strongly bound ( $E_g$ -symmetry). In this symmetry the other 3 orbitals which are ( $d_{xy}$ ,  $d_{yz}$ ,  $d_{zx}$ ) ( $T_{2g}$ -symmetry) point between the neighboring atoms and are less strongly bound. In consequence this leads to an energetic separation of the different d-orbitals depending on their orientation. The size of the splitting  $10D_q$  is typically of the order 1-2eV. This is again larger than the typical bandwidth and energy resolution of the x-rays used in the experiment, thus the ligand field multiplet splitting is observable in the experiment. The ligand field splitting is indicated in the  ${}^3F_4$  ground state shown in figure 2.5.

### Charge Transfer Multiplet

Another source of peak splitting is charge transfer. The motivation for this approach is that experimentally observed oxidation numbers in solid states are fractional numbers and therefore an additional charge has to be partly transferred between the neighboring and the central atom. This is accomplished by assuming a mix of a  $d^n$  and  $d^{n+1}$  state as a general ( $d^n + d^{n+1}\underline{L}$ ) ground state. Because of its different symmetry and its different Coulomb interaction the  $d^{n+1}$  state does appear at a slightly different energy and it includes a different set of  $m_J$  states. These are energetically separated from the  $m_J$  states in the  $d^n$  state. It is important to note that using this approach, typical solid state properties like fractional valencies, magnetic moments and d-band occupation can be included into an atomic approach to describe the ground state properties.

### 2.3.3 Dichroism - Magnetic Sensitivity

#### Overview and History

In a next step the polarization dependence of the absorption cross section will be discussed. If the dependence is caused by the magnetism of the sample it is referred to as magnetic dichroism. Magnetic dichroism in the visible region is used for more than a 100 years (e.g. magneto optic kerr effect) to characterize magnetic samples. Using x-rays the approach is rather new. Magnetic linear dichroism in XAS has been predicted in the XAS of rare earth metals in 1985 [96]. The linear and circular dichroism for the 3d metals was predicted in 1991 [101]. The interest in circular dichroism at the L resonances increased with the proposal of sum rules. They connect the dichroism intensity with the orbital moment (Thole *et al.* [94]) the spin density (Carra *et al.* [14]) or the spin moment [88]. A general overview about the correlation between magnetism, spin-orbit coupling and the anisotropy energy and the

dielectric tensor for a wide range of photon energies can be found in articles by H. Ebert *et al.* [21, 20]. More specific reviews focussing on the applications of soft x-ray dichroism are found in [90, 89, 41]. The following explanations are taken from these references.

### Origin of Magnetic Dichroism

The underlying principle of magnetic dichroism is explained in the following. For this purpose the  ${}^2D \rightarrow {}^2P$  transition is considered again. This time the different  $m_J$  sub levels are shown as well. The left column of figure 2.6 shows all possible optical transitions using linear or circular polarization of either helicity contributing to the  ${}^2D_{5/2} \rightarrow {}^2P_{3/2}$  or  $L_3$  transition (top row) and the  ${}^2D_{3/2} \rightarrow {}^2P_{1/2}$  or  $L_2$  resonance (bottom row).

The first observation is that there are twice as many transitions contributing to the  $L_3$  resonance (12) as to the  $L_2$  resonance (6). This holds true as long as the spin-orbit coupling in the d-states is small so that the population of the  ${}^2D_{5/2}$  and  ${}^2D_{3/2}$  is equally possible. In the case of considerable spin-orbit coupling in the ground state, this is not completely true anymore and from the ratio of the white line intensities conclusions about the spin-orbit coupling energy can be drawn [95]. However in general the intensity of the  $L_3$  resonance is twice the  $L_2$  resonance. An example of an L-edge XAS spectra is shown on the bottom including the background resulting from  $p - s$  transitions.

The second observation is that for each of the three different polarizations a different subset of 4(2) excitations contributes to the line shape. If all the different  $m_J$  states appear at the same binding energy and are evenly populated, no dependence of the L-edge XAS line shape on the polarization of the incident x-ray photon is observed. However, a characteristic property of a magnetic sample, a sample with a preferred direction of the magnetic moment is that the  $m_J$  levels are not evenly populated and therefore a difference or *dichroism* in the absorption line shape can be observed. If certain  $m_j$  levels corresponding to configurations where the total moment is parallel to a particular direction (ferromagnet) or collinear to a certain axis (antiferromagnet) are stronger populated than other such an asymmetry in the *density of states* together with the optical transition rules for  $m_j$  lead to magnetic dichroism.

#### 2.3.4 X-Ray Magnetic Circular Dichroism - XMCD

##### Origin of XMCD

In a ferromagnet the net magnetization is caused by the fact that the total energy is lowered when neighboring spins are aligned parallel (*exchange energy*). For this reason electronic states with a particular  $m_J$ , for example corresponding to a spin down configuration, are preferentially occupied. This is illustrated in the middle row of figure 2.6. The light gray areas represent the probability of an electron to populate the corresponding  $m_J$  level in the ground state. The probability is inverted with respect to  $m_J$  between the  ${}^2D_{5/2}$  and  ${}^2D_{3/2}$  state, because the spin-orbit coupling is opposite in these two states. The total  $L_x$  absorption intensity for either left or right circular polarization can be obtained by adding the 4 possible

transitions weighted with the occupation of the particular sub level that has been excited<sup>5</sup>. Red bars correspond to sub levels excited with positive and green bars to sub levels excited with negative helicity. White bars represent sub-levels that are not excited due to the dipole selection rule. One finds that the  $L_3$  absorption intensity is increased if excited with x-rays of a particular helicity,  $\sigma^+$  in this example, while the opposite behavior is observed for the  $L_2$  absorption.

Exactly this observation is referred to as *magnetic circular dichroism*. A typical dichroism spectrum which is obtained by calculating the difference between spectra obtained with different helicity of the x-rays is shown in the lower panel of figure 2.6, it consists of two peaks in opposite direction. The contributions from transitions with different  $m_J$  to the dichroism spectrum are also shown. In a metallic  $3d$  ferromagnet the  $m_j$  sub levels are only separated by a few meV and therefore the different transitions are usually not *resolved* in an XAS experiment. This is why the total observed  $L_x$  absorption intensity is simply the sum of all  $m_J$  contributions, that are depicted in the upper panel of the figure.

### Application of XMCD

From an experimental point of view magnetic circular dichroism can be considered as a modulation of the  $L_3/L_2$  absorption intensity ratio depending on the angle between magnetization and the helicity of the incoming x-rays. The modulation intensity will be proportional to the degree of circular polarization needs and the atomic magnetic moment, which determines the asymmetry in the density. This intensity ratio will be referred to as XMCD intensity. A very general expression for the electron yield intensity originating from a particular absorption resonance can be written in the following

$$I_L = I_0 + C_M P_c |\vec{M}| \cos(\vec{\sigma}, \vec{M}) \quad (2.10)$$

$I_0$  represents the isotropic absorption intensity which can be observed for example if the sample has been demagnetized or by averaging over the spectra obtained with opposite helicity. The isotropic intensity is now modulated due to circular dichroism with an amplitude factor proportional to the size of the magnetic moment  $C_M$ , the degree of circular polarization and the angle between magnetization  $\vec{M}$  and helicity  $\vec{\sigma}$  that means the direction of the magnetic moment. The constant  $C_M$  depends on the material and its particular electronic structure. If the direction of the magnetic moment of the sample is kept fixed, for example by an external field the XMCD allows to determine the atomic spin and orbital moment per electron by using sum rules [94, 14]. These are given in the following for the special case of 2p-3d transitions. Here  $L_X$  denotes the integrated intensity of the  $L_X$  contribution to the XMCD spectra and  $n_{3d}$  is the number of electrons occupying the 3d levels, typically a fractional number .

$$m_o = -\frac{4}{3}(L_3 + L_2)(10 - n_{3d}) \quad (2.11)$$

$$m_s = -2(L_3 + 2L_2)(10 - n_{3d}) \quad (2.12)$$

$$(2.13)$$

---

<sup>5</sup>In principle the transition probability depends on  $m_J$  as well. This is neglected here for simplification

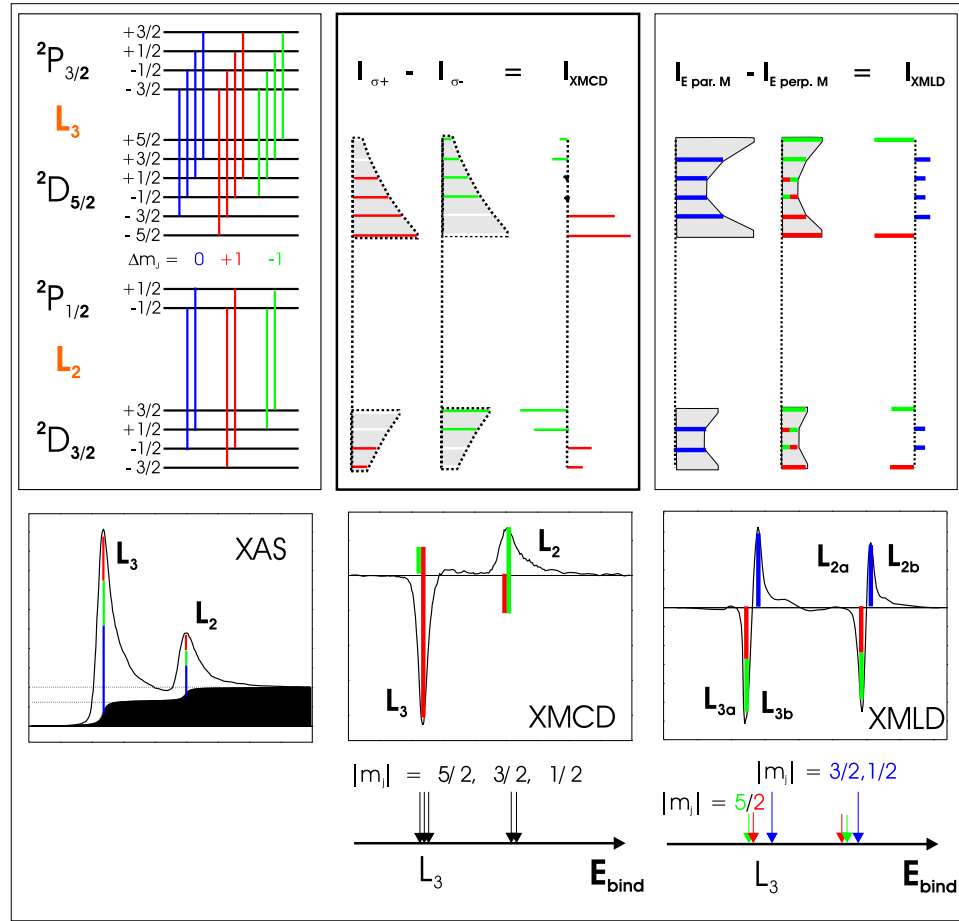


Figure 2.6: Origins of Dichroism

Left: Possible optical  ${}^2D \rightarrow {}^2P$  transitions considering the  $m_j$  sub levels and the polarization of the incoming x-rays. The resulting spectrum and the contribution of the different polarizations are shown on the bottom. The step-like underground included in the spectra (black) results from transitions into s-states. Middle: Excitations observed with circular polarized light of different helicity (indicated by green and red) in a magnetic sample with a preferential occupation of states with negative  $m_j$ . The intensity of each L-resonance is the sum of all excitations and a difference in absorption intensity is observed. All transitions appear at the same energy, because the different binding energies of the  $m_j$  sub levels cannot be resolved experimentally. The XMCD intensities do exhibit a different sign and size at  $L_3$  and  $L_2$  resonance. Right: Transitions observed with two linear x-ray polarization oriented parallel and perpendicular to the magnetization axis. Again different  $m_j$  sub-levels are excited. The sum over all contributions to the difference is close to zero, so a dichroism can only be observed experimentally if these levels are separated in energy. For example if transitions from sub levels with larger  $m_j$  appear at lower binding energies (Zeeman effect) as shown in the lower panel the typical XMLD spectra is observed. The difference spectra at the two  $L_x$  resonances exhibit the same sign and approximatively the same size.

The following experimental details need to be considered to extract the absolute moment. The difference spectra  $I_{\sigma_+} - I_{\sigma_-}$  have to be appropriately normalized so that its values are meaningful, for example by referencing it to the number of holes in the 3d shell. This is done by dividing it by the integrated intensity of the isotropic spectra (white line sum rule) which can be obtained by calculating the sum of  $I_{\sigma_+} + I_{\sigma_-}$ . To exclude contributions from  $2p - 3s$  transitions in the isotropic spectra a step like underground is subtracted first, since the XMCD signal only originates from the  $2p - 3d$  transition.

### Ferromagnetic Contrast Using XMCD

Both sum rules have been experimentally proven for the most prominent ferromagnetic 3d metals by Chen *et al.* [15]. For these materials the constant  $C_M$  is known and the angular term in equation (2.10) can be directly analyzed which allows to exploit XMCD in a *ferromagnetic vectorial magnetometer*. The direction of the magnetization of a sample or in different ferromagnetic domains of a sample can be unambiguously identified by this method. In the following it is illustrated how x-ray magnetic circular dichroism is used in a PEEM to image the lateral distribution of the net magnetic moment in a sample [92], which is often referred to as *domain pattern*.

The variation of the electron yield across ferromagnetic domains after illumination with circular polarized light is shown in the sketch in the upper left of figure 2.7. The magnetization vector of each domain includes a different angle with the helicity of the x-rays and therefore each of the x-ray absorption spectra obtained from each domain (upper right panel) exhibits a different  $L_3/L_2$  ratio and images acquired at the two resonances show four different grey levels with opposite contrast at the two resonances. The final XMCD image on the right is derived by division of the single images and it represents a map of the XMCD intensity that is the  $L_3/L_2$  ratio and thus the direction of the magnetic moment. The further advantage of the calculation of the division image is that electron yield variations that are caused by inhomogeneous illumination or topographic features will cancel out and does not appear.

The basic symmetry of a domain pattern can be already deduced from the XMCD image itself, especially if the experimental setup allows to rotate the sample so that several images in different geometries can be acquired. However a precise determination of the direction of the magnetization in each domain from the XMCD intensity involves an appropriate background subtraction and normalization that can not easily be achieved in a PEEM image. For this purpose the spectra calculated from images stacks acquired in each of the ferromagnetic domains are used. The absolute XMCD intensity within each domain can be extracted and the angle of the magnetic moment can be determined by comparing tyhe experimentally derived values to appropriate references [15].

The ability to acquire high quality spectra from a single ferromagnetic as well as anti-ferromagnetic domains, introduced in the following section, makes PEEM a powerful tool to image the magnetic domain structure of these systems [60, 62, 61].

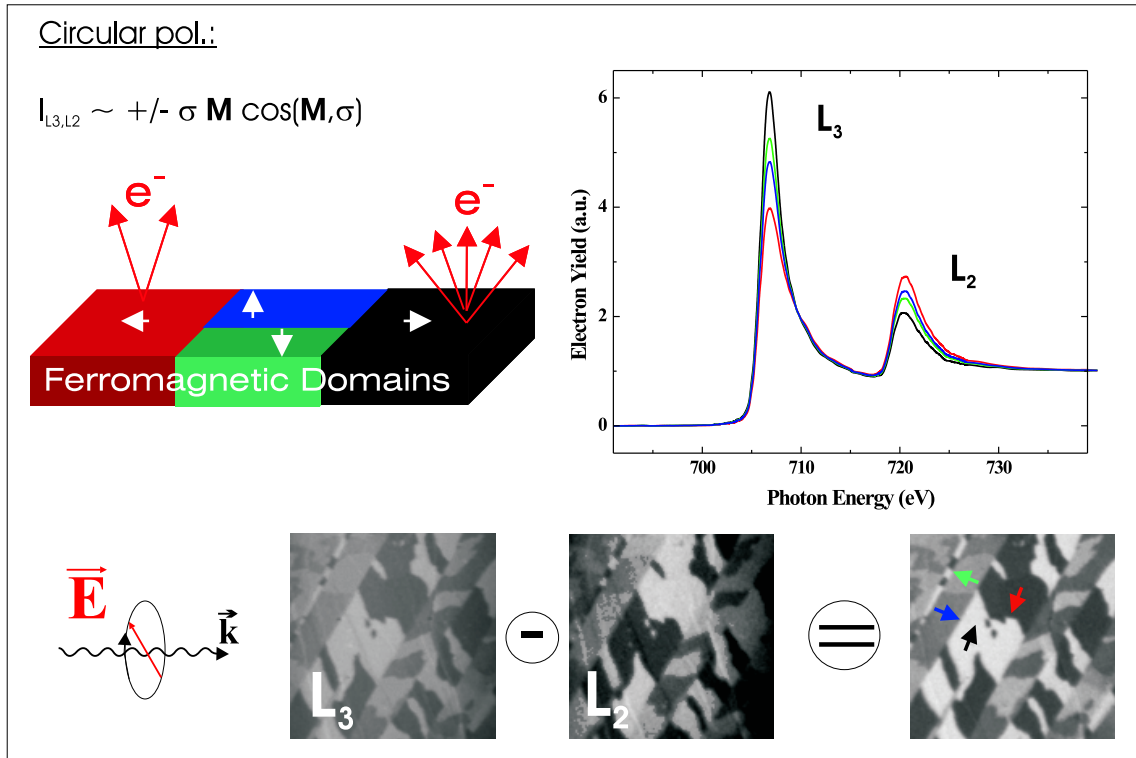


Figure 2.7: Imaging of Ferromagnetic Domains Using XMCD

XMCD of a Fe surface with four different ferromagnetic domains. The electron yield depends on the angle between the helicity and the magnetization (upper left). Four different characteristic absorption spectra are obtained from the four different domains (upper right). PEEM images acquired at each resonance exhibit opposite contrast as shown in the lower panel showing the principal XMCD behavior. The resulting XMCD image is achieved by dividing or calculating the asymmetry of the two single images. The arrows represent the direction of the magnetic moment within each domain .

### 2.3.5 X-ray Magnetic Linear Dichroism - XMLD

#### Origin of XMLD

X-ray magnetic circular dichroism is not useful if there is no net magnetic moment present, for example in an antiferromagnetic system. Nevertheless as long as the magnetic moments are not distributed isotropically but preferentially aligned parallel to a certain crystal axis this will result into an anisotropy of the optical properties as well. This effect is referred to as x-ray magnetic linear dichroism and can be observed when linear polarized light is incident along perpendicular axes of the magnetic system.

In case of an antiferromagnet the exchange energy will cause sub levels with a larger *absolute*  $m_J$  (magnetization collinear with the quantization axis) to be stronger populated than

sub levels with a magnetic moment perpendicular to the quantization axis. This is illustrated in the right panel of figure 2.6. The figure shows that with a polarization perpendicular to the quantization axis, all 6(4) different levels of the  $L_3(L_2)$  line will be excited, while the other polarization only accesses 4(2) ground states. Note that the excitations labelled 'E perp. M' are represented by an equal superposition of excitations of opposite circular polarizations. The contribution of the different  $m_J$  sub levels to the x-ray absorption spectra is shown in the figure as well as their contribution to the difference or XMLD spectrum.

In contrast to the XMCD effect the sign of the difference spectra is the same for both resonances. According to the white line sum rule this would mean that the number of d-holes probed with different x-ray polarization in the initial state are different. In systems with highly anisotropic charge distribution density like High- $T_c$  superconductors or polymers, the number of d-holes might indeed be strongly different along different directions. This behavior is referred to as *charge dichroism* and is observed for example in antiferromagnets like  $\text{LaCuO}_4$  or  $\text{FeF}_2$  in addition to the XMLD effect. However, this is not the case in an antiferromagnet with a simple cubic symmetry like NiO or CoO or in the 3d ferromagnetic metals in which the sum of all contributions from different  $m_j$  sub-levels to the XMLD has to vanish. The conclusion is that in order to observe magnetic linear dichroism the sub levels with the highest absolute  $m_J$  that are only observed with one polarization have to be at a different binding energy than the other sub levels or in other words the J or the  $m_J$  degeneracy needs to be lifted.

One possible origin of sub level splitting is the Zeeman energy, which favors parallel (perpendicular) alignment of the magnetic moment originating from the electron (hole) with the exchange field of the surrounding atoms  $E \sim MH$ . Assuming an exchange field of 1000 Tesla and a magnetic moment of 2 Bohr magneton a splitting of 50meV is expected. For the considered  $^2D$  ground state the binding energy of the  $m_J = \frac{5}{2}$  (hole-) states will therefore be 50meV smaller. This is illustrated in the XMLD spectra on the bottom right of figure 2.6, which is obtained if the difference  $E \parallel M - E \perp M$  is calculated. The colored bars represent the contributions from the excitations with the three different polarizations. The lower binding energy  $m_J = \frac{5}{2}$  is only observed with a perpendicular polarization vector, leading to a negative peak in the difference as calculated. The negative intensity in the XMLD spectra is compensated by the positive intensity in the second peak <sup>6</sup>.

### Application of XMLD

Since the energy resolution of the x-rays is typically more than 50meV the experimental determination of XMLD in a system with Zeeman energy as the only origin of splitting between different  $m_J$  levels represents an experimental challenge (see for example [78]). XMLD on metallic or even ferromagnetic systems is nevertheless of great interest because XMLD probes directly the magnetic anisotropy or in other words is a measure for the expectation value  $\langle M^2 \rangle$  [96, 102, 91]. By using appropriate sum rules [100] the anisotropy energies can be determined [18].

<sup>6</sup>The opposite behavior is observed for a 3d metal with less than half filled shell

The XMLD effect becomes more prominent if the different  $m_J$  states are well separated by multiplet splitting which has been discussed previously. For this reason the first convincing experimental evidence for XMLD has been found on rare earths [102]. A few years later XMLD could be observed on transition metal oxides for example on antiferromagnetic  $\text{Fe}_2\text{O}_3$  [46] where the ligand field and charge transfer mechanisms lead to a distinct multiplet splitting.

Note, that ferrimagnets exhibit compensated as well as uncompensated collinear order and therefore show both types of dichroism. The correlation between these has been shown on  $\text{Fe}_3\text{O}_4$  for example by Kuiper *et al.* [45].

### Quantifying XMLD

For antiferromagnets XMLD is currently the only technique to quantify the orientation of the antiferromagnetic axis at surfaces. For this purpose the observed XMLD signals are analyzed in a quantitative way in this thesis. An XMLD intensity similar to the XMCD intensity will be defined as the x-ray absorption ratio between the low and the high energy absorption fraction *within* an absorption resonance, for example  $L_{2a}$  and  $L_{2b}$  as noted on figure 2.6. The only normalization procedure which is applied in this case is to subtract a linear background such that the XAS intensity equals zero before and after the  $L_2$  resonance. One finds for the dependence of the XMLD intensity ([96, 102]) on the angle between the incident electromagnetic field  $\vec{E}$  and the thermodynamic expectation value of  $\langle M^2 \rangle$ .

$$I_L = I_0 - C \langle M^2 \rangle (3 \cos^2(\vec{E}, \langle \vec{M}^2 \rangle) - 1) \quad (2.14)$$

The XMLD intensity will exhibit maxima for parallel and perpendicular alignment of electric field and magnetization axis, thus it exhibits a  $180^\circ$  periodicity in contrast to the  $360^\circ$  periodicity observed for the XMCD intensity. Similar to the case of XMCD the XMLD intensity can be used as an *antiferromagnetic vectorial magnetometer* if the constant  $C$  is known. In this thesis the antiferromagnetic structure of NiO will be investigated. Van Veenendaal *et al.* [104] and D. Alders, J. Vogel *et al.* [2, 3, 1] studied the angular and temperature dependence of the NiO XMLD signal in detail and their results are used as a reference here. Alders *et al.* found the following relation for the XMLD intensity of NiO at room temperature.

$$I_{\text{XMLD}} = 1.27 - 0.45 \cos^2 \alpha, \text{ or } 21.5\% \text{ maximum contrast} \quad (2.15)$$

This experiment was performed with a energy resolution of the incoming photons that was sufficient to clearly separate the two peaks ( $< 0.4$  eV). For the experiments described in this thesis the best energy resolution that could be achieved was (0.65 eV) and for this reason a smaller contrast is observed. For the two relevant peaks which are separated by 1.3eV the reduction in contrast is estimated to be 15%. Finally the following expression for the determination of the antiferromagnetic axes are obtained.

$$I_{\text{XMLD}} = 1.25 - 0.39 \cos^2 \alpha, \text{ or } 18.5\% \text{ maximum contrast} \quad (2.16)$$

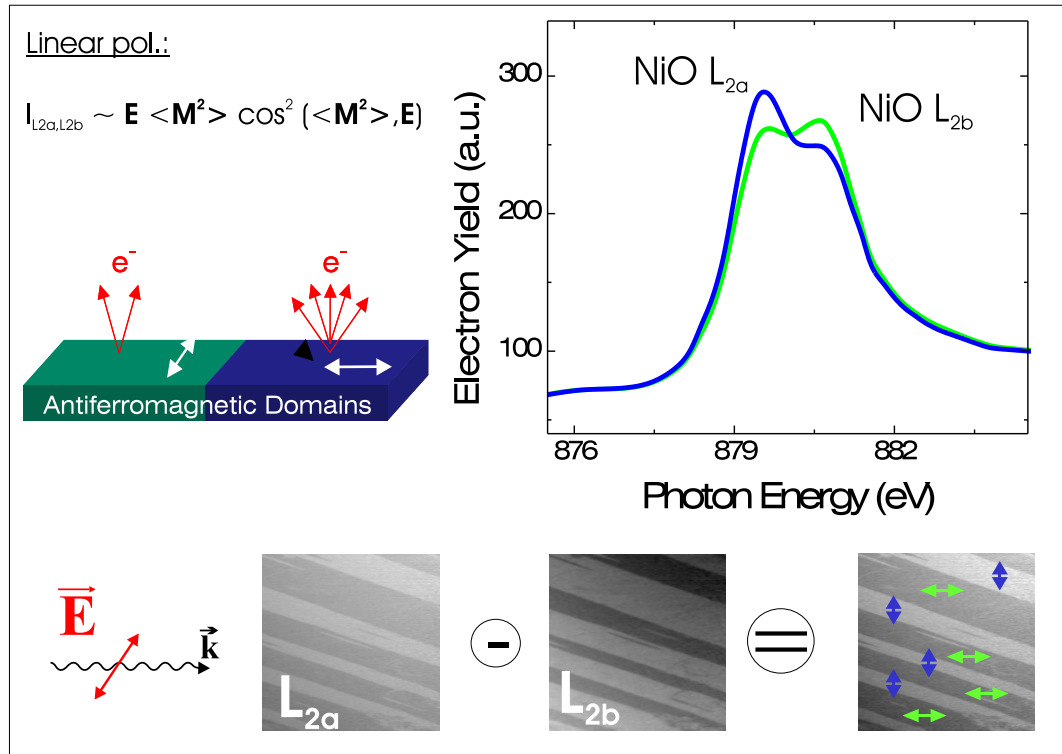


Figure 2.8: Imaging of Antiferromagnetic Domains Using XMLD

XMLD of a NiO(001) surface with two different antiferromagnetic domains. The electron yield depends on the angle between the electric field and the magnetization axis (upper left). The XMLD intensity changes the sign within each fraction of the  $L_2$  resonance (upper right). PEEM images acquired at each resonance therefore exhibit opposite contrast as shown in the lower panel. The resulting XMLD image is achieved by dividing or calculating the asymmetry of the two single images. Arrows indicate the orientation of the magnetic axis in each antiferromagnetic domain.

The maximum values of 1.25 and 0.86 are indeed observed in the experiment. For an angle of  $54.7^\circ$  between electric field and magnetic axis the cosine term vanishes and the line shape is not influenced by the long-range magnetism anymore (*isotropic spectrum*). The isotropic spectrum is determined by the electronic as well as the spin symmetry of the crystal and will be used as a reference for the chemical and structural quality of the sample. Note that both expressions the one found by Alders et al and the one used in this context lead to the same isotropic value of 1.12.

### Antiferromagnetic Contrast Using XMLD

XMLD has been employed to image antiferromagnetic contrast [81, 91] or more recently a particular antiferromagnetic domain pattern [76, 32]. The same procedure for the image acquisition and the data analysis that has been described for XMCD are applied in case of XMLD. The procedure to acquire an XMLD image showing antiferromagnetic domain contrast and the XMLD spectra resulting from image stacks are shown in figure 2.8. For all images of antiferromagnetic domain patterns of NiO shown in this thesis two images are acquired at each peak within the NiO  $L_2$  resonance. The  $L_2$  resonance is chosen because the isotropic absorption intensity of the two peaks is very similar and the same exposure time can be chosen for the two images. This is in contrast to the  $L_3$  resonance, where the isotropic absorption intensity is different by about a factor of 4 (see for example figure 4.2). The final XMLD image represents the ratio of the two images with opposite contrast. Again as for the case of XMCD, useful information about the principal symmetry of the domain pattern and the distribution of antiferromagnetic axes can be extracted from XMLD images obtained in different geometries. Nevertheless an exact determination of the antiferromagnetic axis could only be achieved by acquiring absorption spectra in each antiferromagnetic domain and analyzing the micro-spectroscopic and extracting the XMLD intensity.



## Chapter 3

# Antiferromagnetic Structure of NiO

### 3.1 Introduction

#### 3.1.1 NiO as a Model Antiferromagnet

The characterization of the antiferromagnetic order at surfaces and interfaces, in particular a determination of the direction of the antiferromagnetic axis and magnetic direction within each magnetic domain, is crucial to improve the understanding of exchange anisotropy. For this reason a dichroism spectromicroscopy study will not only be restricted to a single image of the surface domain topology but will also include its quantitative analysis and comparison to the bulk structure. It will make use of the angular dependence of the XMLD and XMCD effect to determine the orientation of the AFM axis as well as the FM direction domain by domain.

This study focusses on antiferromagnetic NiO(001) surfaces and their magnetic coupling behavior to thin ferromagnetic layers. NiO is used as an AFM in technical relevant structures. Its scientific relevance originates in the fact that it can serve as model antiferromagnet. In the following the three major requirements for a model antiferromagnet are listed.

1. The antiferromagnetic bulk structure of NiO is well established since the 1950s from extensive studies using neutron diffraction as described in numerous references [79, 80, 71, 109, 108, 107]. The surface ordering can thus be compared to the situation in the bulk.
2. Recent studies established the angular and temperature dependence of the XMLD effect on NiO thin films quantitatively. This can be used to calibrate the antiferromagnetic *magnetometer* as described in the previous chapter [1].
3. The AFM ordered (001) surface can be prepared by cleaving single crystals. Subsequent cycles of ion etching using Ar<sup>+</sup> ions and annealing at 600K furthers improve the quality of the surface and clean well ordered surfaces are available by means of UHV based techniques.

### 3.1.2 AFM Domain Formation

The following explanations are taken from publications by Yamada *et al.* [109, 108, 107] and Roth *et al.* [71]. The authors studied the bulk antiferromagnetic structure with neutron and x-ray diffraction based techniques.

The appearance of magnetic domains is a typical phenomena of magnetically ordered systems in general. However, the origin of domain formation in an antiferromagnet is of different nature than in a ferromagnet due to the magnetically compensated nature of the spin structure. In a ferromagnet the magneto static energy stored in its stray field caused by the net magnetic moment increases the total energy significantly and so the system decomposes in magnetic domains to decrease the magneto static energy again. Ideally the magnetic flux remains then closed within the sample and the exchange energy needed to rotate spins against each other from one domain to another can be afforded. Furthermore the long range dipolar interaction of spins in the center of the sample with spins at its border leads to so-called *shape anisotropy*. Roughly spoken this anisotropy causes spins to align parallel to the physical borders of the system. Both of these two energies do not contribute significantly to the magnetic energy of an antiferromagnet. The first contribution to the magnetic energy that both systems have in common is the *magneto crystalline anisotropy* energy, which originates in the spin-orbit interaction that couples spin and orbital degree of freedom. The effect of the magneto crystalline anisotropy is that the spins will follow the orbital moment and align parallel to certain crystal axis, which are given by the electronic structure and the symmetry of the crystal. While the interaction between shape and magneto crystalline anisotropy determines the easy axes in a ferromagnet, higher order contributions have to be considered in an antiferromagnet, for example the *magneto elastic anisotropy*. A deformation of the lattice and reduction of its symmetry may lead to a net gain in magneto crystalline anisotropy energy or even short range dipolar energy. The concurrence of magneto elastic, short range dipolar and magneto crystalline energies determines the easy axes in an antiferromagnet. If more than one easy axis is present or lattice defects will change the elastic energy of the system the antiferromagnet will decompose in several magnetic domains. Recently Gomonay *et al.* [28] have been theoretically investigated the correlation between magnetostriction and antiferromagnetic domain formation in the bulk and at surfaces. They found that similar to magnetic charges at ferromagnetic surfaces 'elastic charges' at antiferromagnetic surfaces cause an 'elastic stray field' which determines the domain structure.

## 3.2 Spin Symmetry in NiO

### 3.2.1 T(win)-Domains

In order to compare the antiferromagnetic domain pattern at the surface of NiO to the antiferromagnetic ordering in bulk crystals, which is a major subject of this thesis, the well known bulk structure will be reviewed. At this point only the observed spin symmetry will be described, without considering any lattice deformations or any particular orientation of the spin axis.

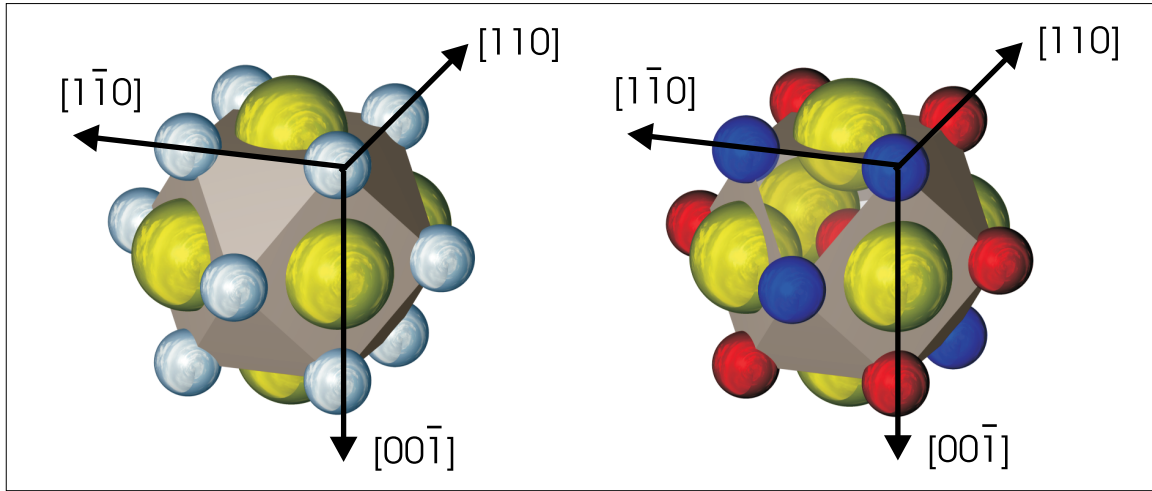


Figure 3.1: The Crystal Structure of NiO

Left: Sketch of the crystal structure of NiO showing the (100) (rectangles) and (111) (triangles) planes. The nickel atoms (small spheres) are positioned on  $[110]$  sites and form an fcc lattice. They are connected by oxygen atoms (large yellow spheres) along  $[100]$ , the direction of the super exchange interaction.

Right: Possible symmetry of the spin lattice. Red and blue spheres represent atoms with spin up or down. The coupling across oxygen atoms along  $[100]$  is always antiparallel resulting in compensated (100) planes. One out of four possible (111) planes, neglecting spin inversion exhibits ferromagnetic order.

Nickel and oxygen atoms form together a rock salt type crystal. The left panel in figure 3.1 shows the principal symmetry. Nickel atoms are represented by little spheres located on  $[110]$  positions forming a fcc sublattice. They are connected by oxygen atoms represented by bigger yellow spheres along the  $[100]$  direction. The oxygen 2p orbital overlaps with a 3d orbital of each of the neighboring nickel atoms leading to the so-called *super exchange interaction*. This interaction between the two otherwise independent electrons causes the antiparallel alignment of their spins by following the Pauli principle and thus the three different  $[100]$  axes define the *intrinsic antiferromagnetic propagation axes*<sup>1</sup> in NiO. A particular  $[100]$  direction is indicated in the figure. Unfortunately the magnetic symmetry of the fcc nickel sublattice is not yet determined by the intrinsic antiferromagnet propagation axes in the rock salt crystal because the  $[100]$  directions do not represent a set of basis vectors in a fcc type lattice.

For an unambiguous characterization of the magnetic symmetry the spin order along the  $[110]$  directions has to be defined. The right panel in figure 3.1 shows one possible spin order obeying the requirement of antiparallel coupling across  $[100]$ . Nickel atoms with spin up or down are distinguished by blue or red spheres in the figure. The central atom at

<sup>1</sup>An antiferromagnetic propagation axis is an axis in the lattice where the spins of adjacent atoms are opposite to each other

Name	FM plane	AFM axis	FM <sub>1</sub> axis (T-wall)	FM <sub>2</sub> axis (S-Domain)
T <sub>1</sub>	(111)	[110] [101] [011]	[ $\bar{1}\bar{1}0$ ] [10 $\bar{1}$ ] [01 $\bar{1}$ ]	[11 $\bar{2}$ ] [ $\bar{1}\bar{2}1$ ] [ $\bar{2}11$ ]
T <sub>2</sub>	( $\bar{1}\bar{1}1$ )	[ $\bar{1}\bar{1}0$ ] [10 $\bar{1}$ ] [011]	[110] [101] [01 $\bar{1}$ ]	[ $\bar{1}\bar{1}2$ ] [12 $\bar{1}$ ] [211]
T <sub>3</sub>	(1 $\bar{1}\bar{1}$ )	[ $\bar{1}\bar{1}0$ ] [101] [01 $\bar{1}$ ]	[110] [10 $\bar{1}$ ] [011]	[ $\bar{1}\bar{1}2$ ] [121] [21 $\bar{1}$ ]
T <sub>4</sub>	(11 $\bar{1}$ )	[110] [10 $\bar{1}$ ] [01 $\bar{1}$ ]	[ $\bar{1}\bar{1}0$ ] [101] [011]	[112] [ $\bar{1}21$ ] [2 $\bar{1}1$ ]

Table 3.1: Possible Spin Symmetries in NiO

Possible AFM symmetries named T-domains and labelled by the (111)-plane which exhibits ferromagnetic order in the particular symmetry. The columns mention the ferromagnetic and antiferromagnetic propagation axes. Note, one of the ferromagnetic propagation axis coincidences with the spin axis realized in antiferromagnetic spin domains, while the other one is realized in walls between twin domains.

(000) is shown in red. To obtain a magnetically compensated cell three of the [110] axes need exhibit antiferromagnetic order while the other three will coincident with ferromagnetic propagation axes. The number of permutations of ferromagnetic and antiferromagnetic axes is now reduced to the intrinsic [100] antiferromagnetic axes. For example [110] and [ $\bar{1}\bar{1}0$ ] cannot represent AFM (or FM) axes at the same time. As a result only four different permutations (neglecting spin inversion) of AFM and FM axes are possible. The characteristic feature for each of these permutations is that atoms within a particular (111) plane (formed for example by the red spheres in figure 3.1) show ferromagnetic order while adjacent (111) planes are aligned antiparallel. A particular spin symmetry is labelled by the normal of the plane which exhibits ferromagnetic order. A macroscopic crystal may now exhibit different spin symmetries in different regions of the crystal. In this case the spin lattice is *twinned* and the different spin symmetry domains are referred to as T(win)-domains. Table 3.1 shows the four possible T-domains as defined by their ferromagnetic plane, or their antiferromagnetic propagation axes. Also included in the table, for later references, are the ferromagnetic propagation axes to the nearest and the next nearest neighbor.

### 3.2.2 T-Domain Walls

Two T-domains adjoining each other will form an *antiferromagnetic domain wall* parallel to a certain crystal plane. The wall plane is defined by the magnetic axes mentioned in table 3.1 that the two domains have in common. For example T<sub>1</sub> and T<sub>2</sub> share the ferromagnetic axis

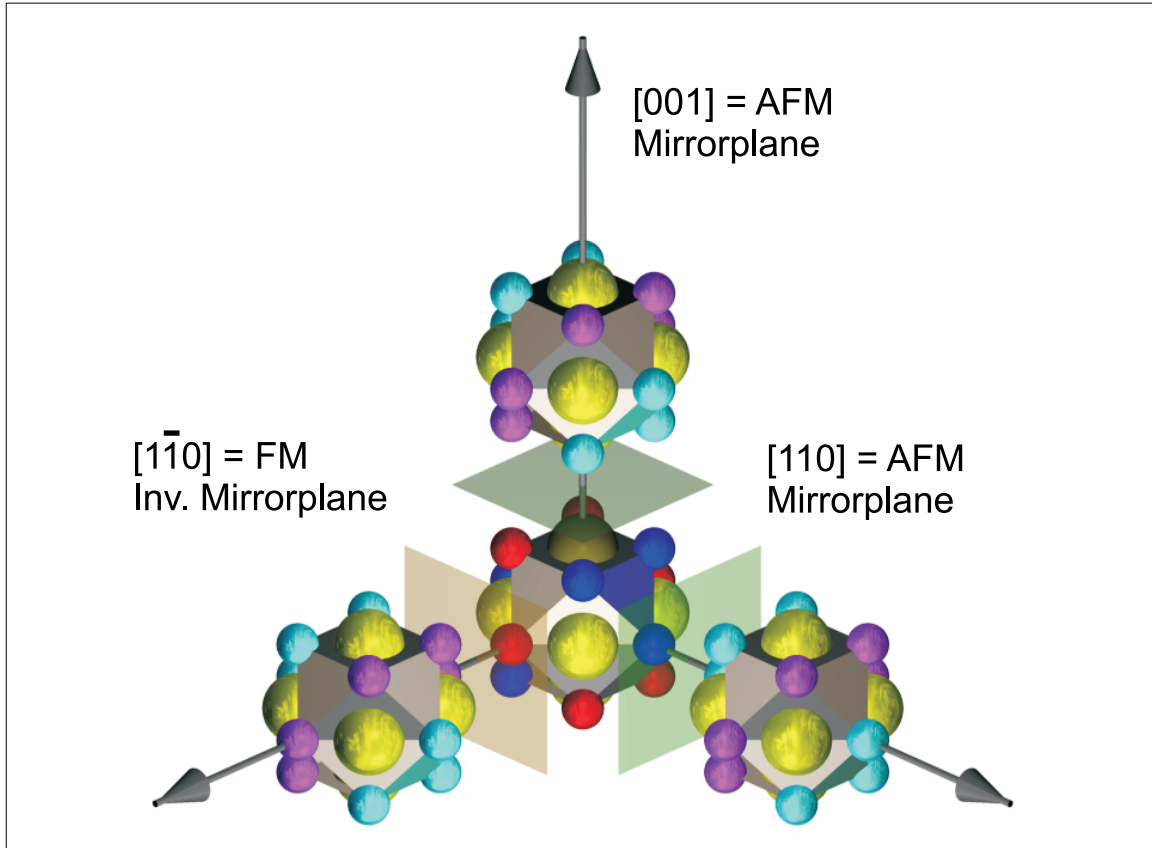


Figure 3.2: Possible Walls between T-domains.

Representation of a particular T-domain (blue spin ( $\uparrow$ ) and red spin ( $\downarrow$ ) spheres) separated by three wall planes from another T-domain (cyan ( $\uparrow$ ) and magenta ( $\downarrow$ ) spheres). The (001) and (110) are mirror planes for the spin symmetry, they represent low energy bulk walls. The ( $1\bar{1}0$ ) wall is not a simple mirror plane and is therefore not observed in the bulk.

$[01\bar{1}]$  and the antiferromagnetic axis  $[011]$ . These two axes together define a (100) plane, which now separates a (111) ordered region from a ( $\bar{1}11$ ) ordered region. The (100) plane is defined by two common magnetic axis. There are two more domain walls possible between  $T_1$  and  $T_2$  defined by only one of the common  $[110]$  axes together with one of the  $[100]$  intrinsic antiferromagnetic axes which all antiferromagnetic domains have in common. In this example these are the (110) and ( $1\bar{1}0$ ) planes.

To elucidate the differences between the three type of *T-domain walls* figure 3.1 shows a particular T-domain represented in the same way as in figure 3.1 with blue and red spheres, and how it can be translated into another T-domain represented by cyan and magenta spheres. The (110) and the (001) wall have in common that they are both perfect mirror planes regarding the spin lattice. Every blue sphere translates into a cyan sphere and every red

$T_1/T_2$	$T_1/T_3$	$T_1/T_4$
$[01\bar{1}][011]$ (100)(011) (01 $\bar{1}$ )	$[10\bar{1}][101]$ (010)(101) (10 $\bar{1}$ )	$[\bar{1}\bar{1}0][110]$ (001)(110) (1 $\bar{1}0$ )
$T_2/T_3$	$T_2/T_4$	$T_3/T_4$
$[110][\bar{1}\bar{1}0]$ (001)(01 $\bar{1}$ ) (011)	$[101][10\bar{1}]$ (010)(10 $\bar{1}$ ) (101)	$[011][01\bar{1}]$ (100)[011] (110)

Table 3.2: Possible Walls Between T-domains

Possible T-walls between T domains  $T_i$  and  $T_j$ . The first row denotes the common magnetic axes. Planes listed in the second row describe high symmetry favorable domain walls. The domain walls listed in the third row are of lower symmetry and are not observed in the bulk.

sphere translates into a magenta sphere if mirrored at the domain wall plane. This is not the case for the  $(\bar{1}10)$  plane which is not a mirror plane for the spin lattice. Roth *et al.* report that only walls, which are mirror planes for the spin lattice will be observed between T-domains in the bulk. This has been corroborated experimentally so far, because the third type of wall has never been observed in the bulk of NiO. It will be shown in the next section that the third wall is incompatible with the magneto elastic forces on both side of the wall. One important result of this work is that the third type of wall can indeed be observed at the surface of NiO, where the mirror symmetry is broken and the magnetic energy of an antiferromagnetic domain wall does not depend anymore on the fact whether it represents a mirror plane or not. For reference, all possible walls and common axes of the four different T-domains are listed in table 3.2.

### 3.3 Easy Spin Axes in NiO

#### 3.3.1 S(pin)-Domains

So far only the spin symmetry of the complete antiferromagnetic crystal has been addressed. Whether or not the *crystallographic T(win)-domains* of the spin lattice also represent *magnetic S(pin)-domains* will depend on the fact whether different T-domains favor a different magnetic spin axis or not. A detailed discussion of the origin of antiferromagnetic domains and their relation to magneto elastic deformation as origin of antiferromagnetic domain formation as mentioned in section 3.1.2 has been presented by Yamada *et al.* [109]. The author calculates the contributions to the magnetic static energy of NiO allowing a complete deviation from the perfect cubic lattice in terms of rhombohedral ( $[111]$ ), monoclinic ( $[\bar{1}\bar{1}0]$ ) and orthorhombic ( $[001]$ ) deformation. The results are presented in the following.

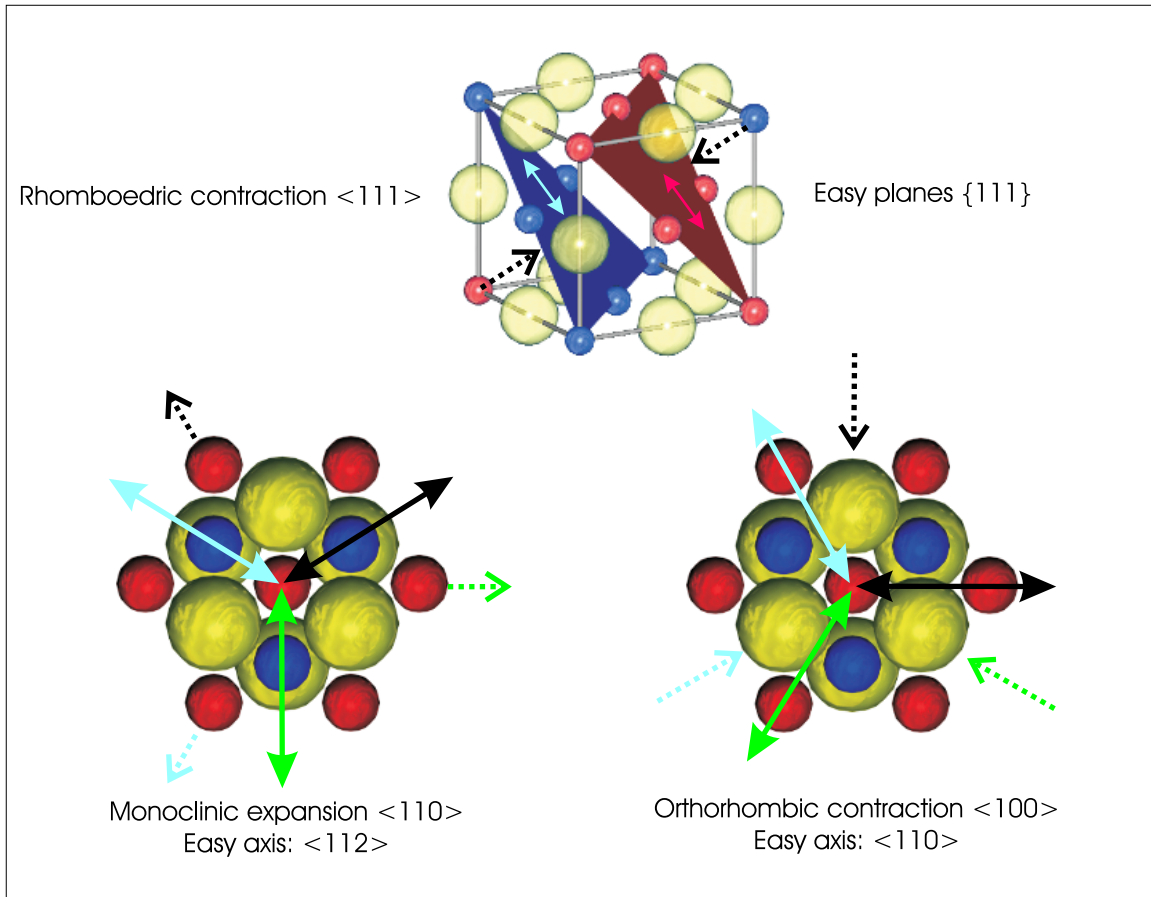


Figure 3.3: Possible Spin Directions in a T-domain.

Top: A lattice cell in NiO. The spins of each atom within a particular  $(111)$  plane exhibit ferromagnetic order and are aligned parallel to the plane. At the same time a rhombohedral lattice contraction along  $[111]$  is observed due to the dipolar interaction between adjacent planes.

Bottom: View onto a  $(111)$  plane. A monoclinic expansion favors spins to align along  $[112]$  into the direction of the next nearest neighbor (left). A orthorhombic contraction along  $[100]$  on the other hand favors a  $[110]$  easy axis towards the next neighbor (right).

### 3.3.2 AFM Domains and Lattice Distortions

#### Spin Axis within Domains

The first conclusion in [109] is that the short range dipolar interaction between ordered (111)-planes contributes strongest to the magneto static energy forcing the spins parallel to the (111) plane ( $10^6 \frac{erg}{cm^3}$ ) and leading to a rhombohedral contraction along [111] of  $\frac{\Delta l}{l} \sim 10^{-4}$ . The anisotropy energy along [100] is comparably small ( $10^3 \frac{erg}{cm^3}$ ) and the spins can easily rotate into the (111) plane which for this reason the *easy planes* of magnetization in NiO. The situation is illustrated on the top of figure 3.3.

Within the (111) plane an additional uniaxial anisotropy exists. Regarding the symmetry within the plane the easy axes can either be parallel to [110] (nearest neighbor) or [112] (next nearest neighbor). This is illustrated in the bottom half of figure 3.3, which shows a view along [111] on the atoms of two (111) planes on top of each other. The calculation presented by Yamada suggested that an orthorhombic contraction along [100] favors [110] as an easy axes; whereas the monoclinic expansion along [110] favors [112]. Both situations are shown in the figure. By comparing their calculations to (bulk) domain patterns generated under stress and external field the author concludes that a monoclinic expansion of the lattice is actually realized in NiO and that the easy spin axes in a T-domain is [112]. Yamada estimates the resulting anisotropy energy within the (111) plane to ( $5 \times 10^4 \frac{erg}{cm^3}$ ).

Altogether, the authors find that the spins within a particular T-domain are aligned parallel to the plane and point toward one of the three possible next nearest neighbor, forming three different S(pin)-domains within each of the four possible T(win)-domains. These twelve different domains in NiO are listed in the last column of Table 3.1.

#### Spin Axis within Domain Walls

Finally the question is addressed which spin axis is realized within a wall between two antiferromagnetic domains. Since only T-domains are observed in the context of this thesis the discussion will be restricted to T-domain walls. For this purpose the example of a  $T_1$  adjoining a  $T_2$  domain is considered. The lattice distortion caused by the magneto elastic forces have to be compatible with the orientation of the wall plane and the spin axis.

On either side of the wall a rhombohedral contraction is realized ( $(\bar{1}\bar{1}\bar{1})$  or  $(1\bar{1}\bar{1})$ ). The spins in each T-domain  $T_1$  and  $T_2$  are oriented perpendicular to the rhombohedral axes as described above and consequently the spins forming the domain wall will align perpendicular to both contraction axes if possible<sup>2</sup>. To achieve this situation the easy spin axis in a T-Domain wall has to be parallel to  $[01\bar{1}]$ . Note, that this axis lies within both possible high symmetry wall planes ( $(100)$  and  $(011)$ ) which are observed between  $T_1$  and  $T_2$  domains in the bulk. This axis coincidences with the next neighbor ferromagnetic axes of the two considered T-domains as noted in table 3.1. As it will be shown in the experimental section of this thesis these conclusions are only valid for bulk T-domains. A different situation will be observed in

<sup>2</sup>In principle the monoclinic expansion would need to be considered as well, but the [111] anisotropy energy is much larger than the [121] anisotropy energy.

walls between surface T-Domains where the spin axis is found to align perpendicular to the wall plane.

### 3.3.3 Summary

The antiferromagnetic spin structure in NiO is summarized in the following.

1. In NiO the nickel spins show ferromagnetic order in each of the four possible (111) planes with adjacent (111) planes aligned antiparallel (T-domains).
2. The spins are aligned parallel to the ordering (111) plane and the lattice is contracted along the corresponding antiferromagnetic propagation axis.
3. Within the (111) plane the spins may point into the three different directions of their next nearest neighbor, [112] (S-domains).
4. Different T-domains (in the bulk) are separated by (001) or (011) walls which represent mirror planes for the spin symmetry. The orientation of the domain wall is governed by the compatibility of strain on each side of the domain wall.
5. The spin axes within walls of bulk T-domains is parallel to the wall plane along [110].



## Part II

# Experiments and Results



## Chapter 4

# Preparation of NiO

### 4.1 NiO(001) Single Crystal Surfaces

Due to the polar nature of the ionic NiO crystal, (001) surfaces can be easily obtained by cutting the crystal with a knife edge parallel to a (001) plane. This procedure is in general referred to as *cleaving*. For the experiments described in chapter 5,6,7 and 8 high quality (001) surfaces were obtained by cleaving a NiO single crystal *ex-situ*<sup>1</sup>.

After introducing the samples into the UHV system the surfaces had to be cleaned from adsorbates. This was achieved *in situ* by ion beam etching or so called sputtering and annealing. Sputtering was performed using Ar<sup>+</sup> ions with a kinetic energy between 0.5 and 1.0 keV. During this procedure the base pressure of the chamber was typically better than  $5 \cdot 10^{-10}$  torr while the Ar<sup>+</sup> partial pressure was kept around  $0.5 \cdot 10^{-6}$  torr. Surface annealing took either place at moderate temperatures (400K) for 10 to 15 hours or at higher temperatures (900K) for 2 hours in an oxygen atmosphere ( $10^{-6}$  torr). The influence of the different cleaning methods onto the magnetic structure will be discussed in chapter 5, while the stoichiometry and the structure of the surface is described in the following section.

#### 4.1.1 Surface Structure

The crystallographic structure of the surface was characterized by Low Energy Electron Diffraction (LEED). The pattern detected on all types of surfaces showed the cubic symmetry of the surface, but the annealed samples in general showed sharper diffraction spots and higher order LEED spots could be observed. This indicates that sputtering introduces surface defects and increases the surface roughness, while annealing decreases the roughness and increases the order. Figure 4.1 shows LEED patterns obtained at 61.2, 76.5 and 147.5 eV from an annealed surface. Images at lower electron energies could not be acquired due to charging of the NiO surface. The images show 2nd and 3rd order (110) and 1st to 3rd order (100) spots. The in-plane lattice constants determined from these images are 4.22 and

---

<sup>1</sup>All the crystals were supplied by Mateck GmbH, Germany [www.mateck.de](http://www.mateck.de).

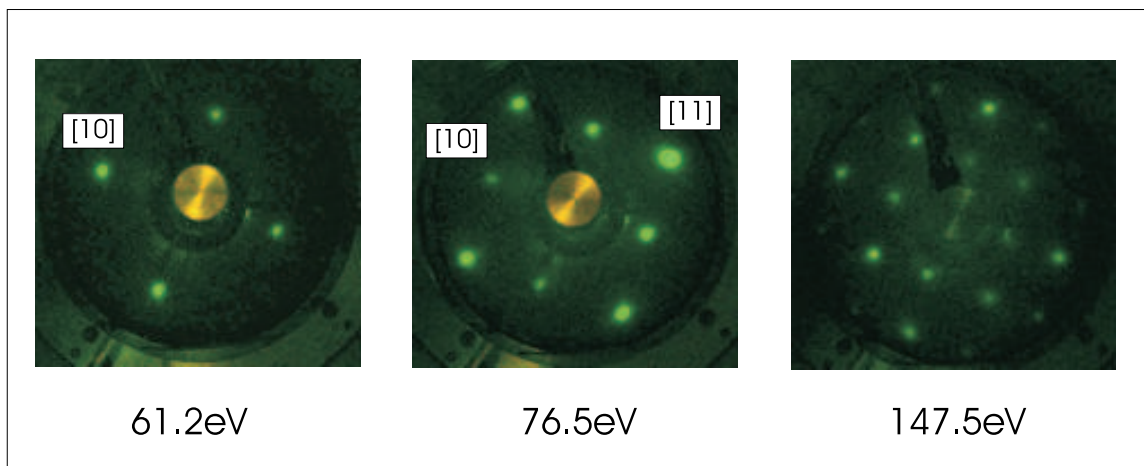


Figure 4.1: LEED of NiO(001) Surface.

LEED pattern at different electron energies of the NiO(001) surface obtained after several cycles of sputtering and annealing in an oxygen atmosphere. LEED spots corresponding to in-plane [10] and [11] directions are marked.

6.28 Angstrom, which is in good agreement with lattice constants determined from x-ray diffraction.

Another indication that sputtered surfaces are richer in defects than surfaces annealed with or without oxygen is the fact that annealed surfaces tend to increased charging in the LEED and in the PEEM instrument. Due to the decreased number of defects on the annealed surface the resistivity of the NiO increases. Note that NiO is in principal a perfect insulator with a band gap of 4eV and that any conductivity across the surface is introduced by defects.

#### 4.1.2 Surface Chemistry

The influence of the preparation method onto the chemical structure of the NiO(001) surface was characterized by X-ray absorption. The spectra obtained from image sequences using PEEM2 for the different surfaces are shown in figure 4.2. All spectra were normalized by subtracting a constant background and dividing the electron yield by the integrated intensity. The black spectrum was taken after annealing at 400K, the black one after subsequent sputtering and the green one after finally annealing the sample at 900K in  $10^{-6}$  mbar oxygen. The main differences between the spectra are larger peak intensity (indicating higher oxidation state of the metal ion) and more pronounced multiplet structure especially for the  $L_2$  peak. The spectra of annealed samples look very similar, nevertheless the resonances themselves are slightly better pronounced after annealing at higher temperature in oxygen atmosphere. The multiplet contrast and the peak intensity observed for the sputtered sample are significantly smaller than for the annealed one. X-ray absorption shows that sputtered surfaces are richer

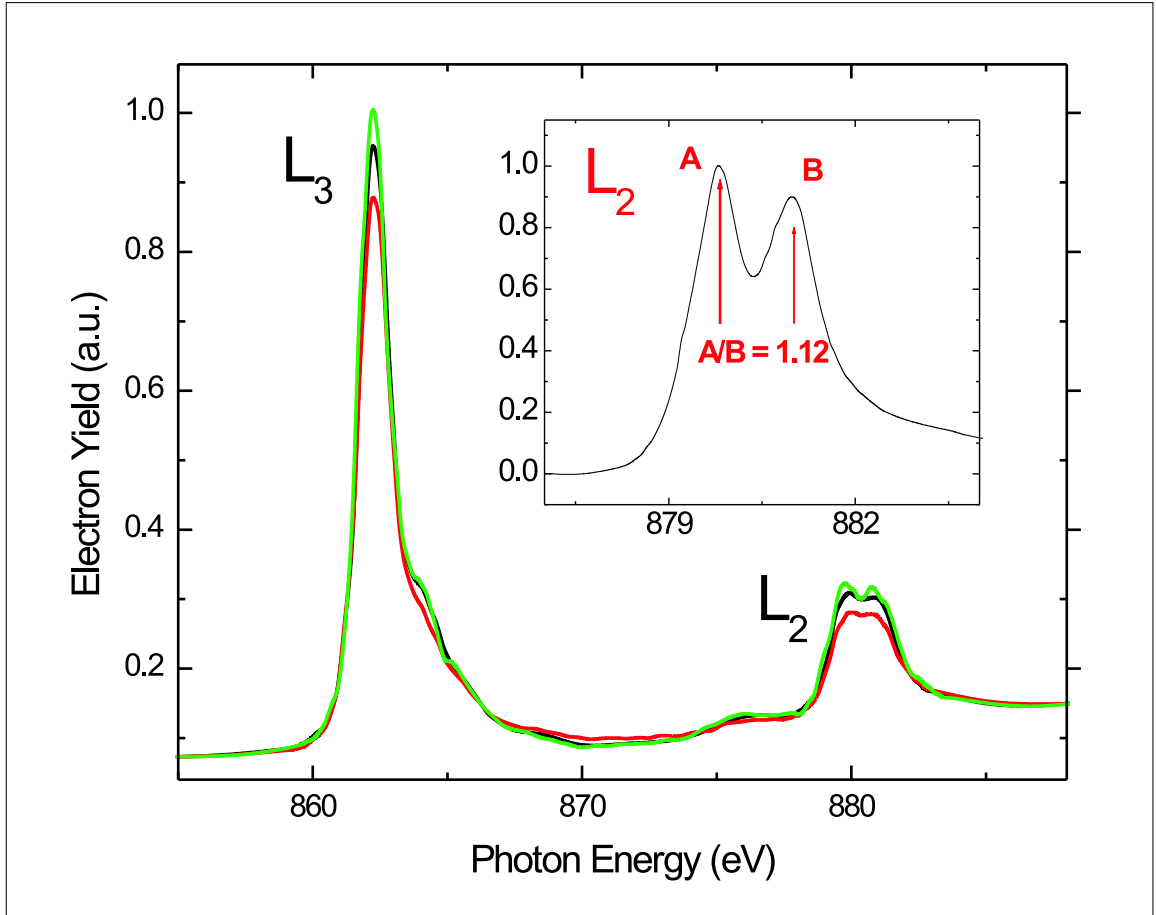


Figure 4.2: XAS of Sputtered and Cleaved NiO(001) Surfaces.

The effect of annealing and sputtering on the surface. A distinct multiplet structure in L<sub>3</sub> and L<sub>2</sub> is observed in the XAS spectra after cleaving (black spectra). After sputtering the multiplet peaks in the L<sub>2</sub> peak are less pronounced and absorption intensity between the resonances is increased (red). The multiplet features even at the L<sub>3</sub> resonance are reestablished by annealing in an oxygen atmosphere (green). The inset shows a high resolution L<sub>2</sub> XAS spectra of a cleaved sample (beamline 10-1 at the Stanford Synchrotron Radiation Laboratory). The ratio of the intensity of the two multiplet peaks A and B is measured (1.12). The same ratio is determined for the NiO spectra measured with PEEM at lower energy resolution after annealing in oxygen atmosphere.

in defects and hence their stoichiometry and chemical structure is stronger disturbed. This is consistent with the LEED results.

'Pronounced multiplet structure' in this context means that the two absorption peaks within the  $L_2$  resonance forming the multiplet are more or less separated. Increasing metallic character causes the multiplet structure to vanish, because the spectral features are superimposed by the broader metallic Ni L edge, which appears at the same energy as the first peak in each the  $L_3$  and the  $L_2$  multiplet. All of these features are shown to be directly linked to the chemical and crystallographic structure in section 2.3.2, where it has been concluded that a pronounced multiplet peak structure an increased peak intensity and a decreased absorption intensity between the peaks are related to the formation of stoichiometric and well ordered NiO.

Results obtained on single crystal surfaces shall finally be compared to results obtained on thin films by Alders *et al.* [1, 2]. It needs to be corroborated that the chemical and structural properties of the NiO(001) surface is the same as in the thin film samples studied by Alders *et al.* To address this issue the isotropic XMLD signals are compared. The XMLD signal was defined by the ratio between the normalized absorption intensities of the two multiplet peaks in the  $L_2$  resonances in equation 2.14. The XAS spectra of a single crystal, obtained from a large area ( $1\text{mm}^2$ ) shows no dependence on the angle of incidence or the direction of the incoming polarization and for this reason the isotropic spectrum can be obtained from such a magnetic isotropic sample. The inset in figure 4.2 shows the spectrum obtained at the NiO  $L_2$  resonance, acquired at beam line 10.1 at SSRL in normal incidence. This setup provides very high energy resolution comparable to the experiment performed by Alders (0.4 eV). The intensity ratio determined at room temperature is determined as 1.12 the same values observed by Alders *et al.* and therefore both NiO samples, thin films on MgO and single crystal exhibit comparable electronic as well as magnetic properties. This is further corroborated by the fact that the Néel temperature is 520K in both systems.

## 4.2 Thin Films

Thin ferromagnetic films were prepared on top of single crystal NiO(001) to study the antiferromagnetic/ferromagnetic exchange coupling. A comparable but polycrystalline sample was prepared by sputter deposition to address the exchange bias effect. Finally thin metal films were prepared on NiO surfaces to describe the chemical reaction at the metal oxide interface. The preparation conditions are listed in the following.

### 4.2.1 Sputter Deposited Exchange Biased Co/NiO

For the hysteresis measurements described in chapter 8.3, exchange biased samples consisting of 3nm Co on 50nm NiO were prepared by DC magnetron sputtering at room temperature onto an oxidized silicon surface (Matt Carey, IBM Almaden Research Center). The oxide film has been sputtered reactively from a Ni target in a 1.2 mbar oxygen atmosphere. The entire structure was grown in an applied magnetic field to introduce the unidirectional anisotropy.

The films were capped with 2nm of Platinum to prevent oxidation of the Co metal.

### 4.2.2 Electron Beam Deposited Metal Films

For the microscopy studies thin ferromagnetic films (3-20 monolayer) have been deposited from a rod of high purity material ( $> 99.99 + \%$ ) onto the clean NiO(001) surfaces by means of electron beam evaporation. The deposition rate was typically about 0.1 nm per minute and the base pressure in the preparation chamber of the PEEM2 experiment was better than  $10^{-9}$  mbar. The metal surfaces did not show any LEED pattern indicating the polycrystalline growth of the ferromagnetic film. Magnetically ordered Fe or Co films could not be observed below a film thickness of 0.8nm possibly due to roughness of the cleaved surfaces which show step edges resulting from the cleavage process along  $[110]^2$ . The samples were finally transferred from the preparation chamber directly into the microscope without breaking the vacuum and contamination of the surfaces.

The chemical reaction at the metal/nickeloxide interface has been studied at the dedicated x-ray absorption spectroscopy beamline 10-1 at the Stanford Synchrotron Radiation Laboratory (see chapter 8.1). A different setup had been chosen for this experiment because it provides a higher photon energy resolution ( $E/\Delta E = 7000$  compared to 1500 for PEEM2), which is needed to detect small changes in the x-ray absorption line shape and quantitatively analyze the resulting spectra. For the studies thin films of Fe and Co (0-2nm) were deposited in the same way as for the microscopy experiment. This has been done at a base pressure of  $5 \times 10^{-10}$  mbar. For these studies other oxide substrates were grown as well, which are not discussed here. A detailed description of these experiments can be found in Ph. D. thesis of T.J. Regan [69, 68]. The particular results obtained on the NiO(001) surface are presented in chapter 8.1. They were obtained in collaboration with T.J. Regan.

---

<sup>2</sup>In principle high quality and smooth Fe and Co films can be grown on metal oxide surfaces like for example MgO which has a similar structure as NiO. For this purpose the MgO surface has to be prepared appropriately by etching and annealing above 1000K in an oxygen atmosphere of  $10^{-6}$ mbar to ensure atomically flat and stoichiometric surface.



## Chapter 5

# Antiferromagnetic Domain Pattern on NiO(001)

In this chapter the antiferromagnetic domain structure of cleaved NiO(001) surfaces, which were either cleaned by sputtering or by annealing is described. For this purpose XMLD images of NiO(001) are obtained for different angles  $(\theta, \phi)$  (see figure 2.2) between the electric field vector and the [100] crystal axis.

The initial experiments were performed using the commercial STAIB PEEM on sputtered NiO surfaces. The elliptical undulator beam line UE56/1 at the BESSY2 synchrotron provided horizontally and vertically linear polarized x-rays. From the qualitative dependence of the AFM contrast on the angle  $(\theta, \phi)$  general information about the symmetry of the magnetic arrangement are extracted. A determination of the exact direction of the magnetic axes in each domain with respect to the crystal axes was not achieved in this setup, since no local x-ray absorption spectra could be acquired (see chapter 2.2.3).

The following experiments used the PEEM2 microscope at the ALS in Berkeley (USA). In a first step the qualitative results obtained on sputtered surfaces were corroborated using this setup. However, the focus of the experiments was the characterization of cleaved surfaces that involved a detailed analysis of the x-ray absorption line shape originating from each AFM domain. Since the instrument is located at the ALS bending magnet beam line 7.3.1.1. the lack for straight forward manipulation of the x-ray polarization had to be compensated for by using circular polarization referred to as *mixed* polarization (see chapter 2.1). The ability to acquire reliable local spectra in each antiferromagnetic domain and the high lateral resolution of the microscope finally allowed for a precise determination of the magnetic axes in each antiferromagnetic domain.

To suppress image contrast arising from the topography of the surface, all the antiferromagnetic domain images presented here are obtained by calculating either the asymmetry or the ratio of two images acquired at the two peaks A and B of the NiO  $L_2$  multiplet. The energies were determined prior to the microscopy experiment using the total electron yield technique in the same setup.

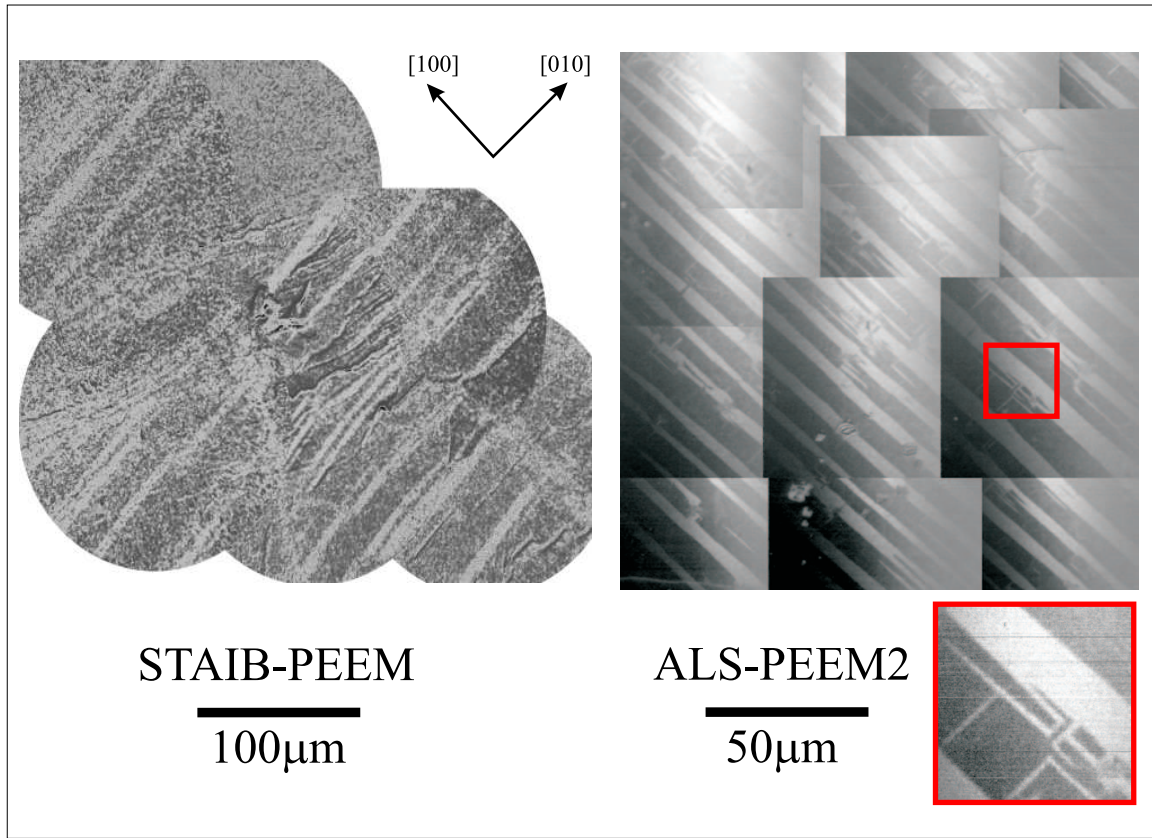


Figure 5.1: Domain Topology of NiO(001)

Large scale domain images on NiO(001). The image on the left was acquired with the STAIB PEEM using horizontal polarization, the one of the right with the ALS PEEM2 using mixed polarization. In both images antiferromagnetic domains separated by domain walls parallel to [100] directions are detected. The red circle indicates a region where (100) and (010) walls can be seen. The resolution of the ALS PEEM2 (20-50 nm) is typically better than the one achieved with the STAIB PEEM (150 nm) using synchrotron radiation. Since the x-rays are horizontally focussed to less than 30  $\mu\text{m}$  into the ALS PEEM2, the illumination appears inhomogeneous within the field of view (FoV) of 50  $\mu\text{m}$ . The size of the x-ray spot at the BESSY2 setup was comparable to the FoV

## 5.1 Sputtered Surfaces

### 5.1.1 Domain Topology on Sputtered Surfaces

Representative images of the domain structure over a large scale are shown in figure 5.1. Several domain images were acquired at different positions and were then stitched together into one picture covering a large field of view. The left image shows such an image acquired using the STAIB PEEM. The right image was obtained using the ALS PEEM2. In

both images dark and bright stripes can be seen, representing regions with different XMLD signal and therefore different antiferromagnetic domains. The width of the stripes reaches from about  $5 \mu\text{m}$  up to more than  $50 \mu\text{m}$  and they extend over hundreds of microns. This is in accordance with results obtained in the bulk of the material [71]. All stripes run along [100] directions and they are separated by walls parallel to (100) planes. Note, that this is an indication that the observed antiferromagnetic contrast is correlated with the bulk antiferromagnetic T-domain structure, because [100] planes represent low energy T-domain walls. (110) domain walls could never be observed on sputtered surfaces.

In each composite image one type of (100) wall dominates and only on a smaller length scale  $90^\circ$  antiferromagnetic walls are observed. Such an area is shown in the ALS-PEEM2 image on the lower right with higher magnification. This behavior is also observed, although less prominent, on annealed surfaces. A possible reason is that the pressure applied to the entire crystal during the cleavage process induces a particular stress pattern. Annealing at moderate temperatures (below 1000K) can not completely relax the lattice and certain antiferromagnetic domains are then stabilized by the particular lattice deformation

### 5.1.2 AFM Axes on Sputtered Surfaces

#### Horizontal versus Vertical X-ray Polarization

To address the observed contrast in more detail figure 5.2 shows two domain images acquired with horizontal or vertical linear polarization of the incoming x-rays. The horizontal polarization lies completely in the surface plane while the vertical polarization inclines an angle  $\theta$  of  $15^\circ$  with the surface normal. In the image acquired using horizontal polarization black and white stripes running along [100] direction can be recognized representing presumably the antiferromagnetic domains.

A single image stack has been acquired using the STAIB PEEM setup. The resulting spectra show the typical XMLD behavior. This finally corroborates the assumption that the stripes observed in the PEEM images do indeed correspond antiferromagnetic T-domains that means areas with different orientation of the antiferromagnetic axis. Another indication for this conclusion is that the observed contrast disappears above the antiferromagnetic ordering temperature of 525K, as reported in [32, 105].

No antiferromagnetic contrast is observed if the incident x-rays are polarized vertically. Hence there is no variation in the antiferromagnetic out-of-plane axes on sputtered NiO(001) surfaces or at least it is too small to be detected. In the following an estimate for the angle between the in-plane axes will be given, from which the maximal out-of-plane sensitivity can be calculated leading to the conclusion that indeed the antiferromagnetic axis is completely parallel to the surface plane.

Altogether, qualitative results obtained using the STAIB PEEM or the ALS-PEEM2 are comparable. In both cases no out-of-plane component of the antiferromagnetic axis is observed. Images obtained with the ALS-PEEM2 with mixed polarization show qualitatively the same domain pattern as the one observed with horizontal polarization indicating that there is no image contrast arising from the additional vertical polarization component.

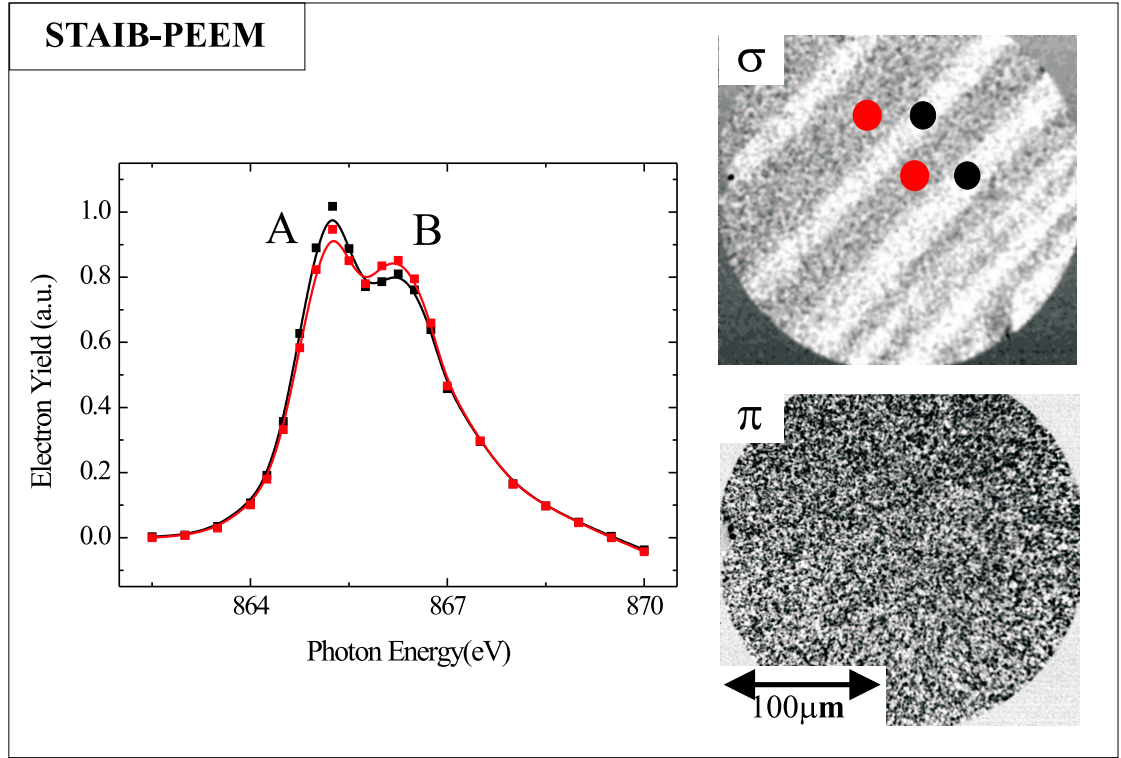


Figure 5.2: Domain Topology of Sputtered NiO(001)

Domain topology of sputtered NiO(001) surfaces imaged using the STAIB PEEM. Black and white areas represent areas with different orientation of the antiferromagnetic axis. The spectra were acquired by moving the incident photon energy over the  $L_2$  resonance and taking an image at each energy. The domain images are the result of the division of images taken at peak A and B. Antiferromagnetic contrast is observed if the x-rays are polarized parallel to the surface (horizontal polarization), while no contrast is observed if the electric field vector is oriented at an angle  $\theta$  of  $15^\circ$  (vertical polarization).

### Azimuthal Dependence of the XMLD Intensity

Finally, an estimate for the angle between the in plane projection of the two antiferromagnetic axis is given. For this purpose six images of the same spot have been acquired for different azimuthal angles  $\varphi$  shown on the bottom of figure 5.3. The field of view was  $220 \mu\text{m}$  in all images. Two values have been calculated from these images. The first value is the average XMLD intensity in each image yielding information about the average orientation of the antiferromagnetic axis in the field of view. The second value is the difference between the XMLD intensity originating from the two antiferromagnetic domains appearing dark and bright in the images. This number is correlated to the angle between the antiferromagnetic axes in the two domains. The azimuthal dependence of the average XMLD intensity (left) and the domain XMLD contrast (right) is shown in the top row of figure 5.3. The lines were

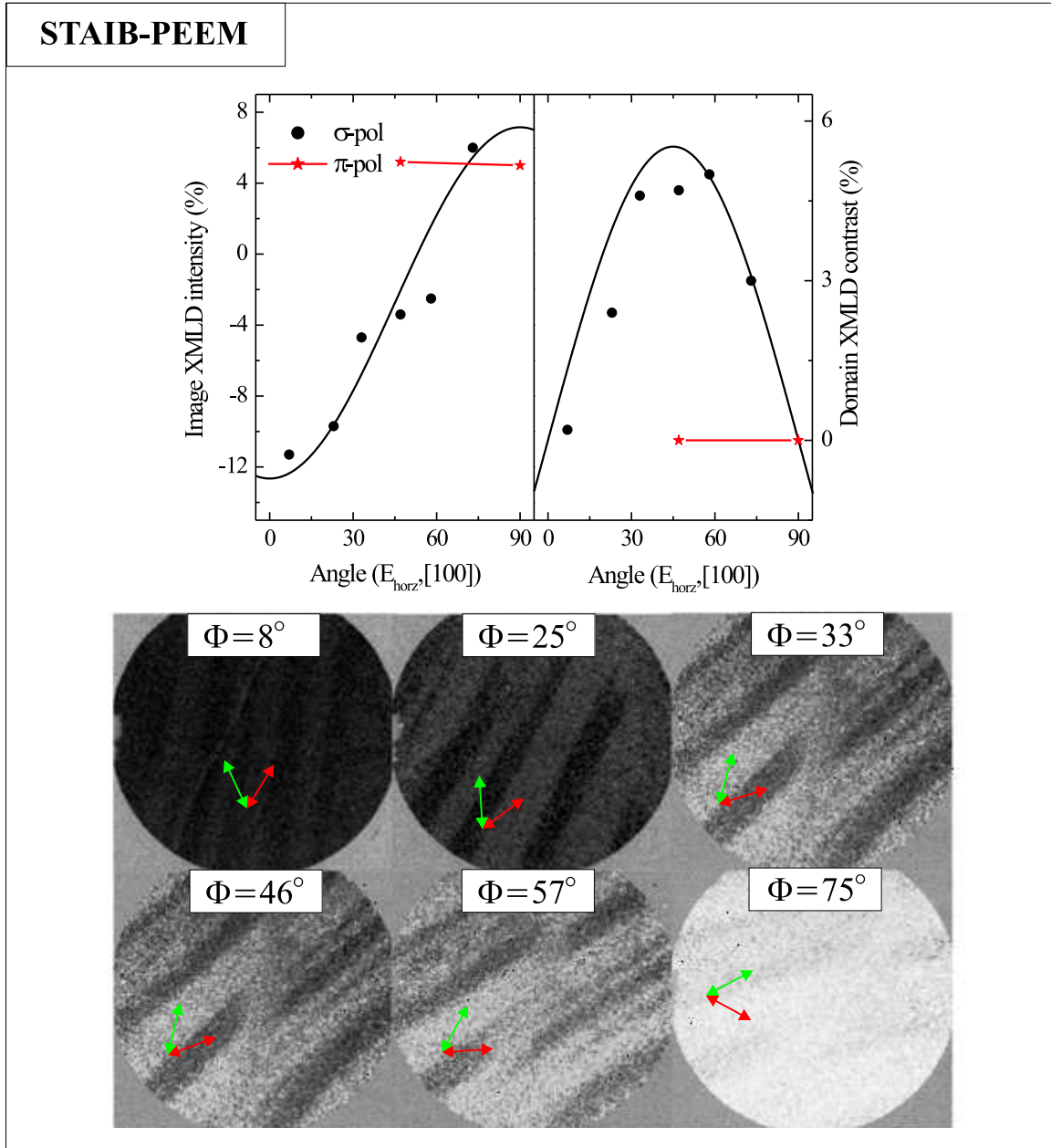


Figure 5.3: Angular Dependence of Contrast on Sputtered NiO(001)

Bottom: XMLD images acquired for different azimuths  $\phi$ . Red and green arrows indicate the supposed orientation of the antiferromagnetic axis.

Top: The left graph shows the XMLD intensity averaged over each image. The top right graph shows the difference in XMLD intensity between the two observed AFM domains in each image. All images were scaled identical so that gray scales are comparable.

fitted by employing the  $\cos^2 \varphi$  dependence of the XMLD effect and a  $\sin(2\varphi)$  dependence of the contrast between two antiferromagnetic domains.

The images as well as the graphs show that the antiferromagnetic contrast between two domains vanishes if the electric field vector is parallel to a [100] crystal axis, which means that the antiferromagnetic axes are oriented symmetrically with respect to this axis. The second observation is that the average XMLD intensity strongly depends on the azimuthal angle as well causing the overall image intensity to shift from a darker gray scale to a much brighter one. This finding indicates that the antiferromagnetic axes do not include an angle of exactly  $45^\circ$  with the domain wall or in other words the angle between the two antiferromagnetic axis differs significantly from  $90^\circ$ . From a comparison of the sign of the average XMLD intensity to the results obtained by Alders *et al.* it follows that the antiferromagnetic axes are oriented more vertically in the image obtained at  $\varphi = 8^\circ$ , while they are oriented more horizontally in the last image of the series.

Altogether the orientation of the antiferromagnetic axes in the two domains can be denoted  $[1bx]$  and  $[1\bar{b}x]$ , where  $x$  represents the out of plane component and is supposed to be small, while  $b \gg 1$ . The antiferromagnetic axes include a small angle with the propagation direction of the domain wall and the projection onto the wall plane is large. This is indicated by the arrows in the figure which sketch the orientation of the antiferromagnetic axis.

### In-plane versus Out-of-plane orientation

An estimate for the angle  $\alpha$  between the antiferromagnetic axis and the wall plane can now be given using equation 2.16. The XMLD reference spectra of the cleaved surfaces and the thin films cannot be used here since the line shape of the x-ray absorption spectrum is distorted on sputtered surfaces. However, an upper limit for the constant  $C$  in equation 2.16 can be extracted from the azimuthal dependence of the average image intensity in figure 5.3. The average XMLD asymmetry for the six different images ranges from  $-12\%$  to  $6\%$ . These two values are now assumed to be the maximum XMLD intensities for parallel and perpendicular alignment of electric field vector and antiferromagnetic axis on sputtered surfaces.

The azimuthal dependence of the XMLD difference is shown in the right panel of figure 5.3, it reaches a maximum of about  $5\%$  for an angle  $\varphi = 45^\circ$ . For this particular geometry the antiferromagnetic axis includes an angle of  $45^\circ \pm \alpha$  with the electric field vector, because the antiferromagnetic axis in each domain is symmetric with respect to the (100) wall. The angular dependence of the XMLD intensity for these two domains can now be written similar to equation 2.16

$$I_{\pm}(\phi = 45^\circ) = 6\% - 12\% \cos^2\left(\frac{\pi}{4} \pm \alpha\right) \quad (5.1)$$

Following this expression a maximum contrast of  $I_{max} = I_+ - I_- = 5\%$  is observed if the antiferromagnetic axis include an angle of not more than  $\alpha = 10^\circ$  with the antiferromagnetic wall<sup>1</sup>. Considering that an angle of  $20^\circ$  between two antiferromagnetic axis corresponds to an

---

<sup>1</sup>Since the XMLD reference intensities used here represent lower limits, the value obtained for  $\alpha$  represents an upper limit.

XMLD contrast of 5% and that furthermore an XMLD contrast of about 1% can still be identified in a PEEM image (see figure 5.3 it follows that the angle which the antiferromagnetic axis form with the sputtered NiO(001) surface need to be smaller than  $5^\circ$ .

### 5.1.3 Summary on Sputtered Surfaces

Altogether the antiferromagnetic domain topology on sputtered surfaces can be described as follows [32]:

- Antiferromagnetic domains appear in form of stripes extending over hundreds of microns. The typical width of these stripes is of the order of  $5\mu m - 10\mu m$ .
- Domains are separated by (100) domain walls parallel.
- The observed domain walls are compatible with the bulk structure.
- The antiferromagnetic domains observed on the sputtered (001) surface are pure in-plane domains. The antiferromagnetic axis is close to a [130] direction, which includes the smallest angle with the domain wall plane.
- The antiferromagnetic axis within each domain is not compatible with the bulk structure [109, 108, 71].

## 5.2 Annealed Surfaces

The samples discussed in this section were obtained by cleaning the cleaved surfaces by annealing at 400K without oxygen. The results were reproduced on samples that were annealed at higher temperatures in  $10^{-6}$  mbar oxygen. As discussed earlier, the preparation at higher temperatures increases the chemical and structural order slightly. However, the changes are not as drastic as observed between the annealed and the sputtered surfaces.

The annealed surfaces were studied exclusively using the ALS microscope<sup>2</sup>. The angle between the antiferromagnetic axis and the electric field vector was changed by either rotating the sample around its surface normal or by changing the polarization from horizontal linear to circular. For each setting an image stack was acquired to determine the NiO  $L_2$  absorption spectrum originating from each antiferromagnetic domain. After normalization of the resulting absorption spectra the XMLD intensity was determined by dividing the intensities of the  $L_{2a}$  and  $L_{2b}$  peak by each other. The resulting values were compared to the values obtained by Alders et al. [3] to derive the angles between the incident horizontal and vertical electric field vector and the antiferromagnetic axis.

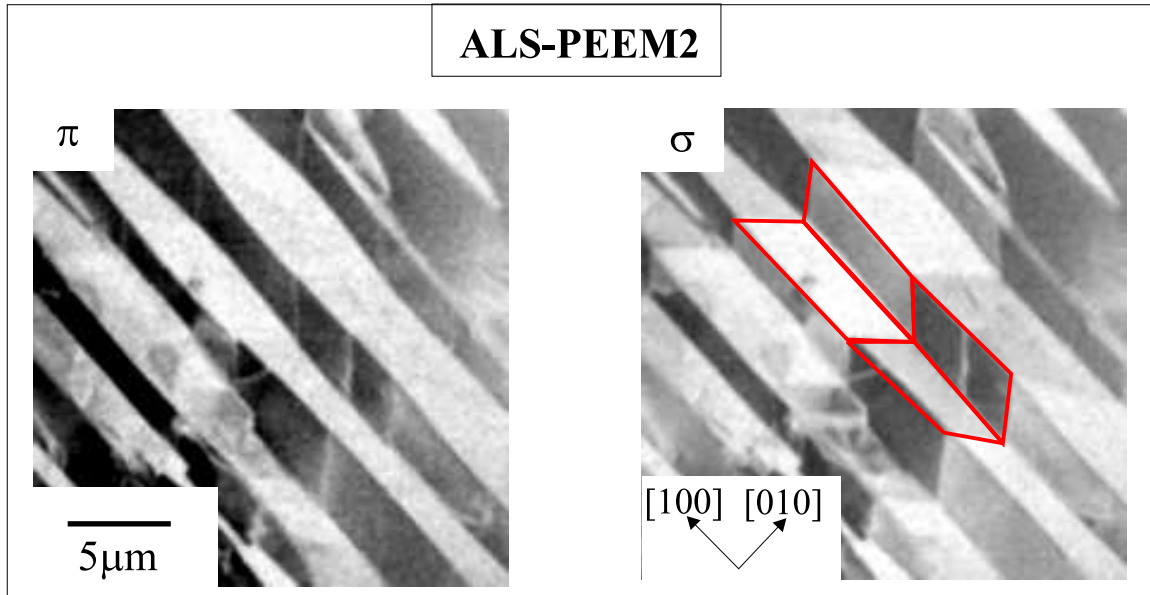


Figure 5.4: Polarization Dependence of AFM Domain Pattern

Two antiferromagnetic domain images acquired using linear polarization  $\pi$  (left) and mixed  $\sigma$  polarization (right). The crystal axes and the dimensions of the image are indicated in the insets. Only (100) domain walls are observed in the left images, while the right image also shows (110) walls.

### 5.2.1 In-Plane Versus Out-Of-Plane Axes

Figure 5.4 shows an example of two antiferromagnetic domain images obtained with the ALS PEEM2 using linear and mixed polarization. Both images were acquired at the same spot, the degree of circular polarization was 75%. The left image shows the distribution of the AFM axes imaged with linear polarization ( $\pi$ ). Because the electric field vector  $E_{\parallel}$  lies completely in the surface only the in-plane projection of the antiferromagnetic axis contributed to the observed contrast. The pattern itself is governed again by stripes running along [100] directions and separated by (100) walls.

Additional contrast appears in the images if the polarization of the incident x-rays is mixed ( $\sigma$ ). The annealed surfaces show a distinct lateral variation of the antiferromagnetic out-of-plane axis in contrast to the sputtered surfaces. Each in-plane domain is split into two domains with different projections of their antiferromagnetic axis on the vertical polarization vector  $E_{\perp}$  which forms an angle of  $\theta = 30^{\circ}$  with the surface normal in this setup. In other words each of the AFM in-plane domains is split into two different AFM out-of-plane domains. These two out-of-plane domains are separated by (110) walls.

Altogether it appears that the annealed NiO(001) surface shows a richer domain pattern

<sup>2</sup>Similar results obtained on *in situ* cleaved surfaces with the STAIB PEEM at BESSY2 were reported by Hillebrecht et al. [32] and can be found in the Ph.D. thesis of N.B. Weber [105]

than the sputtered surface with antiferromagnetic in-plane and out-of-plane domains and separated by (100) as well as (110) walls.

## 5.2.2 AFM Axes on Cleaved Surfaces

### Experimental Geometries

To determine the exact orientation of the antiferromagnetic axes on the cleaved NiO(001) surface, images with linear and mixed polarization were acquired in two different geometries. The geometries were chosen such that the in plane projections of the electric field vector and the [100] and [121] crystal axis are parallel, because these axes coincidence with symmetry directions in the bulk of NiO (see chapter 3). For this purpose it is assumed that the bulk S-domains are realized at the surface as well.

Since the (100) plane is supposed to be the plane with the highest symmetry the first images are acquired in an [100] geometry. From the XMLD intensities observed in this geometry with both types of x-ray polarization it can already be shown that only one type of S-Domain ([121]) but all four T-domains are observed. To determine the spin axis in each of the four T-domains images obtained in a [121] geometry from the same spot on the sample are finally analyzed.

### In-Plane Axis

Figure 5.5 shows an XMLD image obtained with linear polarized x-rays ( $\phi = 0^\circ$ ). In this configuration antiferromagnetic contrast arises only from a variation in the in-plane antiferromagnetic axis. Apart from some spot like defects and vertical lines no in-plane variation of the antiferromagnetic contrast is observed. The white lines coincidence with the direction of antiferromagnetic (100) walls as reported in section 5.1 and section 5.2.1 and are later identified as such.

XMLD spectra were obtained from image stacks on the homogeneous image area where no variation of the antiferromagnetic axis is observed. All spectra were normalized by subtracting a linear background so that the pre-edge and the post-edge intensity equals zero. The  $L_2$  ratio is now determined by dividing the absorption intensity at the two resonances at 870.2 eV and 871.5 eV and a value of 1.197 is obtained. To address the question whether the direction of the antiferromagnetic axis is similar as in the bulk the XMLD intensities that can be expected for the 12 different antiferromagnetic bulk axes (S-Domains) using pure linear polarization are calculated using equation 2.16. Here,  $\phi$  is the azimuthal angle  $\phi$  between  $E_{\parallel}$  and the [100] axis. The angular dependence is depicted in the lower left of figure 5.5. The curves show a  $\cos^2$  dependence with different amplitudes and vertical as well as horizontal offsets. The purple horizontal line indicates the XMLD intensity determined in the experiment. Four S-domains ([211]) lead to a significantly different XMLD intensity (0.99) than observed in the image, while the other eight values are close (1.185) to the experimental value. The ([211]) domains exhibit a larger projection onto  $E_{\parallel}$  in this geometry than the [121] and [112] domains and are oriented more horizontally in the XMLD image.

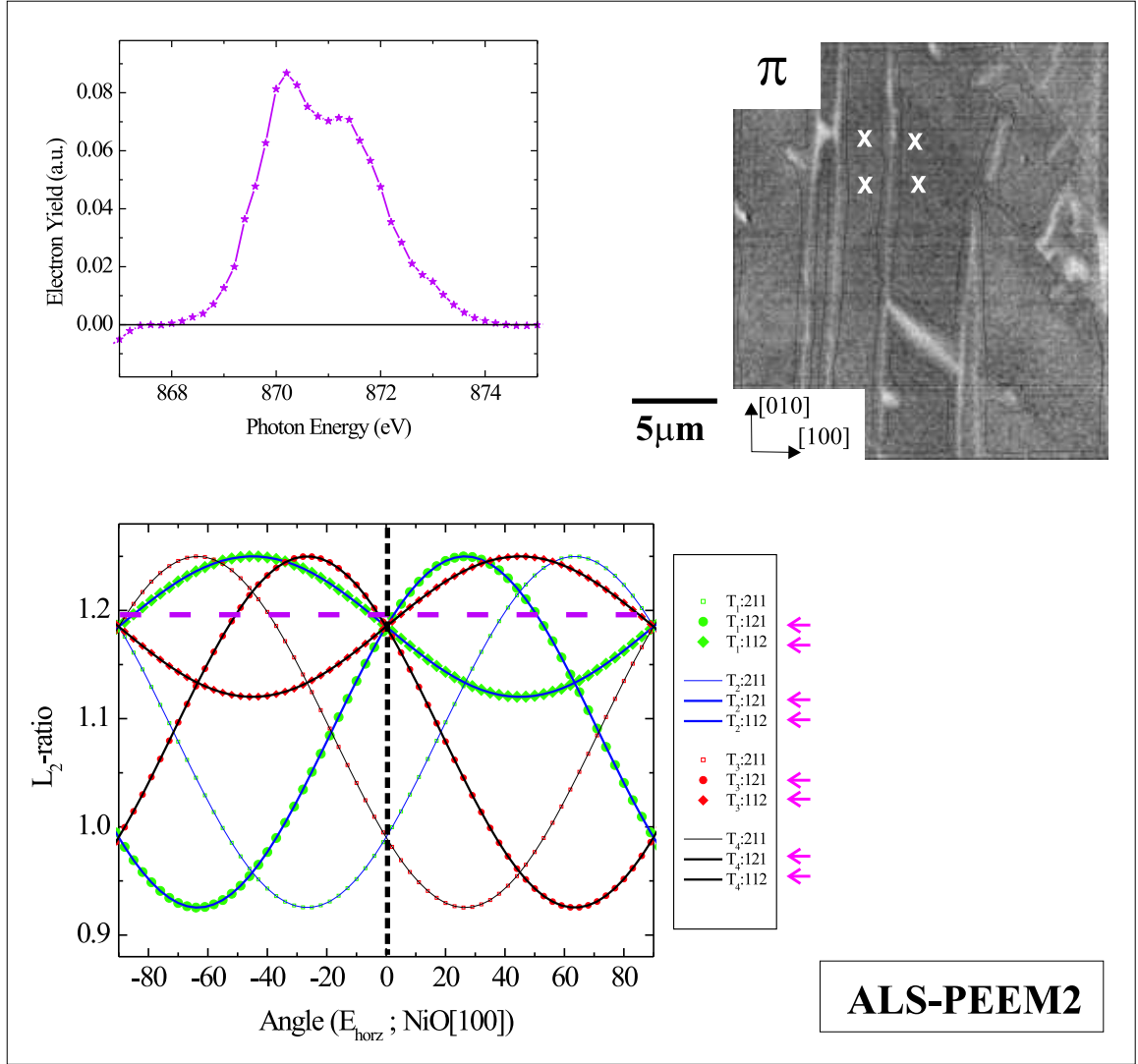


Figure 5.5: In-Plane Domain Pattern on NiO

An XMLD image obtained with linear polarization  $E_{\parallel}$  parallel to the in plane  $[100]$  crystal axis. The vertical lines coincident with  $(100)$ -type in-plane domain walls as shown for example in figure 5.4. NiO  $L_2$  image stacks (upper left) were acquired in the homogenous image areas indicated by a white 'x' and an XMLD intensity of 1.197 was derived.

The expected XMLD intensities (from eqn. 2.16) for the twelve bulk S-domains depending on the azimuthal angle  $\phi$  are shown on the lower left. The experimental geometry  $\phi = 0^\circ$  is indicated by a black line. In this geometry four domains ( $[211]$ , small symbols and thin lines) lead to an XMLD intensity of 0.99 and can be ruled out. The expected XMLD intensity of 1.185 for the remaining eight domains ( $[121]$  and  $[112]$ ) is close to the experimentally derived value. These domains cannot be distinguished in this particular geometry.

The angle between the antiferromagnetic axis and  $E_{\parallel}$  is determined to be  $(66 \pm 5)^{\circ}$  using equation 2.16 from the experimental XMLD intensity. The deviation from the calculated angle for the remaining eight bulk S-domains (see table 5.1 is within  $3^{\circ}$  and for this reason the initial assumption that the bulk spin axes are realized at the cleaved NiO(001) surface appears reasonable and is further corroborated in the following geometry.

### Out-Of-Plane Axis

In a next step the variation of the out-of-plane component of the antiferromagnetic axis will be addressed to decide whether S-domains with a large ( $[121]$ ) or small ( $[112]$ ) projection of the spin axis are realized at the surface. Figure 5.6 shows an image from the same sample area as before but now acquired with mixed polarization. The image exhibits additional contrast arising from the fact that the angle between the spin axis and the vertical polarization component varies laterally. The observed out-of-plane domains form a zigzag pattern, where different domains are separated by  $(110)$  walls<sup>3</sup>.

The XMLD contrast observed with mixed polarization is now analyzed in the same way as in the previous section. Local absorption spectra were acquired in different out-of-plane domains (bright and dark areas). The resulting spectra are shown in the upper left of figure 5.6 and XMLD intensities of 1.215 and 1.143 are extracted from the spectra. Again, equation (2.16) can be used to determine the angle between the vertical polarization component  $E_{\perp}$  and the antiferromagnetic axis. For the bright domains an angle of  $(88 \pm 18)^{\circ}$  is determined, while  $(43 \pm 7)^{\circ}$  is found in case of the dark domains.

Finally the experimental XMLD signals can be compared to the ones expected for the remaining eight S-domains using equation (2.16). For this purpose only the eight bulk domains that were identified to exhibit the correct in-plane projection in the previous section are considered this time. These axes do indeed exhibit different out-of-plane orientation. The  $[121]$  axis are more parallel (inclination  $24.1^{\circ}$ ) to the (001) surface while the  $[112]$  are more perpendicular (inclination  $54.7^{\circ}$ ). Altogether this leads to a different angular dependence of the XMLD signal as shown in the bottom left of figure 5.6. The horizontal lines indicate the experimental XMLD values and the vertical line represents the angle at which the image was acquired. The theoretical angular dependence of the the  $[121]$  S-domain match closely with the experimental values, while the  $[112]$  axes would lead to significantly lower XMLD values. In general only T-domains consisting of a single S-domain, which exhibits a large projection of the spin axis onto the surface and the high symmetry T-domain wall are observed at the NiO(001) surface. In this case where the observed T-domain wall is parallel to the (100) plane the observed S-domain is of  $[121]$  type. In some areas of the surface also (010) T-domain walls are observed. In this case the spin axis of adjacent domains is of  $[211]$  type. The results obtained in the  $[100]$  geometry are summarized in table 5.1. The angles between polarization vector and spin axis that are expected for  $[121]$  bulk domains in the geometry realized in figure 5.6 are listed as well. The experimentally obtained angles between spin axis and

<sup>3</sup>Note, that these domains do not necessarily include different angles with the surface normal, because in the experimental geometry the x-rays incident on the sample under an angle of  $30^{\circ}$  and for this reason  $E_{\perp}$  is not parallel to the surface normal.

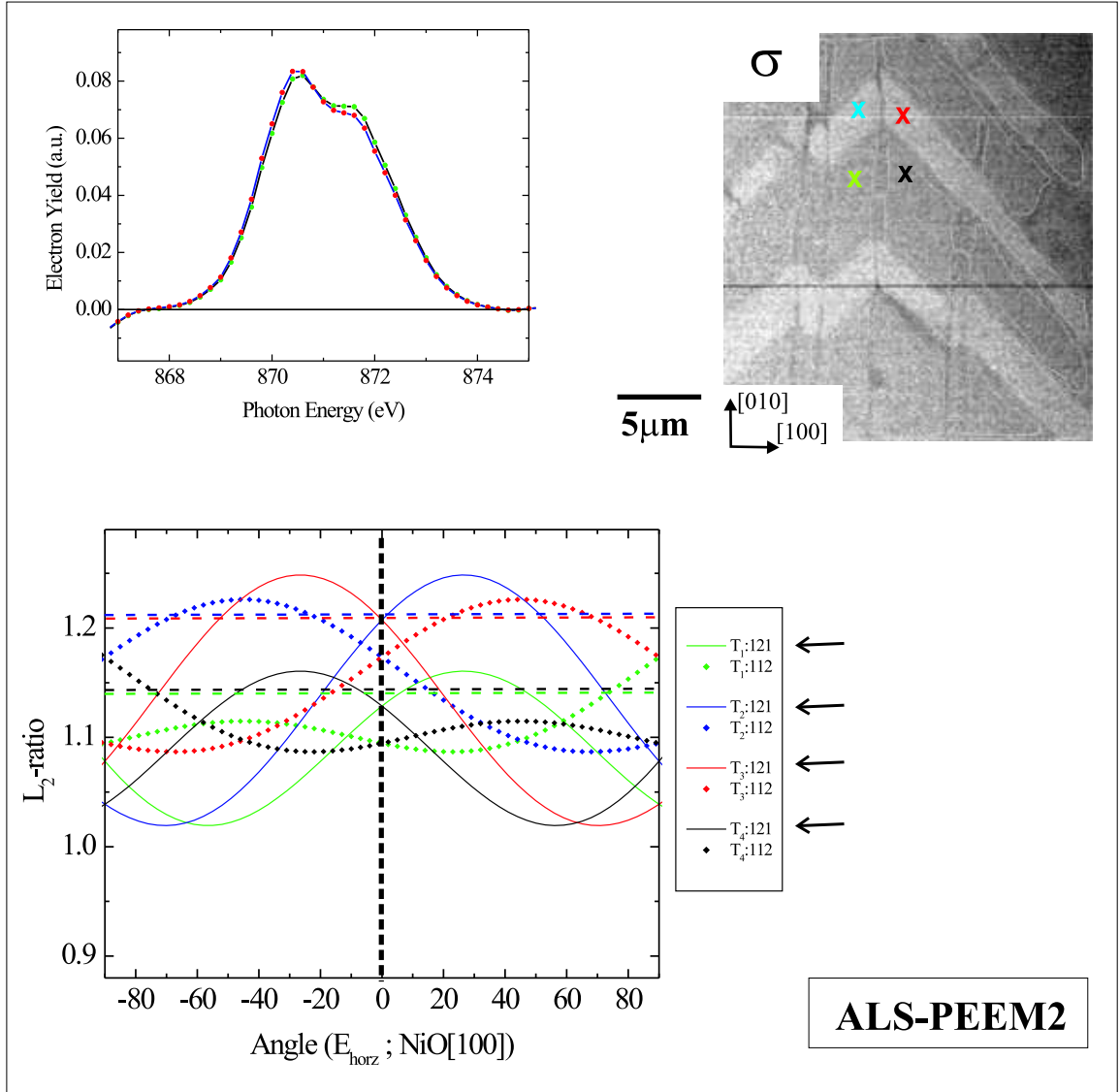


Figure 5.6: Out-Of-Plane Domain Pattern on NiO

XMLD images of the same spot as in figure 5.5 acquired using mixed polarization. Dark and bright areas forming a zigzag pattern are now observed in addition to the vertical (100) lines. The zigzag pattern is caused by a lateral variation of the out-of-plane component of the antiferromagnetic axis. From the XMLD intensities obtained in the two areas another (graph in the upper left) four S-domains ([112]) out of the remaining 8 can be ruled out. Experimental XMLD intensities are represented by the horizontal dashed lines, while theoretical values are drawn in full lines for S-domains with a large projection ([121]) or dotted lines for domains with a small projection ([112]) onto the (001) surface. Only domains with a large in-plane projection of the antiferromagnetic axis are realized.

AFM axis	Exp. pol.	pure $\mathbf{E}$	$L_2$	corr.	exp. Angle	theo. Angle
[121]	$\pi$	horz.	1.197	1.197	$68.4 \pm 5$	65.9
[ $\bar{1}2\bar{1}$ ]	$\sigma$	vert.	1.215	1.248	$87.4 \pm 18$	86.9
[121]	$\sigma$	vert.	1.143	1.043	$43.2 \pm 7$	41.4

Table 5.1: AFM Axes Determined from XMLD Signal and Comparison to Bulk Structure  
 The  $L_2$ -XMLD intensities as they are observed in the experiment for linear  $\pi$  and mixed  $\sigma$  polarization for different antiferromagnetic domains. The corrected values for pure linear polarization are calculated from equation 2.2 assuming a degree of circular polarization of 75%. The in-plane as well as the out-of-plane axes are finally calculated from equation (2.16). The last column gives the angle between the bulk axis and the polarization vector.

horizontal and vertical polarization vector are within  $2^\circ$  of the angles for the bulk structure. All observed S-domains exhibit the same projection onto  $E_{\parallel}$ , but they form different angles with the vertical polarization component  $E_{\perp}$ . S-domains with spin axes along [121] and [ $\bar{1}2\bar{1}$ ] can be assigned to antiferromagnetic domains appearing bright and dark in the image. These S-domains with a different out-of-plane spin axis are separated by (110) domain walls.

The experimental error of this *antiferromagnetic magnetometer* is mostly determined by the accuracy with which the XMLD intensity can be measured ( $\pm 0.010$ ) as well as the accuracy of the reference values in equation (2.16). Furthermore it has to be considered whether a given sample shows the same maximum contrast as the reference sample. For the out-of-plane component the accuracy with which the degree of circular polarization is considered as well. The accuracy actually depends on the angle between spin axis and electric field vector because the  $\cos^2$  function is rather flat at  $0^\circ$  and  $90^\circ$  and a small error in the XMLD accuracy causes a large error in the angle values. In the present context, this is relevant for the angle between [ $\bar{1}2\bar{1}$ ] axis and vertical polarization (an error of  $\pm 18^\circ$ ). This result in particular will be verified in the second experimental geometry.

### Solving the In-Plane Ambiguity

So far only the out-of-plane antiferromagnetic axis has been unambiguously assigned to a particular AFM domain. Due to the quadratic dependence of the XMLD effect, S-domains defined by different in-plane but the same out-of-plane spin axis, for example [121] and [ $\bar{1}2\bar{1}$ ], cannot be distinguished in the [100] geometry. For this purpose a second set of images and spectra for an azimuthal angle  $\varphi$  of  $25^\circ$  was obtained. The results are shown in figure 5.7.

First, the variation of the in-plane antiferromagnetic axis is addressed using pure linear polarization (top row of figure 5.7). The images obtained in the previous geometry are shown for comparison as well. In the second geometry, shown on the left, areas adjacent to the (100) wall become darker or brighter compared to the [100] geometry on the right due to the different projection of the AFM axis onto  $E_{\parallel}$  in each domain. The projection increases for [ $\bar{1}2\bar{1}$ ] or decreases for [121] type axes<sup>4</sup>. The expected dependence of the XMLD

<sup>4</sup>This finding finally proves the assumption that has been made in section 5.2.1 that the vertical lines do

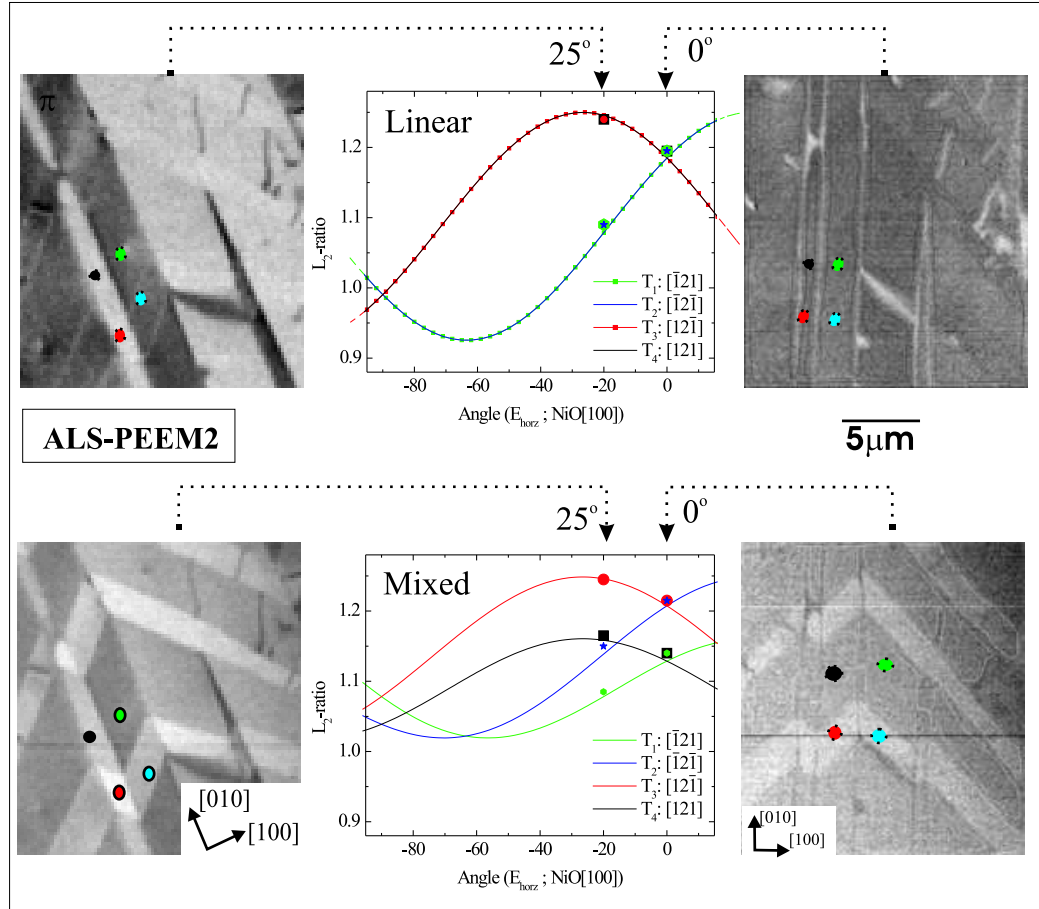


Figure 5.7: Solving the Ambiguity in an XMLD Image

Images obtained for azimuthal angles  $\phi = 25^\circ$  (left) and  $\phi = 0^\circ$  (right) are shown. Linear polarization was used for the images shown in the top row and mixed polarization for the bottom row. From the comparison of observed and calculated angular dependence of the XMLD intensity a particular [121] S-domains can be assigned to each of the four observed antiferromagnetic domains. The top row shows the result obtained for pure linear polarization, from which the in plane variation of the antiferromagnetic axis can be extracted. Using mixed polarization (bottom row) all four S-domains are finally distinguishable.

intensity originating from the two subsets of in-plane domains on the azimuthal angle  $\varphi$  is shown in the graph in the middle. The graph in figure 5.7 is a subset of the graph shown in figure 5.6. The XMLD intensities obtained from local spectra (not shown) match the theoretical curve and the in-plane antiferromagnetic axis can now assigned to each of the observed antiferromagnetic domains.

Finally, another image of the same spot was obtained using mixed polarization. The domain image is shown in the lower panel of figure 5.7. The purpose of this image is to corroborate the results and to verify the finding for the  $[12\bar{1}]$  domain for which the accuracy in the previous geometry was rather poor. The excellent agreement of the experimental XMLD values with the calculations supports the previous assignment for the  $[12\bar{1}]$  domain. All four  $[121]$  S-domains are realized and can be identified in the lower XMLD image in figure 5.7 by their four different grey scales or XMLD intensities. Each domain is labelled by a colored dot, corresponding to the color of its graph.

Altogether the angular dependence of the XMLD intensity observed in the four different areas on the NiO(001) surface is, within the experimental error, identical with the calculated dependence of the four different  $[121]$  bulk S-domains considering the particular experimental geometry. The four domains form a so called *four wall pattern*, where in plane domains are separated by a (100) wall and out-of-plane domains are separated by  $[110]$  type walls. The observed four wall pattern is described in detail in the following section.

### Surface Four Wall Pattern

A graphical representation of the findings on the NiO(001) surface is shown in figure 5.8. All four types of domains can be identified in the PEEM image. The sketch on the bottom of the figure illustrates the results obtained from the experiment. Note, that the spins drawn in the figure do only sketch the spin axis while the experiment does not resolve the spins themselves.

The planes drawn in the figure represent the wall planes between different T-domains and the ferromagnetic ordering planes within each T-domain assuming that the spin axes at the surface are parallel to the ordering (111) plane (see section 3). In addition the spin axis realized in the center of each domain wall is indicated. For this purpose the axis is assumed to be the common spin axis in adjacent domains following the bulk symmetry summarized in table 3.2. Based on this assumption one finds that the spins in the (110) wall are *perpendicular* to the wall plane, while the spins forming the (100) wall are aligned *parallel* to the wall plane. Considering again the bulk structure introduced in table 3.2 this means that the observed (110) walls correspond to the third type low symmetry T-domain wall which is not observed in the bulk. The most obvious difference between a bulk and a surface (110) T-domain wall is that they are rotated by  $90^\circ$  around the  $[001]$  direction, such that the spin axis is either parallel (bulk) or perpendicular (surface) to the wall plane. The low symmetry T-domain wall is observed between surface T-domains with the same in-plane antiferromagnetic axis but different out of plane axis, while high symmetry T-domain walls are observed between surface

---

indeed represent (100) antiferromagnetic domains walls.



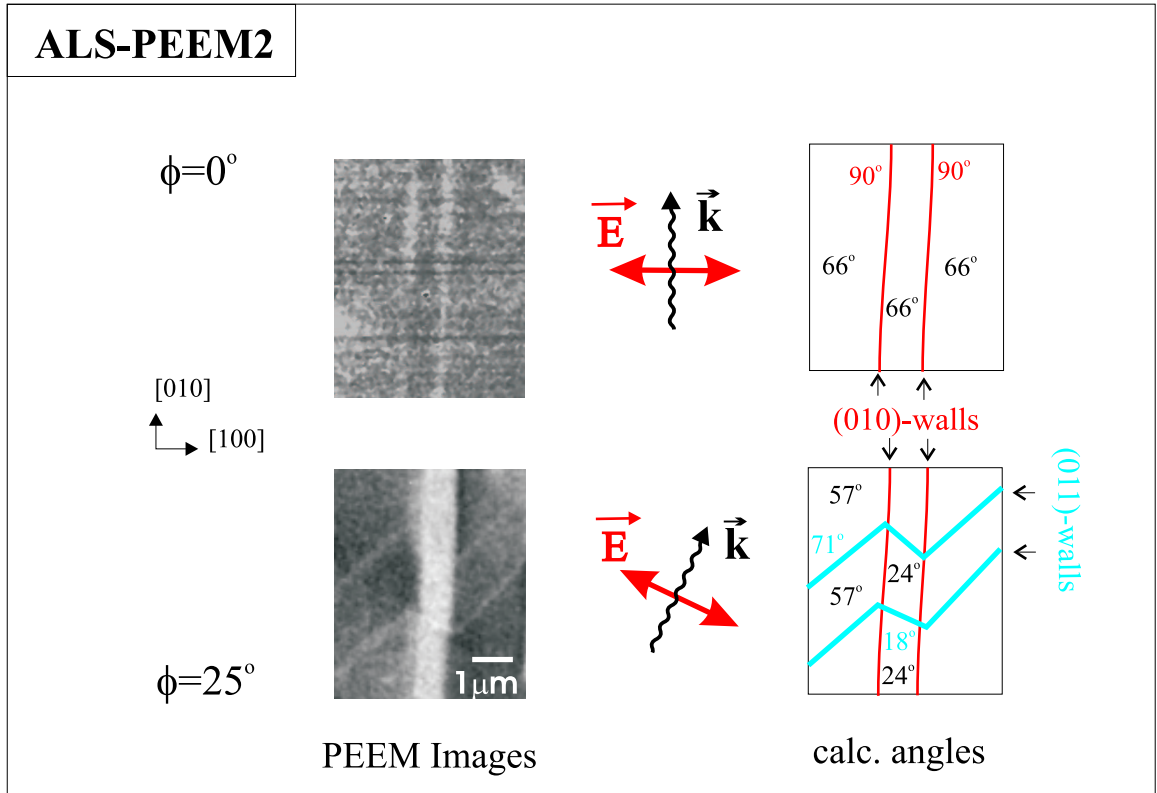


Figure 5.9: Domain Walls on the NiO(001) Surface

Two clippings of XMLD images obtained with linear polarization for  $\phi = 0^\circ$  and  $\phi = 25^\circ$ . The bottom image was rotated so that the orientation of the crystal axis is the same for both images. The direction of the incoming x-rays is indicated. The sketch on the right side shows the angle  $\alpha$  between magnetic axis and  $E_{\parallel}$  for each domain, the (100) wall and the two (110) walls assuming bulk like walls. Areas where the antiferromagnetic axis include a large angle with  $E_{\parallel}$  appear bright (larger XMLD values) in the images.

T-domains with different in-plane spin axis. The appearance of these new type of walls can thus be attributed to the symmetry breaking at the surface of the NiO single crystal, which affect the out of plane periodicity of the spin symmetry but not the in plane periodicity.

Before the structure of the surface wall is discussed it will be qualitatively shown that the spin axis in the observed (110) walls is indeed perpendicular to the wall plane, corroborating the assumption that the same spin axis is realized at the surface between two T-domains  $T_i$  and  $T_j$  as in the bulk. Using linear polarization (100) and (110) walls can be resolved in the XMLD images in the top row of figure 5.7. Figure 5.9 shows magnifications of the image area in figure 5.7 obtained in different geometries. For better comparison the images have been rotated such that the orientation of the crystal axis is the same in both images. The direction

of the incident x-rays is also shown. In the first geometry (upper image) only domain contrast originating from the (100) domain walls can be seen. In the second geometry contrast from the in-plane domain as well as from the domain walls is detected. The sketches on the right side show the domain wall pattern and serve as a guide to the eye. Furthermore, the angle  $\alpha$  between the antiferromagnetic axes in each domain or domain wall and  $E_{\parallel}$  is noted ( $E_{\parallel}$  parallel to  $[2\bar{1}0]$ ).

Because of the small lateral dimensions of the domain walls (100-200nm), no reliable local spectra from domain walls could be obtained. However, a qualitative evaluation of the observed contrast levels fully corroborates the assumption which has been made for the direction of the spin axes realized in the center of the domain wall. In the PEEM images areas with a larger angle  $\alpha$  between electric field vector and magnetization vector are represented by a brighter contrast. In the first geometry domain walls appear brighter than the domains itself, because their magnetic axis forms a larger angle  $90^\circ$  with the polarization vector than the one of the domains  $66^\circ$ . The same is true for one of the  $(\bar{1}10)$  domain walls observed in the second geometry  $71^\circ$  and  $57^\circ$ . The other wall can not be identified because change in XMLD contrast is too small to be detected ( $24^\circ$  and  $18^\circ$ ). In conclusion it can be ruled out that the spin axis in the (110)-type walls is parallel to the wall plane<sup>5</sup>.

### 5.2.3 Surface Domain Wall versus Bulk Domain Wall

The origin of the observed (110) walls and its extension into the bulk of NiO is discussed. The discussion will be restricted to qualitative arguments. It is important to notice upfront that a four wall pattern formed by (100) and (110) walls can also be observed in the bulk of the material [71], when the four different T-domains adjoin each other. This particular arrangement minimizes the stress pattern originating from the rhombohedral contraction.

#### Magnetically Uncompensated Walls

On the upper left of figure 5.10 the surface projection of the spins forming the observed four wall pattern is depicted. On the right, a cut along the (001) plane through the corresponding bulk four wall pattern is illustrated. Two main differences between the (110) walls are observed. First, every bulk domain wall represents a mirror plane but at the surface this is not the case. Second, all the spins in the center of the bulk domain wall point in the same direction such that the wall carries a net magnetic moment while the surface wall orientation assures that the wall does not carry a net magnetic moment. This situation is realized, because the domain wall is either orthogonal or not to the corresponding ferromagnetically ordered (111) planes defining the adjacent T-domains separated by the (110) type wall.

In conclusion the symmetry breaking at the surface would leave the otherwise compensated bulk like wall magnetically uncompensated and finally causes a magnetic stray field which increases the magneto static energy. The low symmetry (110) walls can therefore be

---

<sup>5</sup>A further discussion of the width and structure of the walls observed in this experiments can be found in the Ph. D. thesis of N.B. Weber [105]. In the context of this thesis it is important to consider that (110) walls appearing at the surface of NiO(001) are not necessarily high symmetry planes of the crystal.

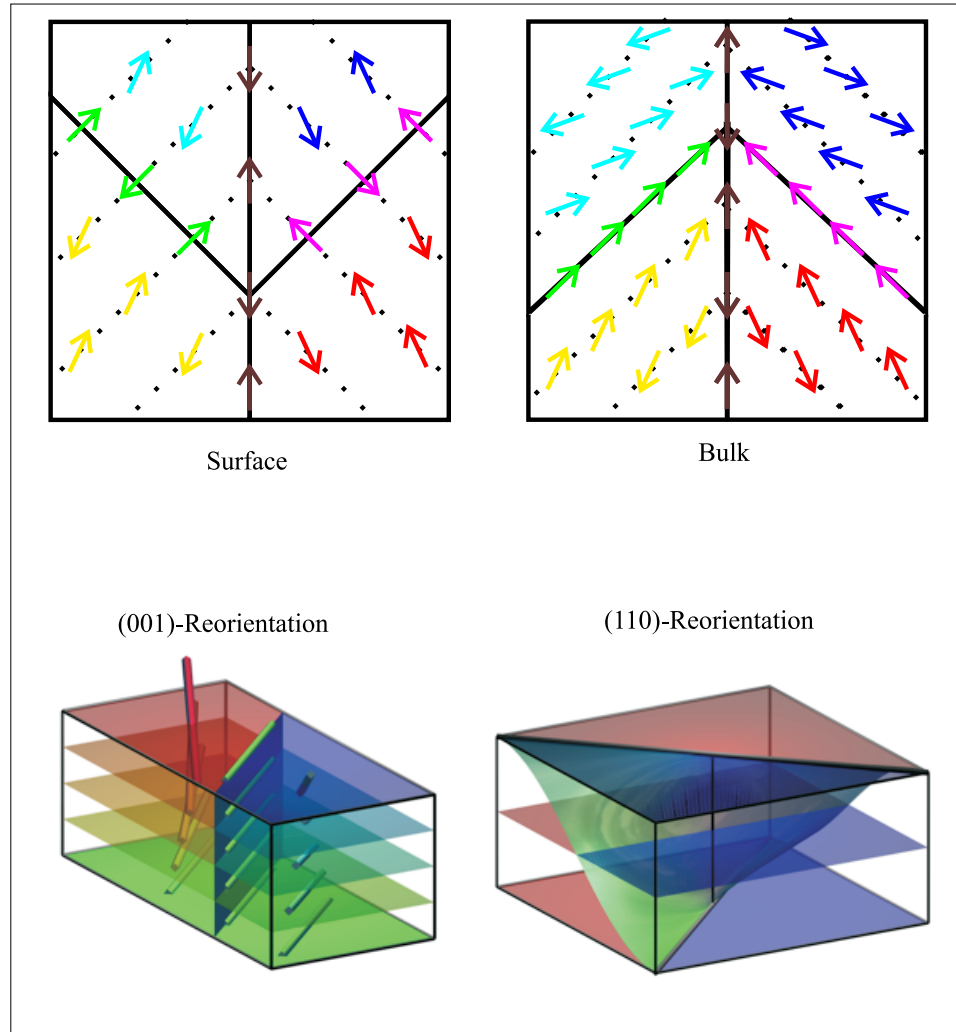


Figure 5.10: Surface and Bulk Domain Walls

Top: Projection of the magnetic axes of the observed domain pattern into the surface plane (left). On the right a cut along a (100) plane through a possible bulk four wall pattern is shown. Diagonal lines indicate the orientation of the (111) ordering planes.

Bottom: Possible bulk reorientation schemes of the observed surface domain walls. Green areas represent planes with a [110] type spin axis, while red and blue areas represent planes with different [121] type spin axis. The schemes are discussed in the text.

afforded at the surface to minimize magneto static energy originating from a net magnetic moment of a bulk like domain wall.

### Bulk Wall Reconstruction

The question remains how the observed (110) surface walls propagates into the bulk and why the surface domain pattern does not only consist of high symmetry (100) type walls avoiding (110) walls completely. Two possible ways to join the observed surface wall into a known bulk wall are shown in the lower part of figure 5.10. For this purpose it is considered that a particular surface (110) wall exhibits the same spin axis as the perpendicular high symmetry  $(1\bar{1}0)$  and (001) bulk wall (see table 3.2).

One possibility is to twist the wall plane around the surface normal by  $90^\circ$  until it reaches a bulk (110) orientation. This is illustrated in the right sketch and referred to as (110)-reorientation. The wall plane is shown in green and two particular antiferromagnetic domains separated by the wall are represented by red and blue areas. The different horizontal layers indicate different sample depths. To achieve this reorientation the wall plane has to continuously change its orientation into every direction parallel to the (001) plane. The translation area will then consist of many different highly non-symmetric walls. For this reorientation the spin direction in the adjacent domains is not affected.

The reconstruction shown on the lower left of figure 5.10 is referred to as (001) reorientation. Here the (110) wall does not change its orientation, but this time the spin direction in adjacent T-domains gradually changes towards the spin axis in the surface domain wall. Finally at a certain distance from the surface all spins are aligned parallel and a (001)-wall parallel to the surface is realized. This reorientation does not require any additional non-bulk like arrangements except the surface (110) wall itself and appears more likely. It can be understood as the reconstruction of a (001) wall at a (001) surface. The depth of this reorientation may be expected to be comparable to the typical wall width, i.e. 100nm. as observed for example in figure 5.5.

Since bulk walls always correspond to mirror planes a (001) T-domain wall can not be observed at a (001) surface because the surface is not a mirror plane. If now the crystal is cleaved close to an area where such a plane exists in the bulk the domain pattern has to be rearranged. The necessary rearrangement can be accomplished without generating magnetic stray fields by forming the observed surface specific (110) walls as illustrated in figure 5.10.

#### 5.2.4 Summary for Annealed Surfaces.

The findings on annealed surfaces are summarized in the following [62].

1. The antiferromagnetic axes observed on cleaved NiO(001) surface can be described assuming bulk axes.
2. Only a subset of bulk axes is observed at the surface, namely those with a large in-plane projection and a large projection on the (100) wall plane.

3. The spin structure of the observed (100) walls is bulk like, such that they form symmetry planes for the magnetic axis on each side of the domains wall. On the other hand surface specific low symmetry (110) walls are observed to reduce the magneto static energy.

The fact that only domains with an antiferromagnetic axis with a large in-plane projection are observed is in contrast to observation on thin NiO films grown on MgO(001) substrates<sup>6</sup>. In these films the preferred axes were found to be [112] exhibiting a large projection onto the surface normal. The reason for this behavior is most likely the fact that the lattice constant of MgO is slightly larger than the one of NiO and for this reason the film experiences an in-plane stress which forces the antiferromagnetic axes out-of-plane. In case of a single crystal which were usually well annealed during or after growth ( $\approx 1500K$ ) no overall stress should be present. However, it is a common observation that the symmetry breaking at the surface of a material causes a reorganization of the atoms at the surfaces and that the lattice constant deviates slightly along the surface normal. The observation that the preferred antiferromagnetic axis is in-plane may be therefore be caused by a lattice expansion parallel at the surface normal.

---

<sup>6</sup>The existence of domains with large out-of-plane components can not be in general excluded, but their fraction appears to be small because they have not been observed on the single crystal surface.



## Chapter 6

# Parallel Exchange Anisotropy in Co(Fe)/NiO(001)

Images of Co/NiO(001) were obtained using the same NiO(001) surface that has been analyzed in chapter 5.2. The Fe/NiO images originate from a different sample. The results reported here are reproducible above a minimum thickness of the ferromagnetic material of about 0.8nm (see chapter 4).

### 6.1 General Domain Pattern on Co/NiO and Fe/NiO

The general characteristic of the domain pattern on exchange coupled Fe/NiO and Co/NiO is described first. Figure 6.1 shows images of the ferromagnetic as well as the antiferromagnetic domain pattern after deposition of 10-12 monolayer of Fe or Co (section 4) on NiO(001). The ability to tune the x-ray energy either to the NiO  $L_{2a}/L_{2b}$  or Co/Fe  $L_3/L_2$  absorption resonance and furthermore vary the polarization of the x-rays allows to study the magnetic structure of the top ferromagnetic layer as well as the buried NiO surface. Although the NiO signal is suppressed by a factor of 4-5 due to the limited escape length of the secondary electrons, the domain pattern of the buried antiferromagnet can still be easily addressed. The lateral scale is rather large to illustrate that the observations are not restricted to a small local area on the sample.

Both XMLD images in figure 6.1 exhibit two grey levels representing two different antiferromagnetic domains. These domains are separated by (100) or (010) walls. The XMCD images on the other hand shows four different grey scales corresponding to four different ferromagnetic domains. These four ferromagnetic domains split up into two different subgroups with each subgroup following one particular antiferromagnetic domain, such that antiferromagnetic (100) walls in the XMLD images coincident with ferromagnetic (100) walls in the XMCD images. Considering only these walls the ferromagnetic domains form an exact replica of the antiferromagnetic domains.

The contrast arising from the different magnetic domains is now analyzed qualitatively.

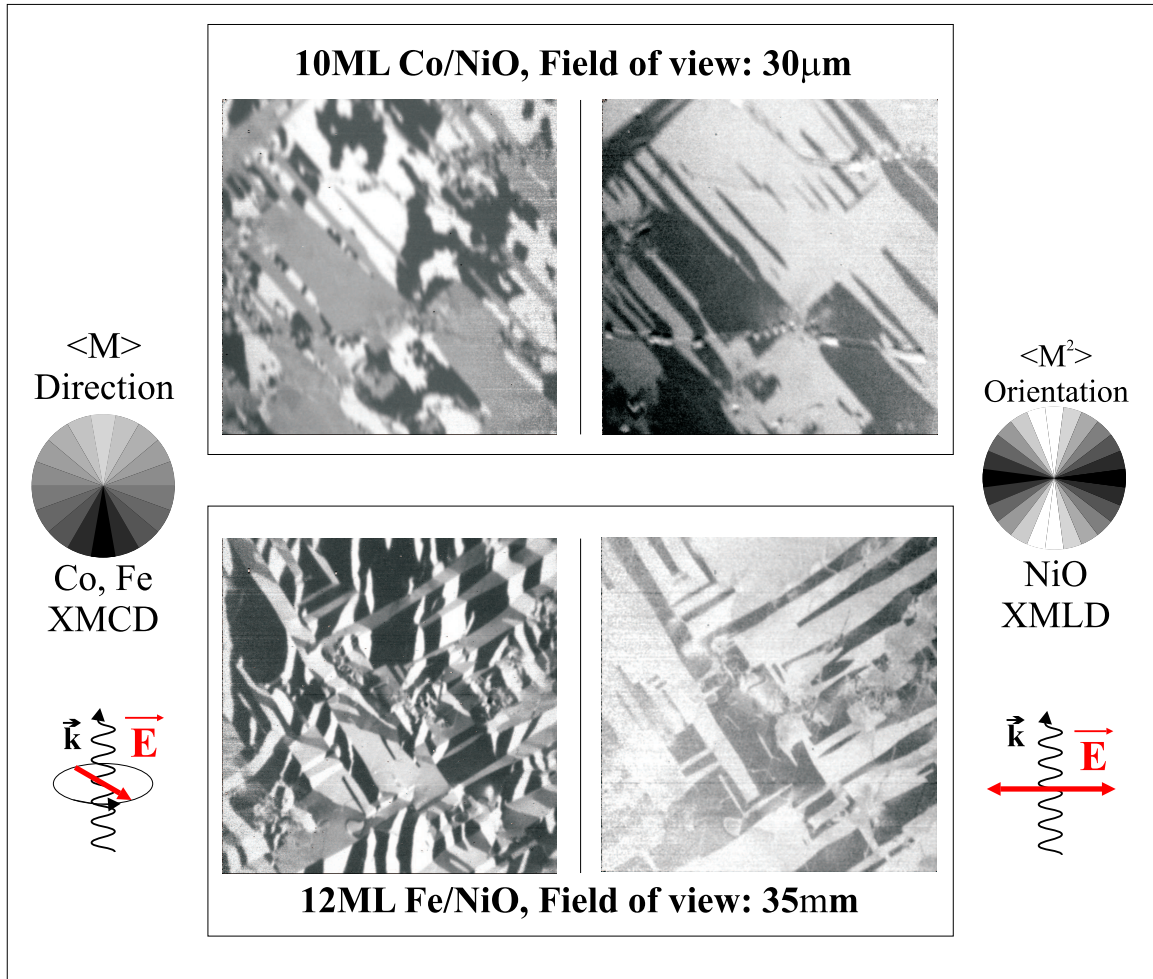


Figure 6.1: FM and AFM Domain Topology on Coupled Systems

XMCD images (left) and XMLD (right) images of 10ML of Co/NiO (top) and 12ML of Fe/NiO (bottom). X-rays are incident along the vertical image direction. The legends on the side correlate the observed grey levels to the direction of the magnetic moment in each ferromagnetic domain and the orientation of the magnetic axis in each antiferromagnetic moment. Collinear alignment between ferromagnetic moment and antiferromagnetic axis is observed.

For this purpose legends are shown in figure 6.1 which correlate the observed dichroism intensity with the magnetic orientation. Image areas showing strong bright and dark XMCD intensity represent domains where the projection of the spins onto the helicity of the light is large, that means the magnetic moment is pointing up and down in the image plane. The more greyish domains exhibit smaller projections onto the polarization vector indicating that their moment are aligned rather perpendicular to the helicity of the x rays. In the XMLD images antiferromagnetic domains with a more vertical orientation of the magnetic axis are shown in a bright grey scales compared to horizontal domains shown in darker colors.

A qualitative conclusion can already be made about the orientation of the exchange coupling between ferromagnetic Fe or Co and the antiferromagnetic NiO(001) surface. Altogether, *parallel or better collinear coupling between ferromagnetic directions and antiferromagnetic axes is observed*. Results obtained from Fe/NiO and Co/NiO are qualitatively identical. In the following only results obtained from the Co/NiO(001) sample are shown.

## 6.2 Observations on Co/NiO(001)

The determination of the exact direction of antiferromagnetic and ferromagnetic axes is achieved similar to the determination of the antiferromagnetic axis on bare surfaces. First the general symmetry properties of the magnetic structure are analyzed leading to a hypothesis for the orientation of the magnetic moments. It is demonstrated that by choosing subtle experimental geometries the magnetic domain configuration can be very nicely deduced from the images itself due to the unambiguous angular dependence of XMCD and XMLD. Finally the hypothesis is then proven by a quantitative analysis of the dichroism contrast arising from each domain via local absorption spectra.

### 6.2.1 Azimuthal Dependence of XMLD and XMCD Images

NiO XMLD and Co XMCD images acquired in different geometries are depicted in figure 6.2. The first row shows the same images for Co/NiO as in figure 6.1 with four different ferromagnetic (up, down, left and right) and antiferromagnetic domains (vertical and horizontal). The wheels on each side of the figure correlate the direction or orientation of the magnetic moment with the dichroism intensity. The arrows indicate the directions of the magnetic moment or axis within each magnetic domain suggested in the previous section.

To address the issue whether the (100) wall is still a symmetry plane for the coupled magnetic structure as it observed for the bare NiO(001) surface, XMLD images were obtained for  $E_{\parallel}$  parallel [100] and XMCD images were acquired with  $\vec{\sigma}$  parallel to the (100) plane (middle row in figure 6.2). As for the bare surface no antiferromagnetic contrast is observed in this geometry, indicating that indeed the projection of the magnetic axis onto the (100) plane is the same for both antiferromagnetic domains. Considering the XMCD image only two contrast levels remain after the azimuthal rotation. A comparison with the previous geometry reveals that domains which exhibited a darker XMCD intensity (black and dark grey) appear still dark but cannot be distinguished anymore. The two bright domains (white

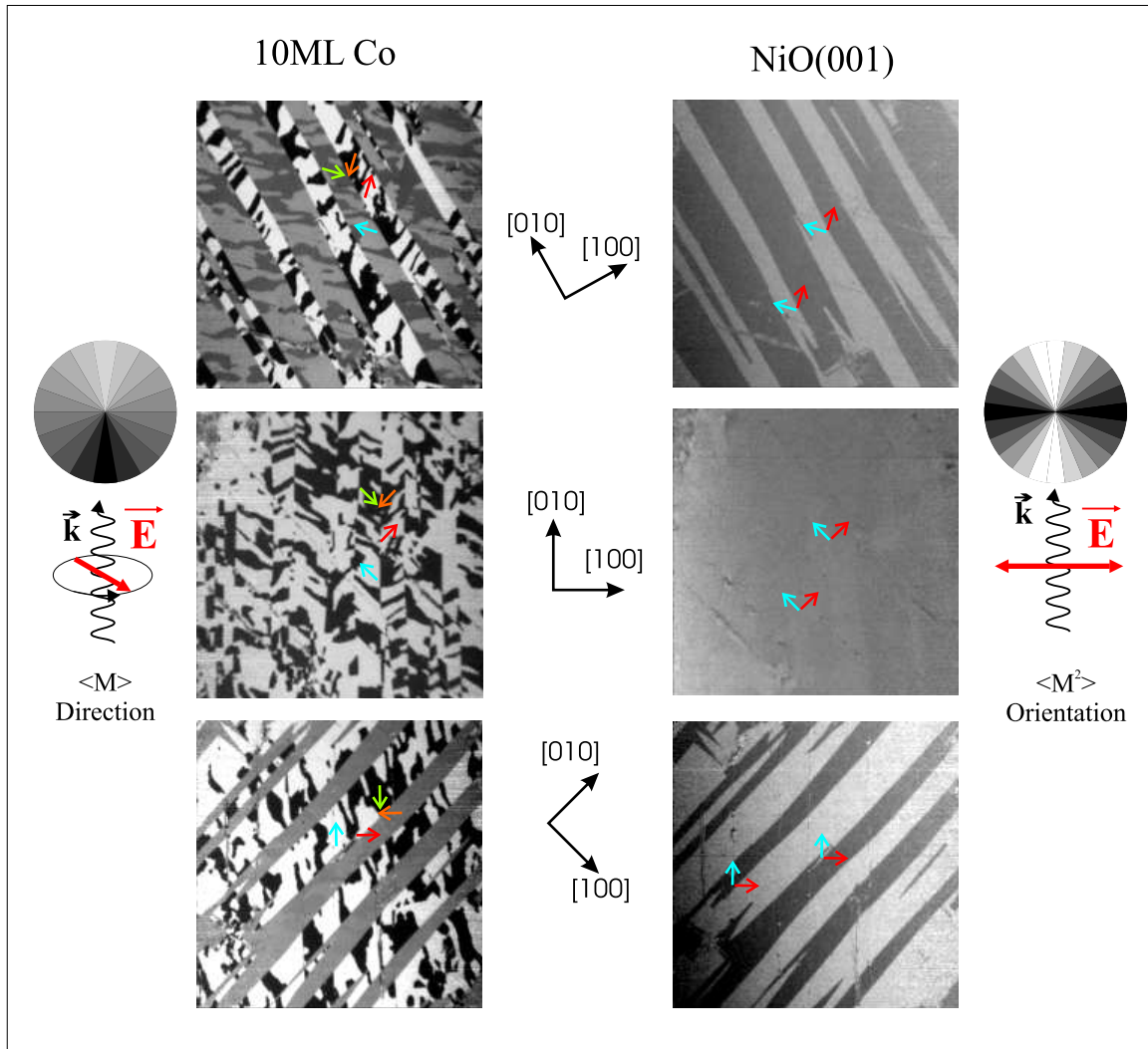


Figure 6.2: Azimuthal Dependence of FM and AFM Contrast on Co/NiO(001)

Images of antiferromagnetic and ferromagnetic domains acquired with different angles  $\phi$  between the electric field vector and the crystal axes. All images were taken at the same position on the sample surface. The legends on the side correlate the observed grey levels to the direction of the magnetic moment in each ferromagnetic domain and the orientation of the magnetic axis in each antiferromagnetic domain. The arrows indicate the direction of the spin moment or axis in each magnetic domain.

a.) Same geometry as in figure 6.1. b.) The incoming x-rays are parallel to a high symmetry direction ([100]). No antiferromagnetic contrast and only two ferromagnetic domains are visible. c.) The electric field vector is parallel to a [110] direction. The ferromagnetic contrast of one subset of domain vanishes while the other one reaches a value of 18%. Ferromagnetic and antiferromagnetic contrast arising from each domain is reversed compared to the situation depicted in a.)

and bright grey) show the same behavior. This means, since the helicity of the incoming x-rays is parallel to the (100) wall, that the magnetic moment in each ferromagnetic domain appearing dark or bright forms the same angle with the (100) wall. In conclusion the (100) wall represents a mirror plane for each type of ferromagnetic domains represented by dark and bright areas.

An upper and lower limit for the angles which the magnetic moment in each of the ferromagnetic domains forms with the (100) wall plane is now derived from the evolution of the XMCD contrast between the two experimental geometries. The sign of the XMCD intensity remains the same for all four ferromagnetic domains, which means dark domains remain dark and bright domains remain bright. Since the XMCD intensity is determined by the scalar product of the helicity of the x-rays ( $\vec{\sigma}$ ) and the magnetization vector ( $\vec{M}$ ), this indicates that a rotation of  $30^\circ$  leaves magnetic moments which pointed up (in the image) before the rotation still pointing up and vice versa. This behavior can only be realized if the angle between the magnetic moment and the (100) wall is considerably less than  $60^\circ$ . The lower limit for the inclined angle is estimated from the observation that the contrast of one subset of ferromagnetic domains (dark black and bright white) appears to be already maximal in the first geometry and then decreases significantly upon sample rotation. This can be achieved if the scalar product  $\vec{\sigma}\vec{M}$  is already close to maximal for this particular subset of domains in the first geometry. In other words the moment is oriented roughly parallel to the helicity of the x-rays. In this case the minimum angle between the (100) wall and the magnetic moment has to be at least about  $20^\circ$ . The arrows in figure 6.2 representing the direction of the magnetic moment or the magnetic axis in each ferromagnetic or antiferromagnetic domain reflect the above findings.

Finally the angle that each magnetic domain (ferromagnetic or antiferromagnetic) includes with the (100) wall is determined. For this purpose the same geometry which has been used in section 5.1 to determine the angle between the axis of the two observed antiferromagnetic domains is investigated. The sample is rotated by  $45^\circ$  around its surface normal compared to the previous geometry. Images obtained with the in plane electric field vector  $E_{\parallel}$  parallel to [100] are shown on the bottom of figure 6.2. The ferromagnetic domains that appeared with the strongest contrast in the first geometry are not distinguishable anymore after a total rotation of  $75^\circ$ . This behavior is observed, because the magnetic moment in each domain is now oriented perpendicular to the helicity  $\vec{\sigma}$ . Assuming furthermore that the ferromagnetic spins are completely parallel surface plane this means that the direction of the ferromagnetic domains is parallel to [110] or  $[\bar{1}\bar{1}0]$ <sup>1</sup>. The other subset of ferromagnetic domains that appeared only with a very weak contrast in the first geometry now shows a very strong contrast suggesting that the magnetic moments pointing parallel to  $\vec{\sigma}$ . Following the condition that the (100) plane is a symmetry plane the direction in these ferromagnetic domains is assumed to be parallel to  $[\bar{1}10]$ . Altogether the magnetic moments of the four ferromagnetic domains point in the four different in plane [110] directions.

The antiferromagnetic contrast observed in this geometry (11%) is larger than in the first

---

<sup>1</sup>The presence of an out-of-plane anisotropy or polycrystalline Fe or Co films of this thickness would be very unexpected. The assumption of in-plane anisotropy will be further corroborated in the next section

geometry. The absolute size of the XMLD contrast is close to the maximum contrast that can be expected in this experiment (13%). It is therefore presumed that the antiferromagnetic axes in each domain are oriented close to parallel respectively perpendicular to the electric field vector to achieve this XMLD value. Note, that no additional contrast is observed when XMLD with mixed polarization were acquired, indicating that the out of plane projection of the antiferromagnetic axes is negligible. Similar to the findings reported in the previous chapter this altogether leads to the hypothesis that the antiferromagnetic axis in each antiferromagnetic domain is parallel to an in plane [110] direction and collinear to the magnetic moment in adjacent ferromagnetic domains.

### 6.2.2 Local XMCD and XMLD Spectra

To quantitatively prove the assumption that the coupling between ferromagnetic and antiferromagnetic domains is collinear parallel to [110] local spectra within each antiferromagnetic and ferromagnetic domain were acquired. Figure 6.3 shows NiO  $L_2$  XMLD and Co  $L_3$  XMCD local spectra obtained from different magnetic domains. The lateral scale in the images is only  $10\mu m$ . The fact that Co spectra of each pair of domains (black/white and dark grey/light grey) deviate symmetric from the same average spectra is consistent with the situation that the magnetic domains are separated by  $180^\circ$  walls or in other words the magnetic moments of adjacent domains are antiparallel within each subset. This has been implicitly assumed so far and can now unambiguously concluded.

The black white (blue and green spectra) contrast corresponds to an XMCD contrast of 19% whereas the contrast between the greyish domains (red and black spectra) equals 7%. Assuming a maximum XMCD contrast of 30% [15] for Co metal and taking into account a finite degree of circular polarization  $P_c = 75\%$  finally the angle between the helicity vector and the ferromagnetic axes are calculated to be  $32^\circ$  and  $71^\circ$ . This is identical within the experimental error of  $4^\circ$  to the angles expected for [110] directions ( $30^\circ$  and  $73^\circ$ ). Regarding the antiferromagnetic axes the agreement is very good as well. For antiferromagnetic axes parallel to [110] the expected NiO  $L_2$  ratios are 1.21 and 0.91 in this particular geometry. The values determined in the experiment are 1.20 and 0.90 (with an experimental error of  $\pm 0.01$ ). This can also be expressed in angles again. The angles which the [110] directions include with the electric field vector in this geometry are  $20^\circ$  and  $110^\circ$  or  $-70^\circ$  respectively. The values determined by the experiment are  $71^\circ$  and  $18^\circ$ . Since it has been found in the previous chapter that the antiferromagnetic axis on the bare surface is parallel to a [121] direction the antiferromagnet spin structure has experienced an in-plane reorientation due to the deposition of the ferromagnetic Co film.

The following conclusion about the coupling between antiferromagnetic NiO and ferromagnetic Co are now made:

- The ferromagnetic domain pattern is a result of parallel exchange coupling to antiferromagnetic NiO.
- Both systems align collinear to in plane [110] axes. The ferromagnetic Co shows a distinct anisotropy along [110].

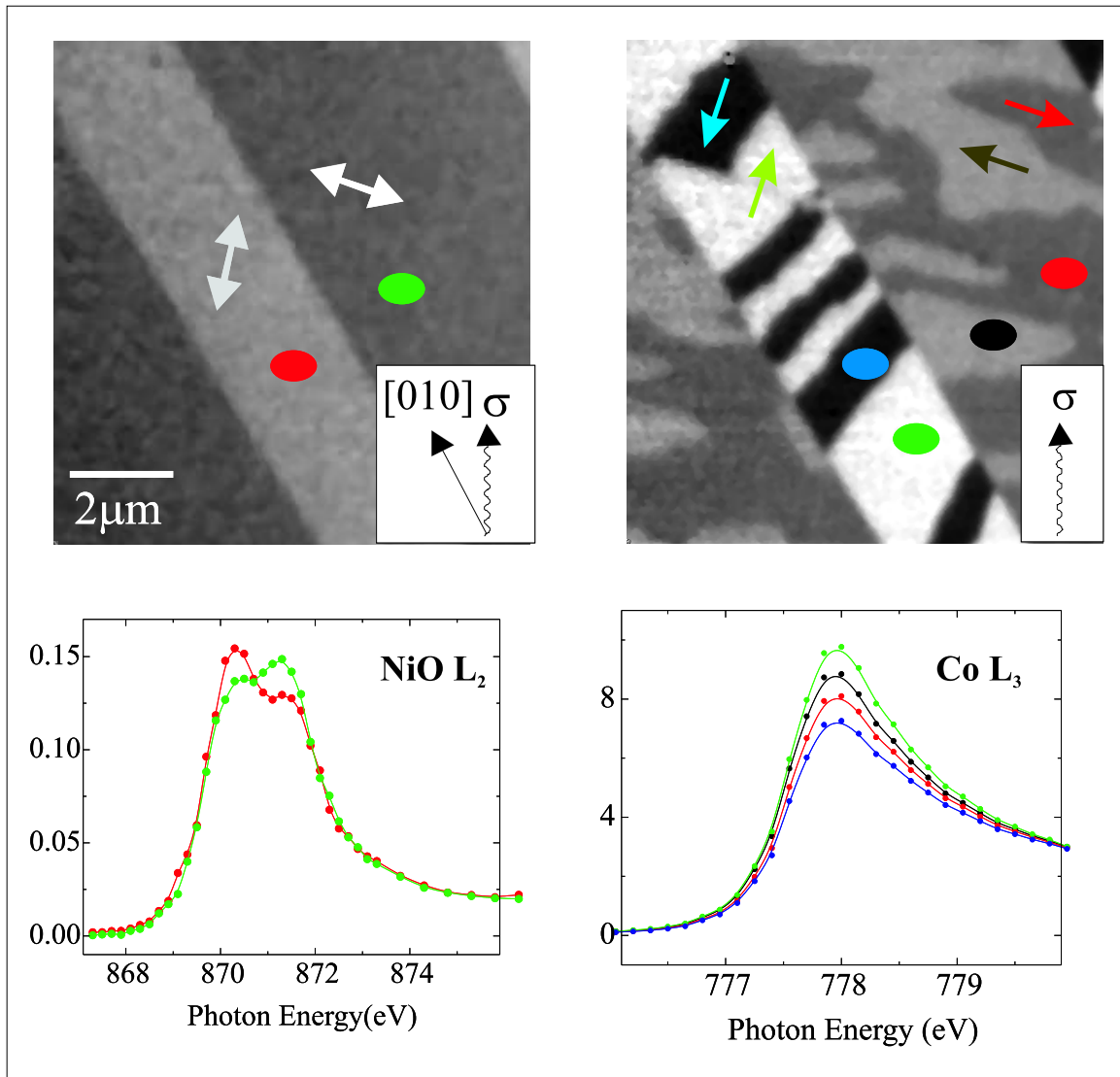


Figure 6.3: Local Spectra of Co and NiO domains

XMLD and XMCD image of Co/NiO(001). The arrows indicate the magnetic axes or direction as deduced from the local dichroism intensity. Local absorption spectra obtained from each domain are shown on the bottom. The color of the lines in the spectra correspond to the colored dots in the images indicating the type of domain where the spectra were taken from.

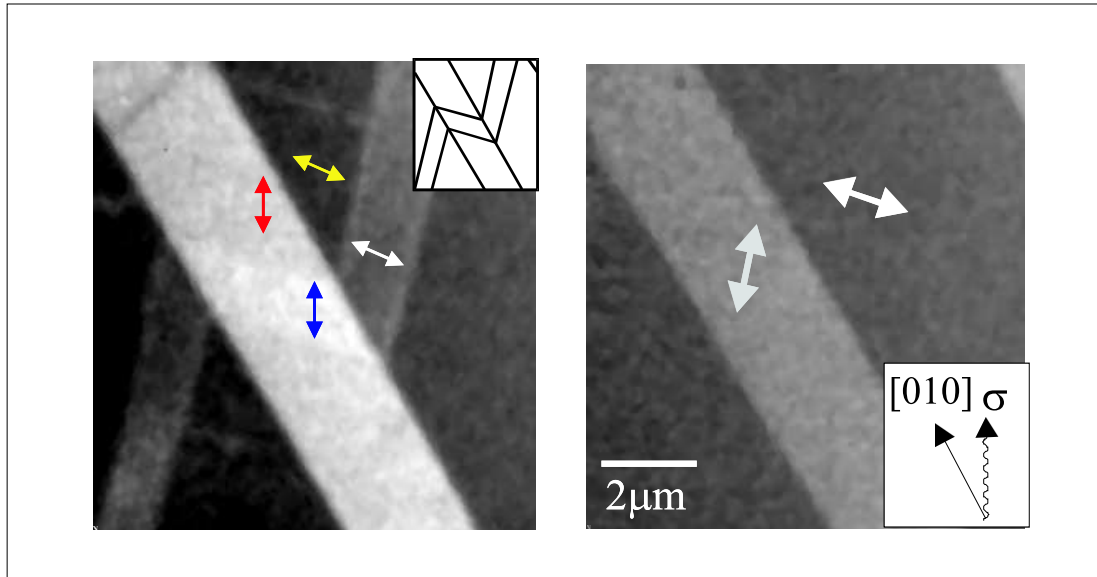


Figure 6.4: In-Plane Reorientation of AFM NiO upon Co Deposition

The XMLD image on the left side shows the four wall pattern observed on the bare NiO(001) surface before deposition of Co with in-plane and out-of-plane domain walls. The out-of-plane domain wall disappears upon Co deposition (right image). The sketch in the top right corner of the left XMLD images shows the domain AFM domains structure and serves as a guide to the eye. Arrows in the left XMLD image indicate the in plane projection of the antiferromagnetic axis within each domain.

- To achieve the parallel exchange coupling a reorientation of the antiferromagnet compared to the bare NiO(001) surface takes place.

### 6.3 AFM Reorientation

The in-plane reorientation of the antiferromagnetic domain pattern mentioned in the previous summary on exchange coupled Co/NiO will be addressed in the following in more detail. Possible reasons for the reorientation will be discussed.

#### 6.3.1 AFM Reorientation upon Deposition of a FM

Figure 6.4 illustrates the antiferromagnetic domain pattern before and after deposition of 10 monolayer of Co using mixed polarization. The domain structure of the bare surface shows the already well known herring bone pattern (see section 5.2.1 and figure 5.4). The arrows represent the in-plane projection of the antiferromagnetic axes. Domains with different in-plane axes are separated by a (100) wall. Domains with the same in-plane axes but different out-of-plane axes are separated by a (110) wall. The domain image on the right side was

obtained after Co deposition. The (110) walls completely disappear upon Co deposition and hence there is no variation in the out-of-plane component of the antiferromagnetic axes in the exchange coupled structure. The location of the in-plane domain wall remains unchanged.

This qualitative observation illustrates very beautifully that the antiferromagnetic domain structure reorients upon Co deposition. The number of antiferromagnetic domains that are realized at the antiferromagnetic/ferromagnetic interface is reduced from four to two compared to the bare antiferromagnetic surface. The modified symmetry along the [001] direction due to the translation from a (001) surface to an [001] interface obviously suppresses the variation of the [001] out of plane component of the antiferromagnetic axes.

### 6.3.2 Possible Reasons for the AFM Reorientation

The left side of figure 6.5 illustrates the spin arrangement at the antiferromagnetic surface before and after Co deposition. Prior to Co deposition the spins include an angle of  $26.6^\circ$  with the surface plane. Every pair of out-of-plane domains (yellow/green and red/blue) is separated by a (110) wall within which the spins are aligned parallel to an in plane [110] direction. After the reorientation (bottom) *all* spins are parallel to the (001) surface and parallel to the [110] direction which formerly defined the each of the (110) walls. This observation is of particular interest, since the a particular bulk wall (see table 3.2) which exhibits exactly this spin arrangement is a bulk (001) wall, a bulk wall parallel to the surface plane. Altogether this leads to the conclusion that the antiferromagnetic spin reorientation observed at the Co/NiO interface can be described as the formation of an antiferromagnetic bulk like (001) domain wall parallel to the surface.

### 6.3.3 Reorientation and Lattice Distortion

The right panel in figure 6.5 illustrates the realized spin axis and correlates them to lattice distortions that were identified in chapter 3 to favor a particular spin axis. The representation Nickel and Oxygen atoms is similar to chapter 3.

For the bare surface a monoclinic expansion along [110] favors the [112] orientation (blue arrows). The six oxygen atoms surrounding the central Ni atom are shown as yellow spheres. On the bottom the situation which favors a [110] spin axis as observed for the exchange coupled interface is illustrated. The [110] axis (green double headed arrow) and the orthorhombic contraction is shown (green dotted arrow). The orthorhombic contraction is here realized by moving all outer Ni atoms (red) closer together along [110] (yellow dotted arrows). As a result the lattice is contracted along [100]. This can for example be achieved by oxygen deficiency as indicating by the transparent spheres representing the oxygen atoms in the figure. It will be demonstrated in chapter 8 that oxygen diffusion across the interface into the Co layer leading to a chemical reaction at the interface is indeed observed.

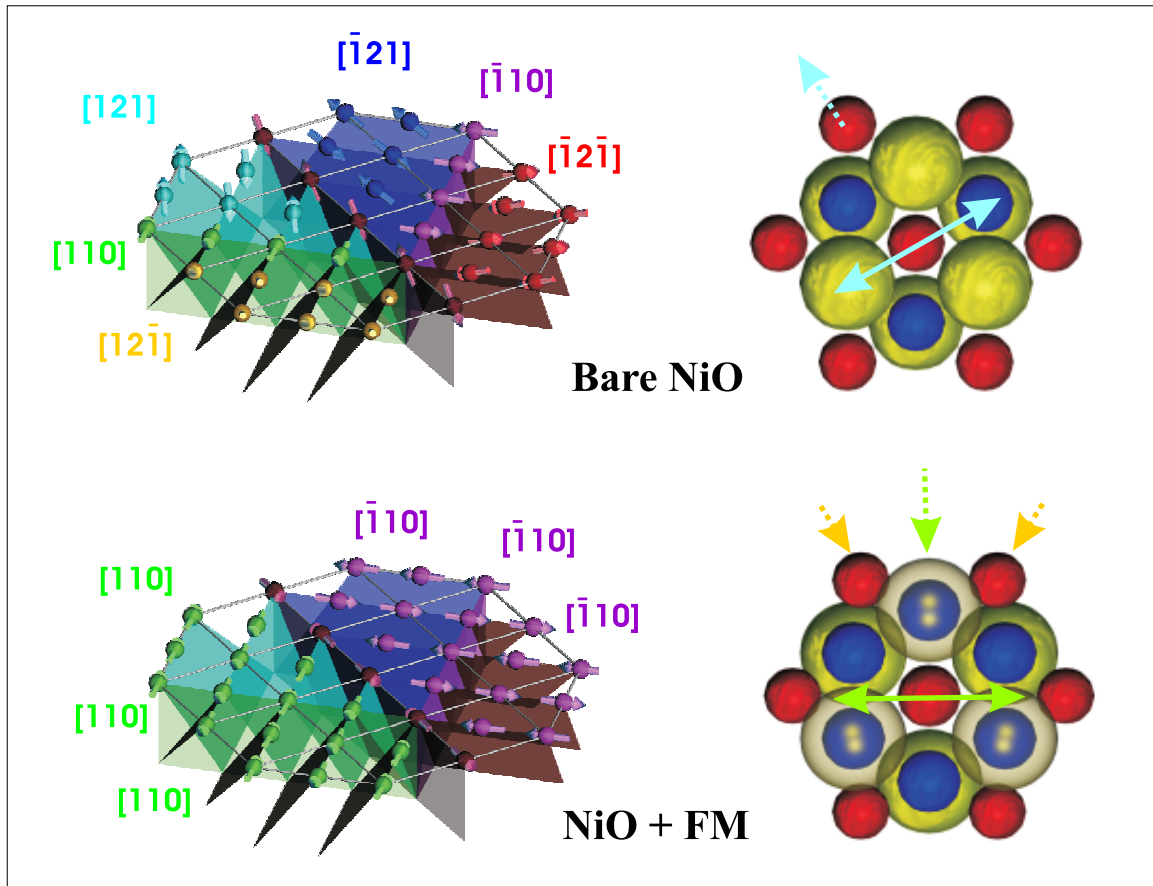


Figure 6.5: Visualization of the In-Plane Reorientation

Left: Direction of spin axis in each antiferromagnetic domain and the center of the domain wall before (top) and after Co deposition (bottom).

Right: Top view onto a (111) lattice cell formed by nickel and oxygen atoms. A monoclinic expansion (dotted blue arrow) favoring a spin axis parallel to [121] (double headed blue) is depicted on top. Oxygen deficiency leads to a compression along [110] (dotted yellow arrows) and thus a orthorhombic compression along [100] (dotted green arrow). The resulting easy spin axis is parallel to [110]

### 6.3.4 Interfacial Exchange Anisotropy

The magnetic configuration of a single polycrystalline 2nm thin Cobalt layer typically exhibits a strong in-plane anisotropy. Any out-of-plane component of the magnetization increases the magneto static energy by several  $10^7 \text{erg/cm}^3$  due to the magnetic dipole field. For this reason the easy axis of the Co film itself is parallel to the surface plane. Here the spins at the antiferromagnetic NiO(001) surface are coupled to the ferromagnetic Co spins by an exchange anisotropy energy which favors parallel alignment. Hence the antiferromagnet spin axis rotates into the surface towards into the [110] direction following the Co spins and forming a (100) wall.

The energy which is necessary to form the (100) wall can now be estimated. Following the explanations in chapter 3 both spin orientations [112] and [110] parallel to the (111) plane can in principle be realized but the [112] configuration is energetically slightly more favorable. The energy difference is about  $5 \times 10^4 \text{erg/cm}^3$  (or  $2.5 \mu\text{eV/atom}$ ). The anisotropy energy perpendicular to the (111) plane is much larger ( $100 \mu\text{eV/atom}$ ), so that the antiferromagnetic spin lattice will first try to achieve an energy minimum by rotating the spins within the (111) plane rather than tilting any spins perpendicular to it.

The width of a (100) wall has been observed in the previous chapter to be about 150 nm and consequently the observed spin reorientation or wall is estimated to extend about 100 nm into the bulk<sup>2</sup>. The excess in anisotropy energy caused by formation of the wall (about 500 atoms  $\times$   $2.5 \mu\text{eV/atom} = 1.3 \text{meV}$  has to be compensated for by the exchange coupling to the ferromagnet right at the interface. The increase in magneto static energy within the parallel domain wall of this size therefore corresponds to an anisotropy energy per interfacial unit area of  $1.3 \text{meV/atom}$  or  $1.2 \text{erg/cm}^2$ .

The estimated value for the interfacial exchange energy density is in particular interesting because it is very close to the Heisenberg Spin-Spin exchange energy of 3d-transition metals [66]. Following the simple model of Meiklejohn and Bean (see section 1.2) the interfacial exchange anisotropy energy is determined by the Heisenberg Spin-Spin exchange energy. However, if one uses this simple model to estimate the macroscopic exchange bias field exhibited by a 'real' ferromagnet exchange coupled to an antiferromagnet, the calculated values are usually a factor of 10 or more bigger. In this microscopy experiment however, where the ferromagnetic **and** antiferromagnetic domain pattern can be addressed in parallel the origin of this discrepancy is directly obvious<sup>3</sup>. Exchange coupling across the magnetically compensated Co/NiO(001) interface (no net magnetic fields arise from the ideal NiO(001) surface) does not manifest itself as a unidirectional anisotropy detected by the ferromagnetic layer but rather leads to a reorientation of the antiferromagnetic surface. Finally, this leads to the following assumption, which will be corroborated in the next chapter. While an ideal uncompensated interface exhibits a unidirectional coupling of  $1 \frac{\text{erg}}{\text{cm}^2}$  it appears that a compensated surface leads to an interfacial uniaxial coupling of  $1 \frac{\text{erg}}{\text{cm}^2}$ .

<sup>2</sup>This is speculative in so far as the same mechanism responsible for domain wall formation is assumed. Other mechanism will lead to totally different thicknesses

<sup>3</sup>Note, that hysteresis loops acquired from samples discussed in this thesis never showed any horizontal loop shift after field cooling in fields up to 1kOe

## 6.4 Summary on Parallel Exchange Anisotropy

The results obtained from the exchange coupled samples are summarized in the following [62].

1. The ability to tune the x-ray energy as well as its polarization allows to image the ferromagnetic domain pattern in Co or Fe and the antiferromagnetic domains at the buried NiO(001) surface.
2. The qualitative analysis of the NiO XMLD and Fe/Co XMCD contrast reveals a collinear coupling between the spin axis of each antiferromagnetic domain and the uniaxial anisotropy of adjacent ferromagnetic domains.
3. The quantitative analysis yields a common preferred axis of the two magnetic systems which is parallel to [110].
4. Two different antiferromagnetic [110] in-plane domains remain out of the four out-of-plane domains observed prior to deposition of the ferromagnet. The antiferromagnet experiences an in-plane reorientation.
5. The antiferromagnetic configuration at the buried (001) surface resembles the one of an antiferromagnetic domain wall parallel to the interface.

## Chapter 7

# Blocking Temperature and AFM Domain Structure

In this chapter the question is addressed how the observed domain pattern on NiO(001) and Co/NiO(001) evolves if the temperature is increased above the Néel temperature  $T_N$ . Especially the behavior close to  $T_N$  is of interest, because it is a common observation that the exchange bias field disappears at the so called *Blocking Temperature*  $T_B$  significantly below  $T_N$  [59]. It will be demonstrated that the ability to distinguish between antiferromagnetic and ferromagnetic order gives interesting new insight into the origin of  $T_B$  and how it can be related to the antiferromagnetic domain structure. For this experiment 30-40 XMLD or XMCD images were acquired while the sample was slowly annealed from room temperature up to 600K. XMCD images are the results of images acquired with circular polarization at the Co  $L_3$  and  $L_2$  absorption edges. XMLD images were obtained using linear polarized x-rays at the NiO  $L_{2a}$  and  $L_{2b}$  resonance.

The dependence of the dichroism signal on the magnetic properties will be reviewed first. In chapter 2.3.4 and 2.3.5 expressions for the XMCD and XMLD intensity in general were given. The dichroism intensity depends on the thermodynamic expectation values of the magnetic moment  $\langle M \rangle$  for the ferromagnet or its square  $\langle M^2 \rangle$  in case of an antiferromagnet. The second term denotes the dependence on the angle between the relevant polarization vector and the magnetic direction or axis.

$$I_{\text{XMCD}} \sim \langle M \rangle \cos(\vec{\sigma}\vec{M}) \quad (7.1)$$

$$I_{\text{XMLD}} \sim \langle M^2 \rangle \cos^2(\vec{E}\vec{M}^2) \quad (7.2)$$

If now an dichroism image is acquired the intensity of every image point is given by these expressions and changes in the dichroism intensity may be attributed to two different effects.

1. The thermodynamic average of the magnetization  $\langle M \rangle$  or its square  $\langle M^2 \rangle$  changes.
2. The direction of  $\langle M \rangle$  or its square  $\langle M^2 \rangle$  changes.

A decrease in the thermodynamic average will be observed if the temperature is increased. For the temperature range considered here (300-600 K) the average of the magnetic moment  $\langle M_{\text{Co}} \rangle$  of the ferromagnet will decrease linearly by a very small amount, because the Curie temperature is much higher (1398K).

The temperature dependence of  $\langle M^2 \rangle$  is more complicated and is denoted in the following, derived from a molecular field approximation [68].

$$\langle M^2 \rangle = g^2 \mu_B^2 J(J+1) - g\mu \langle M \rangle \coth(g\mu_B H/2kT) \quad (7.3)$$

In this equation  $g$  stands for the gyromagnetic ratio,  $J$  for the quantum number of the total spin (1 for a  $3d^8$  system),  $\mu_B$  for the Bohr magneton,  $k$  for the Boltzmann constant,  $H$  for the molecular field and  $\langle M \rangle$  for the expectation value of the moment of the antiferromagnet. It can now be shown that above  $T > 0.6 T_N$   $\langle M^2 \rangle$  and the XMLD intensity decreases linear with temperature [68, 91, 76]. This behavior is shown for example by the blue line in figure 7.1. It is important to note that, if the experimental observation does *not* show a linear decrease of the XMLD signal the second origin for a change of the XMLD intensity has to be considered and a reorientation of the magnetic moment or the magnetic axis needs to be assumed.

In the following a distinct deviation from the linear dependence is observed in NiO and Co/NiO. The deviation reaches its maximum in a temperature region which is typically attributed to the vanishing of exchange anisotropy (0.85-0.95 of  $T_N$ ). The existence of the blocking temperature is then attributed to a reorganization of the antiferromagnetic domain pattern.

## 7.1 Antiferromagnetic Domains Pattern near $T_N$

Temperature dependent XMLD images were obtained from a cleaved NiO(001) surface. For each XMLD image the average XMLD intensity  $I_{\text{XMLD}}$  of the image has been calculated. The result  $I_{\text{XMLD}}$  is divided by the value obtained above  $T_N$  for normalization purposes. In addition the standard deviation has been calculated from the image data. These two values are plotted versus the relative sample temperature  $T/T_N$  in figure 7.1. For comparison a straight line representing the expected linear decrease for  $I_{\text{XMLD}}$  is shown as well.

The temperature dependence of the XMLD intensity deviates significantly from the expected linear decrease. The maximum deviation occurs between 85% and 95% of  $T_N$ . Following the considerations in the previous section this indicates that the direction of the antiferromagnetic axis averaged over the image area changes during the annealing process. The assumption is corroborated by the behavior of the standard deviation which exhibits a maximum at this temperature range. This behavior indicates that the XMLD intensities which are present in the image are distributed in a larger range around the average value than at room temperature.

This shall be demonstrated by four selected images from this temperature series. Except the fact that the overall contrast is reduced there are only small differences in the domain patterns observed at 300K and at 420K ( $0.8 \times T_N$ ). Increasing the temperature just a little

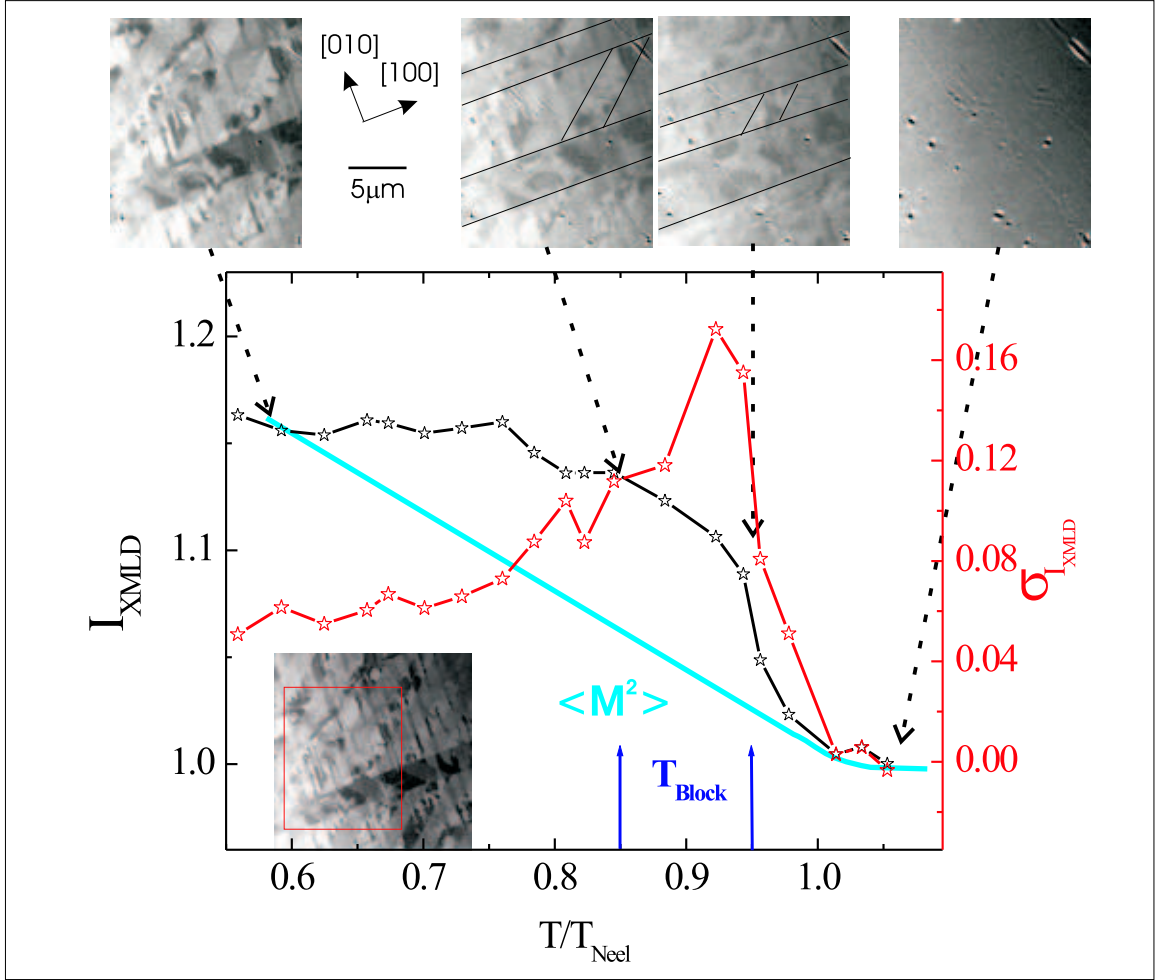


Figure 7.1: Temperature Dependence of AFM Surface Domain Pattern

The plot shows the dependence of the average XMLD intensity obtained from all pixels in the acquired images and the standard deviation of their intensity distribution. The straight (blue) line indicates the expected linear decrease of  $\langle M^2 \rangle$  (see text). The maximum deviation from the linear decrease coincides with a maximum in the standard deviation around  $T_B$ . Images for some characteristic temperature values are shown. The black lines in these images serve as a guide to the eye to enhance domain wall features.

bit more to 460K ( $0.87 \times T_N$ ) the domain pattern does change drastically. Most of the (110) walls that could still be observed at 420K have disappeared and a new (100) wall appeared. At 540K above  $1.03 \times T_N$  no XMLD contrast can be observed anymore.

Altogether, annealing the NiO(001) surface does not only lead to a decrease in  $\langle M^2 \rangle$  which will eventually cause the antiferromagnetic order to vanish above  $T_N$  but also leads to a reorientation of the antiferromagnetic domain pattern. As a possible reason for the reorganization the fact that the anisotropy energies in NiO(001) are temperature as well as changes in the lattice parameter which will lead to changes in the magneto static energy are mentioned. The observed reorganization processes are especially pronounced around  $0.9 \times T_N$ , a temperature which is usually attributed to the blocking temperature of NiO(001)[59].

## 7.2 Temperature Dependence of the Coupled Domain Pattern

A similar experiment as before has been performed after deposition of 10 monolayer of cobalt onto a cleaved and annealed NiO(001) surface. This time XMCD as well as XMLD images were obtained during annealing and cooling. Only the average XMCD intensity has been calculated from the images and is shown together with the images in figure 7.2.

At room temperature the same domain patterns are observed as it has been reported in the previous chapter. Above the Néel temperature the antiferromagnetic contrast vanishes and only two ferromagnetic domains are left. Judging from the XMCD contrast Co domains with their spin direction left and right in the image plane have vanished in favor of domains with their spins up and down. Secondly most of the ferromagnetic domain walls have changed their orientation from (110) at room temperature to a plane parallel to the image vertical. A possible reason for this preferential alignment of magnetic moments within the domains and the domain walls may be the small magnetic field originating from the filament used to anneal the sample. Note that the ferromagnetic domain pattern observed above  $T_N$  is partly preserved throughout the cooling process in areas with vertical orientation of the antiferromagnetic axis.

During the cooling process the antiferromagnetic domain pattern observed at room temperature is not directly reinstated below the Néel temperature and additional domains appear around 80% of  $T_N$ . Similar to the findings on the bare surface this indicates that reorganization of the antiferromagnetic domain pattern also in the exchange coupled structure takes place around 85% of the Néel temperature. The XMCD intensities shown in figure 7.2 corroborate this observation. As the XMLD intensity on the bare surface the measured XMCD intensity shows a distinct deviation from the expected linear behavior. This deviation from the expected linear dependence can now again be linked to a reorganization process in the domain pattern. It has been reported in the previous chapter that in exchange coupled Co/NiO(001) the spin in the Co layer force the antiferromagnetic spins to realign at room temperature. On the other hand it is demonstrated here, that the Co domain pattern itself is still determined by the overall arrangement of the antiferromagnetic domains.

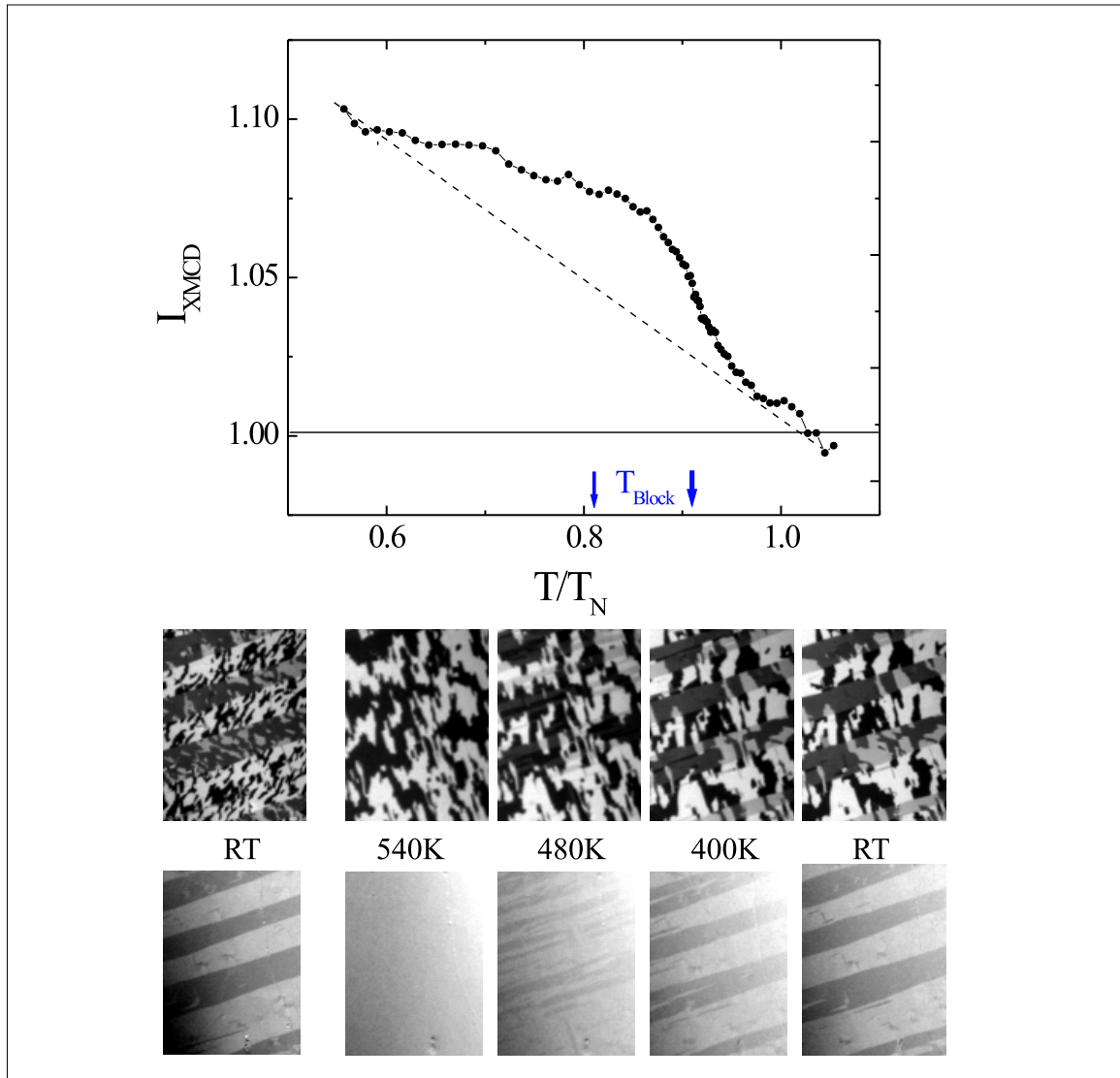


Figure 7.2: Temperature Dependence of AFM/FM Exchange Coupled Domain Pattern  
 Images of the antiferromagnetic and the ferromagnetic domain structure while cooling the sample through  $T_N$ . Four different FM and two different AFM domains can be identified below  $T_N$ . The antiferromagnetic domain pattern disappears above 525K and is reestablished without significant changes at room temperature after cooling. However a different domain pattern is observed right below  $T_N$ . The average XMCD intensity is plotted during the annealing and cooling cycle showing a deviation from the expected linear decrease around  $T_B$ . The field of view and the sample orientation is similar to the previous figure 7.1

### 7.3 Summary on AFM/FM Domain Structure Close to $T_N$

First of all the findings in this chapter corroborate two conclusions that were made in chapter 5 and chapter 6. The observed contrast on the NiO surface is indeed caused by antiferromagnetic domains and the Co domain pattern which evolves on Co/NiO is caused by exchange coupling to the NiO. Both observed effects disappear above the ordering temperature of NiO.

The more striking information obtained from the temperature dependent experiments is that the antiferromagnetic domain structure in a single crystal is not static upon annealing. This behavior is common for ferromagnetic systems but has not yet observed for antiferromagnets. Especially the fact that exchange bias disappears significantly below  $T_N$  especially for NiO(001) can now be understood. Exchange bias is typically achieved by field cooling during which a certain antiferromagnetic domain configuration is frozen in. In this context the antiferromagnetic domain configuration serves as a matrix, which will not change at room temperature or if external fields are applied. However as soon as the matrix does change the observed exchange anisotropy linked to it will also change or even vanish.

Although the samples grown on single crystal surfaces do not exhibit exchange bias these results present strong evidence and represent the very first experimental observation for the fact that the antiferromagnetic domain structure on NiO(001) rearranges significantly below the ordering temperature. This behavior is identified to be a possible origin of the disappearance of unidirectional anisotropy below  $T_N$ .

## Chapter 8

# Interfacial Spins in Co/NiO and Exchange Anisotropy

The chemical and magnetic structure **at the interface** between antiferromagnetic NiO and ferromagnetic Co is investigated in this chapter. The chemical reaction at interface between Fe, Ni Co and their native oxides has been extensively studied by T.J. Regan at Stanford University using high resolution XAS [68, 69]. These results will be reviewed in chapter 8.1.

Upon deposition of a thin Co film on a NiO surface changes in the NiO and Co XAS spectra are observed that are attributed to the formation of a thin  $\text{CoNiO}_x$  like layer at the interface. An element specific XMCD experiment reveals that the interfacial Ni spins are aligned parallel to the spins in the Co layer by ferromagnetic exchange coupling resulting into a net interfacial spin polarization. Subsequent annealing leads to further reduction of the NiO at the interface and an increased ferromagnetic Ni signal. Finally the coercivity of the system is found to be proportional to the interfacial magnetization, indicating that the amount of interfacial Ni spins or the thickness of the  $\text{CoNiO}_x$  layer determines the interfacial exchange anisotropy.

The investigated samples grown on single crystal NiO(001) do not show exchange bias due to their large domain size<sup>1</sup>. On the other hand they do show a distinct interfacial spin polarization, which has typically been attributed with the existence of exchange bias (see chapter 1). The results presented in the first part of this chapter however demonstrate that an interface polarization at the compensated surface only contributes to the *uniaxial anisotropy* of the system and not to the *unidirectional anisotropy*. Upon field reversal the observed Ni interfacial moments simply follow the ferromagnet Co spins. For this reason these moments are regarded as *rotating* or *free* moments.

Finally an exchange biased polycrystalline Co/NiO sample is investigated for comparison. Element specific hysteresis loops of the ferromagnetic Co and the interfacial Ni are acquired using XMCD. The hysteresis loops of only the interfacial Ni spins exhibit an additional vertical loop shift which can be attributed to moments that do not rotate in an external

---

<sup>1</sup>Takano *et al.* [93] have shown that the size of exchange bias decreases with  $1/d$  where  $d$  is the typical domain size. For  $d$  larger than  $1 \mu\text{m}$  the bias field appears negligible.

field. These moments are referred to as *pinned* moments and are identified as the origin of the horizontal loop shift. The size of the macroscopic exchange bias field is calculated from the microscopic number of pinned spins using the Meiklejohn and Bean approach.

## 8.1 Chemical Reaction at the Metal/NiO Interface

### 8.1.1 Introduction

Using the soft x-ray beamline 10-1 at the Stanford Synchrotron Radiation Laboratory high resolution x-ray absorption spectra of Co/NiO interfaces are acquired. The energy resolution in the region between 700-900 eV is typically about 0.1-0.15 eV considering a constant relative energy resolution  $E/\Delta E$  of 5000 to 7000. The spectra are acquired in the total electron yield mode.

As already been introduced in chapter 2.3 the XAS line shape is extremely sensitive to any changes in the local chemical environment of the investigated species. The investigated samples are prepared by microwave sputtering or electron beam evaporation techniques in UHV (see chapter 4). Figure 2.5 in chapter 2.3.2 shows the qualitative differences between the spectra of the 3d-metals Fe/Co or Ni and their native oxides  $\text{Fe}_2\text{O}_3$ , CoO and NiO. These XAS spectra will serve in the following as reference spectra for the quantitative analysis of the XAS spectra of exchange coupled samples.

To compare spectra obtained from different samples with different electronic configurations they need to be appropriately normalized. First the standard normalization procedure is applied. For this purpose the sample electron yield signal is divided by the electron yield signal originating from an upstream gold mesh which measures the incoming intensity. This step ensures that the measured XAS spectra do not depend on the spectral function of the optical system of the soft x ray beamline. After that a linear background is subtracted such that the XAS signal vanishes for photon energies smaller than the investigated absorption resonance. This linear background signal originates from other absorption resonances with lower binding energies. Finally the XAS spectra are divided by the integrated intensity so that all spectra are normalized to the same number of electrons/holes in the ground state because the integrated intensity is proportional to the number of holes in the ground state (for details and choice of integrations boundaries see [69]).

For an unknown sample which consists of atoms in a metallic as well as an oxidic environment it is assumed that the resulting spectra is a direct results of a linear combination of metal and oxide spectra. By fitting the unknown spectra with suitable reference spectra it is then possible to extract the relative concentrations of metal and oxide from the weighting factors. For this purpose one needs to consider carefully the escape length of the electrons. For a interfacial chemical reaction not only the relative concentration of metal and oxide changes but also the changing distance from the interface for both metal and oxide species plays a role[69].

	Electronegativity	$E^0[V]$
Fe	1.6	-0.47
Co	1.7	-0.27
Ni	1.8	-0.23

Table 8.1: Thermodynamic Properties of Selected 3d-metals and their Oxides  
The table shows the electronegativity for Fe, Co and Ni as well as their reduction potential  $M^+ + e^-$ .

### 8.1.2 Results on Co/NiO

#### Thermodynamic Properties

One may already intuitively expect that an interface between a metal and an oxide is not sharp, because chemical forces that are not negligible at  $T > 0$  might drive oxygen to diffuse from the oxide into the metal layer. Table 8.1 shows the electronegativity and reduction potential of the three investigated species to illustrate this assumption. The electronegativity is a measure for the ability of a particular species to attract electrons. Fe and Co exhibit a lower electronegativity than Ni, which means that in the presence of oxygen predominantly Fe and Co will be oxidized compared to Ni.

This is also reflected in the reduction potential, which is lowest for Ni. It is concluded from these elemental data the general tendency that Co or Fe might be able to reduce NiO if they are in close contact.

#### XAS of the Co/NiO Interface

Co  $L_3$  and Ni  $L_2$  XAS spectra obtained from a (1nm)Co/(1nm)NiO sample are shown in figure 8.1. The reference spectra for the metals are represented in blue and the ones for the mono oxides are drawn in green. For demonstration purposes the thicknesses of the layers have been chosen so small so that the observed effects are very pronounced because the interfacial layer contributes with more than 25% to the total XAS signal. The spectra of the unknown sample is shown in red. The XAS intensity for the Ni- $L_2$  edge appears to be decreased compared to the oxide sample, indicating the increasing metallic character of Ni atoms in the film. On the other hand the spectrum obtained at the Co  $L_3$  resonance exhibits a multiplet character now and increased peak intensity. Both observations are an indicator of more oxidic character of the original metallic Co film.

Altogether the line shape observed for the unknown samples suggest that their XAS spectra can be represented as a superposition of the pure metal and the oxide. To corroborate this assumption the last spectrum in the graph (black) shows a linear combination of metal and oxide spectra to best fit the unknown spectra. An excellent agreement is achieved demonstrating that indeed at the interface a certain amount of Co is oxidized to CoO and NiO is reduced at the same time to Ni. The thickness of the interfacial layer consisting of  $\text{CoNiO}_x$  can be derived from the weighting factors used to for the fit. Considering an electron escape length of 2.5 nm one estimates that about a monolayer of Ni is formed on top of the

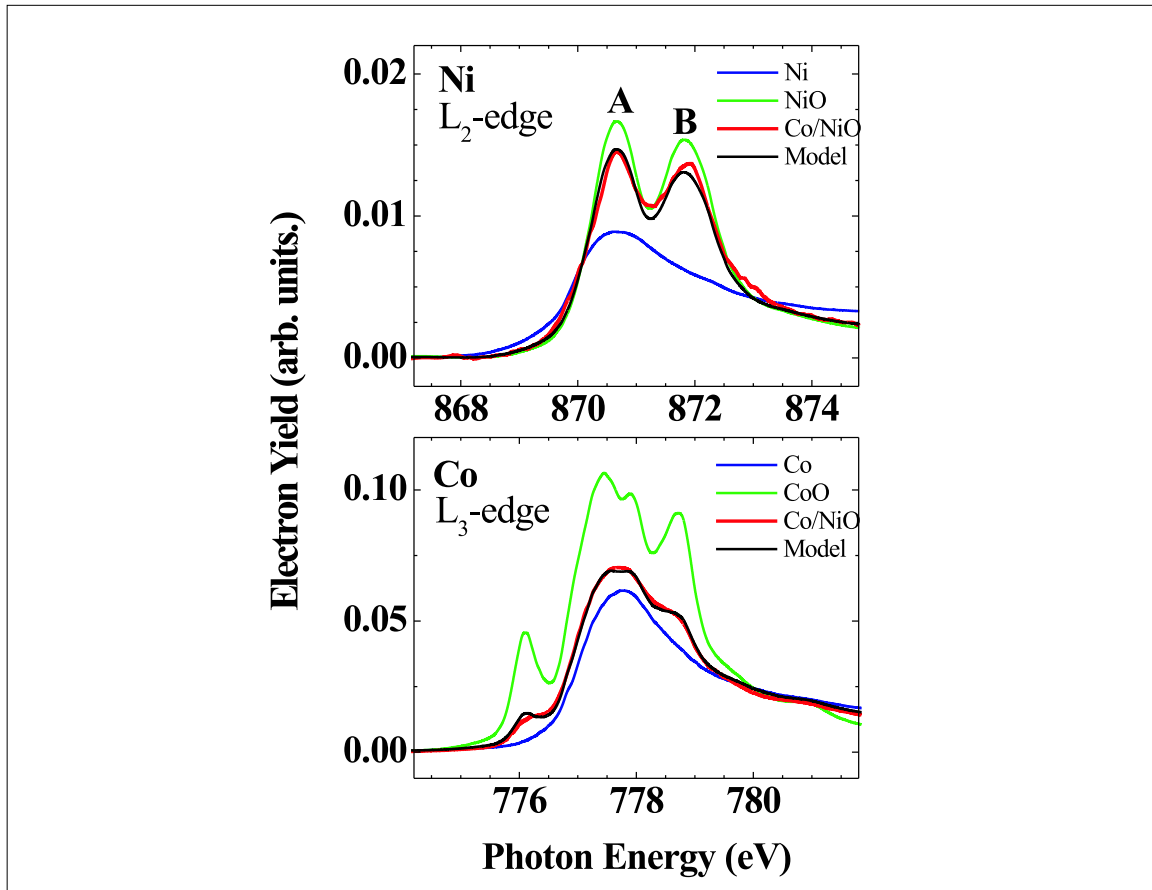


Figure 8.1: Absorption Spectra of Co/NiO

Absorption spectra obtained from (1nm)Co/(1nm)NiO in Co/NiO (red). These are compared to the reference metal (blue) and oxide (green) spectra. The black spectra shows a fit to the (red) Co/NiO spectra assuming that 1 monolayer of Co is oxidized and 1 monolayer of NiO is reduced at the interface.

NiO and a monolayer of CoO at the bottom of Co. Therefore the thickness of the interfacial  $\text{CoNiO}_x$  layer is 2 monolayer [61, 69].

For Fe/NiO a stronger initial interfacial redox reaction has been reported [69] due to the larger difference in the chemical potential. However the identification of the particular oxide which is realized at the interface is more difficult, because iron forms different stable oxides such as  $\text{Fe}_2\text{O}_3$ ,  $\text{Fe}_3\text{O}_4$  at room temperature. For Fe the best fit can be obtained by assuming a mostly  $\text{Fe}_3\text{O}_4$ -like interface, which is in accordance with electron energy loss spectroscopy studies<sup>2</sup>.

<sup>2</sup>V. Bocatius, private communication

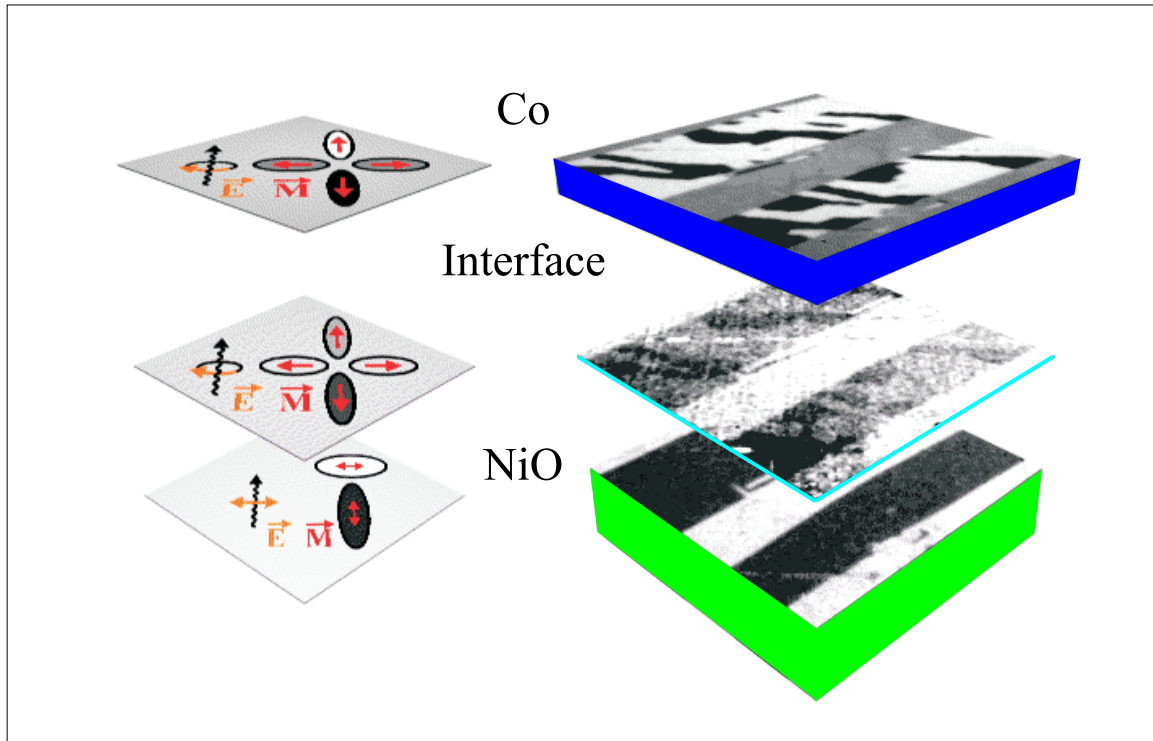


Figure 8.2: Interfacial Ni Moment in Co/NiO with AFM Contrast

Dichroism images of ferromagnetic Co (top, blue), antiferromagnetic NiO (green, bottom) and ferromagnetic Ni (cyan, middle) in Co/NiO. The legend on the left shows the polarization of the incoming light and the direction of the magnetization within each magnetic domain.

## 8.2 Free Interfacial Spins and Uniaxial Exchange Anisotropy

The knowledge about the *chemical interfacial reaction* obtained from thin films is now applied to the Co/NiO(001) samples discussed in the previous chapter to address the *magnetic order at the interface*. The XMCD signal arising from ferromagnetic metallic Ni sites within the  $\text{CoNiO}_x$  like interface is employed to obtain an image of the spatial distribution of the magnetic order at the interface. The possible formation and ordering of CoO at the interface is discussed as well.

The following experiments were again preformed using the PEEM2 instrument. Local absorption spectra were obtained from ferromagnetic Co and Ni domains. The energy resolution of beamline 7.3.1.1. is limited to  $E/\Delta E = 1500$ . For this reason it was difficult to perform a similar data analysis as discussed previously to extract the thickness of the chemical active layer. In this case the thickness will be estimated from the size of the magnetic signal arising from metallic Ni spins in the microscopy experiments.

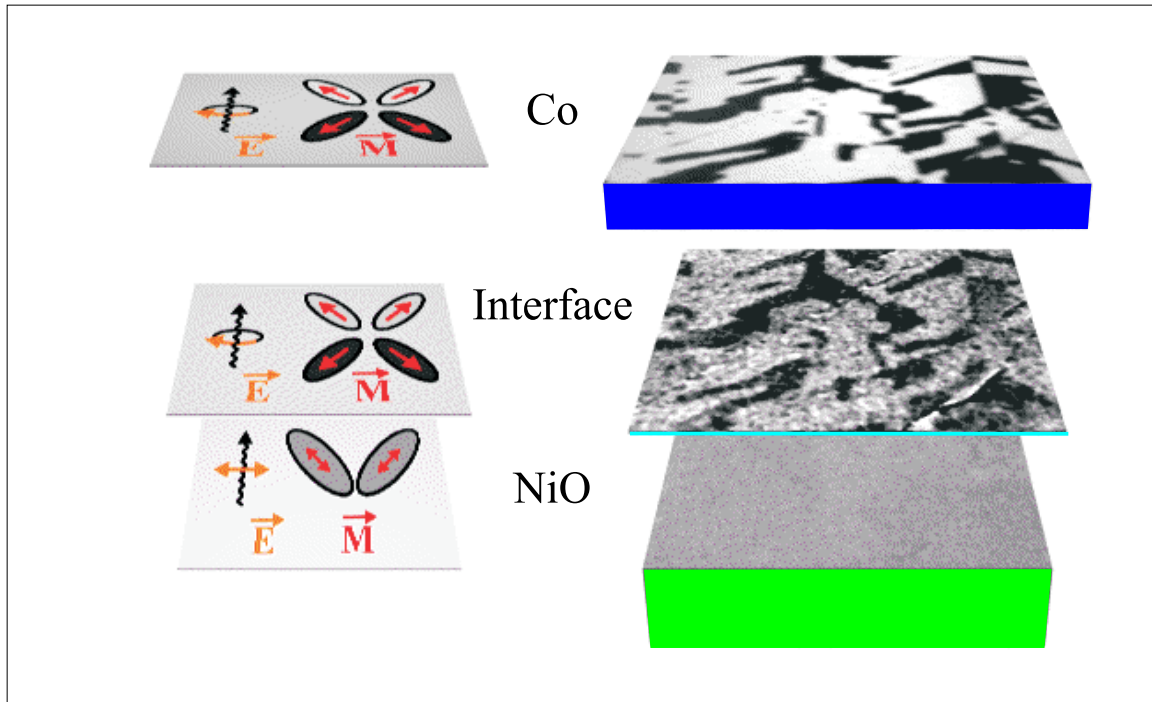


Figure 8.3: Pure Interfacial Ni Moment in Co/NiO without AFM Contrast  
 Dichroism images of ferromagnetic Co (top, blue), antiferromagnetic NiO (green, bottom) and ferromagnetic Ni (cyan, middle). Compared to figure 8.2 the sample had been rotated by  $45^\circ$  around its surface normal. No antiferromagnetic contrast is visible in this geometry. The ferromagnetic domain pattern observed for interfacial Ni forms an exact replica of the pattern observed in the Co layer.

### 8.2.1 Ni XMCD of a Buried Co/NiO Interfaces

Figure 8.2 shows XMCD images of ferromagnetic Co and Ni as well as an XMLD image of antiferromagnetic NiO. The geometry is chosen such that the in-plane electromagnetic field vector is parallel to  $[110]$ . The legend on the left side of the figure shows the direction of the incident x-rays, the polarization vectors and correlates image grey levels with the orientation of the magnetic moment within each domain. The Co XMCD images reveal three different contrast levels representing parallel, antiparallel and perpendicular alignment of the spin moment with respect to the helicity of the light. In addition XMLD contrast arising from antiferromagnetic domains in NiO can be seen and the parallel alignment between antiferromagnetic NiO and ferromagnetic Co is again observed.

By employing the Ni XMCD effect the interfacial spin polarization finally becomes visible. Again three different contrast levels are observed as in the Co XMCD images. The spatial distribution of the ferromagnetic Ni domains is a complete replica of the Co ferromagnetic

domain pattern demonstrating that they are the result of metallic Ni moments ferromagnetically exchange coupled to the Co domains. However, the relative contrast levels are different in the Co and the Ni XMCD images. This is due to the fact that the very small XMCD signal (0.3%) is still superimposed by the XMLD effect which does not exactly cancel out<sup>3</sup>

For this reason a second set of images had been acquired in another geometry in which no XMLD contrast is expected. This is shown in figure 8.3. The angle between antiferromagnetic axes and electric field vector is the same for both AFM domains and they cannot be distinguished. Now, the nickel XMCD contrast is not superimposed by the residual XMLD contrast in this geometry and the observed domain pattern for the interfacial Ni moments forms an *exact* replica of the domain pattern observed for the Co film and parallel coupling between interfacial Ni and Co along [110] is observed.

In the following the thickness of the  $\text{CoNiO}_x$  like layer is estimated from the size of the XMCD contrast. The XMCD contrast between two domains calculated from the image intensity is 0.5% in figure 8.3. The [110] directions include an angle of  $52^\circ$  with the polarization vector and the degree of circular polarization is 75%. Hence the corrected XMCD value is 1.0%. Taking into account these geometrical factors the corrected XMCD asymmetry between opposite domains reaches 1% in the *as prepared* state.

The maximum XMCD value expected for metallic Ni is 16% [16]. Assuming an electron escape length in NiO of 2.5nm the first monolayer contributes to the total signal with 8%. Hence an XMCD signal of 1.3% can be expected from a full monolayer of Ni on top of NiO. This leads to the conclusion that about 0.75 monolayer of Ni or 1.5 monolayer of  $\text{CoNiO}_x$  are produced by the interfacial chemical reaction and give rise to the interfacial spin polarization. Assuming layer by layer reduction of the NiO the following general expression is derived to calculate the thickness of the metallic Nickel layer from the corrected XMCD difference  $I_{XMCD}$ .

$$x = -2.5 \text{ nm} \ln\left(1 - \frac{I_{XMCD}}{16\%}\right) \quad (8.1)$$

A thickness of 0.75 monolayer for the *as prepared* sample is in accordance with results obtained on thin film samples earlier by Regan et al. [69]. The observed thickness of the  $\text{CoNiO}_x$  like interfacial layer is similar for single crystalline or polycrystalline samples. This shows that the thickness of the interfacial layer can be extracted from the size of the magnetic contrast arising from the metallic Ni atoms located at the interface as well as from a linear combination of metal and oxide reference spectra.

### 8.2.2 CoO XMLD of the Co/NiO Interface

The question remains whether or not the interfacial CoO is antiferromagnetic or forms a magnetically homogenous ferro(i)magnetic layer together with the Ni atoms. In other words, the question is whether the final sample structure is  $\text{Co/CoNiO}_x/\text{NiO}$  or  $\text{Co/CoO/Ni/NiO}$ . To address this question CoO XMLD images are acquired. Although the Néel temperature

<sup>3</sup>In principle the XMLD asymmetry is identical at the  $L_3$  and  $L_2$  NiO resonances. But since the line shape is slightly different it does not cancel out completely

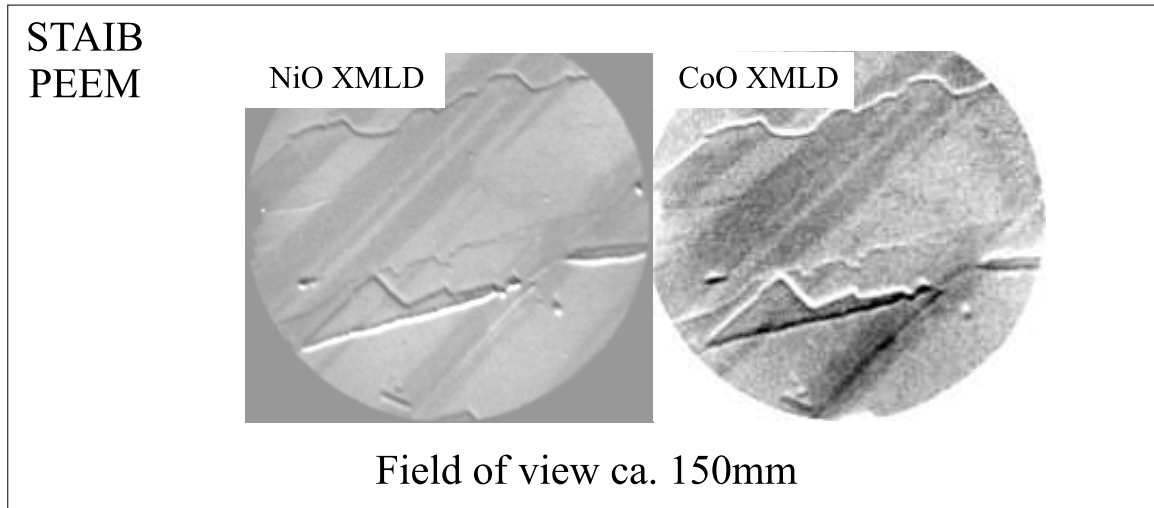


Figure 8.4: XMLD Images of 2ML of CoO Prepared on NiO at RT.

of bulk CoO is below room temperature (290K), a thin film of CoO will show magnetic order since it is exchange coupled to the other magnetic layers with much higher ordering temperature (see for example [13]). However images obtained with the ALS-PEEM2 on exchange coupled Co/NiO(001) never exhibited any CoO XMLD contrast.

To demonstrate that this is not due to the limited energy resolution of the beamline XMLD images obtained from 2 monolayers of CoO directly deposited on NiO obtained with the STAIB PEEM are shown in Figure 8.4. The CoO layer was deposited on a sputtered NiO surface in a  $10^{-6}$  mbar oxygen atmosphere using a Co electron beam evaporator at a deposition rate of about 0.5 monolayer/minute. The beamline optics were positioned such that the photon flux and the energy resolution of the UE56/1 at BESSY2 beamline were similar to beamline 7.3.1.1 at the ALS. CoO XMLD images are acquired by scanning the X-ray energy 0.6 eV lower and higher than the energy for the center of the CoO L3 absorption resonance. Comparing the XMLD images of CoO and NiO the parallel coupling and the antiferromagnetic order of the thin CoO film at room temperature can clearly be seen. The CoO domain pattern is identical to the NiO domain pattern. The XMLD asymmetry between adjacent CoO domains is about 2%. Using the same energies relative to the peak position a similar effect was never observed in the CoNiO<sub>x</sub> interfaces, although in principal dichroism effects of less than 0.5% can be observed. This leads to the conclusion that the interfacial CoO is not antiferromagnetically ordered but rather forms a single magnetic film together with the interfacial Ni spins

### 8.2.3 Temperature Dependence of the Interfacial Spin Polarization

So far the formation of an interfacial  $\text{CoNiO}_x$  layer as the results of a chemical reaction has been found. A gradient in chemical potentials across the interface is supposed to be the origin of this reaction. To corroborate this assumption the effect of annealing on the interface thickness will be studied. In particular the dependence of the interface thickness on the annealing time at 600K will be investigated. Six different samples were prepared by e-beam evaporation of 2nm Co on cleaved NiO(001) surfaces. Each of the sample was annealed at 600K in a base pressure of better than  $10^{-9}$  mbar, for 10, 20 (3 samples), 30 or 45 mins. The temperature was reached within less than one minute and dropped again below 400K within less than a minute. The data were taken at room temperature after waiting for typically another 10-15 minutes. Finally, a Ni XMCD image has been acquired for each sample before is was annealed. In all cases the initial XMCD contrast is about (0.3%-0.5%) and the net polarization of the interfacial Ni atoms follows perfectly the ferromagnetic Co domain pattern.

#### Determining the XMCD intensity

Results obtained from a particular sample after annealing for 30 minutes are now shown in Figure 8.5. In contrast to previous Ni XMCD images the XMCD contrast can easily be recognized and there is no superimposed XMLD information visible. The amount of ferromagnetic Ni at the interface appears to be increased compared to previous experiments.

To quantify the XMCD contrast image stacks across the L-absorption edges of Co and NiO were acquired. Local XMCD spectra of ferromagnetic Co and the still highly diluted ferromagnetic Ni spins within the buried interface are derived. Both spectra represent the average of black and white domains in the upper and lower part of the field of view of  $30 \mu\text{m}$ . The Co XMCD spectra does not show any deviations from bare Co metal. Of more interest is the line shape of the Ni XMCD. The photon energies at which the difference spectra reaches its maximum are 0.3 eV below the  $L_3$  edge and at the first peak of the  $L_2$  edge. As shown earlier in chapter 2.3.2 (see figure 8.1 for the NiO  $L_2$  resonance) these are exactly the energies where the absorption features of Ni metal appear relative to NiO. The observed ferromagnetically ordered Ni atoms in the XMCD images are therefore indeed the result of a chemical reaction and are located in a more metallic environment<sup>4</sup>.

It has been shown that for diluted ferromagnetic systems the  $L_3$  XMCD asymmetry scales with the total magnetic moment of the investigated species [64]. For this purpose the  $L_3$  XMCD asymmetry is calculated by  $(I^+ - I^- / I^+ + I^-)$ , where  $I^\pm$  denotes the XAS intensity for spin up or down domains at the  $L_3$  edge. Here, one obtains 2.2% (or 3.4% after taking into account the degree of circular polarization  $P_c = 75\%$ ). The thickness of the interfacial  $\text{CoNiO}_x$  like layer can be estimated from the size of the XMCD signal (or the number of ferromagnetic spins) by using equation (8.1).

<sup>4</sup>The small structures which appear on the high energy side of each peak in the XMCD spectra are most likely due to the energy dispersion of the monochromator which leads to a continuous energy shift of +(50-100) meV from the top of the image to the bottom. The spectra were not corrected for this energy shift.

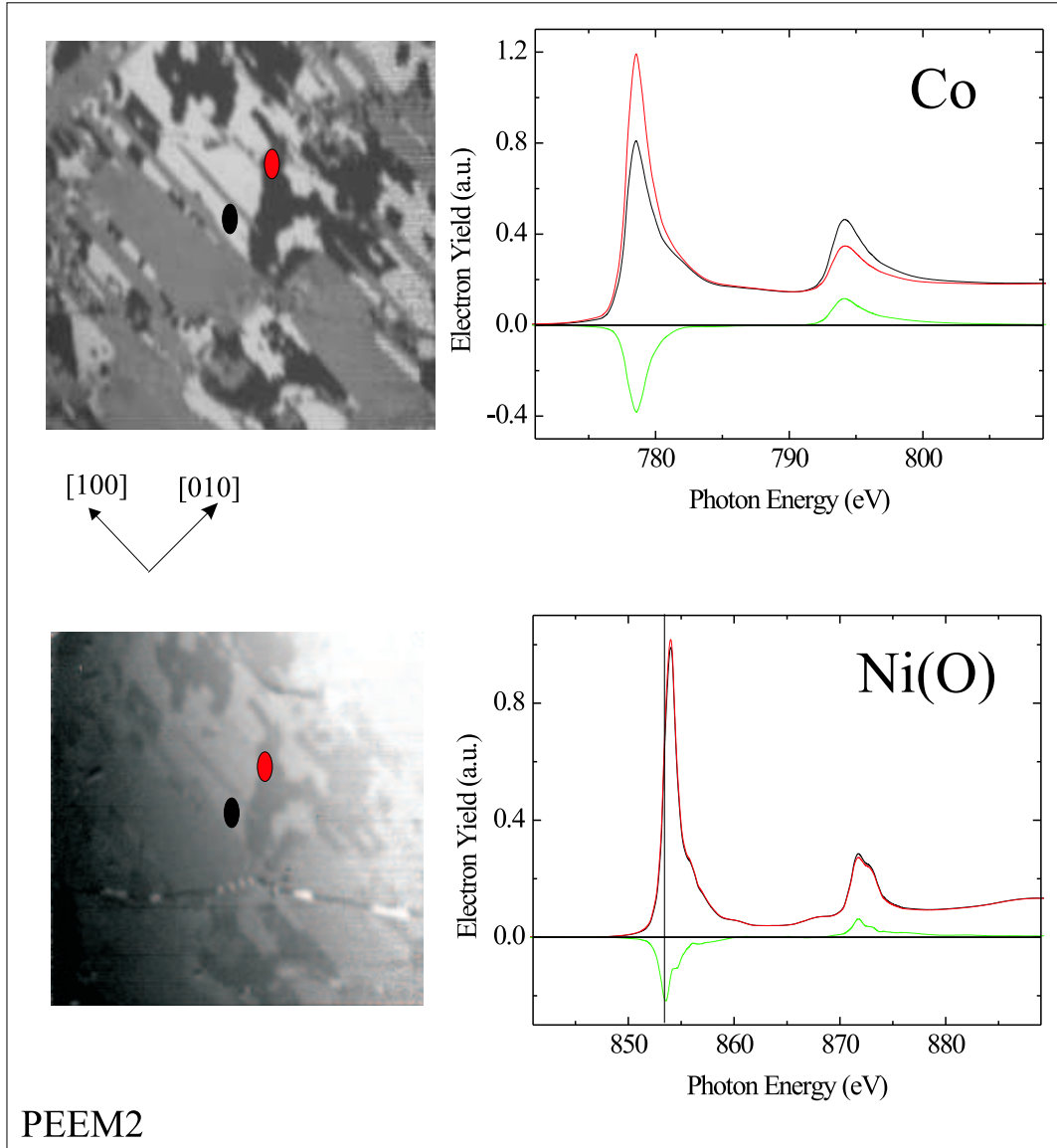


Figure 8.5: XMCD Spectra of Co and Interfacial Ni in  $\text{CoNiO}_x$

XMCD images of Co and Ni are shown. Image stacks are acquired at the Co and Ni L absorption resonances. XAS (black and red) and dichroism (green) spectra of ferromagnetic domains with opposite magnetization are shown on the right. The field of view is  $40\mu\text{m}$ .

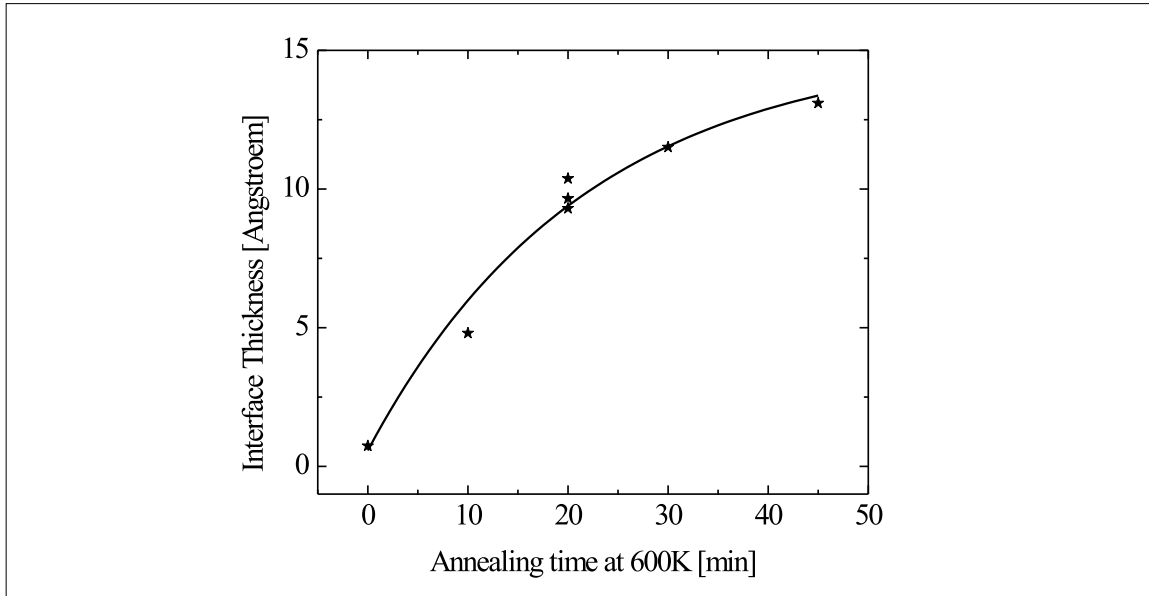


Figure 8.6: Interfacial Spin Polarization and Annealing

The interfacial spin polarization as determined from the Ni XMCD signal after annealing at 600K for 10, 20, 30 or 45 mins. The data were fitted with an exponential function. The saturation thickness is 1.5nm with a decay time of 21min. The arrow marks the data point obtained from the sample discussed in detail.

### Temperature Dependence

Figure 8.6 summarizes the result obtained from all samples. After an initially very strong increase the chemical reaction appears to slow down. This is a direct result of the decreasing gradient in oxygen concentration and difference in chemical potential with increasing interface thickness. After 45 mins of annealing at 600K the Ni metal layer reaches a thickness of 1.3 nm corresponding to a complete interface thickness of 2.6 nm.

At this point it should be noted that annealing of an exchange coupled system above its Néel temperature and subsequent cooling in an external field is a procedure often used to introduce the exchange bias field (field cooling). From the data presented here it becomes clear that already a very short annealing time of a minute above the Néel temperature of 520K will lead to a Ni metal thickness of 0.2nm or an interface thickness of 0.4nm. This already corresponds to one complete lattice plane. Since most theories attempt to describe exchange anisotropy assuming atomically flat interfaces, the reported observations are of crucial importance.

A study which corroborates the findings reported on NiO surfaces here has been presented by Farrow *et al.* [23] who investigated  $\text{Fe}_2\text{O}_3/\text{NiO}$  interfaces using transmission electron

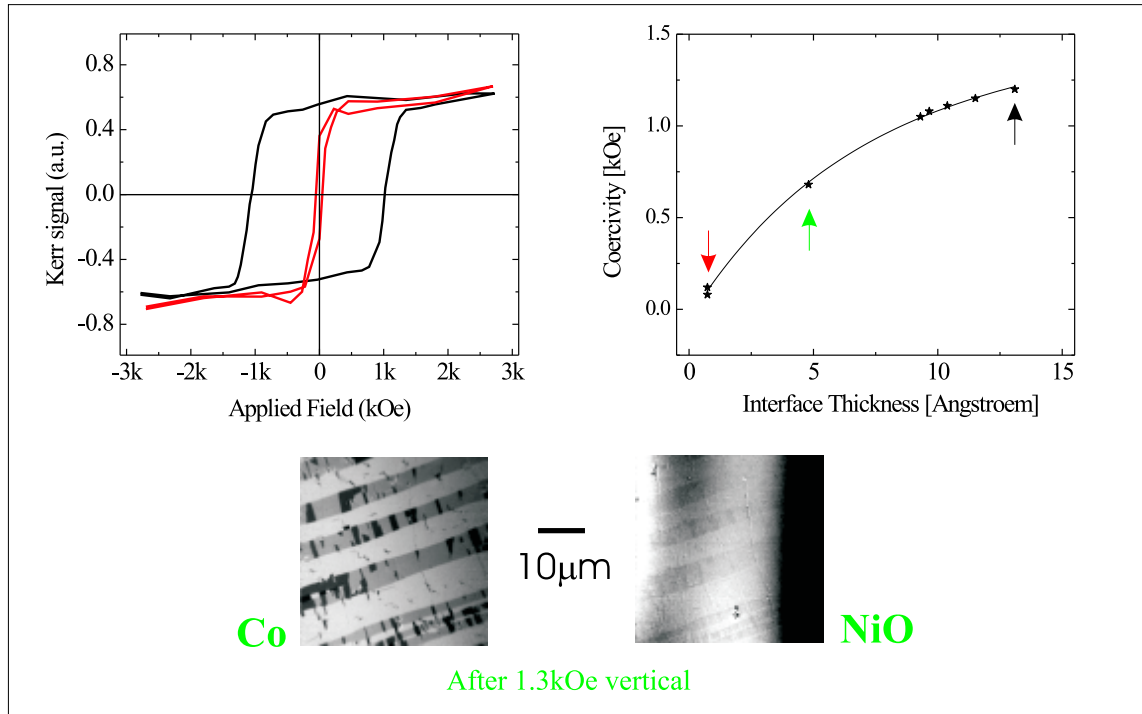


Figure 8.7: Relation between Interfacial Thickness and Coercivity.

Hysteresis loops obtained from Co/NiO(001) as prepared (red) and after annealing for 45 mins at 600K (red). The coercive fields for the samples described in figure 8.6 are shown on the right. The data were fitted exponentially with a maximum field of 1250Oe and a decay length of 0.7nm. On the bottom Co and Ni XMCD images of a third sample are shown before and after applying a vertical field of 1.3kOe. All the observed interfacial Ni moments follow the Co moments on top. Areas exhibiting an easy axis perpendicular to the direction of the applied field are not affected by the field indicating the existence of an uniaxial anisotropy.

microscopy (TEM). Upon annealing the formation of a  $\text{NiFe}_2\text{O}_4$  interfacial layer is observed. The advantage of the present XAS study that the samples can be studied *in-situ*, while the TEM samples need to be prepared to be penetrated by the electron beam. Furthermore magnetic information can be directly extracted, which has not been addressed in the TEM experiment.

### 8.2.4 Magnetic Properties

#### Temperature Dependence of Coercivity

The coercivity of the six samples investigated in the previous section is now determined by acquiring hysteresis loops using an *ex-situ* magneto-optical kerr effect (MOKE) to investigate

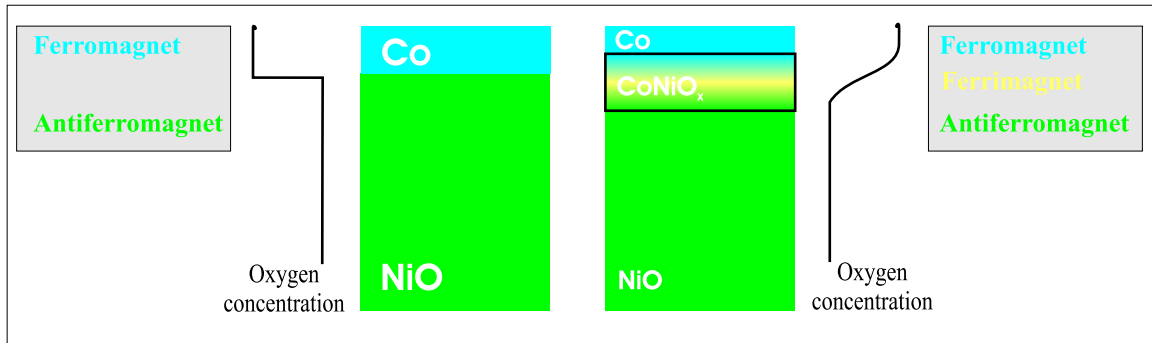


Figure 8.8: The 'Third' Layer in AFM/FM Pairs.

The figure illustrates the difference between AFM/FM model systems often assumed in theoretical work and the situation found in Co/NiO(001). Instead of a sharp interface between ferromagnet and antiferromagnet an additional third layer is formed by an interfacial chemical reaction. The magnetic properties of the layer are assumed to change gradually from antiferromagnetic over ferrimagnetic to ferromagnetic.

the correlation between the macroscopic magnetic properties and the chemical properties of the interface. The samples were capped with 5nm of Cu to prevent the Co layer from oxidation. The hysteresis loops were measured with the external field applied along one of the in-plane [110] axes. On the top left of figure 8.7 two hysteresis loops are shown. The loop drawn in black has been acquired from the sample with the largest interface thickness while the red loop has been taken from an *as prepared* sample. The difference in coercivity is obvious. The *as grown* film shows hardly any coercivity while the switching field of the annealed film is more than 1kOe. Nevertheless both hysteresis loops shows a distinct square shape pointing out that the system exhibits a uniaxial anisotropy. Note, that the MOKE signal still increases beyond the switching field. This behavior is caused by domains exhibiting an easy axis perpendicular to the applied field. They will show magnetic saturation at much higher fields, because of the uniaxial anisotropy.

The dependence of the coercivity on the thickness of the interfacial layer obtained from the six different samples is shown in the right panel of figure 8.7. The colored arrows indicate the data points obtained from samples discussed here in detail. Of special importance is the fact that the coercivity does not simply increase linearly. The increase in coercivity slows down with increasing interfacial thickness, exhibiting an exponential like behavior. This behavior rules out that the coercivity increase is simply caused by the additional volume anisotropy energy originating from the additional ferromagnetic material generated at the interface. A possible origin for this behavior is presented in the following.

### 8.2.5 Discussion: Interfacial Uniaxial Exchange Anisotropy

The reported observation can be understood by assuming that first only the *interfaces* contribute significantly to the increased coercivity and second a certain amount of  $\text{CoNiO}_x$  is necessary to form a complete interface. In figure 8.6 the dependence of the coercive field (and hence the uniaxial anisotropy) on the thickness of the interfacial layer  $t$  is fitted with the following exponential function:

$$H_c(t) = A \times (1 - \exp(\frac{-t}{0.7nm})) + B t + 50Oe \quad (8.2)$$

The linear term  $B$  represents the contribution to the coercive field caused by the volume anisotropy of the  $\text{CoNiO}_x$  layer, since the total thickness of the  $\text{CoNiO}_x$  layer is small this contribution is also relatively small. The fit yields a value of 30 Oe/nm for  $B$ . The last term in the equation corresponds to the coercivity resulting from the volume anisotropy of the top Co layer, which is assumed in good approximation to be constant (50Oe). The exponential term finally corresponds to the coercivity introduced by the uniaxial interfacial exchange coupling between Co and NiO mediated by the  $\text{CoNiO}_x$  layer. The exponential decay length of 0.7nm can be interpreted as the thickness which is necessary to establish a magnetically 'complete' interface. The value found here (0.7nm) is comparable to exchange lengths in ferromagnetic systems and appears therefore reasonable. It corresponds to about two lattice constants in the Co/NiO lattice, which means that two complete monolayers of  $\text{CoNiO}_x$  are needed to establish the full parallel uniaxial coupling between Co and NiO. The factor  $A$  represents the coercivity caused by this coupling and a value of 1.2 kOe is obtained. Exchange coupling across the 'third layer' is therefore the dominant source of coercivity in Co/NiO.

Figure 8.8 illustrates the role of the magnetically active interface. On the left side the situation at an ideal interface with a sharp drop in oxygen concentration is shown. Such an ideal magnetically compensated interface would show spin flop coupling as predicted by Koon *et al.* [40]. However, the results reported here suggest that the ideal compensated interface does not exist and chemical roughness has to be taken into account. The oxygen concentration decays gradually into the Co forming the  $\text{CoNiO}_x$  region. The magnetic ordering in this region is assumed to be changing gradually from antiferromagnetic over ferrimagnetic to ferromagnetic. For this reason spin frustration at the interface as the main source of (perpendicular) spin flop coupling is avoided and parallel coupling between the ferromagnet the antiferromagnetic can be achieved.

### 8.2.6 Summary: Origin of Coercivity Increase

1. For the first time a complete chemical and magnetic characterization of interfacial spins in an antiferromagnetic/ferromagnetic system has been achieved.
2. A chemical reaction at the Co/NiO interface is observed which leads to the formation of an ultrathin  $\text{CoNiO}_x$  like layer at the interface.

3. This interfacial layer exhibits a net magnetic moment which can be detected employing the XMCD effect of metallic Ni spins. The net interfacial moment is parallel to the Co moment and collinear to the antiferromagnetic axis in NiO.
4. The size of the parallel uniaxial exchange anisotropy is correlated to the size of the interfacial moment.

It has been demonstrated that on a presumably compensated antiferromagnetic surface as NiO(001) an uncompensated spin structure can be obtained. **All** the theoretical models presented in section 1 hold the presence of uncompensated interfacial spins essential for exchange bias, however it appears that this is not sufficient. It is shown here that interfacial spins follow the ferromagnetic spins if they are not tightly locked to the antiferromagnet. This is the situation of strong interfacial coupling between a ferromagnet and an antiferromagnet exhibiting a small anisotropy, where and no preferential magnetic direction can be established. As a result only uniaxial interfacial coupling or an increase in coercivity is found in such a system and no unidirectional coupling [61].

It is finally important to note how these results connect the model for AFM/FM exchange coupling predicted by Koon [40] in which perpendicular coupling instead of parallel coupling is predicted for the same system considered here. However, Koon assumed perfectly flat interfaces and stated that already small imperfections might lead to the observation of parallel coupling. Since it appears that perfect interfaces in that sense are not achievable, spin-flop coupling is not observed on magnetically compensated NiO(001) surfaces.

### 8.3 Interfacial Spins and Unidirectional Exchange Anisotropy

In the previous chapter the observation of uncompensated spins at the Co/NiO(001) interface have been reported. The findings indicated that these interfacial spins are more strongly coupled to the ferromagnetic Co layer than to the antiferromagnetic NiO spin matrix and they have been identified as the source for the **uniaxial interface exchange coupling**. The goal is now to identify the fraction of interfacial spins that are responsible for the **unidirectional exchange coupling**. These spins are assumed not to follow the ferromagnet along upon field reversal but keep their original direction which is defined by the cooling field.

For this purpose a polycrystalline (3nm)Co/(50nm)NiO films has been deposited on a Si wafer with an average grain size of 25nm (section 4) which is small enough so that such a sample shows exchange bias. XMCD hysteresis loops of the interfacial Ni moments as well as the Co moments have been acquired. Both loops are analyzed regarding their horizontal loop shift as well as their saturation magnetization. Only the loop originating from interfacial Ni spins exhibit an asymmetry in saturation magnetization, a vertical loop shift, caused by so-called *pinned moments*. The fraction of pinned moments covering the interface is estimated to be about 4% and finally the size of the observed bias field can be accounted for by this coverage.

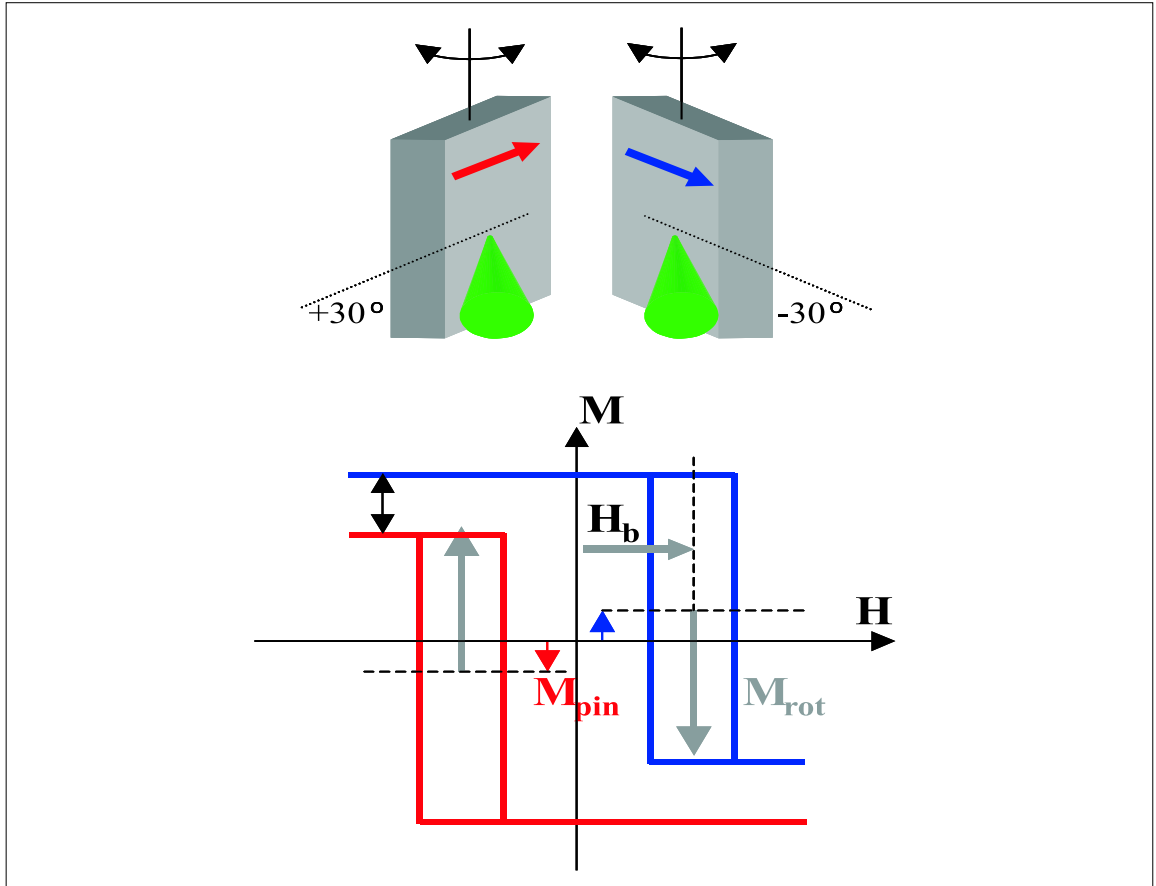


Figure 8.9: Vertical versus Horizontal Loop Shift in Interfacial Hysteresis

Top: X-rays are incident onto the sample under an angle of  $\pm 30^\circ$  such that the bias field (red and blue arrow) exhibits either a positive or negative projection onto the propagation direction of the x rays. An external magnetic field is applied collinear to the propagation direction of the light.

Bottom: Interfacial hysteresis loops acquired in the two geometries exhibit an opposite horizontal loop shift due to the opposite unidirectional anisotropy  $H_b$ . If not all the moments at the interface rotate ( $M_{\text{rot}}$ ) with the ferromagnet, but remain pinned ( $M_{\text{pin}}$ ) in one direction defined by the cooling field an additional vertical loop shift is observed.

### 8.3.1 Pinned Interfacial Spins and Exchange Bias

In the following the experimental setup is described. The experiments were performed using the elliptical undulator source at beamline 4.0.1 at the Advanced Light Source in Berkeley. For the experiments reported here the degree of circular polarization was switched between  $\pm 81\%$ . The top panel of figure 8.9 shows the experimental geometry. X-rays focussed on the sample are represented by the green cones. The sample can be rotated such that the

grazing angle is changed between  $+30^\circ$  and  $-30^\circ$ , so that the direction of the horizontal loop shift, indicated by the blue and red arrows can be changed. The external magnetic field and the propagation direction of the incoming x-rays are parallel. The XAS signal was detected in the total electron yield mode while the field was swept between  $\pm 2800$  Oe to acquire the hysteresis loop. An electric field of  $+1$  keV was applied to the sample to extract the secondary electrons.

In the lower panel the effect of pinned interfacial spins on the shape of the interfacial Ni hysteresis loops acquired in the two different geometries is sketched. The difference between the two geometries is that the direction of the unidirectional anisotropy and a particular helicity of the incident x-rays is either parallel or antiparallel. As a result two hysteresis loops of identical amplitude but shifted vertically against each other will be measured, since the amplitude of the hysteresis loop originating from the rotatable spins does not depend on the geometry. On the other hand the XMCD signal originating from the pinned spins does change its sign. Upon reversal of the helicity the vertical shift is then reversed as well. The fraction of the pinned moments with respect to all ferromagnetic (Ni) moments at the interface can be directly determined from the vertical loop shift.

$$\frac{M_{pin}}{M_{rot}} = \frac{V}{2M_{sat}} \quad (8.3)$$

In principle the vertical loops shift can be determined from just one loop, by simply comparing the saturation magnetization for positive and negative applied field. However this requires to determine the zero line, the signal that is obtained for zero magnetization very precisely.<sup>5</sup> In the following it will be shown that this cannot be guaranteed with the necessary precision by using XMCD because of the feedback between magnetic field and electron yield. For this reason two loops in 'opposite' geometries are acquired.

### 8.3.2 Hysteresis Loops using XMCD

Before the results obtained from the element specific hysteresis loops are presented, the technique itself is discussed in more detail and a qualitative idea will be presented why it is possible to measure element specific magnetic hysteresis loops by employing the XMCD effect. Although the sensitivity of x ray circular dichroism to ferromagnetic order has been already well established only recently experiments were published which made use of this effect to measure element specific hysteresis loops [29, 47]. The major difficulty, is that the electron yield itself is affected by magnetic fields around the sample as illustrated in figure 8.10. X-rays are incident on the sample and eventually will excite secondary electrons as shown in the left panel. If the component of the kinetic energy of such an electron perpendicular to the surface is large enough (blue arrow) it will leave the surface and contribute to the electron yield, otherwise the electron will not be able to leave the sample (red). If now an additional magnetic field is present the electron propagation is not straight anymore but

<sup>5</sup>Note, that as described in section 2.3.3 dichroism based methods typically detect the projection of the magnetization along *one* particular direction

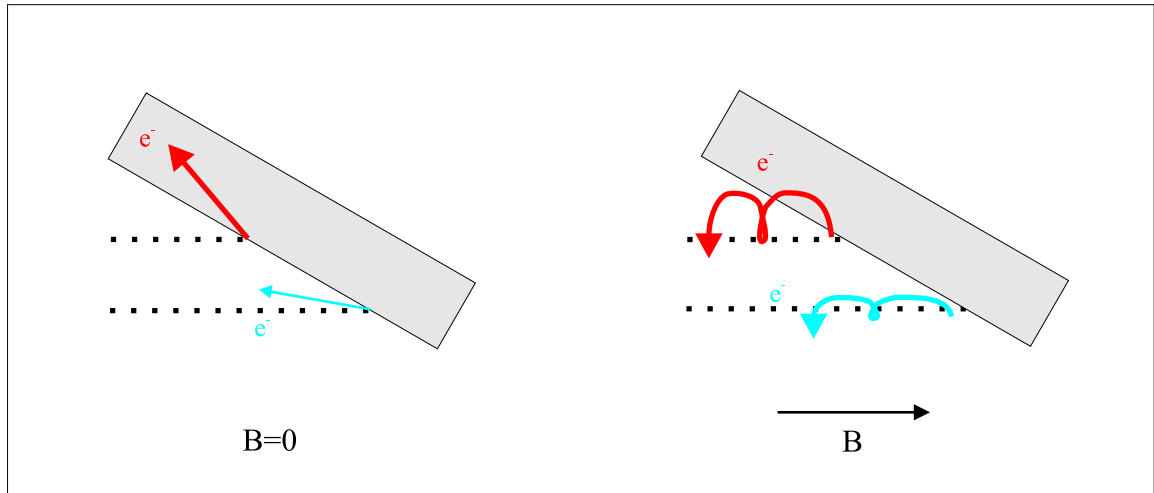


Figure 8.10: How External Magnetic Fields Influence the Electron Yield

Without an external magnetic field the size of the component of the velocity of the electrons perpendicular to the surface will decide whether the electron can leave the sample or not (left). In the presence of a magnetic field however (right) electrons propagate on cycloids. In this case it is possible that an electron which would originally remain in the sample comes close to the surface on such a trajectory and finally passes the surface into the vacuum.

rather forms a cycloid. The orbiting frequency equals the cyclotron frequency typically a few GHz. Furthermore, the radius is given by the velocity perpendicular to the applied field and is inversely proportional to the field. For electrons with a kinetic energy of less than 10 eV which contribute most of the electron yield the radius and the height of the cycloid both are of the order of  $100 \mu m$ , so that the situation depicted in the figure can indeed be realized. This means that an electron which would not be able to leave the sample without external magnetic field can eventually contribute to the electron yield in a magnetic field. The electron yield signal detected in an external field  $I^B$  is now the result of a modulation of the original electron yield  $I$  and a function of the external field  $f(B)$ , or  $I^B = I f(B)$ <sup>6</sup>. In general the presence of an external field will lead to an increase in the electron yield up to a certain value until a saturation situation is reached. It has now been proposed [29, 47] that it is possible to suppress the influence of this modulation by appropriate normalization procedures. All of these procedures have in common that they assume that the modulation function  $f(B)$  does not depend on the photon energy or the original electron yield. The normalization procedure which is used here and is similar to the one used by Lee *et al.* is described in the following. The polarization and magnetization dependent absorption signal at the L resonances has

<sup>6</sup>To the best of the authors knowledge no theoretical description of the function  $f(B)$  has been published so far. The empirical approach presented here has been corroborated by other authors as well [29, 47]

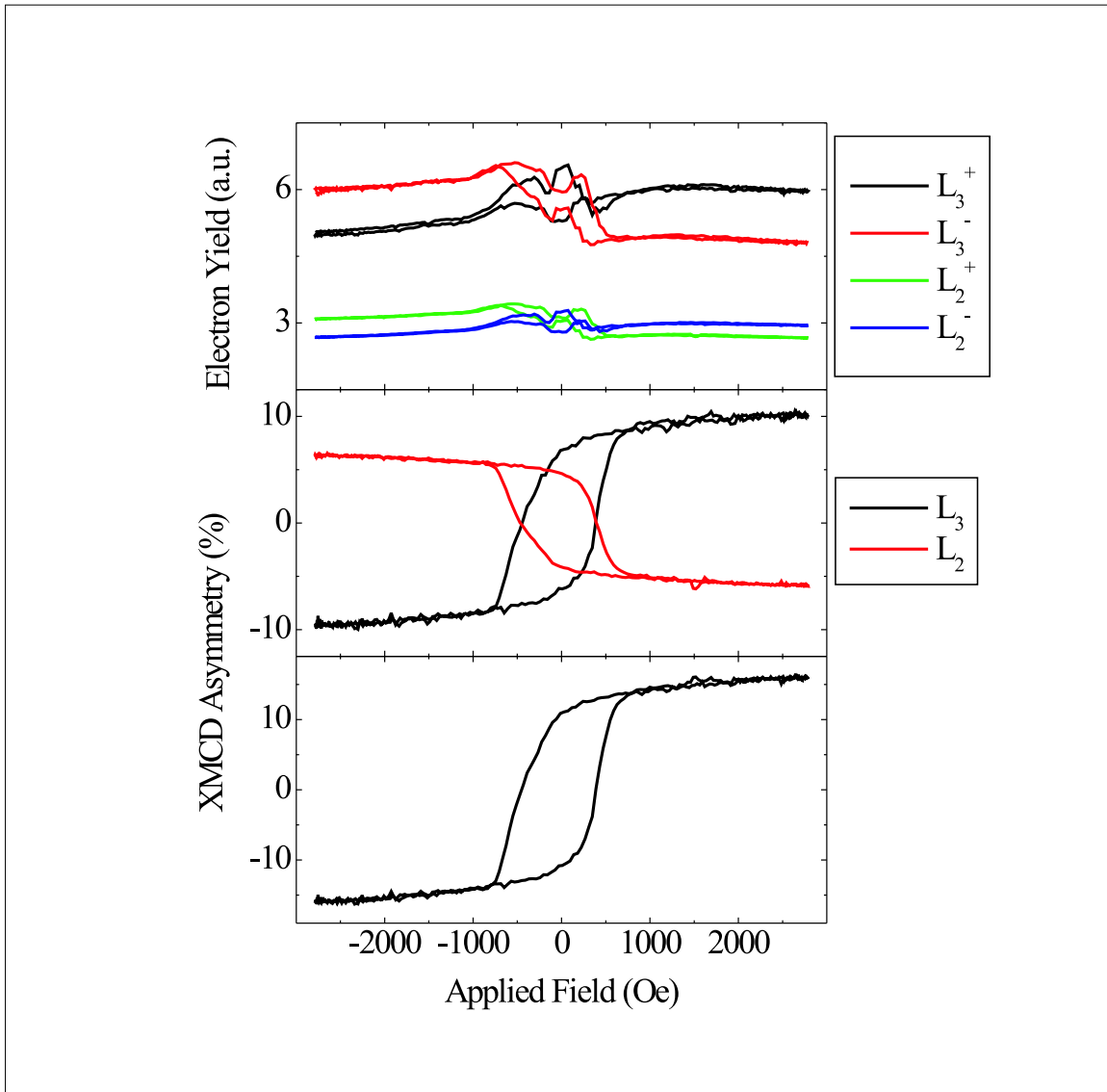


Figure 8.11: How To Measure Element Specific Hysteresis Loops Using XMCD

Top: Four hysteresis loops acquired at the Co  $L_3$  and  $L_2$  absorption resonance by electron yield detection using left and right circular polarization. The loops exhibit magnetic hysteresis-like behavior superimposed by a field dependent distortion centered around zero field.

Center: Asymmetry of two loops acquired at the same x-ray energy but with opposite helicity. The sign and the size of the loops is in accordance with the  $L_3$  and the  $L_2$  XMCD effect. A small positive vertical shift of +1% is still present in both loops.

Bottom: The difference loop between the two loops shown in the center panel is centered around zero magnetization.

been introduced in chapter 2.3.4 using equation 2.10. In a particular geometry the electron yield intensity  $I_{3/2}^{\pm}$  for positive or negative but equal absolute value of the x ray helicity<sup>7</sup> is given in the following. The previously discussed field dependent modulation function  $f(B)$  is considered as well. At the  $L_3$  or  $L_2$  resonance the electron yield intensity is then given by the sum of an isotropic contribution  $I^0$  and a contribution proportional to the expectation value of the magnetic moment parallel to the helicity of the x rays. The proportionality factor  $c$  is different for the two resonances and of opposite(!) sign.

$$\begin{aligned} I_3^{\pm} &= [I_3^0 \pm c_3 \langle M \rangle] f(B) \\ I_2^{\pm} &= [I_2^0 \pm c_2 \langle M \rangle] f(B) \end{aligned} \quad (8.4)$$

In principle it is now possible to acquire four different loops, two at each resonance with opposite polarization of the x rays. Such loops acquired at the Co L edges are shown in the top panel of figure 8.11. Data taken at the  $L_3$  or  $L_2$  edge can be identified by their different average intensity, since the x-ray absorption at the  $L_3$  edge is twice as strong as at the  $L_2$  edge. Altogether a hysteresis like behavior of these loops is observed. The loops show features similar to saturation and remanence but appear distorted especially around zero field. This distortion is caused by the feedback of electron yield and magnetic field ( $f(B)$ ). Since the variation of the electron yield signal due to the circular dichroism is much stronger than modulation  $f(B)$  in this case only a 'dip' in the signal around zero field up to 300 Oe is detected.

To extract the signal which originates from the magnetic moment of the sample alone, the asymmetry of two loops acquired at the same absorption edge is calculated.

$$\begin{aligned} I_3 &= \frac{I_3^+ - I_3^-}{I_3^+ + I_3^-} = \frac{c_3 \langle M \rangle}{I_3^0} \\ I_2 &= \frac{I_2^+ - I_2^-}{I_2^+ + I_2^-} = \frac{c_2 \langle M \rangle}{I_2^0} \end{aligned} \quad (8.5)$$

The resulting loops are directly proportional to the magnetic moment of the investigated species, since they directly correspond to the XMCD asymmetry at the respective L-edge. The middle panel in figure 8.11 shows the result. The loops now clearly resemble magnetic hysteresis loops and characteristics like saturation and remanence are clearly visible. The two loops exhibit a different sign and amplitude, however the general symmetry is identical. Even the fact that the magnetization reversal is not symmetric (different curvature for different branches of the hysteresis loops) is observed in both loops. The final hysteresis data set  $I_M(H)$  is now obtained by subtracting the two loops from each other  $I_M(H) = I_3 - I_2$ , shown in the lower part of figure 8.11<sup>8</sup>. This particular normalization step improves the overall signal to noise ratio and it eliminates the residual small vertical loop shift of about

<sup>7</sup>For example  $P_c = 81\%$  as used in this setup.

<sup>8</sup>Note that the saturation branches of the loops do still show a little gradient which is due to the fact that the external field is applied at  $30^\circ$  to the surface and thus the magnetization of the sample will be slowly dragged out of the surface plane into the field direction at higher fields.

0.5% observed for both loops. This so called 'isotropic' shift is observed even at non-resonant photon energies. By subtracting the two loops the resulting data set is centered around zero magnetization. It could empirically be shown, that this step of the normalization procedure leads to satisfactory results even when the XMCD signal is much smaller ( $< 1\%$ ) as for example on unbiased Co/NiO(001) or Co/IrMn.

In principle XMCD hysteresis loops can also be acquired by detecting the intensity of the reflected light with an photodiode appropriate for the wavelength used here. The detection of photons does have the advantage that they are not influenced by the external magnetic field, however their detection is much less surface and interface sensitive. Even right at absorption resonance where the penetration depth is short it is still of the order of 10nm<sup>9</sup>. Furthermore the size the shape and even the sign of the dichroism depends strongly on the experimental geometry and the sample structure. A straight forward interpretation of the acquired data as in case of the electron yield is typically not achieved for data obtained in reflection.

### 8.3.3 Diluted Pinned Interfacial Spins

The experimental results obtained from interfacial hysteresis loops on exchange biased Co/NiO are presented in the following. To quantify the total number of interfacial spins XMCD spectra of Co and NiO were obtained first, shown in the upper panel of figure 8.12. The external magnetic field was switched for every data point between  $\pm 2800Oe$ , while the helicity of the incoming x-rays had been kept fixed. The thicker Co film shows a strong XMCD effect. A very small but nevertheless clearly visible dichroism signal parallel to the one arising from the Co layer is observed in the Ni signal. Similar to the microscopy study the size of the dichroism at the Ni L<sub>3</sub> is used to determine the Ni thickness. After background subtraction the XMCD signal equals 0.4% from which a coverage of 0.45 monolayer is estimated (eqn. (8.1)). Regarding the 'free' interfacial moments these results are in perfect agreement with the results obtained from single crystalline NiO.

Next, element specific hysteresis loops are acquired. For each geometry a single Co loop (L<sub>3</sub>, L<sub>2</sub>, both polarizations as described in the previous section) and the average of 22 Ni loops are shown. All loops exhibit a horizontal loop shift. Loops acquired in different geometries (red and black) consequently exhibit an opposite loop shift, since the relative orientation of unidirectional anisotropy and external field axis is opposite. The interfacial energy density  $\sigma$  of this particular sample is determined from the exchange bias field measured in the Co loop,  $H_B = 1200e$  or 9.6kA/m. The interfacial energy density has been defined in section 1 as the actual loop shift normalized to the thickness and the magnetization of the ferromagnet.

$$\sigma = H_B M_{FM} t_{FM} \quad (8.6)$$

Together with the thickness of the ferromagnet (3nm) and the bulk magnetization of Co ( $1.82 \frac{Vs}{m^2}$ ) an interfacial energy density of  $50 \frac{\mu J}{m^2}$  is obtained. The error for this value is estimated to be 12%, mainly originating from the accuracy with which the external field and the film thickness can be measured.

---

<sup>9</sup>J. B. Kortright private communication

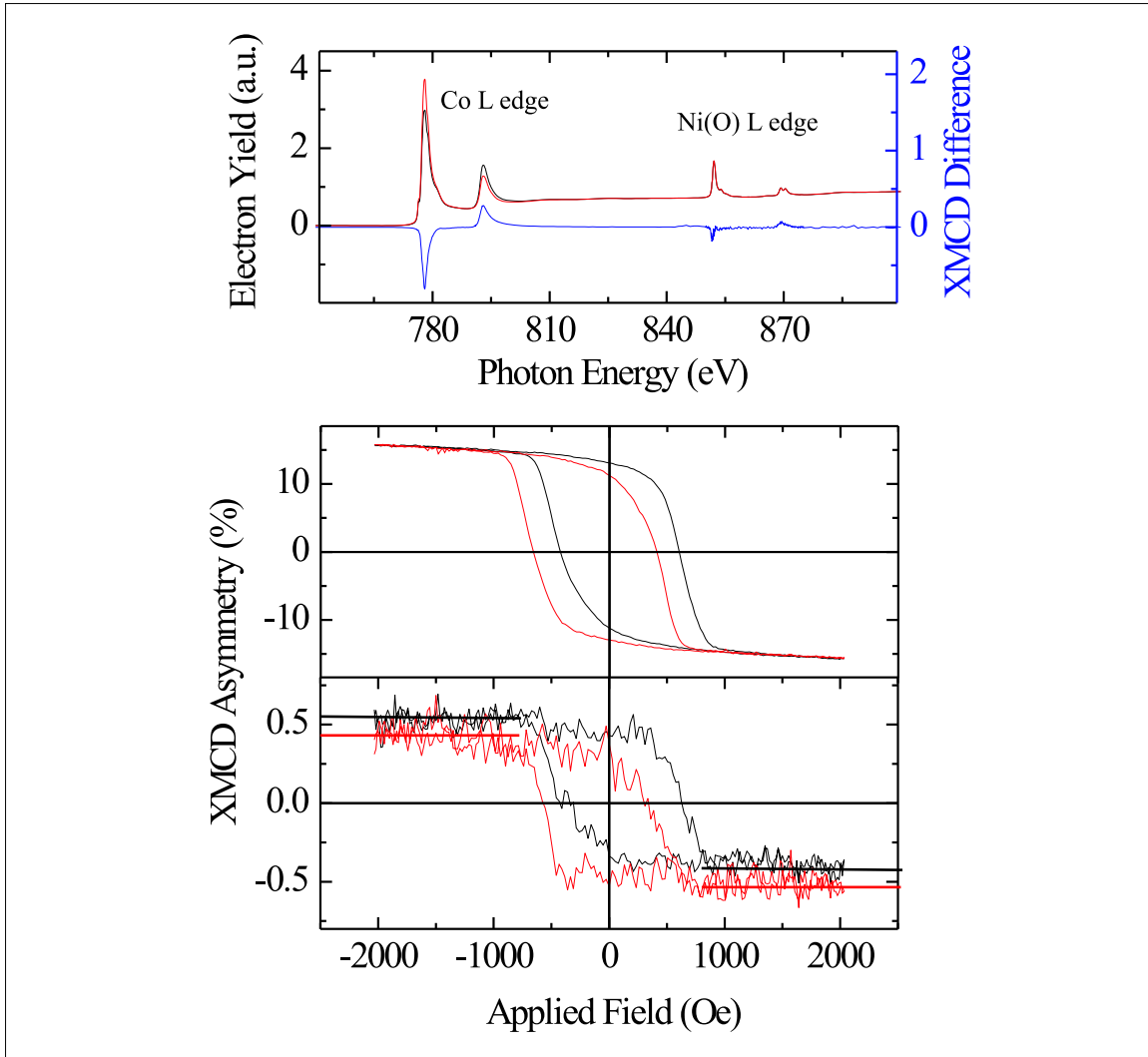


Figure 8.12: XMCD Spectra of Co and NiO in Polycrystalline Co/NiO

Top: XMCD spectra of Co and NiO. The difference shows the same behavior for both species (negative values at the  $L_3$  and positive values at  $L_2$  resonance), indicating the parallel alignment of Co and Ni spins.

Bottom: Hysteresis loops of Co and Ni acquired in the two different geometries (black and red) introduced earlier. The saturation magnetization of the two Co loops are identical while the Ni loops exhibit a small vertical loop shift, originating from pinned interfacial spins. Horizontal lines serve as a guide to the eye. The horizontal symmetry of the two loops is identical. Co and Ni loops show a distinct horizontal loop shift and coercivity which is identical for both species indicating again the parallel interfacial exchange coupling between 'free' interfacial moments and the ferromagnetic Co layer.

The Ni hysteresis loop appear noisier than the Co loop due to the much smaller signal, however the parallel exchange coupling between 'free' interfacial moments and Co layer is clearly demonstrated by the identical exchange bias and coercive field. In addition a vertical displacement as predicted earlier is observed. For example, the black loop is vertically shifted upwards, indicating a 'positive' pinned magnetization. At the same time the loop is shifted horizontally to the right, along the 'positive' field direction<sup>10</sup>. Altogether, the positive pinned magnetization causes the system to be preferentially magnetized into the positive magnetization direction. This means that the exchange coupling between pinned moments and the Co layer is ferromagnetic as well. The Co loop does not show any vertical shift, indicating that the pinned moments are exclusively located within the interfacial layer formed by the metallic like Ni moments and adjacent Co atoms. Even if the bottommost Co layer contains the same fraction of pinned spins as the topmost Ni layer their contribution to the total Co signal is 20 times smaller due to the larger thickness of the Co layer, compared to the CoNiO<sub>x</sub> interfacial layer.

The fraction of pinned moments is finally calculated from the vertical loop shift. The maximum XMCD signal detected in the loops is  $\pm 0.55\%$ , while the vertical offset is  $0.1\%$ . The fraction of pinned spins of the total uncompensated spins is then  $9\%$  of  $0.45$  monolayer or  $0.04$  monolayer. The experimental error for this number is estimated in the following. The maximum XMCD is known with an accuracy of  $10\%$ . The error for each of the determined XMCD intensities as well as the vertical loop shift is assumed to be about  $20\%$ , while the fraction with which the first monolayer contributes to the total signal exhibits an accuracy of  $15\%$ . Altogether the overall uncompensated spin coverage can be determined with an error of  $27\%$ , while the error for the pinned fraction is  $34\%$ .

#### 8.3.4 Discussion: Interfacial Unidirectional Exchange Anisotropy

In section 1.2 the rather simple Meiklejohn-Bean approach for Exchange Bias has been introduced. In this model the antiferromagnet is imagined to be completely rigid and uncompensated at the interface. A Heisenberg type exchange right at the interface is further assumed and the following expression for the exchange bias field and interfacial energy can be derived.

$$H_B = \frac{\sigma_{\text{int}}}{M_{\text{FM}}T_{\text{FM}}} = \frac{J_{\text{F/AF}}}{a^2 M_{\text{FM}}t_{\text{FM}}} \quad (8.7)$$

For reasonable values of  $J = 2.5$  meV [66] the exchange bias field is overestimated by several orders of magnitude using this approach. Assuming a typical lattice constant of  $0.4\text{nm}$  one would expect to observe a macroscopic bias field of about  $5700\text{Oe}$  from a fully uncompensated and rigid interface.

The experimental results now suggest that the interfacial energy  $\sigma_{\text{int}}$  has to be replaced by an effective value  $\sigma_{\text{int}}^{\text{eff}}$ , which is obtained by multiplying  $\sigma_{\text{int}}$  with the coverage of pinned

---

<sup>10</sup>Note, that positive and negative are not defined in an absolute way in this experiment. However, as long as the experimental setup is not systematically changed (switching cables, changing the undulator etc), the relative orientation is kept fixed

spins, in this case 0.041. This is warrantable because it has been 'microscopically' found that only  $(0.041 \pm 0.014)$  monolayer of the interface does contribute to the unidirectional anisotropy. In this case the expected loop shift is decreased to 230Oe, which represents an excellent agreement with the actual value (130Oe), considering the experimental challenge to detect the magnetic signal of much less than 10% of a buried monolayer.

A possible source for the remaining discrepancy is that the approach described here assumes that pinned as well as the rotatable spins are only located right at the interface. Nevertheless it is likely that the uniaxial coupling as well as the pinning decreases gradually over a few monolayer into the bulk of the antiferromagnet. In this case spins that are separated by one or two monolayer from the interface are detected in the interfacial hysteresis loop and contribute to the *vertical* loop shift. On the other hand their contribution to the *horizontal* loop shift is much smaller due to the very short ferromagnetic exchange length which is of the order of atomic distances.

Finally the value for the coverage with pinned spins of 0.041 is discussed considering the work by Takano again [93]. He suggested that the spins which are responsible for exchange bias are mostly located at grain boundaries. The average grain size in the investigated sample is about 25nm as shown by atomic force microscopy<sup>11</sup>. The area covered by a 25nm grain is  $6.25 \cdot 10^{-16} m^2$ , including 3900 unit cells with a lattice constant of 0.4nm. Its circumference is 78nm, consisting of about 200 atomic sites. Altogether one finds that grain boundaries cover about 2-3% of the interface, considering that two grains share a boundary. A comparison of this number with the pinned coverage determined in the experiment indeed suggests that the location of the pinned spins coincidences with grain boundaries as proposed by Takano.

### 8.3.5 Summary: Origin of Exchange Bias

1. Element specific hysteresis loops on a polycrystalline Co/NiO sample are acquired using XMCD. A horizontal loop shift of 130Oe is observed. Furthermore the surface sensitivity of the electron yield method allows to detect the hysteresis loop originating from 0.45 monolayer of Ni at the interface between NiO and Co.
2. The interfacial hysteresis loop exhibits a vertical shift caused by pinned moments covering about 4% of the interface, which do not follow the external magnetic field. These 'pinned' interfacial moments are ferromagnetically coupled to the Co layer as it has been observed for the 'free' moments.
3. The size of the horizontal loop shift can be attributed for by employing the simple Meiklejohn and Bean approach for exchange bias and assuming that only pinned spins contribute to the unidirectional anisotropy.
4. The coverage with pinned spins is close to the fraction of the interface that is covered with grain boundaries (2.5%), suggesting that pinned spins are mainly located at grain boundaries.

---

<sup>11</sup>S. Maat, IBM Almaden private communication

5. The remaining discrepancy can be accounted for by assuming that pinned spins are not only located right at the interface but also in directly adjacent layers.
6. The results represent the first clear correlation between microscopic magnetic properties of a 'real' antiferromagnetic/ferromagnetic interface and macroscopic exchange bias. They have meanwhile been completely reproduced on other systems like Co/Ir<sub>80</sub>Mn<sub>20</sub> and Co<sub>0.9</sub>Fe<sub>0.1</sub>/PtMn [63].



## Chapter 9

# Summary

The results presented in this thesis provide important new insight into the physics of antiferromagnetic/ferromagnetic interfaces. This significant scientific progress has been made possible by the use of polarization dependent soft x ray absorption spectromicroscopy, an experimental tool with the unique possibility to investigate the chemical as well as the magnetic structure of complex magnetic multilayer systems at the same time.

Our understanding of the relevant processes at antiferromagnetic/ferromagnetic interfaces had been limited so far by the lack of information about their actual structure. Many theoretical models, some of them introduced in the first chapter, try to quantitatively explain effects like coercivity increase and exchange bias. However, these models have to assume magnetic model structures and hence the agreement of theoretical predictions and experimental results was often poor.

Here, for the very first time a complete magnetic and chemical spectro-microscopic characterization of antiferromagnetic/ferromagnetic interfaces, namely thin Co or Fe films on NiO(001), has been achieved. For this purpose thin metal films (10 monolayers) were deposited on cleaved NiO(001) single crystals. The bare surfaces of these crystals were studied as well. The following observations are reported. An illustration of these findings is shown in figure 9.1

1. The domain structure at the surface of antiferromagnetic NiO(001) is dominated by bulk like antiferromagnetic domain walls parallel to crystallographic (100) planes. The observed domains are on average larger than  $1 \mu\text{m}$ . The antiferromagnetic axis realized in each domain depends on the preparation method. Sputtering appears to distort the lattice and only in plane domains exhibiting a spin axis along [110] unlike antiferromagnetic bulk domains are observed. Annealing in an oxygen atmosphere on the other hand preserves the bulk spin configuration parallel to [121], which exhibits a component perpendicular to the surface. However non bulk like domain walls are observed on these samples. These walls are parallel to (110) planes and are identified to be surface specific since they reduce the magneto static energy at the surface where the spin symmetry is lowered.

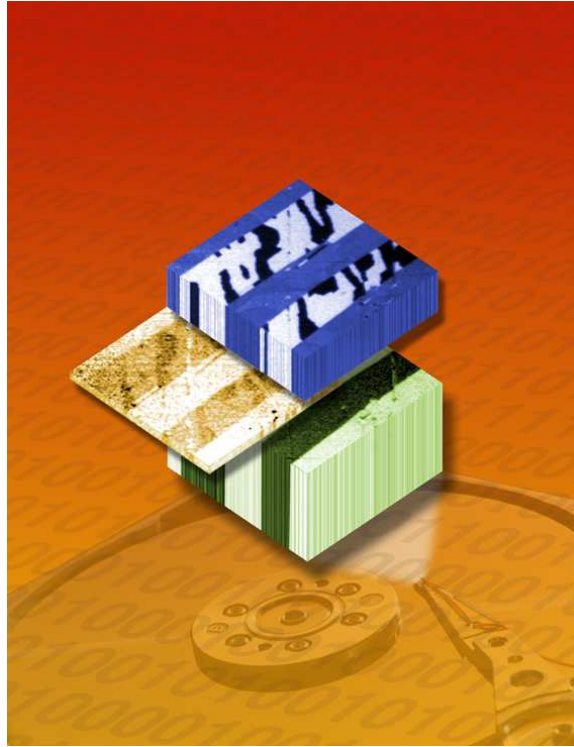


Figure 9.1: The Summary Image

A graphic illustration (by F. Robles, LBNL) of the magnetic configuration at the Co/NiO(001) interface. Antiferromagnetic/ferromagnetic interfaces play an important role in today's highly sensitive magnetic sensor as they are used in magnetic storage media.

Ferromagnetic Co layer (blue) and antiferromagnetic NiO surface (green) are separated by an ultrathin  $\text{CoNiO}_x$  layer. Discovering this layer has brought new insight into exchange coupling phenomena at such an interface, by using the distinct spectroscopic properties of this layer to separate bulk and interface magnetic properties. For this reason the artist chose to represent it in a golden color.

It could be shown that two different kinds of interfacial spins exist within this layer. The majority ('free') is strongly coupled to the ferromagnet and will follow an external field. These spins are responsible for the parallel *uniaxial* exchange coupling. A very small percentage of spins ('pinned') is coupled stronger to the antiferromagnet and cause the *unidirectional* exchange coupling.

2. Antiferromagnetic as well as ferromagnetic domain patterns in exchange coupled Co/NiO and Fe/NiO are observed. For the very first time the magnetic coupling could be directly observed and has been found to be parallel rather than perpendicular. To achieve this situation an in plane reorientation of the the antiferromagnetic spin axis takes place upon deposition of the ferromagnetic layer.
3. The intuitive assumption that such an metal/oxide interface is chemically not stable has been proven by means of high resolution x-ray absorption spectroscopy. The experiment reveals the formation of an ultrathin CoNiO<sub>x</sub> layer. Ni atoms within this layer are found to order ferromagnetically and to furthermore form an domain pattern which represents an exact replica of the Co domain pattern.

The possibility to detect the interfacial CoNiO<sub>x</sub> layer finally opened the door to a direct characterization of interfacial magnetic properties. Since metallic like Ni spins are assumed to be exclusively located at the interface, the location where the chemical reduction takes place, their magnetic properties directly reflect the characteristics of the interfacial exchange coupling. By employing the polarization dependence of the soft x ray absorption cross section element specific hysteresis loops could be obtained. The data originating from the ferromagnetic Ni spins were carefully analyzed and compared to the Co data regarding vertical and horizontal shifts. It could be demonstrated that two types of interfacial spins exist.

1. 'Free' interfacial spins, which are loosely coupled to the antiferromagnet and stronger coupled to the ferromagnetic layer. These spins exactly follow the magnetization of the Co layer in an external field and their hysteresis loop exhibit the same horizontal loop shift. They are responsible for the parallel uniaxial exchange coupling since they act as a 'buffer' between ferromagnetic and antiferromagnetic order and to suppress spin frustration which would lead to perpendicular coupling. It is demonstrated that the number of interfacial spins is directly linked to the size of the uniaxial exchange anisotropy and hence the coercivity increase in ferromagnetic/antiferromagnetic exchange coupled layers. Depending on the preparation condition the thickness of this layer varies between 0.5-4 monolayer.
2. 'Pinned' interfacial spins cover less than 5% of the interface. These spins are tightly locked to the underlying antiferromagnet which serves as a rigid matrix since it does not follow external fields. On the other hand these spins are still coupled to the ferromagnetic layer. Because they keep their orientation defined during the field cooling process, they can act as a constant internal field onto the ferromagnet and cause the hysteresis loop to be shifted along the *magnetization or vertical axis*. It is shown that the number of pinned spins accounts for the size of the unidirectional anisotropy and these spins are finally identified as the origin of exchange bias.

Altogether exiting new insight, which most likely will help to solve a more than 40 year old problem, has been obtained by **shining x-rays on interfaces**.



# Bibliography

- [1] D. Alders, *Epitaxial transition metal oxide films studied by high energy spectroscopy*, Ph.D. thesis, Rijksuniversiteit Groningen, 1996.
- [2] D. Alders, L. H. Tjeng, F. C. Voogt, T. Hibma, G. A. Sawatzky, C. T. Chen, J. Vogel, M. Sacchi, and S. Iacobucci, *Temperature and thickness dependence of magnetic moments in nio epitaxial thin films*, Phys. Rev. B **57** (1998), 11623.
- [3] D. Alders, J. Vogel, C. Levelut, S. D. Peacor, T. Hibma, M. Sacchi, L. H. Tjeng, C. T. Chen, G. van der Laan, B. T. Thole, and G. A. Sawatzky, *Magnetic x-ray dichroism study of the nearest-neighbor spin-spin correlation function and long-range magnetic order parameter in antiferromagnetic nio*, Europhys. Lett. **32** (1995), 259.
- [4] S. Anders, H. A. Padmore, R. M. Duarte, T. Renner, T. Stammer, A. Scholl, M. R. Scheinfein, J. Stöhr, L. Séve, and B. Sinkovic, *Photoemission electron microscope for the study of magnetic materials*, Rev. Sci. Instrum. **70** (1999), 3973.
- [5] D. Attwood, *Soft x-rays and extreme ultraviolet radiation: Principles and applications*, Cambridge University Press, Cambridge, 1999.
- [6] M. N. Baibich, J. M. Broto, A. Fert, F. Nguyen Van Dau, F. Petroff, P. Eitenne, G. Creuzet, A. Friederich, and J. Chazelas, *Giant magnetoresistance of (001)fe/(001)cr magnetic superlattices*, Phys. Rev. Lett. **61** (1988), 2472.
- [7] E. Bauer, *Photoelectron microscopy*, J. Phys. Cond. Mat. **13** (2001), 11391.
- [8] A. E Berkowitz and K. Takano, *Exchange anisotropy*, J. Magn. Magn. Mater. **200** (1999), 552.
- [9] G. Binasch, P. Grünberg, F. Saurenbach, and W. Zinn, *Enhance magnetoresistance in layered magnetic structures with antiferromagnetic interlayer exchange*, Phys. Rev. B **39** (1989), 4828.
- [10] C. Binek, A. Hochstrat, and W. Kleemann, *Exchange bias in a general meiklejohn-bean approach*, J. Magn. Magn. Mater. **234** (2001), 353.

- [11] J. A. Borchers, R. W. Erwin, S. D. Berry, D. M. Lind, J. F. Ankner, E. Lochner, K. A. Shaw, and D. Hilton, *Long range magnetic order in  $fe_3o_4/nio$  superlattices*, Phys. Rev. B **51** (1995), 8276.
- [12] D. M. Brink and G. R. Satchler, *Angular momentum*, Clarendon Press, Oxford, 1993.
- [13] M. J. Carey and A. E. Berkowitz, *Exchange anisotropy in coupled films of  $nis_1fe_19$  with  $nio$  and  $co_xni_{1-x}o$* , Appl. Phys. Lett. **60** (1992), 3060.
- [14] P. Carra, B. T. Thole, M. Altarelli, and X. Wang, *X-ray circular dichroism and local magnetic fields*, Phys. Rev. Lett. **70** (1993), 694.
- [15] C. T. Chen, Y. U. Idzerda, H.-J. Lin, N. V. Smith, G. Meigs, E. Chaban, G. H. Ho, E. Pellegrin, and F. Sette, *Experimental confirmation of the x-ray magnetic circular dichroism sum rules for iron and cobalt.*, Phys. Rev. Lett. **75** (1995), 152.
- [16] C. T. Chen, N. V. Smith, and F. Sette, *Exchange, spin-orbit and correlation effects in the soft x-ray magnetic circular dichroism spectrum of nickel*, Phys. Rev. B **43** (1991), 6785.
- [17] F. M. F. de Groot, *High resolution x-ray emission and x-ray absorption spectroscopy*, Chemical Review **101** (2001), 1779.
- [18] S.S. Dhesi, G. van der Laan, E. Dudzik, and A.B. Shick, *Anisotropic spin-orbit coupling and magnetocrystalline anisotropy in vicinal  $co$  films*, prl **87** (2001), 7201.
- [19] B. Dieny, V. S. Speriosu, S. S. P. Parkin, B. A. Gurney, D. R. Wilhoit, and D. Mauri, *To be defined*, Phys. Rev. B **43** (1991), 1279.
- [20] H. Ebert and Ya. Perlov, *Magneto-optische effekte (theorie)*, Magnetische Schichtsysteme (Jülich) (P. H. Dederichs and P. Grünberg, eds.), Forschungszentrum Jülich, 1999, p. C5.
- [21] H. Ebert and G. Schütz, *Spin-orbit influenced spectroscopies of magnetic solids*, Springer, Berlin, 1996.
- [22] W. Engel, M.E. Kordesch, H.H. Rothermund, S. Kubala, and A.v. Oertzen, *A uhv-compatible photoelectron emission microscope for applications in surface science*, Ultramicroscopy **36** (1991), 148.
- [23] R. F. C. Farrow, M. J. Carey, R. F. Marks, and P. M. Rice, *Enhanced blocking temperature in  $nio$  spin valves: Role of cubic spinel ferrite layer between pinned layer and  $nio$* , Appl. Phys. Lett. **77** (2000), 1191.
- [24] M. Fiebig, D. Frölich, T. Lottermoser, V. V. Pavlow, R. V. Pisarev, and H. J. Weber, *Second harmonic generation in the centrosymmetric antiferromagnet  $nio$* , Phys. Rev. Lett. **87** (2001), 137202.

- [25] M. Fiebig, D. Frölich, G. Sluyterman v. L., and R. V. Pisarev, *Domain topography of antiferromagnetic  $cr_2o_3$  by second-harmonic generation*, Appl. Phys. Lett. **66** (1995), 2906.
- [26] B. Fromme, Ch. Koch, R. Deussen, and E. Kisker, *Resonant exchange scattering in dipole forbidden  $d-d$  excitations in  $nio(001)$* , Phys. Rev. Lett. **75** (1995), 693.
- [27] B. Fromme, M. Möller, Th. Anschütz, C. Bethke, and E. Kisker, *Electron exchange processes in the excitations of  $nio(001)$  surface  $d$  states*, Phys. Rev. Lett. **77** (1996), 1548.
- [28] H. Gomonay and V. M. Loktev, *Magnetostriction and magnetoelastic domains in anti-ferromagnets*, J. Phys. Cond. Mat. **14** (2002), 3959.
- [29] E. Göring, A. Fuss, W. Weber, J. Will, and G. Schütz, *Element specific x-ray magnetic circular dichroism magnetization curves using total electron yield*, J. Appl. Phys. **88** (2000), 5920.
- [30] S. Heinze, M. Bode, A. Kubetzka, O. Pietzsch, X. Nie, S. Blügel, and R. Wiesendanger, *Real space imaging of two-dimensional antiferromagnetism on the atomic scale*, Science **288** (2000), 1805.
- [31] F. U. Hillebrecht, *Magnetic imaging*, J. Phys. Cond. Mat. **13** (2001), 11163.
- [32] F. U. Hillebrecht, H. Ohldag, N.B. Weber, C. Bethke, M. Weiss U. Mick, and J. Bahrdt, *Magnetic moments at the surface of antiferromagnetic  $nio(100)$* , Phys. Rev. Lett. **86** (2001), 3419.
- [33] Y. Ijiri, J. A. Borchers, R. W. Erwin, S. H. Lee, P. J. van der Zaag, and R. M. Wolf, *Perpendicular coupling in exchange biased  $fe_3o_4/coo$  superlattices*, Phys. Rev. Lett. **80** (1998), 608.
- [34] STAIB Instruments, *Peem 350 operating manual*, see also [22].
- [35] J. D. Jackson, *Classical electrodynamics*, Wiley, New York, 1962.
- [36] J. S. Jiang, G. P. Felcher, A. Inomata, R. Goyette, C. Nelson, and S. D. Bader, *Exchange bias effect in  $fe/cr(211)$  double superlattice structures*, Phys. Rev. B **61** (2000), 9653.
- [37] Joo-Von Kim and R. L. Stamps, *Defect modified exchange bias*, Appl. Phys. Lett. **79** (2001), 2785.
- [38] Joo-Von Kim, R. L. Stamps, B. V. McGrath, and R. E. Campley, *Angular dependence and interfacial roughness in exchange-biased ferromagnetic/antiferromagnetic bilayers*, Phys. Rev. B **61** (2000), 8888.
- [39] M. Kiwi, *Exchange bias theory*, J. Magn. Magn. Mater. **234** (2000), 584.

- [40] N. C. Koon, *Calculations of exchange bias in thin films with ferromagnetic/antiferromagnetic interfaces*, Phys. Rev. Lett. **78** (1997), 4865.
- [41] J. B. Kortright, D. D. Awschalom, J. Stöhr, S. D. Bader, Y. U. Idzerda, S. S. P. Parkin, I. K. Schuller, and H.-C. Siegmann, *Research frontiers in magnetic materials at soft x-ray synchrotron radiation facilities*, J. Magn. Magn. Mater. **207** (1999), 7.
- [42] J. S. Kouvel, J. Appl. Phys. **31** (1960), 142.
- [43] J. S. Kouvel and C. D. Graham, J. Appl. Phys. **30** (1959), 312.
- [44] W. Kuch, *Imaging magnetic microspectroscopy*, Magnetic Microscopy of Nanostructures (Berlin) (H. Hopster and H. P. Oepen, eds.), Springer Verlag, to be published.
- [45] P. Kuiper, B. G. Searle, L. C. Duda, R. M. Wolf, and P. J. van der Zaag, *Fe  $l_{2,3}$  linear and circular magnetic dichroism of  $fe_3o_4$* , J. Electron Spectrosc Rel. Phenom. **86** (1997), 107.
- [46] P. Kuiper, B. G. Searle, P. Rudolf, L. H. Tjeng, and C. T. Chen, *X-ray magnetic dichroism of antiferromagnetic  $fe_2o_3$ : The orientation of magnetic moments observed by  $fe_{2p}$  x-ray absorption spectroscopy*, Phys. Rev. Lett. **70** (1993), 1549.
- [47] D. R. Lee, Y. Choi, C.-Y. You, J. C. Lang, D. Haskel, G. Srajer, V. Metlusko, B. Ilic, and S. D. Bader, *Magnetization reversal measurements in  $gd/fe$  multilayer antidot arrays by vector magnetometry using x ray magnetic circular dichroism*, Appl. Phys. Lett. **81** (2002), 4997.
- [48] A.P. Malozemoff, *Random-field model of exchange anisotropy at rough ferromagnetic-antiferromagnetic interfaces*, Phys. Rev. B **37** (1987), 7673.
- [49] ———, *Mechanisms of exchange anisotropy*, J. Appl. Phys. **63** (1988), 3874.
- [50] D. Mauri, H.C. Siegmann, P.S. Bagus, and E. Kay, *Simple model for thin ferromagnetic films exchange coupled to an antiferromagnetic substrate*, J. Appl. Phys. **62** (1987), 3047.
- [51] W. H. Meiklejohn, *Exchange anisotropy - a review*, J. Appl. Phys. **33** (1962), 1328.
- [52] W. H. Meiklejohn and C. P. Bean, *New magnetic anisotropy*, Phys. Rev. **102** (1956), 1413.
- [53] ———, *New magnetic anisotropy*, Phys. Rev. **103** (1956), 904.
- [54] A. Messiah, *Quantenmechanik*, Walter de Gruyter, Berlin and New York, 1990.
- [55] P. Miltényi, M. Gierlings, J. Keller, B. Beschoten, G. Güntherodt, U. Nowak, and K. D. Usadel, *Diluted antiferromagnets in exchange bias: Proof of the domain state model*, Phys. Rev. Lett. **84** (2000), 4224.

- [56] R. Nakajima, *X-ray magnetic circular dichroism spectroscopy in transition metal thin films*, Ph.D. thesis, Stanford University, 1999.
- [57] L. Néel, *Ann. Phys.* **2** (1967), 61.
- [58] J. Nogues, D. Lederman, T.J. Moran, and I.K. Schuller, *Positive exchange bias in fe-f<sub>2</sub>-fe bilayer*, *Phys. Rev. Lett.* **76** (1996), 4624.
- [59] J. Nogués and I. K. Schuller, *Exchange bias*, *J. Magn. Magn. Mater.* **192** (1999), 203.
- [60] F. Nolting, A. Scholl, J. Stöhr, J. W. Seo, J. Fompeyrine, H. Siegart, J.-P. Locquet, S. Anders, J. Lüning, E. E. Fullerton, M. F. Toney, M. R. Scheinfein, and H. A. Padmore, *Direct observation of the alignment of ferromagnetic spins by antiferromagnetic spins*, *Nature* **405** (2000), 767.
- [61] H. Ohldag, T.J. Regan, J. Stöhr, A. Scholl, F. Nolting, J. Lüning, C. Stamm, S. Anders, and R. L. White, *Spectroscopic identification and direct imaging of interfacial magnetic spins*, *Phys. Rev. Lett.* **87** (2001), 247201.
- [62] H. Ohldag, A. Scholl, F. Nolting, S. Anders, F. U. Hillebrecht, and J. Stöhr, *Spin reorientation at the antiferromagnetic nio(001) surface in response to an adjacent ferromagnet*, *Phys. Rev. Lett.* **86** (2001), 2878.
- [63] H. Ohldag, A. Scholl, F. Nolting, E. Arenholz, S. Maat, A. T. Young, M. J. Carey, and J. Stöhr, *Correlation between exchange bias and pinned interfacial spins*, *Phys. Rev. Lett.* **91** (2003), 017203.
- [64] H. Ohldag, V. Solinus, F. U. Hillebrecht, J. B. Goedkoop, M. Finazzi, F. Matsukara, and H. Ohno, *Magnetic moment of mn in the ferromagnetic semiconductor (ga<sub>0.98</sub>mn<sub>0.02</sub>)as*, *Appl. Phys. Lett.* **76** (2000), 2928.
- [65] H. A. Padmore and J. Feng, 2002, *private communication*.
- [66] M. Pajda, J. Kudrnovsky, I. Turek, V. Drchal, and P. Bruno, *Ab initio calculations of exchange interactions, spin wave constants and curie temperatures of fe, co and ni*, *Phys. Rev. B* **64** (2001), 174402.
- [67] G. A. Prinz, *Magnetoelectronics*, *Science* **282** (1998), 1660.
- [68] T. J. Regan, *X-ray absorption spectroscopy and microscopy study of ferro- and anti-ferromagnetic thin films with application to exchange anisotropy*, Ph.D. thesis, Stanford University, 2001.
- [69] T.J. Regan, H. Ohldag, C. Stamm, F. Nolting, J. Lüning, and J. Stöhr, *Chemical effects at metal/oxide interfaces studied by x-ray absorption spectroscopy*, *Phys. Rev. B* **64** (2001), 214422.

- [70] G. F. Rempfer, G. M. Desloge, W. P. Skoczylas, and O. H. Griffith, *simultaneous correction of spherical and chromatic aberration with an electron optical mirror: An electron optical achromat*, *Microscopy and Microanalysis* **3** (1997), 14.
- [71] W. L. Roth, *Neutron and optical studies of nio*, *J. Appl. Phys.* **31** (1960), 2000.
- [72] V. Saile, *Properties of synchrotron radiation*, *Synchrotronstrahlung zur Erforschung kondensierter Materie*, 23. Ferienschule Forschungszentrum Jülich (Jülich) (W. Eberhardt and W. Schilling, eds.), Forschungszentrum Jülich, 1992, p. 1.
- [73] O. Scherzer, *Z. f. Physik* **101** (1936), 593.
- [74] Th. Schmidt, U. Groh, R. Fink, E. Umbach, O. Schaff, W. Engel, B. Richter, H. Kuhlbeck, R. Schlögel, H.-J. Freund, A. M. Bradshaw, D. Preikszas, P. Hartel, R. Spehr, E. Bauer, and G. Benner, *Xpeem with energy-filtering: Advantages and first results from the smart project*, *Surf. Rev. Lett.* **9** (2002), 223.
- [75] A. Scholl, H. Ohldag, F. Nolting, S. Anders, and J. Stöhr, *Study of ferromagnet-antiferromagnet interfaces using x-ray peem*, *Magnetic Microscopy of Nanostructures* (Berlin) (H. Hopster and H. P. Oepen, eds.), Springer Verlag, to be published.
- [76] A. Scholl, J. Stöhr, J. Lüning, J. W. Seo, J. Fompeyrine, H. Siegart, J.-P. Locquet, F. Nolting, S. Anders, E. E. Fullerton, M. R. Scheinfein, and H. A. Padmore, *Observation of antiferromagnetic domains in epitaxial thin films*, *Science* **287** (2000), 1014.
- [77] T. C. Schulthess and W. H. Butler, *Consequences of spin-flop coupling in exchange biased films*, *Phys. Rev. Lett.* **81** (1998), 4516.
- [78] M. M. Schwickert, G. Y. Guo, M. A. Tomaz, M. L. O'Brian, and G. R. Harp, *X-ray magnetic linear dichroism in absorption at the l-edge of metallic co, fe, cr and v*, *Phys. Rev. B* **58** (1998), 4289.
- [79] C.G. Shull, W.A. Strausser, and E.O. Wollan, *Phys. Rev.* **83** (1951), 333.
- [80] G. A. Slack, *Crystallography and domain walls in antiferromagnetic nio crystals*, *J. Appl. Phys.* **31** (1960), 1571.
- [81] D. Spanke, V. Solinus, D. Knabben, F. U. Hillebrecht, F. Ciccacci, L. Gregoratti, and M. Marsi, *evidence for in-plane antiferromagnetic domains in ultrathin nio films*, *Phys. Rev. B* **58** (1998), 5201.
- [82] R.L. Stamps, *Dynamic magnetic hysteresis and anomolous viscosity in exchange bias systems*, *Phys. Rev. B* **61** (2000), 12174.
- [83] ———, *Mechanisms for exchange bias*, *J. Phys. D: Appl. Phys.* **33** (2000), 247.
- [84] M. D. Stiles and R. D. McMichael, *Model for exchange bias in polycrystalline ferromagnet-antiferromagnet bilayers*, *Phys. Rev. B* **59** (1999), 3722.

- [85] ———, *Temperature dependence of exchange bias in polycrystalline ferromagnet-antiferromagnet bilayers*, Phys. Rev. B **60** (1999), 12950.
- [86] ———, *Coercivity in exchange bias bilayers*, Phys. Rev. B **63** (2001), 064405.
- [87] J. Stöhr, *Nexafs spectroscopy*, Springer Series in Surface Sciences, vol. 25, Springer, Heidelberg, 1992.
- [88] J. Stöhr and H. König, *Determination of spin and orbital moment anisotropies in transition metals by angle dependent x-ray magnetic circular dichroism*, Phys. Rev. Lett. **75** (1995), 3748.
- [89] J. Stöhr and R. Nakajima, *Magnetic properties of transition-metal multilayers studied with x-ray magnetic circular dichroism.*, IBM J. Res. Develop. **42** (1998), 73.
- [90] J. Stöhr, H. A. Padmore, S. Anders, T. Stammler, and M. R. Scheinfein, *Principles of x-ray magnetic dichroism spectromicroscopy*, Surface Rev. Lett. **5** (1998), 1297.
- [91] J. Stöhr, A. Scholl, T. J. Regan, S. Anders, J. Lüning, M. R. Scheinfein, H. A. Padmore, and R. L. White, *Images of antiferromagnetic structure of a nio(001) surface by means of x-ray magnetic linear dichroism spectromicroscopy*, Phys. Rev. Lett. **83** (1999), 1862.
- [92] J. Stöhr, Y. Wu, B. D. Hermsmeier, M. G. Samant, G. R. Harp, S. Koranda, D. Dunham, and B. P. Tonner, *Element specific magnetic microscopy with circularly polarized x-rays.*, Science **259** (1993), 658.
- [93] K. Takano, R. H. Kodama, A. E. Berkowitz, W. Cao, and G. Thomas, *Interfacial uncompensated antiferromagnetic spins: Role in unidirectional anisotropy in polychrystalline ni<sub>81</sub>co<sub>19</sub>/coo bilayers*, Phys. Rev. Lett. **79** (1997), 1130.
- [94] B. T. Thole, P. Carra, F. Sette, and G. van der Laan, *X-ray circular dichroism as a probe of orbital magnetization*, Phys. Rev. Lett. **68** (1992), 1943.
- [95] B. T. Thole and G. van der Laan, *Branching ratio in x-ray absorption*, Phys. Rev. B **38** (1988), 3158.
- [96] B. T. Thole, G. van der Laan, and G. A. Sawatzky, *Strong magnetic dichroism predicted in the m<sub>4,5</sub> x-ray absorption spectra of magnetic rare earth materials*, Phys. Rev. Lett. **55** (1985), 2086.
- [97] L. Thomas, A. J. Kellock, and S. S. P. Parkin, *On the exchange biasing through a nonmagnetic spacer layer*, J. Appl. Phys. **87** (2000), 5061.
- [98] B. P. Tonner and G. R. Harp, *Photoelectron microscopy with synchrotron radiation*, Rev. Sci. Instrum. **59** (1988), 853.

- [99] C. Tsang, R. E. Fontana Jr., T. Lin, D. E. Heim, V. S. Speriosu, B. A. Gurney, and M. L. Williams, *Design, fabrication and testing of spin-valve read heads for high-density recording*, IEEE Trans. Mag. **30** (1994), 3801.
- [100] G. van der Laan, *Magnetic linear x-ray dichroism as a probe of magnetocrystalline anisotropy*, prl **82** (1999), 640.
- [101] G. van der Laan and B. T. Thole, *Strong magnetic dichroism in 2p absorption spectra of 3d transition metal ions*, Phys. Rev. B **43** (1991), 13401.
- [102] G. van der Laan, B. T. Thole, G. A. Sawatzky, J. B. Goedkoop, J. C. Fuggle, J.-M. Esteva, R. Karnatak, J. P. Remeika, and H. A. Dabkowska, *Experimental proof of magnetic x-ray dichroism*, Phys. Rev. B **34** (1986), 6529.
- [103] P. J. van der Zaag, Y. Ijiri, J. A. Borchers, L. F. Feiner, R. M. Wolf, J. M. Gaines, R. W. Erwin, and M. A. Verheijen, *Difference between blocking and Néel temperatures in the exchange biased  $fe_3o_4/coo$  system*, prl **84** (2000), 6102.
- [104] M. A. van Veenendaal, D. Alders, and G. A. Sawatzky, *Influence of superexchange on  $ni$  2p x-ray absorption spectroscopy in  $nio$* , Phys. Rev. B **51** (1995), 13966.
- [105] N. B. Weber, *Untersuchung von Übergangsmetallen und Übergangsmetalloxiden mit Hilfe von Synchrotronstrahlung*, Ph.D. thesis, University of Düsseldorf, 2002.
- [106] R. Wiesendanger, H.-J. Güntherodt, G. Güntherodt, R.J. Gambino, and R. Ruf, *Observation of vacuum tunneling of spin polarized electrons with the scanning tunneling microscope*, Phys. Rev. Lett. **65** (1990), 247.
- [107] T. Yamada, *Spin configuration in antiferromagnetic domain walls of the  $nio$ -type crystal*, J. Phys. Soc. Japan **21** (1966), 650.
- [108] T. Yamada, S. Saito, and Y. Shimomura, *Magnetic anisotropy, magnetostriction and magnetic domain walls in  $nio$ : Ii. experiment*, J. Phys. Soc. Japan **21** (1966), 672.
- [109] ———, *Magnetic anisotropy, magnetostriction and magnetic domain walls in  $nio$ : I. theory*, J. Phys. Soc. Japan **21** (1966), 664.

# Appendix



## Curriculum Vitae

January 24th 1970	Born in Düsseldorf, Germany
1976-1980	Grundschule (Elementary School) 1st to 4th grade in Düsseldorf
1980-1989	Gymnasium (High School) 5th to 13th grade in Düsseldorf
1989-1990	Military Services in Neumünster, Germany
1990-1997	Diploma in Physics (Bachelor/Master) at the University of Düsseldorf
1998-2002	Ph.D student in the group of Prof. Dr. E. Kisker and Prof. Dr. F. U. Hillebrecht at the Institute for Applied Physics, University of Düsseldorf.
Summer 1998	Visiting scientist in the group of Dr. J. B. Kortright, Materials Sciences Division, Lawrence Berkeley National Laboratory
1999-2002	Research Assistant in the group of Prof. Dr. J. Stöhr, Stanford Synchrotron Radiation Laboratory, Stanford University
1999-today	Visiting Scientist in the group of Dr. H. Padmore, Advanced Light Source, Lawrence Berkeley National Laboratory.
October 2002	Ph.D graduation.
November 2002 - today	Postdoctoral Research Associate in the group of Prof. Dr. J. Stöhr, Stanford Synchrotron Radiation Laboratory, Stanford University

## Awards

- Nominated for the Nottingham Prize 2000 at the Physical Electronics Conference, June 2000, Taos NM, USA.
- Award for outstanding graduate research performed at the Advanced Light Source at the ALS Users Meeting 2001, Berkeley CA, USA.
- Gold Award for the conduct of outstanding graduate research in the field of materials sciences at the spring meeting 2002 of the Materials Research Society in San Francisco CA, USA.
- Student Award granted by the Education and Award Committees of the IEEE Magnetics Society on the occasion of the INTERMAG 2002 conference in Amsterdam, Netherlands.

## Memberships in Professional Societies

- Deutsche Physikalische Gesellschaft since 1996
- European Physical Society since 1996
- American Physical Society since 1999
- Founding Member of the California Section of the American Physical Society (2000)
- Materials Research Society since 2002

## Publications

1. M. Pretorius, J. Friedrich, A. Ranck, M. Schröder, J. Voss, V. Wedemeier, D. Spanke, D. Knabben, I. Rozhko, H. Ohldag, F. U. Hillebrecht, E. Kisker.  
"Transverse magneto-optical Kerr effect of Fe at the Fe 3p threshold"  
Phys.Rev B 55(21),1997, pp.14133-5
2. J. B. Kortright, S. Kim, H. Ohldag, G. Meigs, and T. Warwick,  
"Magnetization imaging using scanning transmission x-ray microscopy"  
X-ray Microscopy: Proceedings of 6th International Conference of the X-ray Microscopy,  
August 2-6,1999, Berkeley USA. (Conference Proceedings)
3. J. B. Kortright, S. Kim, and H. Ohldag,  
"Sigma like phase and nano-scale segregation in polycrystalline  $\text{Fe}_x\text{Cr}_{1-x}$  films:  
An element-resolved magnetic and structural study"  
Phys. Rev. B 61(1), 2000, pp. 64-67.
4. H. Ohldag, V. Solinus, F. U. Hillebrecht, J. B. Goedkoop, M. Finazzi, F. Matsukura,  
H. Ohno  
"Magnetic moment of Mn in the ferromagnetic semiconductor  $(\text{Ga}_{0.98}\text{Mn}_{0.02})\text{As}$ "  
Appl. Phys. Lett 76(20), 2000, pp.2928-30
5. H. Ohldag, N. B. Weber, C. Bethke, U. Mick, F. U. Hillebrecht, M. Weiss and J. Bahrdt  
"Imaging of Antiferromagnetic Domains by Linear Magnetic Dichroism in Photoemis-  
sion Microscopy of NiO(100)."  
Synchrotron Radiation News 13(6), 2000, pp 25-32
6. A. Scholl, F. Nolting, J. Stöhr, J. Lüning, J. W. Seo, J. P. Locquet, J. Fompeyrine, S.  
Anders, H. Ohldag and H. A. Padmore.  
"Studies of the magnetic structure at the ferromagnet-antiferromagnet interface."  
Journ. Synch. Rad., 8(2), 2001, pp.101.

7. H. Ohldag, A. Scholl, F. Nolting, S. Anders, F. U. Hillebrecht and J. Stöhr  
 "Spin Reorientation at the Antiferromagnetic NiO(001) Surface in Response to an Adjacent Ferromagnet"  
 Phys. Rev. Lett. 86(13), 2001, pp 2878-2881.
8. F. U. Hillebrecht, H. Ohldag, N. B. Weber, C. Bethke, U. Mick, M. Weiss and J. Bahrdt  
 "Magnetic Moments at the Surface of Antiferromagnetic NiO(100)"  
 Phys. Rev Lett. 86(15), 2001, pp. 3419-3422
9. H. Ohldag, N. B. Weber, C. Bethke and F. U. Hillebrecht  
 "Surface antiferromagnetism of NiO studied by photoemission microscopy"  
 Jour. Elec. Spec., 114-116, 2001, pp. 765. (Conference Proceedings)
10. A. Scholl, F. Nolting, J. Stöhr, T. J. Regan, J. Lüning, J. W. Seo, J. P. Loquet, J. Fompeyrine, S. Anders, H. Ohldag and H. A. Padmore.  
 "Exploring the microscopic origin of exchange bias with photoelectron emission microscopy"  
 Journal of Applied Physics 89(11), pp 7266 (2001) (Conference Proceedings)
11. H. Ohldag, T. J. Regan, J. Stöhr, A. Scholl, F. Nolting, J. Lüning, C. Stamm, S. Anders and R. L. White  
 "Spectroscopic Identification and Direct Imaging of Interfacial Magnetic Spins"  
 Phys. Rev Lett 87(24), 2001, pp. 7201.
12. T. J. Regan, H. Ohldag, C. Stamm, F. Nolting, J. Lüning, J. Stöhr and R. L. White.  
 "Chemical Effects at Metal/Oxide Interfaces Studied By X-ray Absorption Spectroscopy"  
 Phys. Rev. B. 64(21), 2001, pp 4422.
13. H. Ohldag, N. B. Weber, F. U. Hillebrecht and E. Kisker.  
 "Observation of In-Plane Magnetization Reversal Using Polarization Dependent Magneto-Optical Kerr Effect"  
 Journal of Applied Physics, 91(4) pp. 2228 (2001).
14. S. A. Nepijko, N. N. Sedov, H. Ohldag and E. Kisker.  
 "Measurement of local magnetic fields in photoelectron emission microscopy by restriction of the electron beam"  
 Rev. Sci. Inst. 73(3), pp 1224 (2002)
15. A. Scholl, H. Ohldag, F. Nolting, J. Stöhr and H. A. Padmore.  
 "X-Ray photoemission electron microscopy, a tool for the investigation of complex magnetic structures".  
 Rev. Sci. Inst. 73(3), pp. 1362 (2002). (Conference Proceedings)
16. H. Ohldag, A. Scholl, F. Nolting, E. Arenholz, S. Maat, A. T. Young, M. J. Carey and J. Stöhr.

- "Correlation between exchange bias and pinned interfacial spins."  
Phys. Rev. Lett. 91(1), art. no 017203 (2003)
17. J. Lüning, F. Nolting, A. Scholl, H. Ohldag, J. W. Seo, J. Fompeyrine, J.-P. Locquet and , J. Stöhr  
"Determination of the antiferromagnetic spin axis in epitaxial LaFeO/sub 3/ films by x-ray magnetic linear dichroism spectroscopy."  
Phys. Rev. B 67(21), pp. 214433 (2003)
18. A. Scholl, H. Ohldag, F. Nolting, S. Anders, and J. Stöhr  
"Magnetic Structure and Coupling at Ferromagnet-Antiferromagnet Interfaces: Studies with Polarization Dependent PEEM "  
to appear in Magnetic Microscopies of Nano-structures edited by H. Hopster, H P Oepen, Springer (2003)

## Presentations

### Contributed

1. "Element specific investigation of magnetic domains on Fe and Fe/Co thin film systems using Scanning Transmission X-Ray Microscope" Spring Meeting of the German Physical Society, Münster Germany, March 1999
2. "Imaging magnetic domains on micro-structured Fe and Co stripes using PEEM" Spring Meeting of the German Physical Society, Münster Germany, March 1999
3. "Magnetic Moments of Mn in (Ga(-xMnx)As" 44th Annual Conference on Magnetism and Magnetic Materials, San Jose USA August 1999
4. "Magnetic Moments of Mn in (Ga(-xMnx)As" Spring Meeting of the German Physical Society, Münster Germany, March 2000
5. "Imaging antiferromagnetic domains on NiO(001) using PEEM" Spring Meeting of the German Physics Society (DPG), Münster Germany, March 2000
6. "Investigating Exchange coupling in Co/Nio(001) using XPEEM" 2nd PEEM/LEEM Workshop, Paris France, October 2000
7. "Direct observation of parallel magnetic coupling in Co/Nio(001)" 8th joint MMM-Intermag Conference, San Antonio USA, January 2001
8. "Magnetic Coupling In Antiferromagnetic/Ferromagnetic Sandwiches - A Spectromicroscopy Study" Inaugural Spring Meeting of the California Section of the APS, Irvine USA, March 2001

9. "Chemical and Magnetic Characterization of Buried Antiferromagnet-Ferromagnet Interfaces Using Polarization Dependent Photoemission Electron Spectromicroscopy." 61st Physical Electronics Conference, June 2001, Taos, USA. (Contribution to the Nottingham Competition)

### **Invited**

1. "Magnetic Coupling In Antiferromagnetic/Ferromagnetic Sandwiches - A Spectromicroscopy Study" CRISM Review Meeting February 2001, Stanford USA
2. "Interface magnetic structure of Co/NiO" Highlights of young Researcher at the ALS Users Meeting, October 2001, Berkeley USA
3. "Magnetic Coupling At Antiferromagnetic/Ferromagnetic Interfaces - A Spectromicroscopy Study" XRMS01 Workshop, December 2001, Halle Germany.
4. "A Close Look At Antiferromagnetic/Ferromagnetic Interfaces - A Spectromicroscopy Study" Swiss Light Source, December 2001.
5. "Understanding Magnetic Coupling At Antiferromagnetic/Ferromagnetic Interfaces - A Spectromicroscopy Study" Spring Meeting of the Materials Research Society, April 2001, San Francisco USA.
6. "Imaging Antiferromagnetic Domains at Surfaces and Interfaces using Dichroism XPEEM" INTERMAG Europe, May 2002, Amsterdam, The Netherlands.
7. "Interfaces and Exchange Bias - A Spectromicroscopy Study" Workshop on Prospects in magnetic oxide thin films and hetero-structures, May 2002, Versailles, France.
8. "Spectromicroscopy of Magnetic Interfaces using XPEEM" 7th International Conference on X-Ray Microscopy, July/August 2002, Grenoble France.
9. "Shining Light on Magnetic Interfaces - X-Ray Photoemission Electron Spectromicroscopy", Monthly Colloquia of the Santa Clara Valley IEEE Magnetics Society, September 2002, Milpitas, USA
10. "Polarized X-rays and Magnetic Interfaces", 49th AVS International Symposium, November 2002, Denver, USA.
11. "Magnetische Grenzflächen ins Licht gerückt", Januar 2003, Colloquia, Berlin BESSY2, Germany
12. "Imaging compensated and uncompensated magnetic order using polarized x-rays.", March 2003, International Symposium on Synchrotron Radiation, Hiroshima, Japan.
13. "Imaging compensated and uncompensated magnetic order using polarized x-rays.", March 2003, Colloquia, National Synchrotron Radiation Research Center, Hsintchu, Taiwan.